THÈSE POUR OBTENIR LE GRADE DE DOCTEUR DE L'UNIVERSITÉ DE MONTPELLIER

En Mathématiques et Modélisation

École doctorale Information, Structures et Systèmes

Unité de recherche IMAG UMR 5149

NUMERICAL SIMULATION OF BLOOD PLATELETS ADHESION ON STRUCTURED ARTIFICIAL SURFACES

Présentée par Corentin RAVELEAU
le 12 Décembre 2025

Sous la direction de Franck NICOUD

Devant le jury composé de

Micheline ABBAS, Maitresse de conférences, Université de Toulouse	Rapportrice
Manouk ABKARIAN, Directeur de recherche, CNRS	Examinateur
Laurence BERGOUGNOUX, Professeure des universités, Aix-Marseille Université	Présidente du jury
Blaise DELMOTTE, Chargé de recherche, CNRS	Rapporteur
Simon MENDEZ, Chargé de recherche, CNRS	Co-directeur
Franck NICOUD, Professeur des universités, Université de Montepellier	Directeur

UNIVERSITÉ DE MONTPELLIER

Remerciements

J'aimerais remercier en premier lieu Franck Nicoud et Simon Mendez, pour leur encadrement tout au long de cette thèse. Je sais bien que quand il s'agit d'encadrement de thèse, nous ne sommes pas tous logés à la même enseigne, mais j'estime avoir été très chanceux sur ce coup-là. Je ne serais jamais allé aussi loin dans ce projet sans votre aide.

Merci Franck de m'avoir fait confiance pour travailler sur ce projet qui m'a énormément inspiré. J'ai sincèrement apprécié travailler avec toi durant ces trois années durant lesquelles ton expertise et tes conseils m'ont été très précieux, le tout dans l'excellente ambiance des "réunions hebdomadaires".

Merci Simon pour ton aide précieuse sur les aspects plus techniques de la thèse, notamment sur YALES2BIO. Tes remarques et conseils toujours bienveillants sont un vrai soutien pour mener à bien un projet de cette envergure.

J'aimerais ensuite remercier Micheline Abbas et Blaise Delmotte d'avoir accepté de relire mon manuscrit. Merci également à Laurence Bergougnoux et Manouk Abkarian d'avoir accepté de faire partie du jury lors de la soutenance. Merci à tous pour les remarques constructives sur le manuscrit et votre bienveillance lors de la soutenance.

I would like to thank Marlene, Johanna and Michael from the Cardiovascular Engineering lab in Aachen for the very interesting discussions regarding this project. Being able to follow the experimental aspect of my simulations was really great, hopefully a complete comparison between our work will be possible at some point. Vielen Dank für alles !

Merci également à Manouk et Rémy au CBS d'avoir accepté de réaliser la validation expériementale de mes résultats.

Merci Brigitte, Céline et Nathalie pour leur aide sur tous les aspects administratifs de la thèse et de la vie au labo. Merci au personnel du RA pour les repas durant ces 3 années, notamment à Betty, Mohamed et toute personne impliquée dans la préparation des tartes salées. Les passages au RA sont toujours un moment agréable de la journée (sauf peut-être le crumble aux 25 légumes).

Merci à tous les doctorants, post-docs, stagiaires et autres non-permanents que j'ai pu croiser au labo. La bonne ambiance qui règne et l'entraide permanente sont extrêmement appréciables. Merci sans ordre particulier à Antoine, Sacha, Grégoire, Guillaume, Allessandra, Luca, Christelle, Baptiste, Adam, Hermès, Guillaume, Pierrick, King, Arax, Fabien, Luca, Clément, Delfin, Yefei, Christina, Victor, Malo, Abel, Pablo, Joris, Giulia, Raphael, Vito, Arax, Joseph, Anatole, Ulysse, Gabriele, Marwa, Aurelio, Nathan, Patrick, Chloé, Nikola, Sofian, Amélie, Julien, Raphaël, Thiziri, Andrea, Hugoledidacticien, Marien et tous ceux que j'ai pu oublier de citer.

Merci aux différentes personnes qui ont partagé avec moi le magnifique bureau 128. Merci à Salomé d'avoir écouté mes plaintes lorsque les clusters tombent en panne, merci à Juliette pour les décorations saisonnières, les gâteaux et les updates sur les potins du labo. Merci Nicolas pour ta ponctualité et les recommandations de jeux. J'espère que mes cailloux, balles de golf, globules, et autres non-plaquettes vous laisseront un aussi bon souvenir que celui que je garderai de l'ambiance du bureau.

J'ai volontairement oublié certains noms précédemment, pour qui des remerciements plus en détail sont nécessaires. Merci à Orlane pour les cannelés, les conseils sur Bisca' et la région Bordelaise qui t'est si chère. Si ça t'a fait lever les yeux au ciel tu me dois un pot de "cacamerde beurksalé" (c'est un banger (c'est une expression de djeuns)). Merci à Barth de m'avoir initié à l'escalade, au Vélodrome et d'égayer nos journées avec ton accent chantant et tes cueillettes sur le campus. Merci à Morgane de rappeler à Barth de ne pas laisser traîner ses caleçons. Merci mille fois à Axel pour m'avoir fait replonger dans une addiction sombre. Merci à Tanguy pour les leçons diverses et variées, et pour les fraises. Mmmmmmmmmerci à Pierre-Louis pour les refs et la moustache. Mmmmmmmmmmmerci à Alexandre pour les blagues encore moins drôles que les miennes, ce qui est une belle perf, mais qui

me fait énormément rire. Merci Anne pour le teasing des freestyles de Brutus, même si on commence à ne plus y croire. Merci à Mathilde, j'espère que Véro et Patrick vont bien, je ne crois pas avoir eu de nouvelles d'eux depuis leurs vacances dans le Vercors, tiens-moi au courant. Un merci particulier à Pierre, je ne sais pas si j'aurai eu le courage de m'embarquer dans cette aventure tout seul, savoir que j'étais dans le même bateau que ta bonne humeur et ta connerie contagieuse a été hyper motivant pour moi. Oublie pas de rendre les clés de la CAB en partant quand même. Merci à tous pour les fous rires, les discussions d'adultes, les discussions de pas adultes, les pauses trop longues, les soirées qui finissent en crise de nerfs, les parties de tarot endiablées ...

Merci à ma famille pour leur soutien inconditionnel. Votre avis et vos encouragements ont été essentiels pour mener à bien ce projet et pour prendre les décisions importantes en cours de route. Merci en particulier à Jeanne, même si tu as l'impression de ne pas y être pour grand-chose, le simple fait de t'avoir à mes côtés m'a permis de donner le meilleur de moi-même. J'espère que l'on est qu'au début d'un long voyage. Je vous aime.

Résumé

Les maladies cardiovasculaires demeurent la principale cause de mortalité à l'échelle mondiale, malgré les avancées en prévention et en traitement. Les dispositifs médicaux implantables, tels que les stents, valves mécaniques et dispositifs d'assistance ventriculaire, sont essentiels dans la prise en charge de ces pathologies. Toutefois, leur interaction avec le sang induit des phénomènes d'activation et d'adhérence plaquettaire susceptibles de générer des thrombus, compromettant la sécurité et l'efficacité clinique de ces dispositifs et nécessitant un traitement anti-thrombotique.

L'amélioration de l'hémocompatibilité de ces appareils médicaux constitue donc un enjeu majeur. Les stratégies les plus étudiées reposent sur le choix de matériaux biocompatibles, l'application de revêtements anti-adhésifs ou l'endothélialisation des surfaces. Récemment, la structuration topographique à l'échelle micro et nanométrique a émergé comme une solution prometteuse, inspirée par la morphologie de l'endothélium vasculaire, pour limiter l'adhérence des plaquettes comme montré sur la figure 1.5. Une revue de certains résultats expérimentaux de la litérature à permis de montrer que les études à ce sujet sont parfois incomplètes voire contradictoires. L'objectif de cette thèse est donc de développer un modèle numérique de l'adhérence plaquettaire permettant de s'affranchir de certaines difficultées expérimentales, dans l'objectif d'étudier en détail les intéractions entre les plaquettes sanguines et des surfaces structurées, autant du point de vue des méchanismes d'adhérence que d'un point de vue purement hydrodynamique.

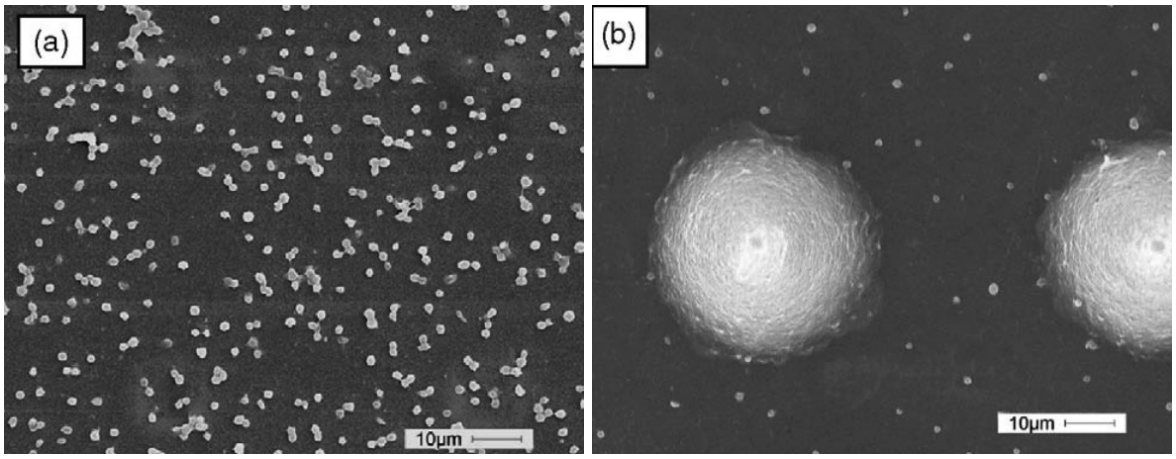

Figure 1: Adhérence de plaquettes sur (a) une surface plane et (b) une surface structurée. Tiré de [Ye *et al.* 2009]. La réduction d'adhérence plaquettaire sur la surface structurée peut être observée.

Pour développer ce modèle, une conaissance fondamentale des méchanismes impliquants les plaquettes et leurs mode d'action est nécessaire. Le premier chapitre de cette thèse présente notamment le rôle du sang dans le transport des nutriments et de l'oxygène dans notre corps, caractérisé par une suspension de particules (globules rouges, globules blancs et plaquettes) dans un fluide nommé plasma. Dans des conditions physiologiques de fonctionnement, les parois des vaisseaux sanguins recouvertes de cellules endothéliales garantissent les bonnes conditions de l'écoulement. Lorsque le vaisseau sanguin est endommagé, les cellules endothéliales libèrent et révèlent des espèces thrombogéniques qui vont permettre l'adhérence des plaquettes, comme le collagène ou le facteur de von Willebrand. Les plaquettes une fois stabilisées sur le site de la lésion vont s'activer, entrainant un changement de leur morphologie, passant d'une forme d'éllipsoïde rigide à la formation de protrusions appelées pseudopodes puis de leur étalement sur la surface endommagée, ainsi que la libération d'autres espèces thrombogéniques et l'activation de récepteurs à leur surface, permettant l'aggrégation d'autres plaquettes. Cet aggrégat

initial de plaquettes va finalement conduire à la formation d'un caillot suite à la cascade de coagulation, permettant l'arrêt du saignement et le soin de la lésion.

Ces mécanismes vitaux dans le cas d'une lésion sont également déclenchés par la présence d'un corps étranger comme un appareil médical pouvant conduire à une embolie ou au dysfonctionnement de l'appareil.

De plus, un certain nombre de modèles numériques de thrombose existent déjà dans la litérature et sont brièvement présentés dans le chapitre 1. Ils sont classés selon l'échelle à laquelle ils se concentrent, de l'échelle macroscopique de l'appareil médical ou du caillot, à l'échelle microscopique d'une plaquette en passant par des modèles mésoscopiques intermédiaires. Les avantages et inconvénients de ces modèles pour le problème considéré dans cette thèse sont également présentés.

A partir des informations biologiques et des modèles numériques exsitant, un modèle est développé dans cette thèse. Les plaquettes sanguines sont représentées par des ellipsoides rigides transportés par un fluide Newtonien homogène. Pour servir de première intuition ainsi que de validation pour le modèle numérique, une expression analytique des forces agissant sur une particule sphérique transportée proche d'une paroi avec des rugosités d'amplitude négligeable par rapport au rayon de la particule [Assoudi *et al.* 2018] est également utilisé. Ce modèle présente donc des limitations par rapport au modèle numérique, qui permetra une fois validé d'observer les interactions hydrodynamiques d'une particule ellipsoidale sur des surfaces d'amplitude comparable à la taille de la particule.

Le chapitre 2 présente les détails des calculs aboutissant à l'obtention de cette expression analytique. Ce résultat repose sur l'utilisation du théorème de réciprocité de Lorentz ainsi qu'un développement limité au premier ordre de la structure vers une surface plane. Notamment, dans le développement proposé par [Assoudi *et al.* 2018], un point d'incompréhension est soulevé et discuté à partir du développement réalisé dans ce travail. Le modèle analytique à permis de conclure que les structures d'amplitude négligeable devant le rayon de la particule ne permettent pas de générer une dérive d'une particule sphérique, peut importe la forme de la géométrie de surface. Cette conclusion justifie l'utilisation d'un modèle numérique pour étudier des structures d'amplitude finie.

Le chapitre 3 présente le modèle numérique implémenté dans le solveur YALES2BIO qui utilise la Force Coupling Method (FCM) pour représenter les plaquettes comme des particules ellipsoidales rigides. La FCM repose sur la méthode du développement en multipole pour la représentation d'une particule dans un écoulement de Stokes, généralisée à des écoulements à nombre de Reynolds faible mais non-nul en utilisant des supports Gaussiens pour les différents termes du développement plutôt que des distributions de Dirac singulières. Les détails théoriques de la FCM sont présentés ainsi que les détails sur l'implémentation numérique de cette méthode dans la résolution des équations de Navier-Stokes par la méthode des Volumes Finis réalisée dans YALES2BIO. Une validation extensive de l'implémentation de cette méthode est également présentée, avec notemment une étude sur l'effet de la taille de maille, l'effet de la proximité d'une paroi plane ou encore l'effet du ratio d'aspect de la particule. Cette étape de validation a permis de déterminer les paramètres de simulations assurant une résolution la plus précise possible tout en assurant des performances de simulation correctes.

Une fois le modèle numérique validé, son exploitation peut se diriger dans deux directions différentes. Tout d'abord l'intéraction purement hydrodynamique entre une particule et une paroi structurée est étudiée avec le modèle dans son état actuel. La comparaison avec le modèle analytique est également réalisée garantissant ainsi l'accord entre les deux modèles pour une particule sphérique et des structures de faible amplitude. 2 géométries de structure différentes sont présentées dans cette étude. Tout d'abord, des rainures carrées perpendiculaires à la direction de l'écoulement sont étudiées pour lesquelles la réversibilité des écoulements de Stokes garantissent qu'une sphère ne peut subire aucune force de portance moyenne la repoussant ou l'attirant vers la paroi à cause de la symmétrie de la géométrie. Cependant, une particule ellipsoidale permet de briser cette géométrie, aboutissant à des

dérives de la particule après une rotation de 180°. Cependant, une fois moyenné sur un ensemble de positions initiales, cet effet s'annule et est comparable à la dérive d'une particule proche d'une paroi plane causée par les effets inertiels faibles mais non-nuls.

Ensuite, une structure asymmétrique en dents de scie est étudiée, pour laquelle l'argument de réversibilité ne permet plus d'affirmer l'inexistance d'une dérive de la particule. Dans ce cas, un effet net de dérive est observé, la particule étant repoussée ou attirée vers la structure selon l'orientation des dents de scie comme présenté sur la figure 2. La dérive de la particule est quantifiée par un angle θ, obtenu comme le rapport entre le gain d'altitude de la particule sur une distance donnée, et la distance parcourue. Cette mesure est réalisée pour différentes positions initiales de la particule dans le motif de la structure, permettant d'obtenir une valeur moyenne de cet angle de dérive.

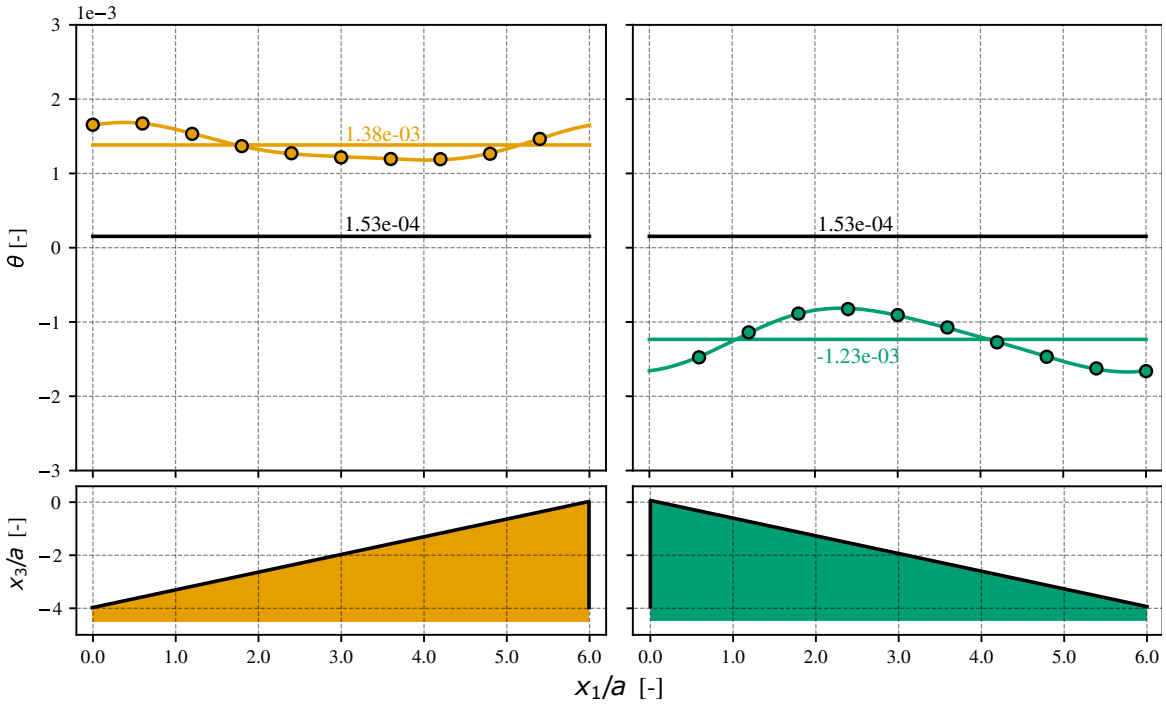

Figure 2: Angle de dérive pour une particule ellipsoïdale à différentes positions initiales, placée à une distance de $x_3 = 2.5a$ (——) d'une surface plane, (—●—) d'une structure en dents de scie orientées vers le haut, (—●—) d'une structure en dents de scie orientées vers le bas. Les marqueurs indiquent l'angle de dérive en radian pour la position initiale correspondante. Les courbes sont ajustées au travers des points pour améliorer la précision du calcul de la valeur moyenne. Les valeurs moyennes sont indiquées par les lignes horizontales de couleur correspondante à la structure.

Egalement, le chapitre 4 étudie la dépendance de cet angle de dérive selon différents paramètres. Il est notamment observé que l'angle de dérive tend vers 0 lorsque l'amplitude de la structure tend également vers 0, en accord avec la théorie analytique. Lorsque l'amplitude de la structure est augmentée, un plateau dans la valeur de l'angle de dérive est observé. Egalement, la période du motif de la géométrie à été étudiée ainsi que la dépendance de l'angle de dérive avec le nombre de Reynolds de l'écoulement. En particulier, l'angle de dérive ne tend pas vers 0 lorsque le nombre de Reynolds décroit, indiquant que la dérive est un effet non-inertiel qui doit être observable dans des écoulements de Stokes.

Le chapitre 5 se concentre ensuite sur une étude plus fine de l'interaction entre une particule et une structure en dents de scie, motivé par une recherche d'explication du phénomène de dérive précédemment observé. Pour cela, le problème est simplifié à l'étude de l'intéraction d'une sphère avec la structure en dents de scie, pour laquelle il est montré que la dérive est toujours présente bien que

plus faible que pour une particule ellipsoïdale. Ensuite, la structure en dents de scie est décomposée en éléments géométriques plus simples à savoir une rampe entre deux plaques planes et une marche verticale entre deux plaques planes pour comprendre les différences entre les effets générés par l'une ou l'autre sur la particule selon la taille de la rampe. Cependant cette étude n'a pas aboutit à une explication du méchanisme de dérive, mais a malgré tout permis de mettre en évidence un effet de la taille de la longeur de la rampe et de la hauteur de cette même rampe sur la force exercée sur la particule lors de son mouvement.

Finalement pour comprendre l'origine de cet dérive, la matrice de mobilité d'une particule sphérique sur la structure en dents de scie a été calculée et a permis d'identifier un effet croisé entre la translation horizontale de la particule causée par l'écoulement porteur et la génération d'une vitesse verticale à l'origine de la dérive de la particule. Cette vitesse verticale causée par la translation de la particule est plus importante que la vitesse verticale négative causée par la force verticale et le couple qui s'éxercent sur la particule, résultant un bilan de vitesse vertical positif qui explique la dérive de la particule.

Dans un second aspect, le modèle est approfondi en incorporant des méchanismes d'adhérence basés sur les méchanismes biologiques d'adhérence des plaquettes. Ces méchanismes d'adhérence sont présentés dans le chapitre 6, et des simulations de l'adhérence d'une particule sur une paroi plane et une paroi structurée avec des dents de scie sont réalisées et commentées. Une simulation de l'adhérence d'une particule sur une paroi plane pour laquelle les zones possibles d'adhérence sont restreintes est également présentée, permettant d'isoler l'effet de restriction de surface disponible créé par la structuration, sans inclure les effets hydrodynamiques discutés précédemment mais qui sont bien présents et observés dans le cas de la structure en dents de scie. Une simulation exploratoire de l'aggrégation de quatres particules sur une plaque plane est également montrée, présentant le potentiel du modèle.

Finalement, une conclusion résume les différentes méthodologies et résultats tout en présentant les perspectives de ce projet.

List of Figures

List of Tables

Contents

Relations between the chapters

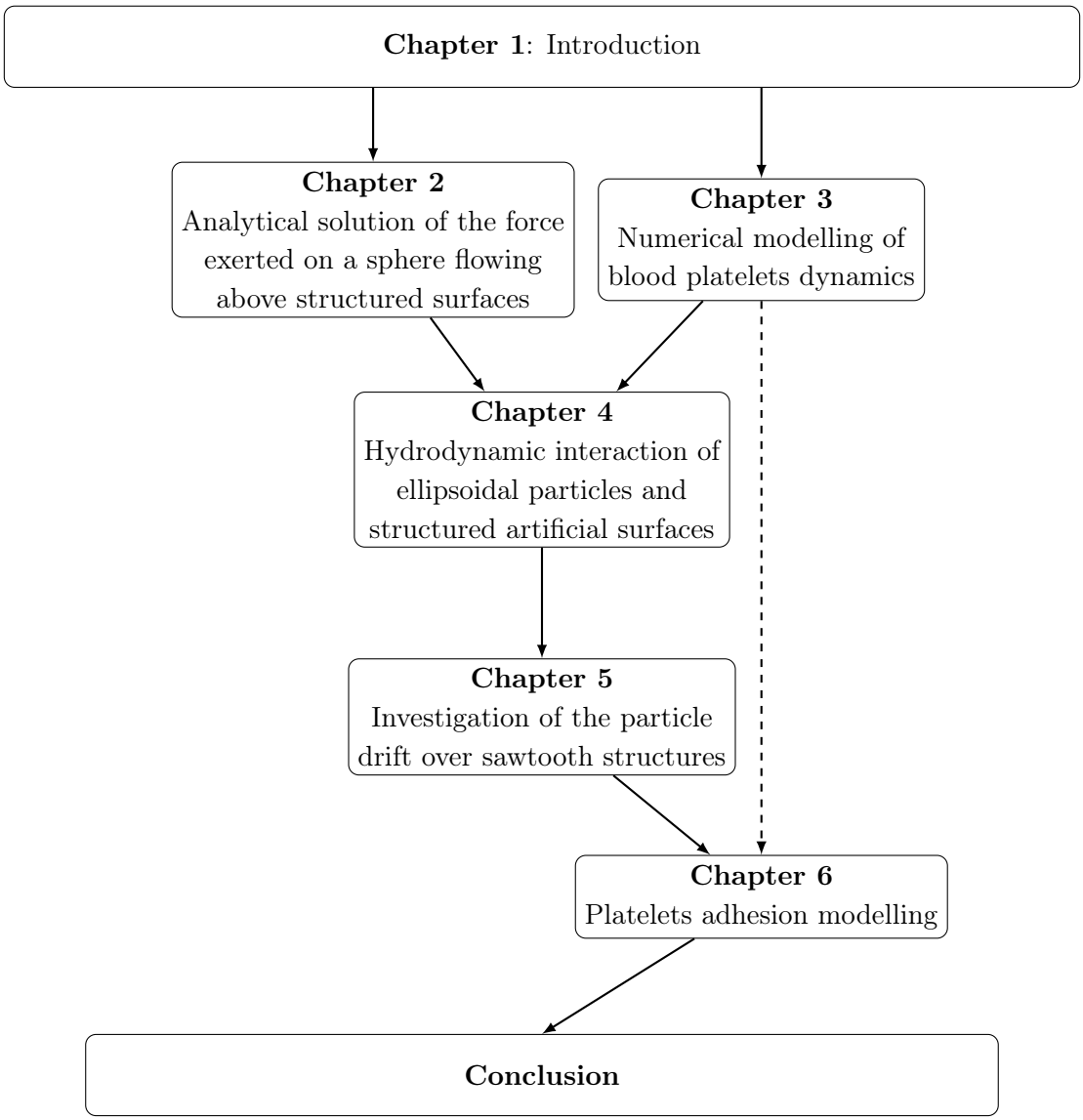

Chapter 1

Introduction

Contents

1.1 Context

According to recent reports by the World Health Organization (WHO), cardiovascular diseases are the leading cause of death worldwide representing about 31% of the world deaths [WHO 2024]. They account for diseases affecting either the heart itself or any element of the blood circulatory system such as vein or arteries. This includes ischemic heart disease and strokes which appear as two of the three leading causes of death in 2021 with COVID-19 as shown in figure 1.1(a), as well as aortic aneurysms, venous thrombosis or thromboembolism to name a few. Even though the global death rate per 100 000 people for all causes considered has been declining over the years up to the COVID-19 pandemic in 2020, the results from the Global Burden of Disease study conducted by the Institute for Health Metrics and Evaluation presented in figure 1.1(b) indicate that the rate of death related to cardiovascular diseases remains constant [Roth *et al.* 2020] while HIV and AIDS for example where in the top 10 list in 2000 but have been reduced by 61% [WHO 2024].

The difficulty to reduce cardiovascular diseases' mortality can be explained by an increase in cardiovascular risk factors in the last decades [Castillo-García *et al.* 2024]. Indeed, lifestyle choices can help reduce the risk of contracting cardiovascular diseases, although this risk still increases with age and can not be completely avoided. A healthy diet, good sleep quality, physical activity, low tobacco or alcohol intake and lower stress levels are all associated with reduced risk of cardiovascular diseases. A recent study on a Spanish cohort reported that only 3.5% of participant had an ideal lifestyle [Castillo-García *et al.* 2024], implying that although our knowledge on the optimal lifestyle towards healthier aging and reduced cardiovascular diseases is increasing, there is still a need for social and cultural changes to adopt these good practices [McGill *et al.* 2008].

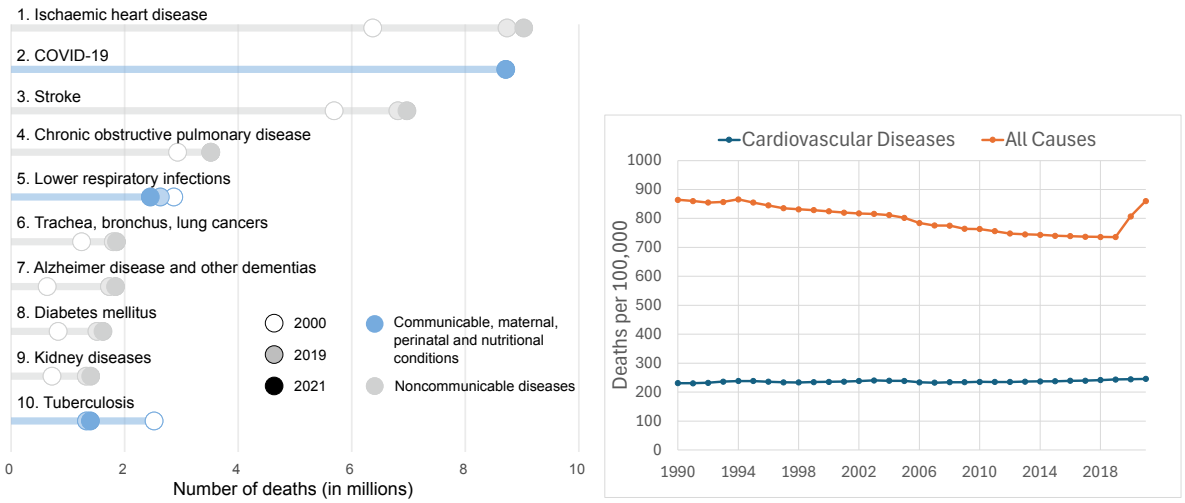

Figure 1.1: Infographics on the evolution and causes of death worldwide. (a) 10 leading causes of death since 2000. Adapted from the World Health Organization's Fact Sheets "The top 10 causes of death" [WHO 2024]. (b) Evolution of the death rate per 100,000 people from any cause and restricted to cardiovascular diseases from 1990 to 2021. Data provided by the Institute for Health Metrics and Evaluation from the Global Burden of Disease study [Roth *et al.* 2020].

The first step towards healthy population in regard to cardiovascular diseases is prevention and developing a good lifestyle throughout our lives as discussed before. However, the risk of cardiovascular diseases can not be reduced to zero, even with an optimal lifestyle, as genetics and age are also cardiovascular risk factor on which we have no control. It follows that cardiovascular diseases are going to be around for a long time and treatments for these diseases are required.

Because cardiovascular diseases encompass a high number of diseases very different from one another there is no such thing as a cardiovascular disease cure, but there are rather individual devices dedicated to the treatment of a single pathology. As examples, stents are used to treat atherosclerosis, bileaflet mechanical valves are used as heart valves replacement and left ventricular assistance devices (LVAD) are used to support a failing heart to pump blood. Although these devices have very different aims, implementation sites and sizes, they all share one key challenge to their development : hemocompatibility.

Hemocompatibility is defined by the quality of an artificial device to be brought to contact with blood without altering the blood state. A poorly hemocompatible device will lead to perturbation of the blood state and flow around the device, disturbing the blood functions, and will lead to thrombus formation at the device surface. Such device would be called thrombogenic. The issue with thrombogenic devices is two-folds: on the one hand thrombus formation on the surface of the device can lead to detachment of the thrombus into the blood circulation which can for example lead to pulmonary embolism or ischemic stroke resulting in the patient's death. On the other hand, the development of a thrombus on the surface of the artificial surface can cause a dysfunction of the medical device, resulting in a poor treatment for the initial pathology. These two problems justify the need for hemocompatible medical devices. Before assessing the currently available or studied technologies to improve the thrombogenicity of blood contacting medical devices, a brief introduction to the physiology of blood and thrombus formation is presented, so that the reader have the required biological knowledge to understand the problematics.

1.2 Blood physiology

1.2.1 General properties

Blood is the fluid transported in the cardiovascular system that is in charge of supplying the organs in our body with the required nutrients, such as oxygen or glucose, and to take away the waste they can generate, so it can be expelled from the body. The heart is at the center of this system as it pumps blood through a network of channels towards the organs and back. These channels are named arteries when the blood flows from the heart towards the organs and veins the other way around. Two arteries are departing from the heart: the aorta carrying oxygen and nutrient rich blood towards the organs and the pulmonary artery through which oxygen poor blood is sent towards the lungs.

When following an artery from the heart towards the organs, the size of the vessel will decrease in diameter when encountering a branching required to share the blood flow through the whole body, starting at around 2-3 centimeters at the aorta down to 10 micrometers for the smallest arterioles [Müller *et al.* 2008]. The arterioles are connected to the capillaries which are the site of nutrient transfer in the organs. Capillaries are even smaller than arterioles, with a diameter of around 8 micrometers, which is ideal to maximize the transfer of nutrient between blood cells and the organs. After passing through the capillaries, nutrient poor blood enters the venules and the veins which have relatively similar size than arterioles and arteries respectively, flowing back to the heart. This wide amplitude of channel size is also related to a broad range of shear rates spanning from about 20 to 5000 s^{-1} in physiological conditions [Ruggeri 2009] and up to 20 000 s^{-1} under pathological conditions [Fogelson & Neeves 2015].

Three layers compose the vessels walls but only the two innermost ones are of important interest for our purpose, so only these two are presented here. The innermost layer is called the endothelium, composed of a monolayer of endothelial cells and is directly in contact with blood. It is anti-thrombotic in physiological conditions as it releases chemicals that inhibit coagulation [Michelson *et al.* 2019], ensuring a stable state of flowing blood, but damage to this endothelial cell layer will trigger the so-called hemostasis process to stop the blood leakage from the injury. The second layer is mainly composed of smooth muscle cells which regulates the diameter of the blood vessel and therefore the blood pressure. It is also rich in prothrombotic species like collagen or tissue factor (TF) explaining why a disruption of the endothelial layer revealing these species will trigger the hemostasis process [Fogelson & Neeves 2015]. These two layers are shown schematically on the upper half of figure 1.2 for a healthy endothelium.

Figure 1.2 also presents the main blood constituents which are red blood cells (RBC), white blood cells (WBC) and platelets, immersed in plasma [Fogelson & Neeves 2015]. RBCs are deformable bi-concave shaped particles composed of a membrane filled with a fluid rich in hemoglobin that serves as binding site for oxygen, which will be transported by the RBCs towards the organs [Glenn & Armstrong 2019]. The RBCs are the most numerous particles in the blood representing about 40-45% of the total blood volume. This fraction of RBCs to whole blood volume is called the hematocrit. The WBCs are rigid spherical particles mainly responsible for the immune response involved in the protection of the body against infections. They are much less numerous than the red blood cells as with the platelets they account for 1% of the whole blood volume [Glenn & Armstrong 2019]. Blood platelets or thrombocytes are smaller than the RBCs and WBCs and have a typical discoid shape [Michelson *et al.* 2019]. They are the main particle involved in hemostasis and are the main focus of this work therefore more details regarding platelets physiology and functions are detailed in the following dedicated section. The remaining 55% of blood volume is blood plasma which is composed of water at about 90% with dissolved proteins, glucose, hormones and many more chemical species [Mathew *et al.* 2025].

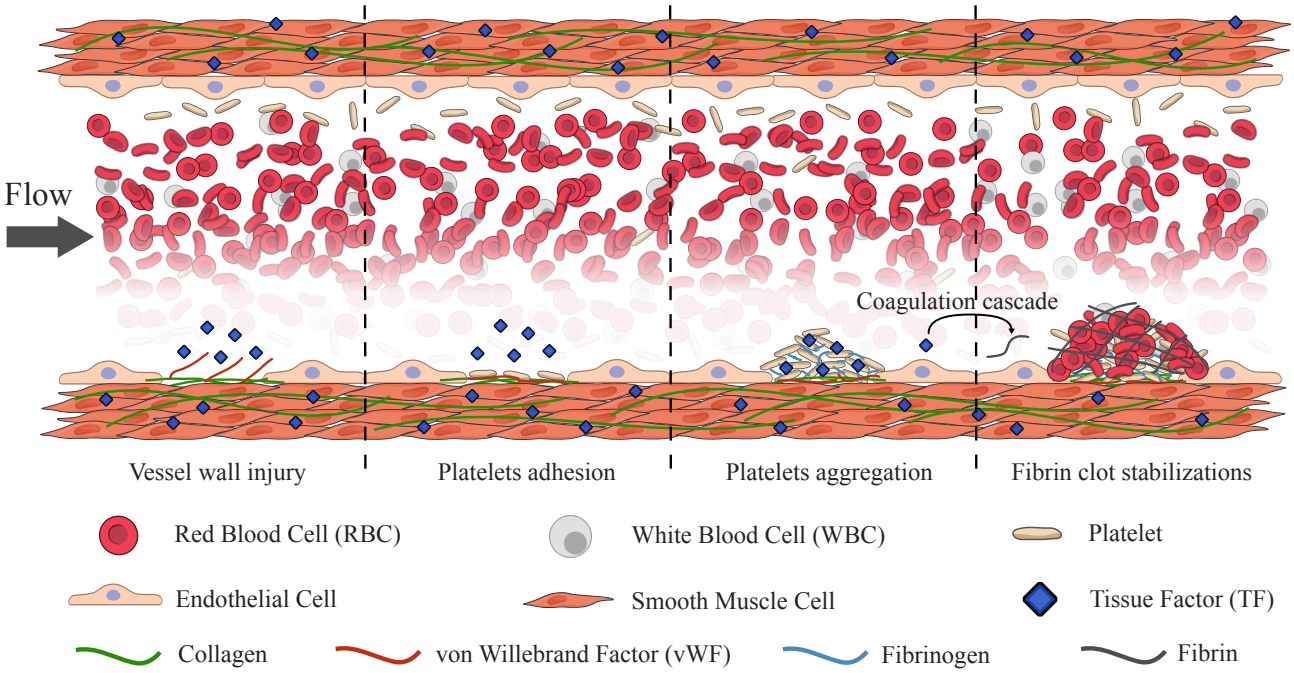

Figure 1.2: Schematic representation of a blood vessel and key mechanisms in thrombus formation. The two innermost layers of the vessel wall are represented as well as the main constituent of the blood namely red blood cells, white blood cells and platelets which are found in excess close to the wall resulting from RBC induced margination. The wall vessel is healthy on the upper half and injured on the lower half. The process of thrombus formation leading to the stopping of the blood leakage (hemostasis) and healing of the wound is presented in the lower half, divided in 4 steps. First step depicts the initial injury of the vessel revealing prothrombotic species like collagen, tissue factor or vWF. Secondly, platelets adhere to these species and subsequently activate from mechanical stimulation. Platelet activation leads to the release of more prothrombotic species as well as activation of platelet receptors allowing platelet aggregation via fibrinogen. The slow flow region through the initial platelet plug allows the coagulation cascade to happen, resulting in the polymerization of fibrinogen into fibrin, finally stabilizing the clot.

1.2.2 Platelets physiology and hemostasis

Blood platelets are small anucleated cells with a discoid shape in their resting and circulating state as shown in the SEM image 1.3(A). They are about 3 μm radius and 1 μm thick [Sachs *et al.* 2020] and are most of the time considered rigid as they are far less deformable than the bigger and more numerous red blood cells [Belyaev 2019, Reasor *et al.* 2013, Yazdani *et al.* 2017]. Their life-span in the body is around eight to ten days and the typical platelet count in a healthy adult is 300 000 platelets per μL of blood [Michelson *et al.* 2019]. The platelet membrane is composed of a lipid bilayer crossed by numerous receptors that can bind to external ligands and will transmit signals under mechanical or chemical stimulation. A cytoskeleton of microtubules coiled inside the platelet provides its structural rigidity and resting ellipsoidal shape [Zaninetti *et al.* 2020].

Because of their high deformability, red blood cells tend to migrate towards the center of a blood vessel creating a cell depleted layer or cell-free layer (CFL) close to the vessel wall. The higher rigidity and small size of platelets lead to their migration towards this CFL and it results in a greater concentration of platelets close to the wall than at the center of the blood vessel [Reasor *et al.* 2013]. This process is called platelets margination and is key for the platelets to fulfill their principal function. Indeed, platelets are responsible for the vessel walls integrity and are the first cell to interact with a wounded vessel, initiating the process of stopping a blood leakage out of the vessel (hemostasis) and

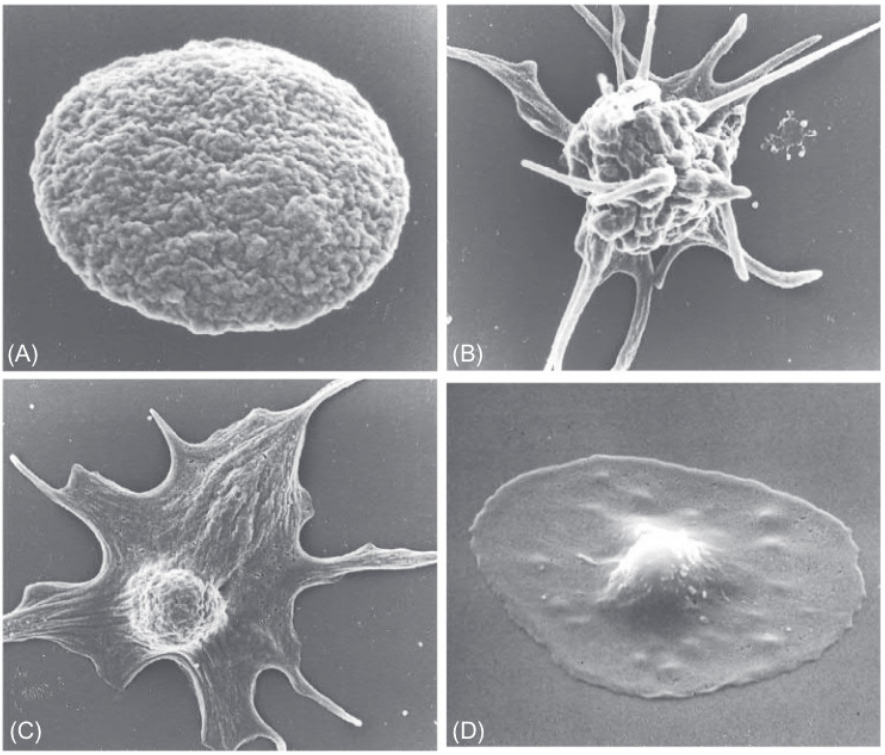

Figure 1.3: SEM images of platelets from there resting shape to their fully spread shape following activation from [Michelson *et al.* 2019]. (A) Resting platelet in a discoid shape. The visible folds on the membrane surface provide additional surface when the particle spreads. (B) After initial adhesion, the platelet evolves to a more rounded shape and pseudopods starts to develop in few minutes after initial adhesion. (C) Spreading of the platelet around the pseudopods. (D) Fully spread platelet maximizing surface of contact with substrate as well as reduced exposed profile to drag. Full spreading of the platelet takes roughly 10 minutes [Allen *et al.* 1979].

the healing of the vessel. The process of hemostasis can be decomposed in 4 steps : platelets adhesion, platelets aggregation and activation, coagulation cascade and fibrinolysis. The first three steps are depicted in the bottom half of figure 1.2.

Once marginated in the vicinity of the wall, platelets are probing for any injury while circulating and are brought to rest at site of injury in a process called platelet adhesion. Figure 1.4 details the main mechanisms involved in this initial platelet adhesion which are platelet integrin $\alpha 2\beta 1$ and immunoreceptor GPVI binding to subendothelial collagen fibers and platelet glycoprotein GP1bα binding to von Willebrand Factor that is itself bound to collagen (figure 1.2, second panel) [Gremmel *et al.* 2016]. Binding to other ligand such as fibronectin, laminin or vitronectin is also possible but either play a less important role than collagen and von Willebrand Factor (vWF) or their contribution to platelet adhesion is not certain [Ruggeri 2009]. vWF is a polymeric chain present in the plasma typically found in a non-reactive globular conformation but eventually revealing its binding sites for platelets when stretched due to sufficiently high shear rates [Springer 2014].

This initial adhesion will trigger platelet activation via mechanical signaling [Estevez & Du 2017], leading to multiple events. First, platelet will undergo a change in shape, evolving from their discoidal shape to a more spherical one and will start to develop some protrusion called pseudopods [Kuwahara *et al.* 2002] as shown in figure 1.3(B). As pseudopods develop, spreading of the platelet membrane between the pseudopods on the surface happens (figure 1.3 (C)) leading to the fully spread state of activated platelet shown in figure 1.3(D). This results in a more stable adhesion of platelets

due to increased contact area with the substrate as well as a reduced fluid induced force as the platelet profile exposed to flow is reduced. Secondly, the platelet will also release some chemicals that were stored in what are called granules. These chemicals contain platelet activating species such as thrombin, adenosine diphosphate (ADP) or thromboxane A2 (TXA2) that will induce chemical activation of nearby platelets [Estevez & Du 2017], as well as procoagulant species like vWF or tissue factor which is also released by the subendothelium layer upon injury, that will initiate the coagulation cascade. Thirdly, platelet surface integrin $\alpha IIb\beta 3$ will switch from its resting low affinity state to a high affinity receptor [Tong *et al.* 2023] that will allow more permanent binding to immobilized vWF and platelets aggregation mediated by vWF and fibrinogen [Ruggeri & Mendolicchio 2007] as shown in the third panel of figure 1.2.

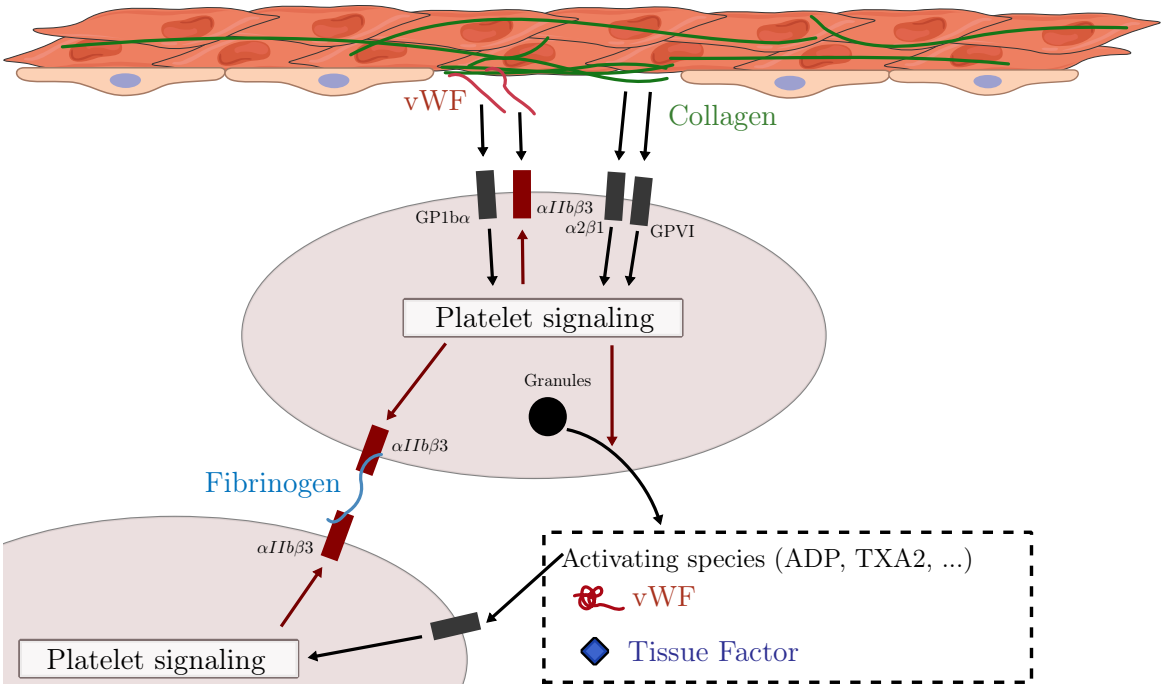

Figure 1.4: Key platelet adhesion mechanisms, adapted from [Gremmel *et al.* 2016]. Initial platelet adhesion to vWF and collagen is mediated by receptors GP1bα and $\alpha 2\beta 1$ and GPVI respectively. Mechanical stimulation from these receptors will trigger platelet signaling leading to conformational change to high affinity state of integrin $\alpha IIb\beta 3$ indicated in red. Activation will also trigger the release of platelet granules including activating species which will chemically trigger signaling of surrounding platelets as well as vWF and Tissue Factor, allowing platelet aggregation mediated by vWF or Fibrinogen and initiation of the coagulation cascade by the Tissue Factor.

Once platelet aggregate starts to grow, this results in a region inside the platelet plug core where blood flow is really slow. This slow flow region is ideal for the coagulation cascade to happen, which requires few minutes and could not happen at the site of injury if the flow was carrying away the reacting chemicals [Fogelson & Neeves 2015]. The coagulation cascade initiated by the interaction of tissue factor with the coagulation factors leads to the generation of thrombin further activating platelets as well as polymerization of soluble fibrinogen into non-soluble fibrin resulting in the formation of a fibrin net stabilizing the platelet plug. The fibrin net will also result in the trapping of red blood cells as depicted in figure 1.2, explaining the red color of a thrombus.

In fact, not all thrombi are red. Indeed, as previously mentioned, the red color is the result of the entrapment of red blood cells in the fibrin net resulting from the coagulation cascade. This is made possible because of the slow flow velocity inside the platelet plug but in some arteries or under patho-

logical flow conditions, the flow velocities are still so high that the coagulation cascade is carried away from the injury site before it has time to produce fibrin, and only platelet aggregation is involved in the hemostasis process. This time, it is almost exclusively resulting from binding to vWF and fibrinogen, collagen being much less important at these higher shear rates [Fogelson & Neeves 2015]. The higher significance of vWF at higher shear rates is explained by its conformational change, the higher shear rates promoting the unfolding of the vWF revealing the binding sites for platelets. This explains why blood clots found in veins are often red while clots in arteries tend to be white [Ruggeri 2009].

Once the clot is stabilized, healing of the wound can take place and the clot is then safely destroyed in a processed called fibrinolysis.

These complex mechanisms are key to ensure the vascular integrity in our body when triggered due to a wound, but these mechanisms can also be triggered by the presence of a foreign body such as a medical device exposed to direct contact with blood. In this case, the artificial nature of the surface of the device will initiate adsorption of blood plasma proteins at its surface which will result in an abnormally high concentration of these species ultimately triggering the hemostasis process [Jaffer *et al.* 2015]. As already introduced, the resulting thrombus formation at the surface of the device can lead to detachment of the thrombus in the circulation which can be fatal for the patient or just result in malfunction of the device. The next section provides insights to the current technologies used for improving the hemocompatibility of these devices.

1.3 Thrombogenicity of blood contacting medical devices

1.3.1 Current technologies for improved hemocompatibility

Even though perfect hemocompatibility of medical devices hasn't been reached yet, medical devices are used extensively as of today. To prevent device induced thrombosis, anti-coagulant and/or anti-platelets therapies are required [Jaffer & Weitz 2019] even though it can lead to severe complications such as excessive bleeding. As presented previously, the blood vessel walls are covered with endothelial cells which acts as an antithrombotic surface in healthy conditions. Rupture of a blood vessel wall and damage to the endothelial cells will trigger the formation of a blood clot at the site of injury by releasing prothrombotic chemicals, stopping the blood flow and allowing healing of the wound. When a medical device is brought to contact with blood, proteins present in the blood plasma will adsorb on the surface of the device. Initial deposition of this protein layer is performed almost instantly, but the composition of the layer is evolving through time [Rabe *et al.* 2011]. This adsorption result in an excessive protein concentration about 1 000 times larger than in the plasma bulk [Jaffer & Weitz 2019] at the device surface, triggering the formation of a thrombus. Blood platelets start to adhere on adsorbed fibrinogen and von Willebrand Factor (vWF) and the coagulation cascade is initiated. Adhesion and subsequent activation of platelets follows, as well as polymerization of fibrinogen into a fibrin net that will firmly trap platelets and red blood cells, leading to the formation of a thrombus.

The various anti-coagulant and anti-platelet therapies available act at short-circuiting this complex reaction by targeting different coagulation factor or platelet receptors, so that implantation of the device does not lead to thrombus formation. However, excessive bleeding can occur when the anti-coagulant therapy does not only target device induced thrombosis but also the physiological response to a vessel wall injury, therefore it is far from a perfect solution and the improvement of the hemocompatibility of the medical devices is required.

Improvement of the hemocompatibility of medical devices is looked for through different approaches that can in the end be complementary to obtain highly hemocompatible materials. Few examples are presented below in a list which is not exhaustive but allows to understand the difficulty encountered in

the development of hemocompatible materials. This difficulty is due to the inherent complexity of the thrombus formation mechanism on artificial surfaces as well as the complexity of access to observations and information due to the small length scales (nano/micrometer) and the long timescale of medical device working conditions (days, months or even years). The first step towards fully hemocompatible material, whatever the techniques used, is to have knowledge on the underlying mechanisms which will then provide answers on the ideal solution. In the end, the perfect solution might be a blend of all the mentioned techniques, and others, as each of them can act on different aspect of hemocompatibility and can be complementary.

Biocompatible materials

The composition of the adsorption layer depends on a lot of parameters including plasma pH, plasma protein concentrations, surface electric potential and chemical composition [Rabe *et al.* 2011]. While the properties of blood are fixed, the chemical and electrical properties of the surface can be modified by choosing or designing adapted materials such as hydrophillic polymers [Liu *et al.* 2014b]. While no perfectly biocompatible material has been developed yet, ensuring maximal compatibility of the bare material is the first step towards hemocompatible device.

Coatings

Addition of a coating on the surface of the device before implantation is used to enhance bare material hemocompatibility. The studied coatings can be decomposed into passive or active coatings. Passive coatings are used to alter the surface properties of the material by acting on surface roughness, surface charges or by deposition of inert biological proteins [Udriște *et al.* 2024]. They aim at altering the composition of the adsorption layer either by preventing it or by favoring adsorption of nonreactive species such as albumin [Luu *et al.* 2024]. It therefore acts as a stealth coating for the artificial device.

On the other hand, active coatings are designed to interact with the plasma proteins by chemical reaction. Drug eluting stents are a great example of such coatings, where an anticoagulant drug is deposited on the stent surface to prevent device induced thrombosis. It is great at providing smaller and local dose of anticoagulant that are less prone to excessive bleeding, but this effect is limited in time as the device runs out of reactive chemical [Udriște *et al.* 2024].

Endothelialization What biocompatible materials and coatings are aiming at is providing a similar blood-device interface as the blood-endothelial cells physiological interface. The ideal way to do so would be to reach full coverage of the artificial surface with endothelial cells, enabling the device to be completely hemocompatible. This can be done either *in-vitro* before the implantation of the device or *in-vivo* by favouring developpment of an endothelial layer once the device is implanted [Liu *et al.* 2014b].
Endothelial cells seeding on a device before its implantation is limited by two major drawbacks. First, full surface coverage of the device with endothelial cells can take up to few days, being incompatible with emergency needs. Also, once the device is implanted, the blood flow tend to degrade the seeded layer of endothelial cells, with reduction of endothelialized surface by 40-60% after one week [Liu *et al.* 2014b].
In-vivo self endothelialization has been recently proposed to be a great alternative to these issues. The idea is to favor adhesion of Endothelial Progenitor cells (EPC) which can differentiate into ECs, onto the device surface. Research on this matter is very recent, as EPCs were only discovered 30 years ago [Liu *et al.* 2014a]

Among the techniques which have not been mentioned yet, the use of artificial surface structuring has been shown experimentally to reduce platelets adhesion and is therefore expected to be more hemocompatible. However, the underlying mechanism causing this reduction in adhesion are not well understood, so this technology might be a great opportunity to enhance hemocompatibility of artificial surfaces but knowledge is lacking at this point. This work aims at providing some knowledge on the key mechanisms involved in the interaction between blood platelets and structured surfaces. The next section describes the current knowledge on this matter.

1.3.2 Experimental observations of platelets adhesion on microstructured surfaces

Endothelial cells are the ideal hemocompatible surface therefore drawing inspiration from their properties to design artificial surfaces seems to be a good approach. Endothelial cells hemocompatibility comes from various mechanisms, such as release of nitric oxide (NO) as a platelet functions inhibitor [Michelson *et al.* 2019], a negative surface potential repelling cells with negative surface potential such as platelets [Michelson *et al.* 2019], but also a typical cobblestone like pattern [Garipcan *et al.* 2011]. Chemical and electrical surface modifications have been mentioned previously and are extensively studied whereas this topological feature is less investigated.

[Ye *et al.* 2009, Ye *et al.* 2014] performed SEM images of rabbit and mouse heart valves and observed a double scale structure composed of the microscale endothelial cell cobblestone pattern covered with nanoscale cilia. They also observed that the cobblestone pattern is not completely random but is oriented in the direction of the flow which they suggest might play a role in the anti-thrombotic property of the endothelial layer. To investigate the effect of this topological feature on the hemocompatibility of an artificial surface, they designed a cobblestone like PDMS surface and compared its performance with a smooth surface in terms of platelet adhesion. To do so they incubated platelet-rich plasma (PRP) for 120 minutes over the samples and observed a qualitative reduction of adhered platelets shown in figure 1.5.

They suggest this reduction of platelet adhesion is due to an increase in the contact angle of the surface when using the structured surface compared to the flat surface. The contact angle of a material is measured by deposing a drop of water on the material sample and observing the angle θ between the

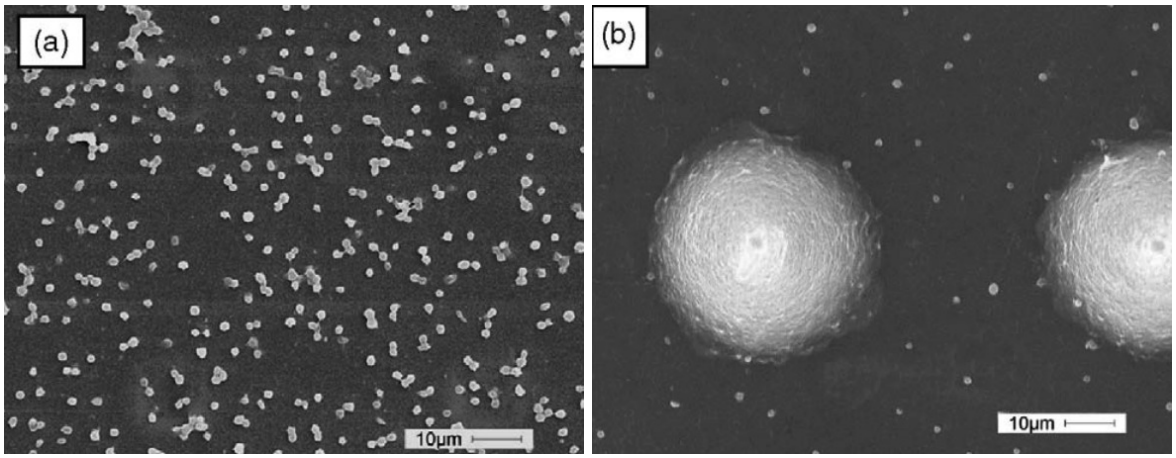

Figure 1.5: Platelet adhesion over a smooth (a) and a cobblestone patterned (b) surface from [Ye *et al.* 2009]. The reduction of platelet adhesion on the cobblestone patterned surface can be observed visually.

substrate and the edge of the drop as represented in figure 1.6. A surface with a small contact angle $\theta < 90°$ is called hydrophilic, meaning it has a high affinity with water and the drop appears spread out on the surface, while a contact angle $\theta > 90°$ is a property of hydrophobic surfaces and the drop has a more rounded shape. When θ is higher than 150°, the surface is referred to as superhydrophobic and water drops deposited on such surfaces appears almost spherical and will glide almost without friction in an effect called the Lotus effect, taking its name from the properties of the Lotus leaves.

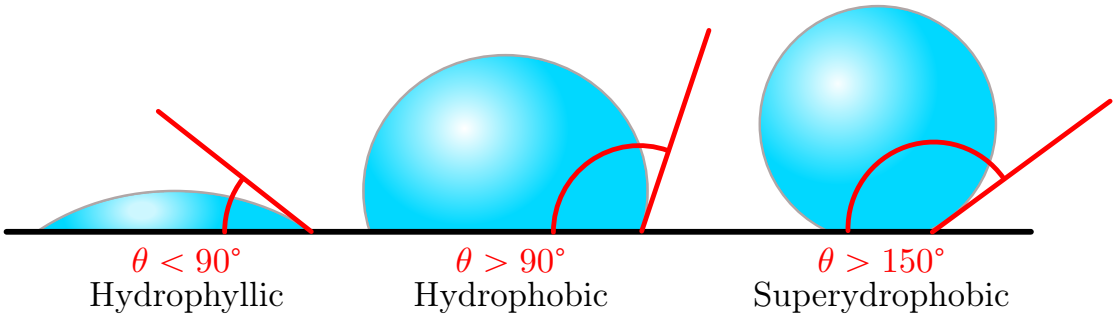

Figure 1.6: Depiction of the contact angle of a water droplet over a hydrophillic, a hydrophobic, and a superhydrophobic surface.

Superhydrophobicity can be achieved by using some structuration of the surface, such as the previously mentioned cobblestone pattern. Indeed, in [Ye *et al.* 2009], the flat surface was hydrophobic while the cobblestone pattern was superhydrophobic even though they were both in PDMS. When hemocompatibility improvement using microstructuration is investigated, the contact angle is almost always measured because a higher contact angle is related to a lowered affinity of water and therefore plasma with the surface, supposedly implying reduced platelet adhesion. [Ding *et al.* 2013, Ye *et al.* 2009, Ye *et al.* 2014, Zhou *et al.* 2008, Lamichhane *et al.* 2016, Pham *et al.* 2016].

Most of these studies observe an effect of the contact angle on platelet adhesion, however they do not agree. For example, [Ye *et al.* 2009] observed a reduction in platelet adhesion between a flat surface ($\theta \approx 113°$) and a cobblestone surface ($\theta \approx 163°$) both in PDMS, while [Ding *et al.* 2013] observed an increase in platelet adhesion between a flat surface ($\theta \approx 60°$) and a groove patterned surface ($\theta \approx 90°$) both in titanium oxide (TiO_2). In this case, the shape of the structure is not anymore based on

biomimetism of endothelial cells but rather on the contact angle manipulation. Great reduction of platelet adhesion using hydrophilic surfaces have also been observed [Kantam *et al.* 2024], highlighting the limitations of the correlation between contact angle and platelets adhesion.

Another thing to consider is that most of the previously mentioned studies were performed in static conditions. This is of interest when considering static applications, such as platelets storage bags [Apte *et al.* 2025], however in the context of blood contacting medical device hemocompatibility improvement, blood is not static but rather flowing past or through the device.

[Milner *et al.* 2005] performed dynamic experiments in a rotating disk system where they were able to observe platelet adhesion on pillars of 700 nm and 400 nm, across a wide amplitude of shear stress. They observed a reduction in platelets adhesion at the lowest values of shear stress investigated ($<$0.2 Pa) between a flat control and the structured surfaces but no difference was observed for higher values. Because the investigated structures are smaller than the typical platelet size, they suggest that the effective available surface for platelets adhesion to occur is restricted to the top of the pillars and is therefore smaller than the flat surface meaning platelets can bind fewer ligands over the structured surface than the flat surface resulting in weaker adhesion. This explanation has also been proposed by other groups that investigated sub-platelet size structures [Zhou *et al.* 2008, Chen *et al.* 2011, Koh *et al.* 2010]. [Koh *et al.* 2010] even concluded that the effect of surface topography on platelet adhesion can overcome the effect of surface chemistry.

This brief review of existing experimental studies regarding platelet adhesion on structured surfaces is sufficient to highlight the lack of understanding of the mechanisms involved. Some groups have obtained significant reduction in platelet adhesion with structures larger than the typical platelet size, for example with cobblestone patterns in the range of $10\mu m$ [Ye *et al.* 2009] or grooves from $1\,\mu m$ to $90\,\mu m$ [Clauser *et al.* 2014], while others suggest the explanation lies in the reduction of available binding area when using submicron structures [Koh *et al.* 2010, Ding *et al.* 2013]. Also, table 1.2 highlights the broad range of investigated materials, structure size, shape and flow conditions and the corresponding observations, which makes it very difficult to draw any clear conclusion on the interaction between platelets and structured surfaces. The only conclusion these studies are agreeing on is that adhesion of platelets can be altered by structuration of the surface. The underlying mechanisms remain unclear and the ideal structure to improve surface hemocompatibility is yet to be found.

References	Flow conditions	Material	Structure Pattern	Structure dimensions	Water Contact Angle	Observations (compared to flat surface)
[Milner *et al.* 2005]	Rotated disk (Linear shear stress variation over the disk from 0 to 1 Pa)	PUU	Square pillars	height: $600\,nm$ width: $400\,nm$ spacing: $400\,nm$		26% PLT adhesion at shear stress $< 0.2Pa$
				height: $650\,nm$ width: $700\,nm$ spacing: $700\,nm$		10% PLT adhesion at shear stress $< 0.2Pa$
[Minelli *et al.* 2008]	Channel flow $\dot{\gamma} = 3700 \pm 700\,s^{-1}$	PMMA	Hexagonal pattern	height: $3 \pm 1\,nm$ size: $40 \pm 15\,nm$		200% PLT adhesion 200% proteins adsorption (Fibrinogen and vWF)
				height: $13 \pm 7\,nm$ size: $80 \pm 20\,nm$		100% PLT adhesion 100% Fibrinogen adsorption 250% vWF adsorption
				height: $50 \pm 30\,nm$ size: $400 \pm 200\,nm$		50% PLT adhesion 50% Fibrinogen adsorption 250% vWF adsorption
[Zhou *et al.* 2008]	Static test (60 min)	PDMS	Micro-pillars	height: $5\,\mu m$ width: $15\,\mu m$ spacing: $25\,\mu m$	175°	20% PLT adhesion
				height: $5\,\mu m$ width: $15\,\mu m$ spacing: $35\,\mu m$	137°	78% PLT adhesion
				height: $5\,\mu m$ width: $15\,\mu m$ spacing: $45\,\mu m$	132°	90% PLT adhesion
			Nano-grooves	height: $130\,nm$ width: $830\,nm$	120°	2% PLT adhesion

References	Flow conditions	Material	Structure Pattern	Structure dimensions	Water Contact Angle	Observations (compared to flat surface)
[Ye *et al.* 2009]	Static test (120 min)	PDMS	Cobblestone	height: 30 μm diameter: 60 μm spacing: 40 μm	163°	Qualitative reduction in PLT adhesion and activation
[Yang *et al.* 2010]	Static (120 min)	TiO_2	Chemically treated nanotubes	height: 350 nm diameter: 80 nm	<5°	28.5% PLT adhesion Spread out but fewer pseudopods
				height: 350 nm diameter: 80 nm	156°	1.2% PLT adhesion Smooth and no pseudopods
[Ding *et al.* 2013] (Selected results)	Static test (45 min or 2h)	Silicon + TiO_2 coating	Grooves	height: 2.5 μm width: 0.5 μm spacing: 0.5 μm	$\theta_x = 130°$, $\theta_y = 45°$	160% PLT adhesion 200% PLT activation
				height: 2.5 μm width: 0.5 μm spacing: 7.5 μm	$\theta_x = 45°$, $\theta_y = 30°$	250% PLT adhesion 68% PLT activation
			Pillars	height: 2.5 μm diameter: 0.5 μm spacing: 0.5 μm	16°	200% PLT adhesion 110% PLT activation
				height: 2.5 μm diameter: 4.0 μm spacing: 4.0 μm	42°	280% PLT adhesion 140% PLT activation
				height: 2.5 μm diameter: 16.0 μm spacing: 16.0 μm	52°	130% PLT adhesion 90% PLT activation

References	Flow conditions	Material	Structure Pattern	Structure dimensions	Water Contact Angle	Observations (compared to flat surface)
[Clauser *et al.* 2014]	Channel flow (Wall shear stress: $0.028\,Pa$)	PCU	Grooves	height: $1.8\,\mu m$ width: $1.8\,\mu m$	$\approx$ 104°-108°	40% small PLT aggregate area 10% large PLT aggregate area 200% partially activated PLT
				height: $3.4\,\mu m$ width: $3.4\,\mu m$		43% small PLT aggregate area 0% large PLT aggregate area 240% partially activated PLT
				height: $90\,\mu m$ width: $90\,\mu m$		32% small PLT aggregate area 35% large PLT aggregate area 480% partially activated PLT
[Lamichhane *et al.* 2016]	Static test (60 min)	PTFE	Flat surfaces from different manufacturing processes	roughness: $0.17 \pm 0.02\,\mu m$	120°	Similar in PLT adhesion and activation than the polystyrene (PS) flat surface
		Expanded PTFE		roughness: $0.37 \pm 0.01\,\mu m$	140°	
		Electrospun PTFE		roughness: $1.08 \pm 0.21\,\mu m$	142°	60% PLT adhesion and 95% PLT activation compare to flat PS
[Pham *et al.* 2016]	Channel flow ($\dot{\gamma} \approx 750\,s^{-1}$)	PDMS	Hemispheres	height: $2.5\,\mu m$ diameter: $15\,\mu m$ spacing: $15\,\mu m$	115.3°	56% PLT surface coverage
				height: $2.7\,\mu m$ diameter: $15\,\mu m$ spacing: $5\,\mu m$	127.7°	21% PLT surface coverage
				height: $0.9\,\mu m$ diameter: $12\,\mu m$ spacing: $3\,\mu m$	120.2°	53% PLT surface coverage

Table 1.2: Experimental results available in the literature regarding artificial surfaces hemocompatibility improvement by using structuration of the surface. Some experimental parameters and results are presented here, but further details are provided in the corresponding papers. The observations are all relative to the control flat surface (which varies between the studies) so that 100% means the same result as the flat surface, values <100% corresponds to a decrease and values >100% corresponds to an increase of the indicated quantity. PLT = Platelet. The author would like to thank Marlene Schadow (CVE, Aachen, Germany) for the help in building this table.

From a different perspective, the use of surface structuring is already well-developed for microfluidic cell sorting applications [Choi 2020] where slanted grooves are used to generate a lateral drift of the particles which magnitude depends on the particle size and shape. When a spherical particle is translating and rotating near a flat wall, there is a pressure increase in front of the particle which is balanced by a pressure drop behind the particle implying no force acts on the particle outside the drag force in the flow direction. [Chase *et al.* 2022] suggest that when introducing the structured geometry underneath the particle, the symmetry of the flat wall and the antisymmetry of the pressure field at the wall are broken, resulting in a net lateral force acting on the particle. Applied to the context of platelets adhesion to structured surfaces, we expect that a similar symmetry breaking effect can also be induced by the structures, affecting the near wall dynamics of blood platelets purely from hydrodynamic interactions and therefore their ability to bind to the surface.

From these observations, this project aims at further investigating this interaction between platelets and structured surface, to provide more understanding on the underlying mechanisms. Experimental methods have paved the way in the study of platelet-structures interactions, but the complexity of the experimental setup, ethical issues with access to human blood, lack of reproducibility and difficulty to observe and measure accurately at such small scales all contribute to the difficulty to access more knowledge on this problem. Therefore, we aim at developing a numerical model of blood platelet dynamics and adhesion in a flow over a structured surface. Once validated properly, such numerical model can be used to investigate precisely individual effects (hydrodynamics, adhesion, structure shape and size) in a reproducible environment and with full control on the experiment parameters alleviating some difficulties encountered when performing *in-vitro* or *in-vivo* experiments [Fan *et al.* 2024].

To understand the underlying mechanisms, the goal is to perform numerical simulation which accounts for a single platelet, a patterned surface, and a plasma flow. Effect of the RBCs and WBCs are not considered in the first place as it will greatly increase the cost of the simulation and will make difficult the analysis of the platelet-structure interaction. The only RBC induced effect on the platelets accounted for in the simulations is the deposition of platelets close to the wall, as if they had already marginated due to collisions with RBCs. Also, simulation with single platelets are the first goal, as the process of platelet adhesion is performed by a single platelet. However, increasing the number of platelet to observe platelet aggregation might be of great interest. Because no other element than the single platelets are considered, the motion of the platelet will be restricted to a 2D motion in a plane defined by the flow direction and the normal to the wall.

In the following section, a state of the art on numerical models of blood platelets dynamics and adhesion is presented as well as their advantages and drawbacks regarding the problem we are focusing on. This review is then followed by a description of our model.

1.4 Numerical models of blood platelets adhesion

The previous sections highlighted the key mechanisms involved in platelets adhesion but were also useful to express the lack of knowledge on certain aspect of thrombosis. This lack of knowledge is due to the difficulty to access *in-vivo* information, the difficulty to reproduce *ex-vivo* or *in-vitro* the whole biological system and even in simplified systems, obtaining a precise measure or controlling all the parameters for reproducibility and interpretation is difficult as the observed length scales are small, and the biological complexity is still high.

Numerical models of thrombosis have gained a lot of attention in the recent years and various methods have been deployed to study platelet adhesion and thrombus formation at various scales. The strengths of numerical models to study thrombosis is the control one can have over the parameters in the simulations and the access to information impossible to obtain precisely in experimental con-

ditions such as flow velocity, pressure, wall shear-stress, etc... However, the drawback of numerical models is that the computational time is directly proportional to the complexity of the system. Indeed, reproducing accurately every single mechanism involved in thrombus formation would require a computational power out of reach as of today. Therefore, choices must be made when developing such model to account for the key mechanisms while discarding "secondary" ones. Obviously, this leads to an incomplete representation of the reality which should be kept in mind when interpreting the results of the model, but this can still lead to valuable knowledge that would have been out of reach experimentally. Validation of the numerical model against *in-vitro* or even *in-vivo* results is always valuable to ensure the numerical model is close to the reality and to know its limitations.

From the previous sections on blood and platelet physiology, it appears that the modeling of thrombus formation must account for fluid dynamics, cells and chemicals transport, initial platelet adhesion, platelet activation and aggregation as well as perturbation of the flow by the growing thrombi [Fogelson & Neeves 2015].

The numerical models available in the literature can be sorted in three categories. First, models attempting to model thrombus growth by accounting for the aggregation of individual platelets are referred to as mesoscopic models. Among these models, the first attempt at modeling thrombus growth was presented by Aaron L. Fogelson in 1984 [Fogelson 1984] following his PhD work, in which point particles representing platelets were transported as well as adenosine diphosphate (ADP) enabling particle activation and formation of elastic links to model adhesion and aggregation. Few years later, Fogelson himself presented a model suited for the study of thrombus growth at larger scales stating that the previous model with discrete particles was not suitable for simulation with a high number of particles [Fogelson 1992]. This second model category, defined as a macroscopic or Eulerian model, no longer considers platelets as individual particles but rather as a density function transported in the flow. This result in a coarser description of the biological mechanisms but faster simulations enabling application to larger scales. On the other hand, micro-scale models trying to improve the biological accuracy in the simulations at the cost of reducing the possible simulation time and scale were developped and form the third category. They only account for single or small number of platelets and focuses on internal particle structure, single particle deformation and dynamics or two-particle dynamics.

The next sections aim at describing in further details the strengths, the weaknesses and the uses for the 3 types of model introduced above and highlight the available or lacking modeling strategies to be implemented in our model.

1.4.1 Meso-scale Models

As mentioned previously, the first numerical models of thrombosis were meso-scale models or discrete particle models. They are very intuitive as they are based on the true nature of blood, namely a suspension of particles (red and white blood cells, platelets) in a fluid: blood plasma. Most of these model consider blood plasma as an incompressible Newtonian fluid governed by the Navier-Stokes [Vahidkhah *et al.* 2014, Yazdani *et al.* 2017], Stokes [Fitzgibbon *et al.* 2015] or Boltzmann [Reasor *et al.* 2013] equations in which particles are immersed. Various ways to model the dynamics of particles in these fluid are available depending on the required level of fidelity compared to real blood platelets [Maxey 2017].

The point-particle approach offers a simplified representation of rigid spherical particles by reducing them to their center of mass. The particles are advected in a Lagrangian manner, with their motion governed by Newton's law at their center of mass, and the drag force evaluated from the local fluid velocity. This method was used in the first model by Fogelson [Fogelson 1984]. He was able to simulate

platelet adhesion, aggregation and activation by a chemical species transported by the flow (ADP), paving the way for future models. Even though it is efficient and easy to implement, this method provides poor description of the real shape of blood platelets and are not able to represent the flow deviation around a platelet aggregate.

This was improved by the use of the Immersed Boundary Method (IBM) [Peskin 2002] which is now widely used to study the dynamics of deformable particles of arbitrary shape, such as red blood cells. In the IBM, a particle is represented by a set of interconnected Lagrangian markers transported over the Eulerian fluid grid and the evolution of the distance between connected nodes can be linked to stresses by appropriate rheological laws. Fogelson used this method as an improvement from his initial model and using an artificial diffusion term to model platelet margination due to red blood cells, he was again able to model platelets adhesion and aggregation [Fogelson & Guy 2008]. As the IBM is also suited for the simulation of RBCs, models incorporating both red blood cells and platelets in the simulation of blood flow often use the same modeling strategies for both particles. [Vahidkhah *et al.* 2014, Vahidkhah & Bagchi 2015] performed such simulations to study the dynamics of platelets margination and platelets dynamics inside the cell-free layer (Figure 1.7(a)). Using the same method for both RBCs and platelets results in an easier implementation however using the IBM for platelets modelling is quite costly in computational power because of the high rigidity of platelets compared to RBCs, resulting in high surface stresses and small deformations requiring small numerical time-steps [Fogelson & Guy 2008].

The Force Coupling Method (FCM) [Maxey & Patel 2001] has also been used to model blood platelets taking advantage of the apparent rigidity of these particles [Yazdani *et al.* 2017]. The FCM is able to represent accurately the flow disturbance caused by the presence of a rigid spherical or ellipsoidal particle from 0 to small Reynolds numbers [Maxey & Patel 2001, Liu *et al.* 2009]. [Yazdani *et al.* 2017] used the FCM to model the dynamics of platelets as rigid spherical particles as well as transport and reaction of 20 chemical species resulting in one of the most complete model to our knowledge. The transport and reaction of the chemical species eventually leads to platelet activation resulting in platelet adhesion on an injury site as shown in figure 1.7(b), and platelet-platelet aggregation by use of a Morse potential of interaction. The amplitude of the adhesion potential was set to be a function of the local shear rate yielding computed thrombus growth rate matching experimental observation. Even though this model is very comprehensive and is able to reproduce experimental observations, the interaction range and the amplitude of the force required to reproduce these observations are not physiological. Indeed, the Morse potential interaction range spans several platelets diameters while the typical adhesive bond length is few hundreds of nanometers (roughly 10% of particle diameter) [Ruggeri 2009].

Dissipative particle dynamics (DPD) where fluid is represented by a collection of particles governed by Newton's law of motion is also used extensively [Wang *et al.* 2020, Tosenberger *et al.* 2012] as the coupling between the fluid and the immersed particles is seamless. Indeed, all particles, both fluid and platelets, are treated the same way and their interaction, whether collision or adhesion, are easily accounted for by Newton's law as shown in figure 1.7(c).

These model are powerful tools to study thrombus growth process as they provide information on individual platelet dynamics in the thrombus. However, they have the drawbacks of being too computationally expensive for large scale simulation as the number of particles to consider is enormous, and they often require extensive simplification or poor resolution of the platelets biological mechanisms (Spherical platelets, long range adhesive forces, ...).

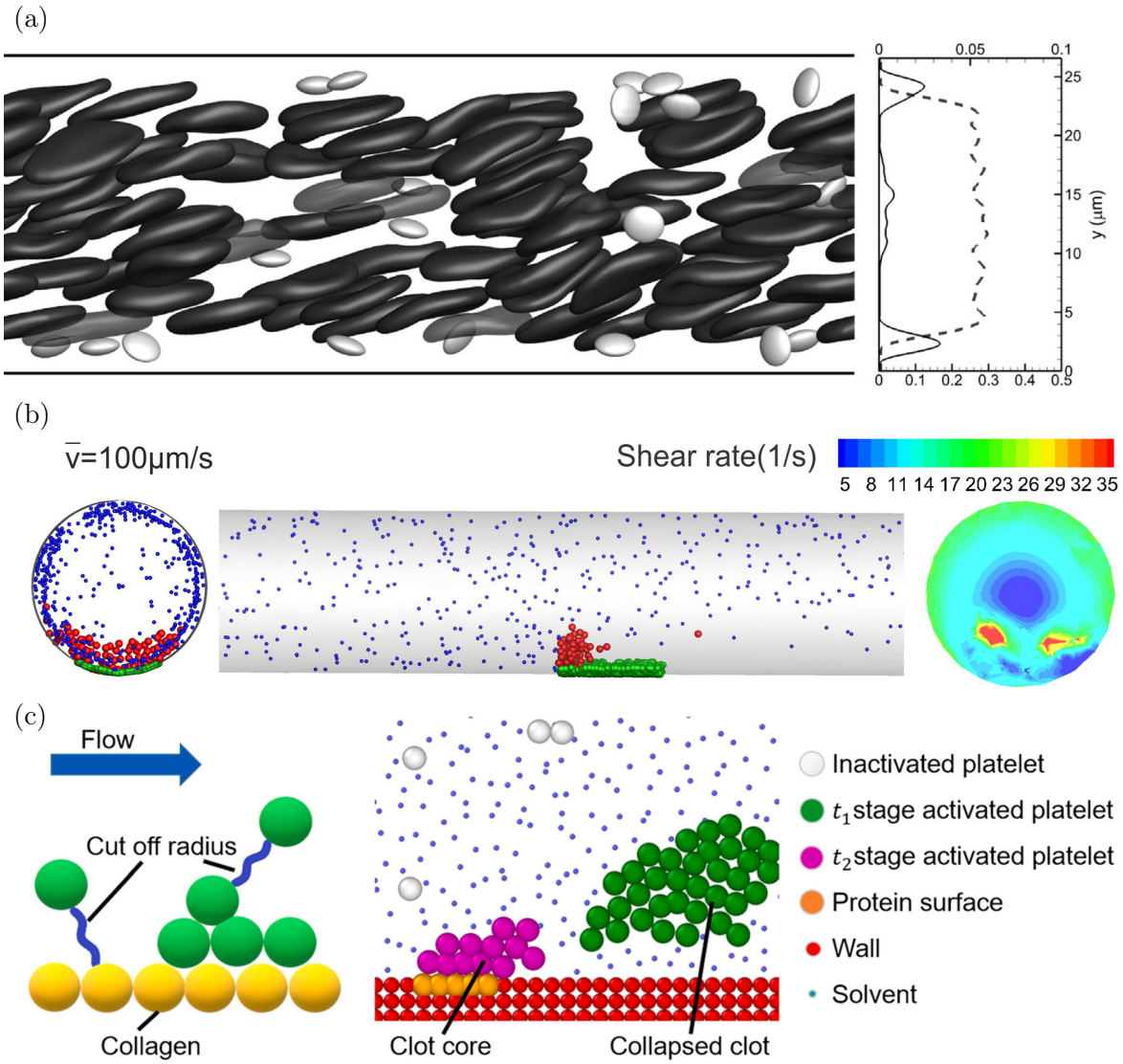

Figure 1.7: Mesoscopic models of platelets dynamics and adhesion. (a) 3D simulation of platelets margination in red blood cells suspension [Vahidkhah *et al.* 2014]. Right graph indicates the concentration of platelets and red blood cells along a channel diameter in continuous and dotted line respectively, highlighting the red blood cell depleted layer near the walls and excess in platelet concentration in this layer. (b) 3D simulation of inactive platelets (blue) flowing near an injury site (green) that releases platelet activating species as well as initiation of the coagulation cascade resulting in platelets activation (red) and subsequent aggregation [Yazdani *et al.* 2017]. Increase in flow shear rate at the top of the thrombus can be measured and is shown in the right insert. (c) DPD model [Wang *et al.* 2020] with multistage platelet activation, bond formation and breaking between platelets and a protein coated part of the surface, transported in a solvent modeled as particles.

1.4.2 Macro-scale Models

When considering a domain much larger than the typical particle size such as a medical device, platelets cannot be accounted for individually. Indeed, as the platelet count is around $300\,000\,\mu l^{-1}$ and a thrombus can range from few millimeters to few centimeters in both length and thickness, models studying the growth of thrombus in a device must take into account billions of platelets. At this scale, accounting for every single platelet is very expensive if not impossible and the platelets are instead modeled as a continuum density field transported by the ambient fluid.

As a transition between the previously described meso-scale models and these continuum models, [Yazdani *et al.* 2018] introduced a two scale model where platelets are tracked individually using the FCM upon their adhesion to the injury site but are converted to a continuum field once they are deposited to prevent the computation of the high number of platelet present in the thrombus. This was done by first having the deposited and activated platelets grow in size up to 60 times their initial radius, representing a collection of activated platelets with a fewer number of these bigger pseudo-platelets. The sum of the FCM Gaussian kernels of all the pseudo-particles are then used to define the continuum platelet density field as shown on figure 1.8(a-b). This method allows simulation of much bigger domain than their previous meso-scale model [Yazdani *et al.* 2017] and is for example suited for the investigation of thrombus development in patient specific geometries.

Most of the macroscale models do not take into account individual platelets at all. The platelets are represented by continuum density field from the start, eventually described by multiple species if different platelet activation or binding states are considered [Du *et al.* 2021, Wu *et al.* 2017]. These models often incorporate other mechanisms of thrombus formation such as vWF unfolding due to local extensionnal flows [Méndez Rojano *et al.* 2021] or ADP and thrombin induced platelet activation through Advection-Diffusion-Reaction equations [Wu *et al.* 2017] in the form of equation 1.1.

$$\frac{\partial c_i}{\partial t} + \boldsymbol{v}_f \cdot \nabla c_i = \nabla \cdot (D_i \nabla c_i) + r_i \tag{1.1}$$

where c_i describes the concentration for a given species such as innactive platelets, ADP, or vWF. D_i and r_i are respectively the diffusion coefficient and the reaction rate which are either drawn from experimental observations or calibrated so that the result of the simulation (*i.e* thrombus growth rate or shape) matches experimental results. $\boldsymbol{v}_f$ is the carrying fluid velocity, obtained by solving the Navier-Stokes equations.

These kind of models are able to accurately predict thrombus growth location and growth rate as shown in figure 1.8(c) and have been successfully applied to the simulation of thrombus formation in both patient specific aortas [Yazdani *et al.* 2018] and real size coagulation testing device [Méndez Rojano *et al.* 2022], highlighting the power of such models to scale up the domain of simulation. This gain in computing efficiency is inevitably linked to a loss in the accuracy of platelets description and when trying to look into the precise interaction of a platelet and a structured wall as we are interested, such continuum models discarding the dynamic of single particle are obviously not suited.

1.4.3 Micro-scale Models

On the other hand, some groups aimed at improving the description of individual platelets by increasing the number of mechanisms implemented in their simulations. This results in computationally expensive models not suitable for long simulations and restricted to simulation with only one or two particles and for short timescales ($<$ 1s), but they provide very important knowledge on some mechanisms which are very difficult to access with experimental observations.

Such models were for example successful at implementing a functional platelet cytoskeleton up to accurate reproduction of mechanical properties of the platelet membrane [Zhang *et al.* 2017] as well as pseudopod development during platelet activation [Zhang *et al.* 2021] shown in figure 1.9(a). At even lower scales, molecular simulations investigated the binding of platelet $GP1b\alpha$ receptor vo vWF-A1 [Shiozaki *et al.* 2016] as well as conformational change of integrin $\alpha IIb\beta 3$ during platelet activation [Tong *et al.* 2023].

At the scale of a single particle, some models are not trying to increase the fidelity of the platelet description, but are rather focusing on the dynamic of a platelet in a simplified isolated environment in

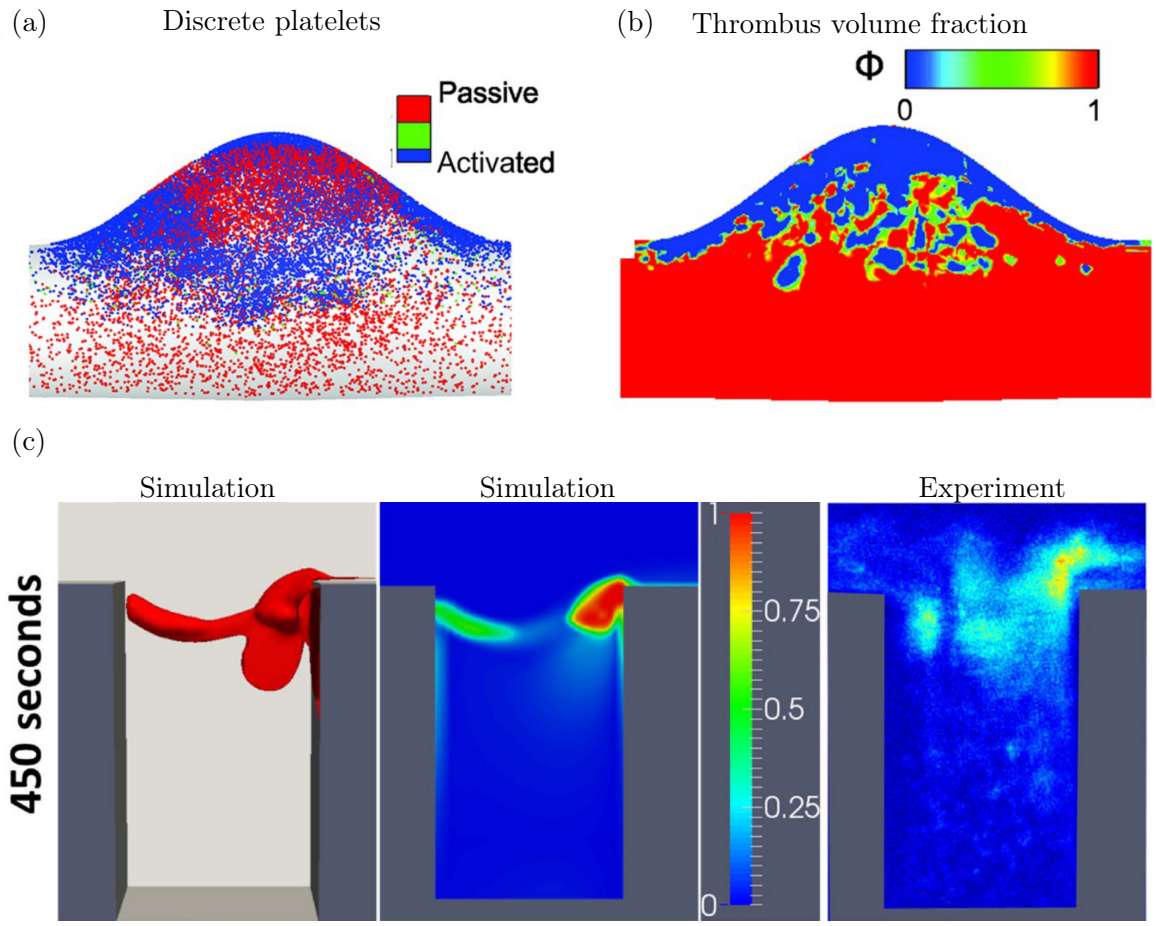

Figure 1.8: Macroscopic models of thrombus growth. (a) and (b) presents the multiscale model of [Zheng *et al.* 2020] in which individual FCM platelets (a) are converted to a continuum phase of thrombus (b). (c) depicts the qualitative success of a continuum model [Wu *et al.* 2017] to predict thrombus growth rate and location by comparing numerical results and experimental observations.

a more theoretical approach. In fact, these models are the closest ones available to the model we aim at developing to investigate the interaction of platelet adhesion to a structured surface. Among these models, [Mody & King 2005] investigated the hydrodynamic interactions between a single rigid oblate spheroid representing a platelet and a flat wall and identified 3 different platelets motion depending on the initial platelet-wall distance. Adhesion of such particles has also been investigated in the context of platelet initial adhesion on a flat surface [Pozrikidis 2006]. These models rely on the Boundary Elements Method (BEM) which is very accurate as it is based on an exact expression of the forces acting on the boundaries, allowing very precise investigation of these interaction mechanisms. These studies suggest that the approximation of platelet by a rigid ellipsoidal particle is good enough to look into wall-platelet interactions.

1.4.4 Our model

Gathering biological information on platelets morphology and mechanisms as well as available modeling technologies, we are able to define the key elements to be implemented in the model. As we are interested in providing knowledge on the interaction between blood platelets and structured artificial surfaces, the typical scale of the study lies in the micrometer range which will be the size of both a single platelet and the microstructure patterns. At this scale, the platelets can not be approximated by

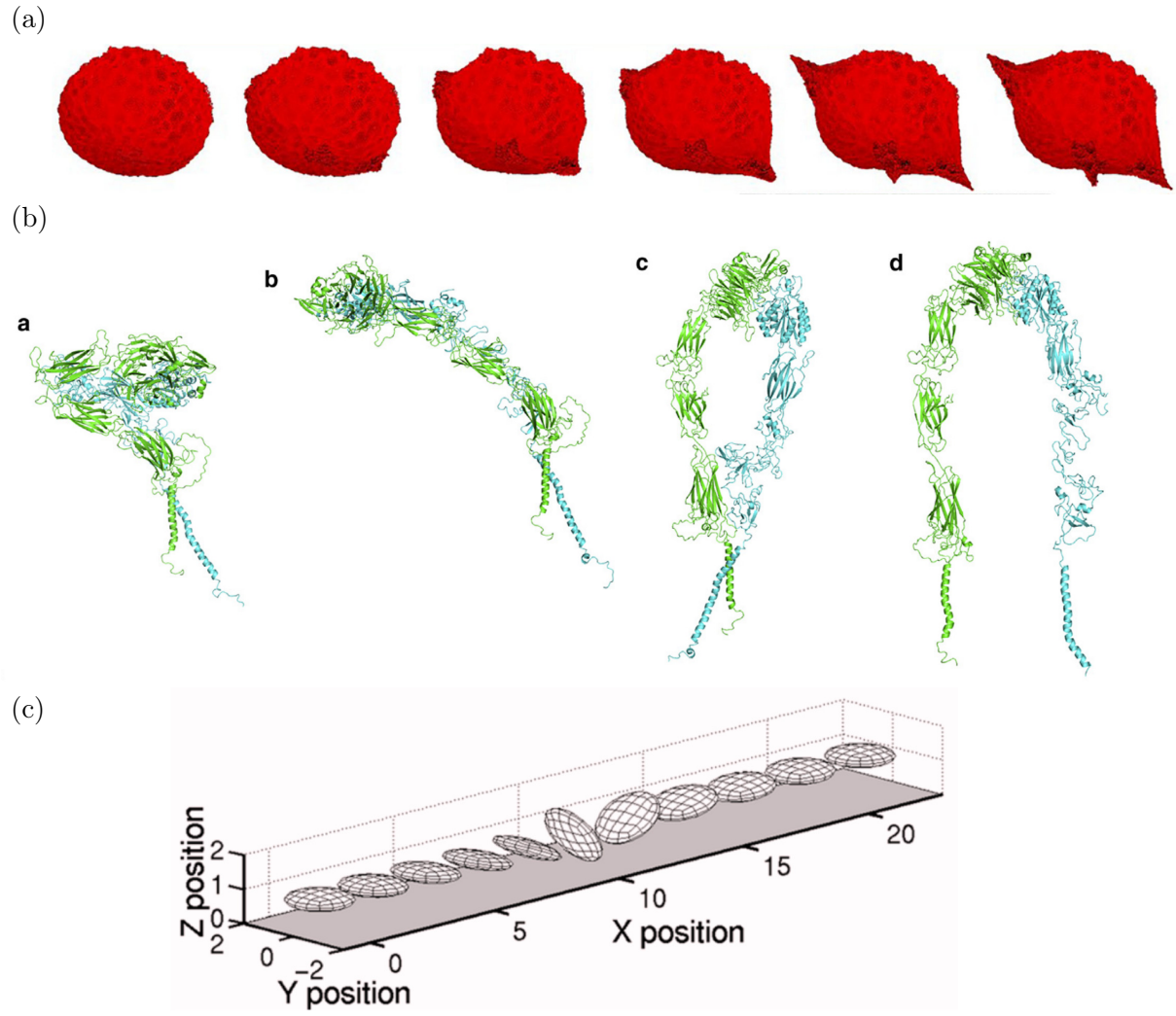

Figure 1.9: Microscopic models of thrombus growth. (a) Pseudopods developement during platelet activation [Zhang *et al.* 2021]. (b) Conformational change of the $\alpha IIb\beta 3$ integrin during platelet activation to a higher affinity state [Tong *et al.* 2023]. (c) Flipping motion of an isolated oblate spheroid close to a wall in a shear flow [Mody & King 2005].

a continuum density field and because we expect to be accurate in the description of the interactions between the particle and the structure, the dynamics of the particle must be resolved accurately, further discarding the continuum modeling for our application.

On the other hand, the timescale for platelet initial adhesion is typically of the order of few milliseconds. We might also be interested in simulating aggregation of a few particles. These 2 elements suggest that models accurately representing the complex structure and deformation of the platelets are not suited for our problem as they are too expensive for such simulation times and above one or two particles. For example [Zhang *et al.* 2017] performed the simulation of a micropipette experiment on a single platelet with resolved internal structure for $4.17\,\mu s$. We therefore chose to represent platelets as rigid particles, as it is widely encountered in the literature. However, the effect of particle shape has a great effect on its margination process [Reasor *et al.* 2013], particle-particle interactions [Mody & King 2008] near wall dynamics [Mody & King 2005] and wall binding efficiency [Vahidkhah & Bagchi 2015]. This is not a dominant effect at the thrombus scale so most of the models at this scale consider spherical particle for simplicity, but close to the wall this non-sphericity effect becomes important and must

be accounted for to describe precisely the wall-particle interaction. The representation of platelets by rigid ellipsoidal particles has already been used to study the hydrodynamic interaction and initial adhesion of a platelet to a flat surface at zero Reynolds number [Mody & King 2005, Pozrikidis 2006]. However, the BEM is limited by the fact that the linear systems to be solved are dense, making it hard to parallelize and impossible to use for simulations with a lot of particles. Even though this is not a concern for this project as we are interested in the initial event of single platelet adhesion, it could prevent further investigations on platelet aggregation or platelet margination for example.

Also, YALES2BIO, an in-house CFD solver developed to perform simulations of blood flows is available for our project [Mendez *et al.* 2022]. It allows the resolution of the Navier-Stokes equations in an arbitrary domain over large unstructured meshes via efficient parallelization. Availability and expertise of our team on this solver favors its use for this work and allows quicker access to results than if a new method such as BEM must have been implemented from scratch. It has also been used to simulate the dynamics of red blood cells [Lanotte *et al.* 2016] which could also be coupled with the simulation of platelets to investigate platelet-RBC interaction close to structured surfaces.

In this solver, only high resolution deformable capsules with the IBM method and point particles are implemented. Therefore, a method to solve for the dynamics of a rigid ellipsoidal particle must be implemented. Among the various methods available [Maxey 2017], the Force Coupling Method seems to be the most suited for our application. Initially developed for rigid spherical particles, it has been extended to ellipsoidal particles and is suitable for small Reynolds number flows up to $Re \approx O(1)$ which lies in the desired simulation range. What favored the choice for the FCM is its apparently simple implementation in the existing framework and the eventual possibility to make the shape of the particle evolve through time. Indeed, the shape of the particle is only defined by 3 values corresponding to the 3 semi-axis length of the ellipsoid. As platelet evolve in shape upon adhesion, direct manipulation of these semi-axis during the simulation is supposed to be possible with the FCM, making it a suitable choice for the considered problem.

1.5 Outline

The following chapters are dedicated to the detailed presentation of the methods and results obtained during this project.

Chapter 2 introduces the governing equations for the motion of particles immersed in a fluid and provides a review on the dynamics of particles in interaction with a wall. To provide further understanding of the mechanisms involved in these interactions, the analytical solution of the lift force acting on a spherical particle immersed in a shear flow over a structured surface of arbitrary shape is presented following [Assoudi *et al.* 2018].

Chapter 3 presents the numerical model introduced in section 1.4.4, from the resolution of the Navier-Stokes equations to the theory behind the Force Coupling Method, its implementation and validation. The FCM has already been validated previously but systematic assessment of the performance of this method close to a wall is performed.

Chapter 4 explores the purely hydrodynamic interaction between ellipsoidal particles and both square and sawtooth shaped grooves. Comparison between the numerical results with the FCM and the analytical expression of the force detailed in chapter 2 provides further validation in the context of near structured wall dynamics. A net particle drift is observed for the particle transported over the sawtooth structure. Effect of the configuration parameters on this drift angle, such as pattern period and amplitude as well as Reynolds number are investigated.

Chapter 5 details work conducted in an attempt at providing an explanation for the previously mentioned lift generated by the sawtooth structure. Simulation on an isolated ramp and step were

performed as well as further comparison with the analytical solution. The mobility matrix of the particle is also computed and allowed to understand in more details the origin of this lift.

Finally, chapter 6 presents the implementation of a model for platelet adhesion and subsequent simulations over both flat and structured surfaces. The model, even though very simplistic, is based on physiological data and is shown to agree with experimental observations on platelets translocation distance. The possibility of the adhesion model to be applied to platelet aggregation is also demonstrated with a simulation of four particles.

Chapter 2

Analytical solution of the force exerted on a sphere flowing above structured surfaces

Contents

As discussed in the previous chapter, rigid ellipsoidal particles are good approximations of blood platelets. Therefore, the introduced problem is reduced to the study of an ellipsoidal particle immersed in a homogeneous fluid interacting with surface structures, and to find out whether such structures can reduce the adhesion of the particles. The ambient flow will also be reduced to a simple shear flow, as the study is conducted in the vicinity of the wall where curvature of the velocity profile can be neglected.

To develop some intuition on this problematic, fluid dynamics fundamentals regarding Stokes flows are first introduced and a literature review on the interaction between rigid particles and a wall is presented. The effect of wall structuration is very rarely discussed, but recent work from [Assoudi *et al.* 2018] provides the derivation of the analytical expression of the force acting on a rigid sphere translating and rotating in a shear flow above an arbitrarily structured surface, considering infinitely small amplitude of surface structure. Even though this analytical model is restricted to spherical particles at perfectly zero Reynolds number and with structures of negligible amplitude, restrictions that will be alleviated by using the numerical model presented in chapter 3, it will be useful to assess the validity of the numerical model and to further develop our intuitions on the interaction between the particle and the surface structures. This chapter presents the important details of this derivation as well as its numerical implementation leading to its exploitation on the problem of interest.

2.1 Creeping flow equations

The Navier-Stokes equations (2.1) describe the evolution of the pressure and velocity fields for a homogeneous fluid.

$$\frac{\partial \rho u_i}{\partial t} + \frac{\partial \rho u_i u_j}{\partial x_j} = \frac{\partial \sigma_{ij}}{\partial x_j} + \rho f_i \tag{2.1a}$$

$$\frac{\partial \rho}{\partial t} + \frac{\partial \rho u_i}{\partial x_i} = 0 \tag{2.1b}$$

where u_i is the velocity component in direction $\mathbf{e}_i$, ρ is the fluid density, $\underline{\underline{\sigma}}$ is the surface stresses tensor and f_i the contribution of body forces in direction $\mathbf{e}_i$. Implicit summation of repeated indices is used.

Equation (2.1a) is referred to as the momentum equation and is the fluid equivalent to Newton's 2nd law of motion stating that the time variation of the fluid momentum is equal to the external forces acting on the fluid. Left-hand side of Equation (2.1a) is the time derivative of the momentum in an Eulerian framework and in the right-hand side both surface forces such as pressure or shear forces, and volumetric forces such as gravity of electromagnetic forces are considered.

The surface stress tensor $\underline{\underline{\sigma}}$ can be decomposed into inviscid forces related to the pressure p and shear forces:

$$\sigma_{ij} = -p\delta_{ij} + \tau_{ij} \tag{2.2}$$

where for a Newtonian fluid such as air, water or blood plasma, the shear stress tensor is proportional to the strain rate tensor:

$$\tau_{ij} = 2\mu S_{ij} = \mu \left(\frac{\partial u_i}{\partial x_j} + \frac{\partial u_j}{\partial x_i} \right) \tag{2.3}$$

where μ is the fluid dynamic viscosity.

Equation (2.1b) is referred to as the mass conservation equation and states that the total mass of the system must not change in time, meaning that if there is fluid injected in the system, as much fluid must go out of the system.

In the case of an incompressible fluid, these equations can be simplified using the fact that ρ is constant both in time and space, and using Equations (2.2) and (2.3), the Navier-Stokes equations for an incompressible homogeneous Newtonian fluid are given by equations (2.4).

$$\rho \left(\frac{\partial u_i}{\partial t} + u_j \frac{\partial u_i}{\partial x_j} \right) = \frac{\partial p}{\partial x_i} + \mu \frac{\partial^2 u_i}{\partial x_j \partial x_j} + \rho f_i \tag{2.4a}$$

$$\frac{\partial u_i}{\partial x_i} = 0 \tag{2.4b}$$

To have a better feeling of these equations it is useful to rewrite them in a non-dimensional form. To do so, we use a typical length scale l and velocity U of the problem (for example the particle size and the particle velocity) and make dimensionless the length and velocity variable, as well as the pressure and time:

$$\mathbf{u}^* = \mathbf{u}/U \qquad \mathbf{x}^* = \mathbf{x}/l$$

$$p^* = p/\rho U^2 \qquad t^* = tU/l$$

Injecting these dimensionless variable into equation (2.4a) gives us the dimensionless momentum equation:

$$\frac{\partial u_i^*}{\partial t^*} + u_j^* \frac{\partial u_i^*}{\partial x_j^*} = -\frac{\partial p^*}{\partial x_i^*} + \frac{1}{Re} \frac{\partial^2 u_i^*}{\partial x_j^* \partial x_j^*} + f_i^* \tag{2.5}$$

where $f_i^* = \frac{l}{U^2} f_i$ and $Re = \frac{\rho l U}{\mu}$ is the Reynolds number. This dimensionless number is of great interest to give an overview of the flow just from key measurable quantities (length of an obstacle, injection velocity ...). Indeed, one of its physical interpretation can be much better seen when written in the following form :

$$Re = \frac{\rho \frac{U^2}{l}}{\mu \frac{U}{l^2}} \tag{2.6}$$

Written this way the Reynolds number appears as the ratio between the inertial forces ($\approx \rho \frac{U^2}{l}$) and the viscous forces ($\approx \mu \frac{U}{l^2}$). Therefore, we can understand from this number whether the flow is dominated by inertial forces (high velocity, large length scale and/or small viscosity) or viscous forces (slow flow, small length scale and high viscosity). An estimated Reynolds number for our application can be obtained by taking the typical length scale as a platelet radius ($a \approx 1\,\mu m$), the typical flow velocity as the product of the platelet radius and a typical physiological shear rate ($U = a\dot{\gamma} \approx 1\,\mu m \times 1000\,s^{-1}$) and using water viscosity and density as an approximation of blood plasma properties, we get:

$$Re = \frac{10^{-6} \times 10^{-6} \times 10^{3}}{10^{-6}} = 10^{-3} \tag{2.7}$$

suggesting that the flow is greatly dominated by the viscous forces over the inertial forces. Even though it is very small, this value is not exactly zero and inertia exists in the dynamics of a blood platelet. For comparison, microswimmers such as bacteria evolve in environment at Reynolds number down to 10^{-5} [Purcell 1976]. Yet, platelets Reynolds number is often considered small enough to fully neglect the effect of inertia as discussed in the previous chapter. Even though it is not the perfect representation of platelets, this has the huge advantage of allowing simplification of the Navier-Stokes equations into the Stokes equations (2.8).

$$-\frac{\partial p}{\partial x_i} + \frac{\partial^2 u_i}{\partial x_j \partial x_j} = 0 \tag{2.8a}$$

$$\frac{\partial u_i}{\partial x_i} = 0 \tag{2.8b}$$

The Stokes equations are linear with respect to the velocity **u** which makes them way easier to solve than the non-linear Navier-Stokes equations. Note that if the boundary conditions of the problem are time dependent (such as the case of a moving particle), the time derivative of the velocity can be kept in the left-hand side of (2.8a) when neglecting the inertia term.

The linearity of the Stokes equations results in one of their key property: reversibility. The reversibility of viscous flows states that applying the opposite boundary conditions generates the opposite behavior of the flow. The fluid streamlines are then the same but are travelled in the opposite direction. A famous visualization of this mechanism comes from G.I. Taylor's video "Low Reynolds Number Flows" [Taylor 1967] shown in figure 2.1. A viscous fluid is stored between 2 cylinders and a text is written using dye deposited on the fluid to observe its deformation. By rotating the outer cylinder the fluid will start to move, and the dye will be deformed accordingly. From there, rotating the outer cylinder in the opposite direction back to its original position also deforms the fluid in the opposite way and brings back the dyed text to its initial shape and position.

Figure 2.1: Reversibility of Stokes flow visualized by G.I. Taylor [Taylor 1967]. (a) A text is written with dye deposited on a viscous fluid in a cylindrical tank. (b) The outer wall is rotated for one and a half turn in the clockwise direction, resulting in the deformation of the dyed text. (c) Rotating the outer cylinder counter-clockwise back to its initial position also brings back the dye to the initial writing according to the reversibility principle.

2.2 Particle interaction with a wall in Stokes flows

The reversibility principle is really powerful to develop an intuition on the behavior of a spherical particle interacting with a wall. Consider the case of a particle sedimenting parallel to an infinite vertical wall. Because the configuration is isotropic, we expect the wall to produce the same effect on the particle whatever the direction of the sedimentation. Therefore, if the particle is falling downwards and a deviation of the particle trajectory away from the vertical direction is resulting from this motion, then reversal of the direction of gravity and therefore of the particle motion should also invert the direction of the deviation according to the reversibility principle. Because the wall should not produce different effect for different particle direction, this deviation away from the vertical trajectory is necessarily zero.

Using similar arguments, this principle says there will be no drift away from the wall for a particle rotating at constant velocity in a quiescent fluid close to a wall, translating at constant velocity in a quiescent fluid close to a wall, neither on a particle freely moving or held fixed in a shear flow close to a wall, due to the symmetry of each of these problems. In all these cases, the pressure excess in front of the particle due to the squeezing of the flow between the particle and the wall, is compensated by a pressure drop of equal magnitude in the rear of the particle. This pressure anti-symmetry can be naturally disrupted at high Reynolds number due to inertia where the pressure drop does not balance the pressure excess resulting in a net lift force pushing the particle away from the wall. At low Reynolds number, this symmetry can also be disrupted due to non-inertial effect such as particle deformation or electrokinetic effects [Bureau *et al.* 2023].

When considering rigid ellipsoidal particles instead of spheres, additional particle dynamics are present. One of the most famous result on this matter is the analytical derivation of the angular velocity of a spheroid immersed in an unbounded shear flow by G.B. Jeffery [Jeffery 1922]. This result referred to as Jeffery's orbit, states that for a given initial orientation of the particle corresponds one rotational orbit that the particle will follow with a varying angular velocity depending on the particle orientation relatively to the shear flow. In the absence of inertia, the particle will remain on this orbit forever.

In the presence of a wall, [Mitchell & Spagnolie 2015] review the behavior of ellipsoidal particles sedimenting due to gravity in the vicinity of a vertical wall and outline 4 particle dynamics in the no-contact range that are depicted on figure 2.2:

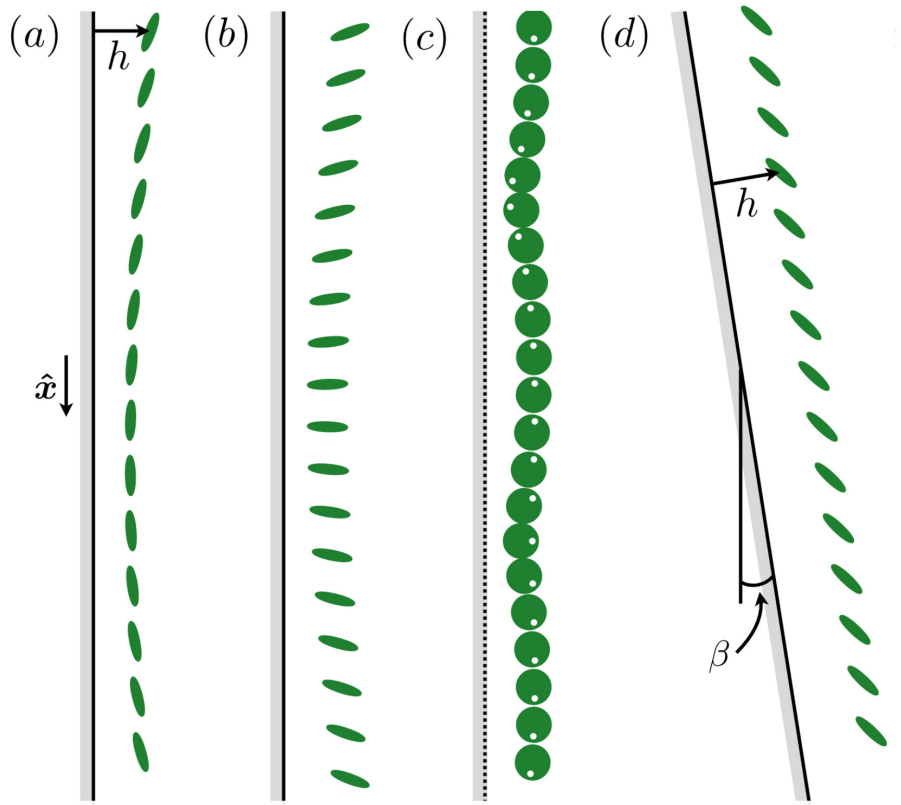

Figure 2.2: 4 different dynamics of an ellipsoidal particle sedimenting near a flat vertical or inclined wall reproduced from [Mitchell & Spagnolie 2015]. (a) Glancing, (b) Reversing, (c) Tumbling and (d) Stable Gliding.

Glancing A slender particle initially placed at a small angle with respect to the wall will drift towards the wall and rotate until it is parallel to the wall. At this point, the reversibility of the flow requires the particle to drift away from the wall where it will reach an equilibrium angle.

Reversing A slender particle initially placed at a larger angle with the wall will drift towards the wall and rotate until it is perpendicular to the wall. At this point, the leading edge will become the trailing edge and vice-versa in a dead leaf movement. The reversibility of the flow once again requires the particle to drift away from the wall where it will reach an equilibrium angle.

Tumbling A slightly deformed sphere, or a slender body really close to the wall can sediment in a periodic motion along the wall, where the distance between the particle and the wall will oscillate due to the non-spherical shape of the particle.

Stable sliding This dynamic is only observed when the particle sediments close to an inclined wall. In this case, the hydrodynamic drag and torque exerted on the particle balance the gravity and the particle will slide at constant distance and orientation along the wall.

The particle aspect ratio, the initial separation distance and the initial angle of the particle determines which of these dynamics is observed.

Considering the dynamics of freely moving spheroids in shear flows close to a wall, [Mody & King 2005] outlined 3 different dynamics for particle movement in the shear plane: Modified Jeffery's orbits, Pole-vaulting and Wobble flow which are depicted on figure 2.3. For bigger aspect

ratio (around 0.4 and above) only the first two dynamics are observed and for all aspect ratios, the transition between the different dynamics again depends on the initial particle distance to the wall.

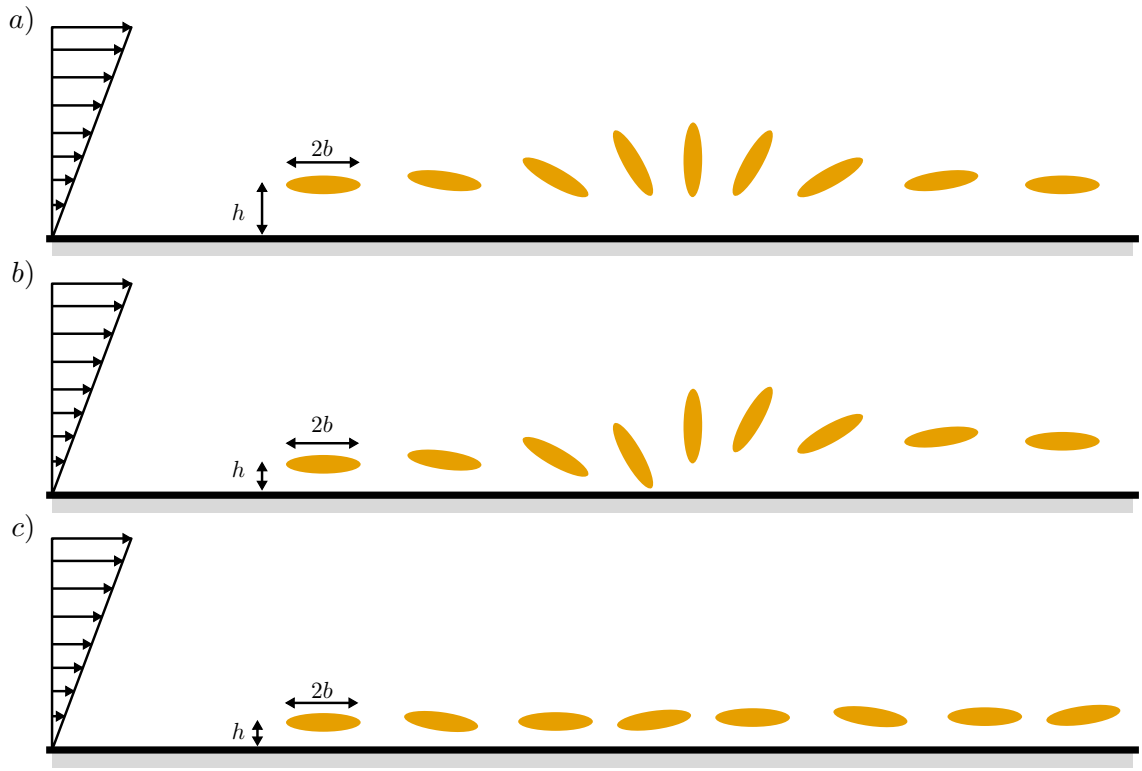

Figure 2.3: 3 different dynamics of an ellipsoidal particle transported near a flat wall by an ambient shear flow [Mody & King 2005]. (a) Modified Jeffery orbits ($h > 1.1b$), (b) Pole-Vaulting ($0.75b < h < 1.1b$), (c) Wobble flow ($h < 0.75b$).

Modified Jeffery orbits The presence of a wall at distances greater than the particle major semi-axis, meaning the particle is free to rotate without colliding the wall, tends to slow down the rotation of the particle predicted by the equations of Jeffery in an unbounded domain [Jeffery 1922]. Also, when the major semi-axis of the particle approaches the wall due to the rotation, the particle center of mass will be lifted until the semi-axis is perpendicular to the wall, before the particle moves back to its original distance to the wall, again following the reversibility principle. Contrary to a sphere, the interaction between an ellipsoidal particle and a wall generates a movement of the particle perpendicular to the wall, even though its mean value over a whole particle rotation is 0.

Pole-vaulting When the particle is close enough to the wall so that it cannot rotate freely without having contact with the wall, one can find particles performing a pole-vault movement. As the particle is rotating, its tip will make contact with the wall repulsing the particle higher in the flow where it will now enter a modified Jeffery's orbit movement at a mean altitude higher than its initial position.

Wobble Flow A particle of aspect ratio under around 0.4 can be observed in this state of wobble flow when it is really close to the wall (initial distance smaller than 0.75 major semi-axis). In this case, the particle will not perform its flipping motion and will oscillate around its initial orientation as the hydrodynamic torque acting on the particle due to the shear flow is balanced by the effect of the wall.

In the examples listed above, only 2D motion is presented, but the authors of these articles investigated the effect of 3D movement by adding an initial particle tilting. The complexity of the trajectory rises rapidly as the combination of the rotation caused by the particle flipping and the initial tilting leads to very complex particle movement.

The hydrodynamic interaction of particles with structured surfaces has been mainly investigated for cell-sorting application in microfluidic devices. The structuration of the wall is used to perform particle separation in a process called hydrophoresis and utilizes slanted grooves to generate a lateral migration of selected particle based on their size [Choi 2020]. An analytical framework has been developed to study this interaction between a sphere and a corrugated surface [Assoudi *et al.* 2018]. [Chase *et al.* 2022, Kurzthaler *et al.* 2024] used this analytical model and compared it with experimental observations of sedimenting particles close to slanted corrugated surfaces. They concluded that the effect of the corrugations on the particle is to break the symmetry of the pressure field in the lateral direction, resulting in a net force pushing the particle sideways. While lateral migration is the main focus of particle sorting, we expect that a similar mechanism can induce a vertical lift on particles that would repel them away from the wall.

To investigate this hypothesis, the analytical model mentioned above have been used. It is detailed in the following section and its use is the first step in the study of the dynamics of blood platelets on these structured surfaces.

2.3 The force exerted on a spherical particle flowing above a patterned surface

Following [Assoudi *et al.* 2018], it is possible to obtain an analytical value of the force acting on a spherical particle immersed in a shear flow, translating at velocity $\mathbf{U}$ and rotating at angular velocity $\mathbf{\Omega}$ above a structured surface of small amplitude compared to the particle radius. This is done by using the Lorentz reciprocal theorem to compute the force acting on the particle without having to compute the whole surrounding flow for which no analytical solution is available considering the complexity of the geometry. The Lorentz reciprocal theorem states that two flows $(\mathbf{u}^a, p^a)$ and $\left(\mathbf{u}^b, p^b\right)$ that are both solution of the Stokes equations over the same domain D but with different boundary conditions, are related by the scalar equation (2.9) [Masoud & Stone 2019] when no volumic forces are considered:

$$\int_{\partial D} \mathbf{u}^a \underline{\underline{\sigma}}^b \mathbf{n} dS = \int_{\partial D} \mathbf{u}^b \underline{\underline{\sigma}}^a \mathbf{n} dS \tag{2.9}$$

where $\underline{\underline{\sigma}}^a$ is the stress tensor associated with flow $(\mathbf{u}^a, p^a)$ as defined by equations (2.2) and (2.3) for a Newtonian fluid.

In our case, one of the two flows is the flow of interest, namely the flow around a spherical particle that translates, rotates, and resists a surrounding shear flow. By choosing the second flow wisely, the force acting on the particle can be obtained without explicitly computing the first flow. Since analytical solutions are only available for flows around a particle moving close to a flat surface, the structured surface must be approximated by an equivalent boundary condition over a flat surface. This ensures that both the adjoint flow and the flow of interest are defined over the same domain. The strength of this theorem, despite its apparent simplicity, is explained in detail in [Masoud & Stone 2019].

2.3.1 Analytical expression of the force

Consider a rigid spherical particle $\mathcal{S}$ of radius a immersed in a surrounding shear flow in the vicinity of an infinite structured wall. The strucures are of negligible amplitude compared to the particle radius

so that the altitude of the wall in the vertical direction $\mathbf{e}_3$ is defined by:

$$x_3^{wall} = \varepsilon a R(x_1, x_2) \tag{2.10}$$

where $R(x_1, x_2)$ is the structure shape function ranging from 0 to 1 and ε is a small dimensionless parameter such that $\varepsilon \ll 1$ as presented in figure 2.4.

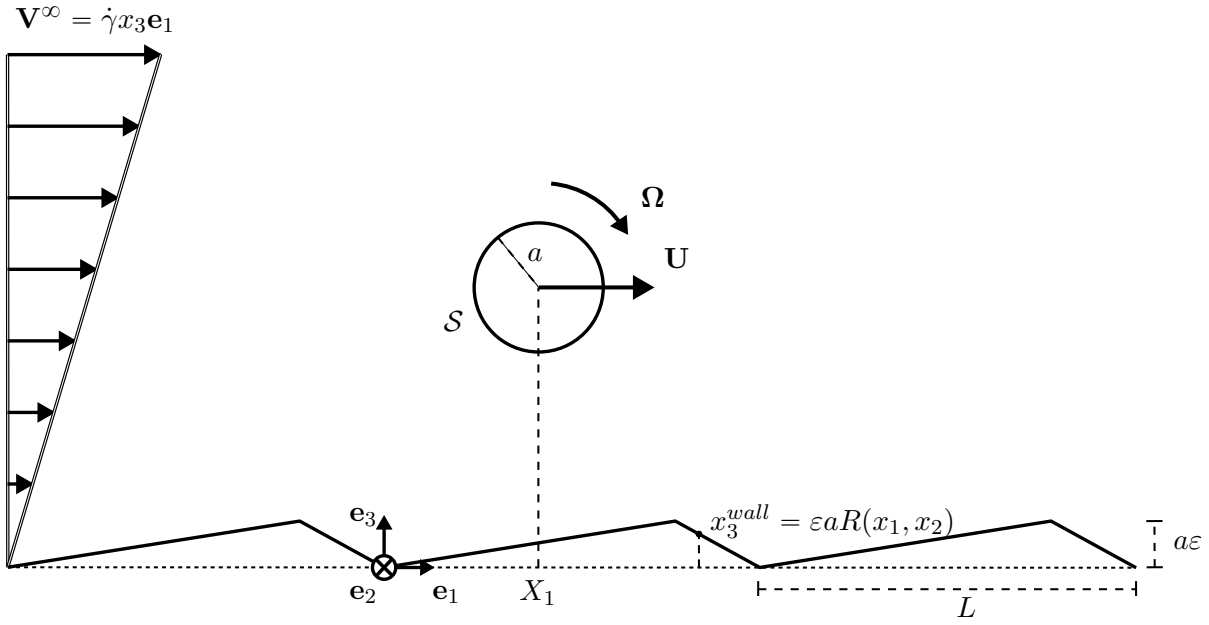

Figure 2.4: Configuration of the flow for a spherical particle translating at velocity $\mathbf{U}$ and rotating at angular velocity $\mathbf{\Omega}$ in an ambient shear over structured surfaces. The surface of the particle is designated by $\mathcal{S}$ and the surface of the plane wall by x_3^{wall}. As the amplitude of the structures are negligible compared to the particle radius, the amplitude is proportionnal to a small dimensionless parameter ε.

Considering the Reynold number to be small, the fluid flow surrounding this particle and structured wall is described by $(\mathbf{V}, P)$ solution of the Stokes equations:

$$-\frac{\partial P}{\partial x_i} + \mu \frac{\partial^2 V_i}{\partial x_j \partial x_j} = 0 \tag{2.11a}$$

$$\frac{\partial V_i}{\partial x_i} = 0 \tag{2.11b}$$

with boundary conditions

$$\mathbf{V}|_{x_3^{wall}} = \mathbf{0} \tag{2.12a}$$

$$\mathbf{V}|_{\mathcal{S}} = \mathbf{U} + \mathbf{\Omega} \times \mathbf{r} \tag{2.12b}$$

$$\mathbf{V}|_{x_3 \to \infty} = \mathbf{V}^\infty = \dot{\gamma} x_3 \mathbf{e}_1 \tag{2.12c}$$

where $\mathbf{U}$ and $\mathbf{\Omega}$ are the translational and rotational velocity of the particle and $\dot{\gamma}$ is the shear rate. For any point $\mathbf{x} = (x_1, x_2, x_3)$ on the particle surface $\mathcal{S}$, the vector $\mathbf{r}$ is defined by $\mathbf{r} = \mathbf{x} - \mathbf{X}$ with $\mathbf{X} = (X_1, X_2, X_3)$ the center of mass of the particle.

By using the linearity of the stokes equation, this flow can be decomposed into the sum of a background shear flow $(\mathbf{V}_s, P_s)$ over the structured surface without the particle and a disturbance flow

caused by the presence of the particle $(\mathbf{v}, p)$, equations (2.13). Note that each of these flows is solution of the Stokes equations.

$$\mathbf{V} = \mathbf{V}_s + \mathbf{v} \tag{2.13a}$$
$$P = P_s + p \tag{2.13b}$$

Because there is no particle in the background flow, all the information on the force exerted by the flow on the particle lies in the disturbance flow and the study of the global problem can be reduced to the study of the disturbance flow. The boundary conditions (2.14) of the disturbance flow are obtained by subtracting the boundary conditions of the background shear flow to the boundary conditions (2.12).

$$\mathbf{v}|_{x_3^{wall}} = \mathbf{0} \tag{2.14a}$$
$$\mathbf{v}|_{\mathcal{S}} = \mathbf{U} + \mathbf{\Omega} \times \mathbf{r} - \mathbf{V}_s \tag{2.14b}$$
$$\mathbf{v}|_{x_3 \to \infty} = \mathbf{0} \tag{2.14c}$$

Using the fact that the amplitude of the structures is of order ε, we also expect the impact of the structures on the particle to be of order ε by linearity of the Stokes equations. Therefore, we decompose the problem into a sum of a problem at order 0 ($O(\varepsilon^0)$), a problem at order 1 ($O(\varepsilon)$) and higher order terms by searching for $(\mathbf{v}^{(0)}, p^{(0)})$ and $(\mathbf{v}^{(1)}, p^{(1)})$ such that:

$$\mathbf{v} = \mathbf{v}^{(0)} + \varepsilon \mathbf{v}^{(1)} + O(\varepsilon^2) \tag{2.15a}$$
$$p = p^{(0)} + \varepsilon p^{(1)} + O(\varepsilon^2) \tag{2.15b}$$

where exponant $.^{(n)}$ indicate a solution at order n ($O(\varepsilon^n)$). The flow at order 0 is the disturbance flow of a spherical particle immersed in a shear flow over a flat surface while the solution at order 1 accounts for the effect of the structures. Because we are interested in measuring the effect of the structures, the solution at order 1 is considered from now on.

However, no solution for this order 1 flow is available analytically, so as mentioned previously we are going to use the Lorentz theorem to compute the force acting on the particle due to this flow without having to compute the pressure and velocity fields. Also, because only solution for flows on flat surfaces are known, the problem over the structured surface is first expressed with an equivalent boundary condition over a flat surface, using the fact that the amplitude of the structure is negligible compared to the particle radius. To do so, a Taylor expansion is used in the vicinity of the flat surface:

$$\mathbf{v}|_{x_3^{wall}} = \mathbf{v}|_{x_3=0} + \varepsilon a R(x_1, x_2) \left.\frac{\partial \mathbf{v}}{\partial x_3}\right|_{x_3=0} + O(\varepsilon^2) \tag{2.16}$$

Injecting the decomposition of $\mathbf{v}$ from equation (2.15a) and factorizing by ε provides the relation between the boundary condition of the order 1 flow on the fictive flat surface and known quantities, namely the gradient in direction of the flow at order 0:

$$\begin{aligned}\mathbf{v}|_{x_3^{wall}} &= \left.\mathbf{v}^{(0)}\right|_{x_3=0} + \varepsilon \left.\mathbf{v}^{(1)}\right|_{x_3=0} + \varepsilon a R(x_1, x_2) \left.\frac{\partial \mathbf{v}^{(0)}}{\partial x_3}\right|_{x_3=0} + O(\varepsilon^2) \\ &= \left.\mathbf{v}^{(0)}\right|_{x_3=0} + \varepsilon \left(\left.\mathbf{v}^{(1)}\right|_{x_3=0} + a R(x_1, x_2) \left.\frac{\partial \mathbf{v}^{(0)}}{\partial x_3}\right|_{x_3=0} \right) + O(\varepsilon^2)\end{aligned} \tag{2.17}$$

By identification between equation (2.17) and the no-slip condition at the wall (2.14a), it results the

following boundary conditions for the order 0 and 1 flows:

$$\mathbf{v}^{(0)}\Big|_{x_3=0} = \mathbf{0} \tag{2.18}$$

$$\mathbf{v}^{(1)}\Big|_{x_3=0} = -aR(x_1,x_2)\left.\frac{\partial \mathbf{v}^{(0)}}{\partial x_3}\right|_{x_3=0} \tag{2.19}$$

This boundary conditions can be understood as a no-slip condition on a flat surface for the order 0 flow, in agreement with the problem over a flat surface, while the condition for the flow at order 1 is a slip condition on the flat surface which depends on the shape of the structure.

The Lorentz theorem, equation (2.9), can now be applied to the flow $(\mathbf{v}^{(1)}, p^{(1)})$ as well as a known and thoughtfully chosen adjoint flow $(\mathbf{u}^*, p^*)$ over a flat surface so that:

$$\int_{\partial D} \mathbf{u}^* \underline{\underline{\sigma}}^{(1)} \mathbf{dS} = \int_{\partial D} \mathbf{v}^{(1)} \underline{\underline{\sigma}}^{*} \mathbf{dS} \tag{2.20}$$

We are interested in finding the force exerted on the particle in the vertical direction as this is the force that dictates the evolution of the particle-wall distance[1]. By choosing the adjoint flow as the flow generated by a particle translating normally towards a plane surface at velocity $-U_3^*\mathbf{e}_3$ in an otherwise quiescent fluid, the integral over the surface of the particle $\mathcal{S}$ in the left-hand side of (2.20) yields :

$$-U_3^* \underbrace{\int_{\mathcal{S}} \underline{\underline{\sigma}}^{(1)} \mathbf{dS}}_{\mathbf{F}^{(1)}} \cdot \mathbf{e}_3 = -U_3^* F_3^{(1)} \tag{2.21}$$

with $F_3^{(1)}$ the force acting on the particle due to the structures in direction $\mathbf{e}_3$. Note that this force is zero when the particle is freely moving. Therefore, the motion of the particle will be imposed as discussed later, resulting in a force acting on the particle. The solution for the adjoint flow introduced above is known analytically [Brenner 1961] so the associated stress tensor $\underline{\underline{\sigma}}^*$ that appears on the left hand side of equation (2.20) is known as well.

Decomposing the borders of the domain into the plane wall $\mathcal{P}$, the sphere surface $\mathcal{S}$ and a surface at infinity $\mathcal{S}^\infty$ in equation (2.20) yields the relation:

$$\int_{\mathcal{P}+\mathcal{S}+\mathcal{S}^\infty} \mathbf{u}^* \underline{\underline{\sigma}}^{(1)} \mathbf{dS} = \int_{\mathcal{P}+\mathcal{S}+\mathcal{S}^\infty} \mathbf{v}^{(1)} \underline{\underline{\sigma}}^{*} \mathbf{dS} \tag{2.22}$$

with boundary conditions:

	$\mathcal{P}$	$\mathcal{S}$	$\mathcal{S}^\infty$
$\mathbf{v}^{(1)}$	$-aR(x_1,x_2)\left.\frac{\partial \mathbf{v}^{(0)}}{\partial x_3}\right\|_{x_3=0}$	$\mathbf{U}^{(1)} + \mathbf{\Omega}^{(1)} \times \mathbf{r} - \mathbf{V}_s^{(1)}$	$\mathbf{0}$
$\mathbf{u}^*$	$\mathbf{0}$	$-U_3^*\mathbf{e}_3$	$\mathbf{0}$

Table 2.1: Boundary conditions for the order 1 perturbation flow and the adjoint flow over the plane wall $\mathcal{P}$, the sphere surface $\mathcal{S}$ and the boundary at infinity $\mathcal{S}^\infty$.

The boundary condition for the order 1 flow at the surface of the sphere is obtained by decomposing

[1] Measuring the vertical force to characterize the structure is relevant as for a flat surface this force is zero. However, it was found later in the project (see chapter 5) that the horizontal force exerted on the particle is related to the particle lift observed over structured surfaces in chapter 4. Measuring the horizontal force with the analytic model could therefore also be interesting.

the translational and rotational velocities of the particle into order 0 and 1 contributions following (2.23) so that:

$$\mathbf{U} = \mathbf{U}^{(0)} + \varepsilon\mathbf{U}^{(1)} + O(\varepsilon^2) \tag{2.23a}$$

$$\mathbf{\Omega} = \mathbf{\Omega}^{(0)} + \varepsilon\mathbf{\Omega}^{(1)} + O(\varepsilon^2) \tag{2.23b}$$

The shear flow without the particle is decomposed in the same manner:

$$\mathbf{V}_s = \mathbf{V}_s^{(0)} + \varepsilon\mathbf{V}_s^{(1)} + O(\varepsilon^2) \tag{2.24}$$

Injecting these decompositions in the boundary condition (2.14b) and identifying the terms at order 1 gives the boundary conditions for $\mathbf{v}^{(1)}$ on the surface of the sphere:

$$\mathbf{v}^{(1)}|_{\mathcal{S}} = \mathbf{U}^{(1)} + \mathbf{\Omega}^{(1)} \times \mathbf{r} - \mathbf{V}_s^{(1)} \tag{2.25}$$

Injecting these boundary conditions in (2.22) and using the relation between the stress tensor and the force given by equation (2.21), the following expression is obtained for the force acting on the particle at order 1 :

$$-U_3^* F_3^{(1)} = -a \int_{\mathcal{P}} R(x_1, x_2) \left.\frac{\partial \mathbf{v}^{(0)}}{\partial x_3}\right|_{x_3=0} \underline{\underline{\sigma}}^* \mathbf{dS} + \mathbf{U}^{(1)} \int_{\mathcal{S}} \underline{\underline{\sigma}}^* \mathbf{dS} + \mathbf{\Omega}^{(1)} \times \int_{\mathcal{S}} \mathbf{r}\underline{\underline{\sigma}}^* \mathbf{dS} - \int_{\mathcal{S}} \mathbf{V}_s^{(1)} \underline{\underline{\sigma}}^* \mathbf{dS} \tag{2.26}$$

where $\mathbf{U}^{(1)}$ and $\mathbf{\Omega}^{(1)}$ are the imposed velocity and angular velocity of the particle at order 1. To simplify further this equation we impose that the movement of the particle is the movement of the same particle over a flat surface therefore $\mathbf{U} = \mathbf{U}^{(0)} = U\mathbf{e}_1$ and $\mathbf{\Omega} = \mathbf{\Omega}^{(0)} = \Omega\mathbf{e}_2$ so that $\mathbf{U}^{(1)} = \mathbf{0}$ and $\mathbf{\Omega}^{(1)} = \mathbf{0}$ cancels terms in equation (2.26). After that, the resulting force we obtain is the vertical force required to constrain a particle transported over structured surfaces, to the movement of a particle transported over a flat surface, which is the opposite of the vertical force acting on the particle due to the structuration of the surface.

In the end we have :

$$U_3^* F_3^{(1)} = a \int_{\mathcal{P}} R(x_1, x_2) \left.\frac{\partial \mathbf{v}^{(0)}}{\partial x_3}\right|_{x_3=0} \underline{\underline{\sigma}}^* \mathbf{dS} + \int_{\mathcal{S}} \mathbf{V}_s^{(1)} \underline{\underline{\sigma}}^* \mathbf{dS} \tag{2.27}$$

where the translational and angular velocities ($\mathbf{U}^{(0)}$ and $\mathbf{\Omega}^{(0)}$) imposed on the particle at order 0 are impacting the flow field $\mathbf{v}^{(0)}$. As a lot of notation have been introduced, table 2.2 sums up the different flow fields used so far and their signification to help the reader navigate through the details of the calculation.

2.3.2 Numerical evaluation of the force

The integrals in equation (2.27) can be computed numerically to obtain the value of the force acting on a sphere translating at imposed velocity $U\mathbf{e}_1$, imposed angular velocity $\Omega\mathbf{e}_2$, in a surrounding shear flow of shear rate $\dot{\gamma}$, above an arbitrary structure defined by the shape function $R(x_1, x_2)$ for a given position of the particle relatively to this structure. The evaluation of this force requires the computation of integrals over the infinite plane. The quantities to be integrated are the velocity gradient on the wall of the perturbation flow over a flat surface $\left.\frac{\partial \mathbf{v}^{(0)}}{\partial x_3}\right|_{x_3=0}$, the adjoint stress tensor $\underline{\underline{\sigma}}^*$ and the contribution

Notation	Related expressions	Signification
$\mathbf{V}$	$\mathbf{V} = \mathbf{V}_s + \mathbf{v}$	Flow field around a particle translating and rotating in a shear flow over a structured surface. It is decomposed into a background shear flow without particle and the disturbance of the particle.
$\mathbf{V}_s$	$\mathbf{V}_s = \mathbf{V}_s^{(0)} + \varepsilon\mathbf{V}_s^{(1)} + O(\varepsilon^2)$	Shear flow without particle over a structured surface. It is decomposed into a shear flow over a flat surface and a perturbation by the structure.
$\mathbf{V}_s^{(0)}$	$\mathbf{V}_s^{(0)} = \dot{\gamma} x_3 \mathbf{e}_1$	Background shear flow without particle over a flat surface.
$\mathbf{V}_s^{(1)}$		Contribution of the structures to the background shear flow without particle.
$\mathbf{v}$	$\mathbf{v} = \mathbf{v}^{(0)} + \varepsilon\mathbf{v}^{(1)} + O(\varepsilon^2)$	Disturbance flow caused by the presence of the particle translating, rotating and resisting to the shear flow over structured surfaces. It is decomposed into a flat surface contribution and a perturbation by the structures.
$\mathbf{v}^{(0)}$	$\mathbf{v}^{(0)} = \mathbf{v}_T^{(0)} + \mathbf{v}_R^{(0)} + \mathbf{v}_S^{(0)}$	Disturbance flow of a particle translating, rotating and resisting to the background shear flow close to a flat surface. Each of these contributions are computed independently and summed to obtain the total disturbance.
$\mathbf{v}_T^{(0)}$		Disturbance flow of a particle translating at velocity $\mathbf{U} = \mathbf{U}^{(0)}$ parallel to a flat wall in quiescent fluid. Analytical solution provided by [O'Neill 1964].
$\mathbf{v}_R^{(0)}$		Disturbance flow of a particle rotating at angular velocity $\mathbf{\Omega} = \mathbf{\Omega}^{(0)}$ over a flat wall in quiescent fluid. Analytical solution provided by [Dean & O'Neill 1963].
$\mathbf{v}_S^{(0)}$		Disturbance flow of a particle resisting the ambient shear flow. Analytical solution provided by [Tözeren & Skalak 1977].
$\mathbf{v}^{(1)}$		Contribution of the structures to the disturbance flow of a particle translating, rotating and resisting the shear flow.
$\mathbf{u}^*$		Adjoint flow field of a particle sedimenting towards the flat surface at velocity U_3^* in quiescent fluid. Analytical solution provided by [Brenner 1961, Pasol *et al.* 2005].

Table 2.2: Velocity fields used throughout the development of the analytical solution. A pressure field with matching case, index and exponent is associated to each velocity field.

of the structures to the undisturbed shear flow $\mathbf{V}_s^{(1)}$. The analytical solution for all of these quantities is known and detailed below.

2.3.2.1 Perturbation flow over a flat surface

The flow at order zero, namely the disturbance flow around a particle translating at velocity $U\mathbf{e}_1$, rotating at angular velocity $\Omega\mathbf{e}_2$ in a shear flow of shear rate $\dot{\gamma}$ over a flat surface, can be decomposed into the sum of these 3 independent problems :

$$\mathbf{v}^{(0)} = \mathbf{v}_T^{(0)} + \mathbf{v}_R^{(0)} + \mathbf{v}_S^{(0)} \tag{2.28}$$

Where $\mathbf{v}_T^{(0)}$, $\mathbf{v}_R^{(0)}$ and $\mathbf{v}_S^{(0)}$ indicate respectively the flow generated by a particle translating parallel to a flat wall in a quiescent fluid, the flow generated by a particle rotating around an axis parallel to a flat wall in a quiescent fluid and the disturbance flow of a particle held fixed in a shear flow. The analytical solution for the velocity and pressure fields of these 3 flows, from now on referred to as the fundamental flows, are known analytically in a bispherical coordinate system using a harmonic decomposition [Dean & O'Neill 1963, O'Neill 1964, Tözeren & Skalak 1977].

The bispherical coordinate system (ξ, η, ϕ) was introduced by Hicks [Hicks 1881] for the study of problems defined at the surface of a tore. He suggested that the coordinate system suitable for the resolution of such problem was the system of circles passing through 2 points called focal points and the system of circles orthogonal to them (Figure 2.5 (a), respectively black and orange lines). By performing a revolution around the line of equal distance between the focal points (indicated by the notation $\xi = 0$ in Figure 2.5 (a)), introducing the coordinate $\phi \in [0, 2\pi]$ as the angle around the revolution axis, the system of orange circles becomes a system of tores and the definition of boundary condition on a toroidal border is made simpler in this coordinate system as the surface of a tore corresponds to an isosurface of ξ.

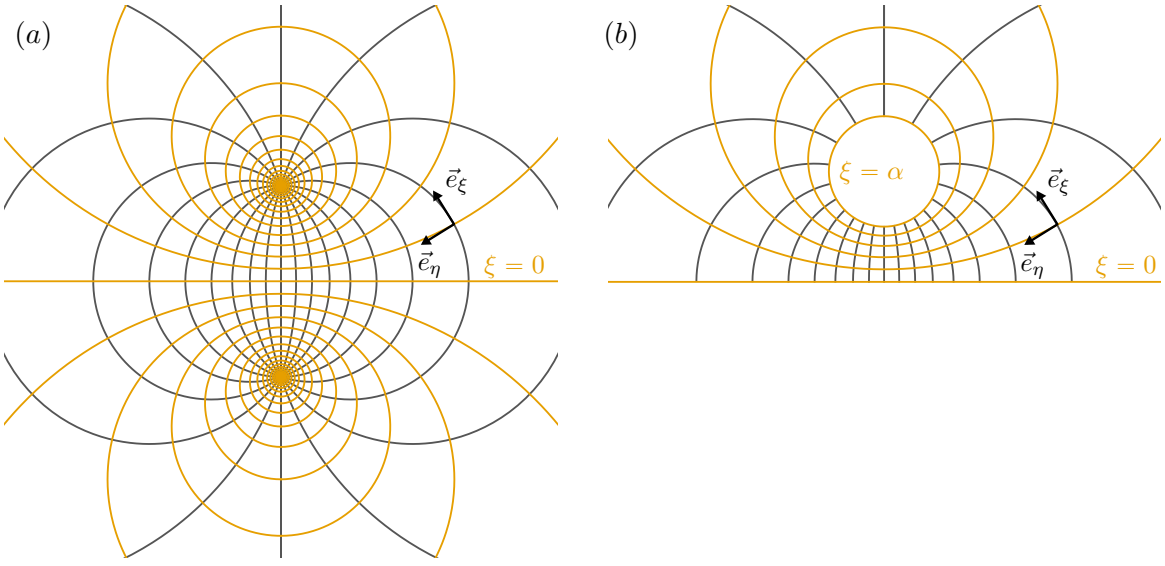

Figure 2.5: Bispherical coordinates systen in the plane $\phi = 0$ (a) in their general form $(\eta, \xi) \in [0; 2\pi] \times [-\infty, \infty]$ and (b) their restriction for the study of a single particle-wall configuration $(\eta, \xi) \in [0; 2\pi] \times [0, \alpha]$. Black lines are the circles passing through the two focal points and isovalues of η. Orange lines are the circles orthogonal to the black ones and the isovalues of ξ. The full 3D coordinates system is obtained by rotating this 2D system around the axis passing through the two focal points.

[Hicks 1881] also states that revolution about the line passing through the two focal points yields a

system suitable for the study of problems defined over 2 spheres in an unbounded domain, which was latter used by Jeffery to solve the Laplace equation [Jeffery 1912]. This is done by choosing the focal points so that the spherical isosurface of ξ and $-\xi$ overlaps the particles surface. The corresponding value of ξ is notated $\xi = \alpha$ and by restricting the bispherical coordinates to values of ξ between 0 and α, we obtain a suitable coordinate system for the study of single sphere interacting with a wall, where the wall is defined by the coordinates $(\xi = 0, \eta, \phi)$ and the sphere surface by the coordinates $(\xi = \alpha, \eta, \phi)$ (Figure 2.5 (b)). The relation between the particle radius a and α is given by [Brenner 1961] as $\alpha = \cosh^{-1}(h/a)$ where h is the distance between the particle center and the wall. The position of the focal point in the associated cylindrical coordinate system (r, z, ϕ) is $(0, c, 0)$ and $c = a \sinh \alpha$.

The relation between the bispherical coordinate system and the cylindrical coordinate system (r, z, ϕ) are given by:

$$r = \frac{c \sin \eta}{\cosh \xi - \cos \eta}, \qquad z = \frac{c \sinh \xi}{\cosh \xi - \cos \eta} \tag{2.29}$$

with $(\xi, \eta, \phi) \in [0, \alpha] \times [0, \pi] \times [0, 2\pi]$ and $(r, z, \phi) \in [0, \infty] \times [0, \infty] \times [0, 2\pi]$.

The solution in the cylindrical coordinate system for the fundamental flows ($\mathbf{u}_\bullet^{(0)} = u_\bullet^{(0)}\mathbf{e}_r + v_\bullet^{(0)}\mathbf{e}_\phi + w_\bullet^{(0)}\mathbf{e}_z, p_\bullet^{(0)}$) with $\bullet \in \{T, R, S\}$ are searched for in the form:

$$p_\bullet^{(0)} = \mu U_c Q_1^\bullet \cos(\phi)/c \tag{2.30a}$$

$$u_\bullet^{(0)} = \frac{1}{2} U_c [r Q_1^\bullet + c(U_2^\bullet + U_0^\bullet)] \cos(\phi)/c \tag{2.30b}$$

$$v_\bullet^{(0)} = \frac{1}{2} U_c (U_2^\bullet - U_0^\bullet) \sin(\phi) \tag{2.30c}$$

$$w_\bullet^{(0)} = \frac{1}{2} U_c [z Q_1^\bullet + 2c w_1^\bullet] \cos(\phi)/c \tag{2.30d}$$

where U_c is a characteristic velocity of the considered problem, namely $U_c = U$ for the particle translating at velocity U, $U_c = c\Omega$ for the particle rotating at angular velocity Ω and $U_c = cS$ for the particle held fixed in a shear rate S. The quantities $Q_1^\bullet$, $U_2^\bullet$, $U_0^\bullet$ and $w_1^\bullet$ with $\bullet \in \{T, R, S\}$ are functions of ξ and η and are searched for in terms of a harmonic decomposition (Equations (2.31)a-d) following [Jeffery 1912].

$$w_1^\bullet = (\cosh \xi - \tilde{\mu})^{1/2} \sin \eta \sum_{n=1}^{\infty} [A_n^\bullet \sinh((n + 1/2)\xi)] P_n'(\tilde{\mu}) \tag{2.31a}$$

$$Q_1^\bullet = (\cosh \xi - \tilde{\mu})^{1/2} \sin \eta \sum_{n=1}^{\infty} [B_n^\bullet \cosh((n + 1/2)\xi) + C_n^\bullet \sinh((n + 1/2)\xi)] P_n'(\tilde{\mu}) \tag{2.31b}$$

$$U_0^\bullet = (\cosh \xi - \tilde{\mu})^{1/2} \sum_{n=0}^{\infty} [D_n^\bullet \cosh((n + 1/2)\xi) + E_n^\bullet \sinh((n + 1/2)\xi)] P_n(\tilde{\mu}) \tag{2.31c}$$

$$U_2^\bullet = (\cosh \xi - \tilde{\mu})^{1/2} \sin^2 \eta \sum_{n=2}^{\infty} [F_n^\bullet \cosh((n + 1/2)\xi) + G_n^\bullet \sinh((n + 1/2)\xi)] P_n''(\tilde{\mu}) \tag{2.31d}$$

where $\tilde{\mu} = \cos \eta$, P_n is the Legendre polynomial of order n, and the harmonic coefficients $A_n^\bullet$, $B_n^\bullet$, $C_n^\bullet$, $D_n^\bullet$, $E_n^\bullet$, $F_n^\bullet$ and $G_n^\bullet$ with $\bullet \in \{T, R, S\}$ are obtained by injecting equations (2.30) into the Stokes equations and solving with the appropriate boundary conditions.

As these flows are perturbation flows, the boundary condition on the flat wall and at infinity are $\mathbf{u}_\bullet^{(0)}|_{\xi=0} = \mathbf{0}$ and $\mathbf{u}_\bullet^{(0)}|_{z\to\infty} = \mathbf{0}$ and the boundary condition on the surface of the sphere depends on the considered problem, so $\mathbf{u}_T^{(0)}|_{\xi=\alpha} = U\mathbf{e}_1$, $\mathbf{u}_R^{(0)}|_{\xi=\alpha} = a\Omega\mathbf{e}_2$ or $\mathbf{u}_S^{(0)}|_{\xi=\alpha} = -x_3\dot{\gamma}\mathbf{e}_1$.

The harmonic coefficient for these three problems where initially provided by [Dean & O'Neill 1963], [O'Neill 1964] and [Tözeren & Skalak 1977] for the translation, rotation and resistance to shear problem respectively. These results have been aggregated by M. Chaoui in his PhD Manuscript which also provides a lot of details regarding the calculation of the harmonic coefficients [Chaoui 1995].

For each of these problems, the coefficients $B_n^\bullet$, $C_n^\bullet$, $D_n^\bullet$, $E_n^\bullet$, $F_n^\bullet$ and $G_n^\bullet$ are first expressed as functions of $A_n^\bullet$ and a recurrence relation is then found for $A_n^\bullet$ with the condition that $\lim_{n\to\infty} A_n^\bullet = 0$. From this relation, the $A_n^\bullet$ cannot be found analytically but solving a linear system numerically provides accurate values of the $A_n^\bullet$ if enough terms are computed, and the other coefficients are then found from their relation with $A_n^\bullet$.

[Chaoui & Feuillebois 2002] suggests a more efficient algorithm for the computation of the $A_n^\bullet$ coefficients. When the particle is almost in contact with the wall, the number of harmonic coefficients required to ensure an accurate result rises very quickly and this more efficient algorithm is needed to reduce computational cost. As we are not interested in such cases, this algorithm was not implemented in this work and the simple matrix inversion was fast enough, the number of required coefficient being always small (<25).

[Chaoui 1995] provides the relations between the force and torque acting on the particle due to the surrounding flow, and the harmonic coefficients, as well as tabulated values of these forces and torques computed at different particle radius to wall distance ratio. The dimensionless force and torque acting on a particle expressed with the associated harmonic coefficients are given in table 2.3 for each of the fundamental flows.

Cases	Force and torque	Dimensionless force and torque	
Translation	$F_1^T = 6\pi\mu a U_1 f_1^T$	$f_1^T = -\frac{\sqrt{2}}{6}\sinh(\alpha)\sum_{n=0}^{\infty}\left[E_n^T + n(n+1)C_n^T\right]$	(2.32a)
	$T_2^T = 8\pi\mu a^2 U_1 t_1^T$	$t_2^T = \frac{\sqrt{2}}{4}\sinh^2(\alpha)\sum_{n=0}^{\infty}\left[E_n^T\coth(\alpha) + 2n(n+1)A_n^T\right]$	(2.32b)
Rotation	$F_1^R = 6\pi\mu a^2\Omega f_1^R$	$f_1^R = -\frac{\sqrt{2}}{6}\sinh^2(\alpha)\sum_{n=0}^{\infty}\left[E_n^R + n(n+1)C_n^R\right]$	(2.33a)
	$T_2^R = -8\pi\mu a^3\Omega t_2^R$	$t_2^R = -\frac{\sqrt{2}}{4}\sinh^3(\alpha)\sum_{n=0}^{\infty}\left[E_n^R\coth(\alpha) + 2n(n+1)A_n^R\right]$	(2.33b)
Resistance to shear	$F_1^S = 6\pi\mu a h\dot{\gamma} f_1^S$	$f_1^S = \frac{\sqrt{2}}{6}\frac{\sinh(\alpha)}{\coth(\alpha)}\sum_{n=0}^{\infty}\left[E_n^S + n(n+1)C_n^S\right]$	(2.34a)
	$T_2^R = 4\pi\mu a^3\dot{\gamma} t_2^S$	$t_2^S = \frac{\sqrt{2}}{2}\sinh^3(\alpha)\sum_{n=0}^{\infty}\left[E_n^S\coth(\alpha) + 2n(n+1)A_n^S\right]$	(2.34b)

Table 2.3: Dimensionless force and torque acting on the particle for each of the fundamental flows, expressed with the respective harmonic decomposition coefficients from [Chaoui 1995].

Computation of the forces and torques with the provided relations and comparison with the tabulated values allowed to verify the correct calculation of the coefficients with the present implementation. Also, verification that the boundary conditions were correctly imposed by analyzing the computed velocity fields confirmed successful calculation of the order 0 flows. The longitudinal and vertical velocity fields for the three fundamental flows are presented on figures 2.6, 2.7 and 2.8 for the particle translating, rotating and resisting the background shear flow respectively. This example configuration is for a

particle at a distance $h/a = 2$ from the wall immersed in water.

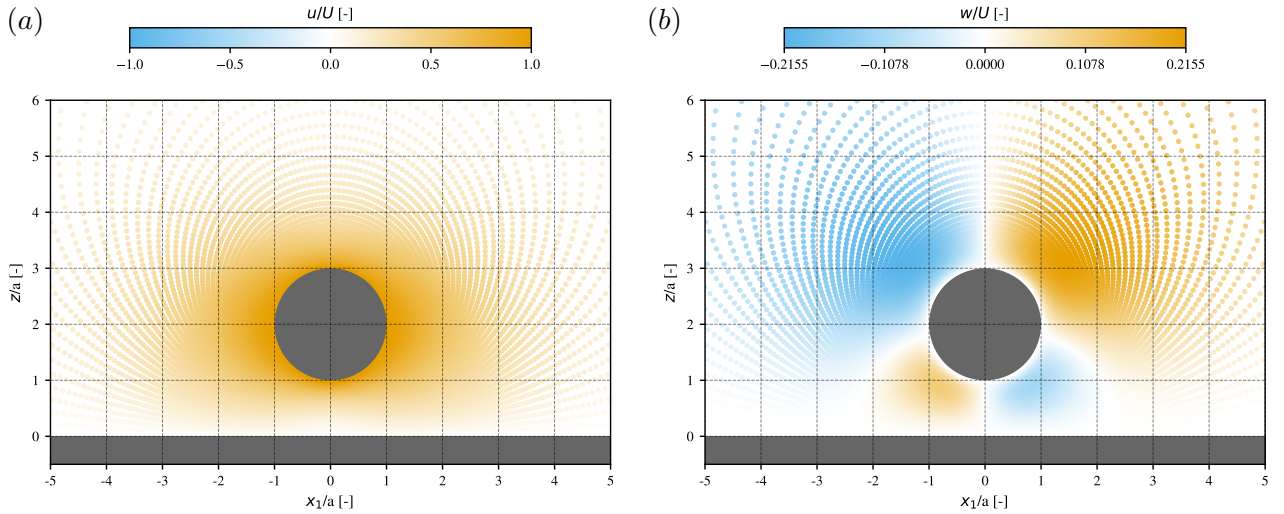

Figure 2.6: (a) Longitudinal and (b) vertical component of the velocity field of a particle translating at velocity $U\mathbf{e}_1$. The longitudinal velocity field is obtained by taking the radial velocity field for $x_1 > 0$ (where $\phi = 0$, $\mathbf{e}_r = \mathbf{e}_1$ and $r = x_1$) and its opposite for $x_1 < 0$ (where $\phi = \pi/2$, $\mathbf{e}_r = -\mathbf{e}_1$ and $r = -x_1$).

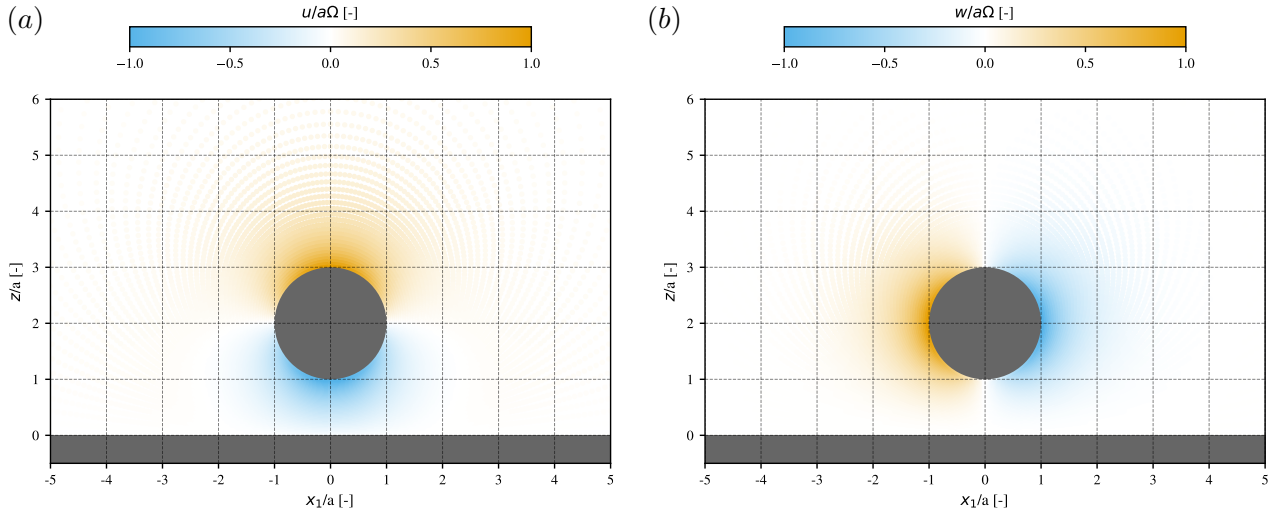

Figure 2.7: (a) Longitudinal and (b) vertical component of the velocity field of a particle rotating at angular velocity $\Omega\mathbf{e}_2$.The longitudinal velocity field is obtained by taking the radial velocity field for $x_1 > 0$ (where $\phi = 0$, $\mathbf{e}_r = \mathbf{e}_1$ and $r = x_1$) and its opposite for $x_1 < 0$ (where $\phi = \pi/2$, $\mathbf{e}_r = -\mathbf{e}_1$ and $r = -x_1$).

2.3.2.2 Adjoint stress tensor

The adjoint stress tensor $\underline{\underline{\sigma}}^*$ is associated to the flow $(\mathbf{u}^*, p^*)$ generated by a particle translating towards a plane wall at a given velocity $-U_z\mathbf{e}_z$ in otherwise quiescent fluid. The resulting velocity field has been first obtained by H. Brenner [Brenner 1961] using the Stokes stream function. However it does not provide an expression for the pressure field which is required to obtain the stress tensor, even though it can be obtained from the velocity field after quite heavy calculations [Pasol *et al.* 2005].

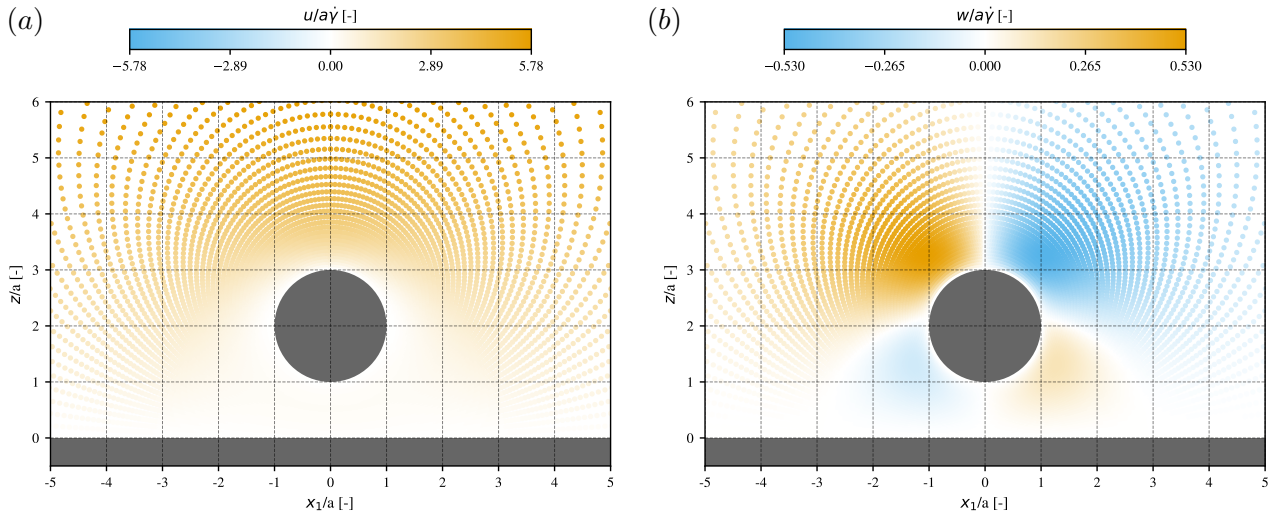

Figure 2.8: (a) Longitudinal and (b) vertical component of the velocity field of a particle held fixed in a background shear flow of shear rate $\dot{\gamma}$. The longitudinal velocity field is obtained by taking the radial velocity field for $x_1 > 0$ (where $\phi = 0$, $\mathbf{e}_r = \mathbf{e}_1$ and $r = x_1$) and its opposite for $x_1 < 0$ (where $\phi = \pi/2$, $\mathbf{e}_r = -\mathbf{e}_1$ and $r = -x_1$). The background shear flow has been added to the computed disturbance flow field computed following equations (2.30) to draw this figure.

[Pasol *et al.* 2005] proposed a new derivation of this velocity and pressure fields inspired by the decomposition of [Dean & O'Neill 1963] introduced for the solution of the fundamental flows at order 0, resulting in a simpler implementation due to similarities in the methodology.

The solution is searched for in the following form:

$$p^* = \frac{\mu U_z}{a} Q_0 \tag{2.35a}$$

$$u^* = U_z\left(\frac{r}{a}\frac{Q_0}{2} + V_1\right) \tag{2.35b}$$

$$v^* = 0 \tag{2.35c}$$

$$w^* = U_z\left(\frac{z}{a}\frac{Q_0}{2} + V_0\right) \tag{2.35d}$$

and the coefficients Q_0, V_0 and V_1 are obtained from the following harmonic decomposition :

$$Q_0 = c^{-1}\left(\cosh\xi - \tilde{\mu}\right)^{1/2} \sum_{n=0}^{\infty} \left[A_n \cosh((n+1/2)\xi) + B_n \sinh((n+1/2)\xi)\right] P_n(\tilde{\mu}) \tag{2.36a}$$

$$V_1 = \left(\cosh\xi - \tilde{\mu}\right)^{1/2} \sin\eta \sum_{n=1}^{\infty} \left[C_n \cosh((n+1/2)\xi) + D_n \sinh((n+1/2)\xi)\right] P'_n(\tilde{\mu}) \tag{2.36b}$$

$$V_0 = \left(\cosh\xi - \tilde{\mu}\right)^{1/2} \sum_{n=0}^{\infty} \left[F_n \sinh((n+1/2)\xi)\right] P_n(\tilde{\mu}) \tag{2.36c}$$

following the notations introduced in the previous section. The harmonic coefficients A_n, B_n, C_n, D_n and F_n are similarly searched for by injecting equations (2.36) into equations (2.35) and solving for the appropriate boundary conditions. Once again, the coefficients are all expressed as a function of F_n, which is itself defined by a recurrence relation. The coefficients F_n are obtained by solving a linear system.

This method works correctly to obtain both w^* and p^*, however the radial velocity field u^* obtained

with this method does not satisfy the expected no-slip boundary condition on the surface of the sphere as can be seen on figure 2.9(a).

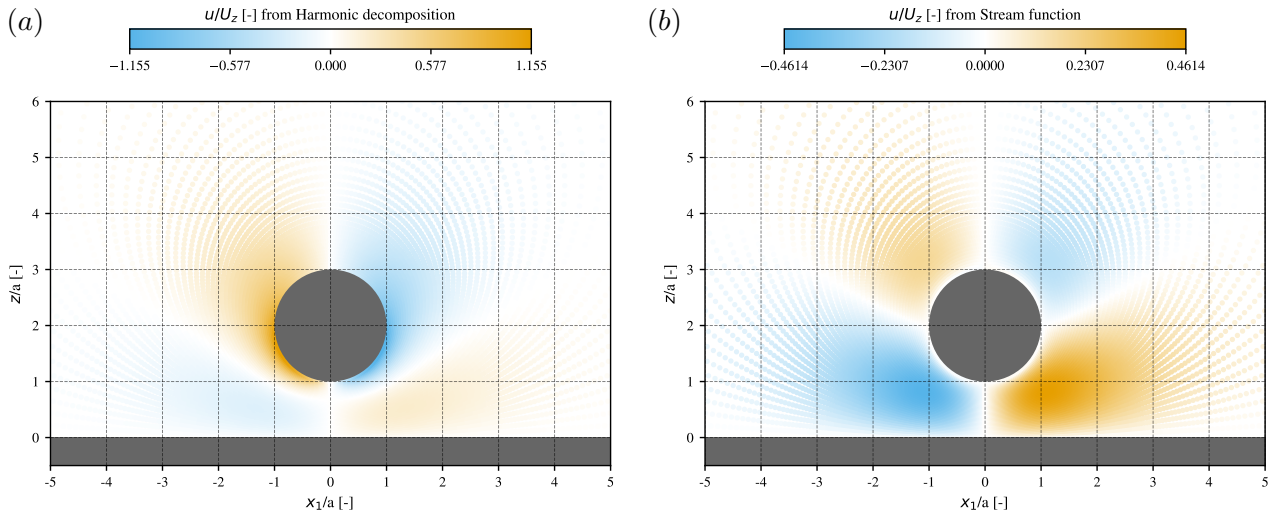

Figure 2.9: Longitudinal component of the velocity field of a particle sedimenting towards a flat wall at velocity $-U_z\mathbf{e}_z$. The longitudinal velocity field is obtained by taking the radial velocity field for $x_1 > 0$ (where $\phi = 0$, $\mathbf{e}_r = \mathbf{e}_1$ and $r = x_1$) and its opposite for $x_1 < 0$ (where $\phi = \pi/2$, $\mathbf{e}_r = -\mathbf{e}_1$ and $r = -x_1$). (a) Obtained via the Harmonic decomposition (2.35b) and (2.36). (b) Obtained from Stokes' stream function (2.38) and (2.39). The boundary condition on the surface of the sphere for this velocity component is expected to be zero which is achieved only using the solution from the stream function.

To find out where the error comes from, we investigated the expression of the harmonic coefficients. [Pasol *et al.* 2005] provides the expression of the force acting on the particle in direction $\mathbf{e}_3$, only based on the values of the coefficients F_n as :

$$f_3 = \frac{F_3}{6\pi\mu a U_3} = \frac{2\sqrt{2}}{3}\sinh(\alpha)\sum_{n=0}^{\infty} F_n \tag{2.37}$$

Because values of this force for different particle-wall distances agree with the values computed by [Brenner 1961], we concluded that the coefficients F_n are correct.

Also, because the correct boundary conditions are obtained for the vertical velocity component w^*, we consider that the coefficients A_n and B_n appearing in Q_0 are correct. Therefore, the error lies in the harmonic coefficients C_n or D_n, only related to u^*. Especially, the coefficient D_n is obtained by applying the no-slip boundary condition for the radial velocity component at the surface of the sphere, so we suspect an error in the expression of this coefficient.

After failing to identify and fix the error, the workaround was to use the radial velocity field obtained via derivation of Brenner's stream function [Brenner 1961] following equation (2.38).

$$u^* = \frac{1}{r}\frac{\partial \Psi^*}{\partial z} \qquad\qquad w^* = -\frac{1}{r}\frac{\partial \Psi^*}{\partial r} \tag{2.38}$$

where the stream function is searched for in the form :

$$\Psi^* = (\cosh\xi - \tilde{\mu})^{-3/2}\sum_{n=0}^{\infty} U_n(\xi)\frac{P_{n-1}(\tilde{\mu}) - P_{n+1}(\tilde{\mu})}{2n-1} \tag{2.39}$$

with

$$\begin{aligned} U_n(\xi) =& a_n \cosh((n-1/2)\xi) + b_n \sinh((n-1/2)\xi) \\ &+ c_n \cosh((n+3/2)\xi) + d_n \sinh((n+3/2)\xi) \end{aligned} \tag{2.40}$$

The coefficients a_n,b_n,c_n and d_n are found from application of the boundary conditions and are given by [Brenner 1961].

This expression of the velocity components is singular at $r = 0$, but from the symmetry of the problem it is known that $u^*(r = 0, z) = 0$ so that u^* is known everywhere. The longitudinal velocity component derived from this radial component is shown on figure 2.9, highlighting the correct application of the boundary conditions. On the other hand, w^* is not known on the axis $r = 0$ when derived from the stream function. Therefore, its solution from the harmonic decomposition is used.

The vertical velocity field and pressure field are therefore obtained via harmonic decomposition from equations (2.35)(a,d) and (2.36) and are shown on figure 2.10. The radial velocity field is obtained via derivation of Stokes stream function using (2.38) and (2.39). Mixing solutions from these two methods was already applied successfully [Ardekani *et al.* 2007].

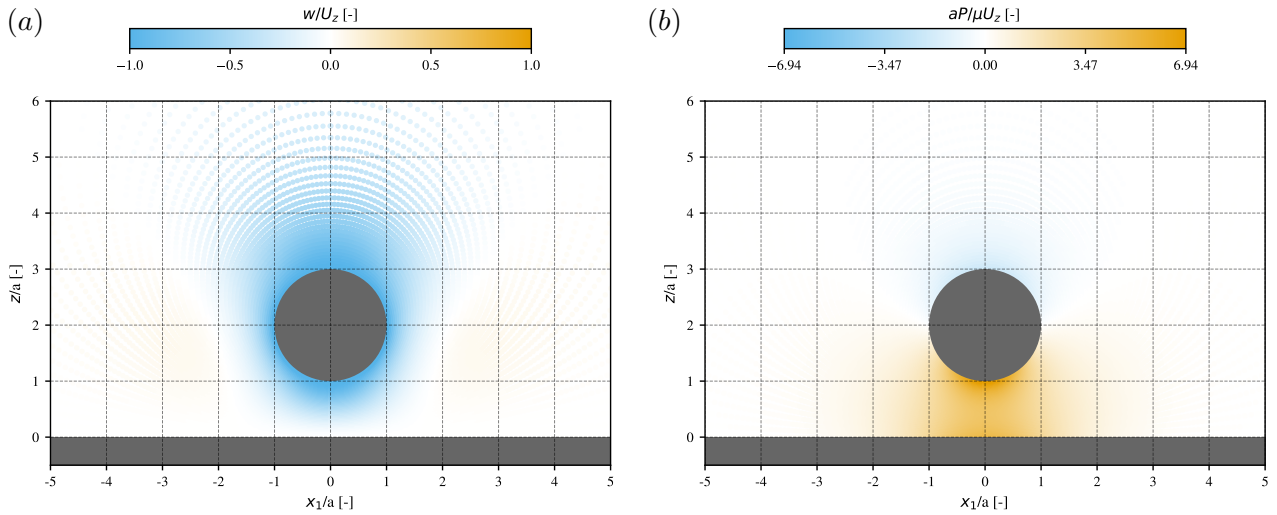

Figure 2.10: (a) Vertical component of the velocity field and (b) pressure field of a particle sedimenting towards a flat wall at velocity $-U_z\mathbf{e}_z$.

From these velocity and pressure fields we are able to construct the stress tensor for the adjoint flow $\underline{\underline{\sigma}}^*$ as defined by (2.2) and (2.3).

2.3.2.3 Undisturbed shear flow

The undisturbed shear flow at order 1 is the additional effect of the structured surfaces to the linear shear flow over a flat surface and its expression is given by [Assoudi *et al.* 2018]. The problem is posed as follows.

The shear flow $(\mathbf{V}_s, P_s)$ over a structured surface of small amplitude is solution of the Stokes equations:

$$-\frac{\partial P_s}{\partial x_i} + \mu \frac{\partial^2 (V_s)_i}{\partial x_j \partial x_j} = 0 \tag{2.41a}$$

$$\frac{\partial (V_s)_i}{\partial x_i} = 0 \tag{2.41b}$$

with boundary conditions:

$$\mathbf{V}_s|_{x_3^{wall}} = \mathbf{0} \tag{2.42a}$$

$$\mathbf{V}_s|_{x_3\to\infty} = \mathbf{V}^\infty = \dot{\gamma} x_3 \mathbf{e}_1 \tag{2.42b}$$

As done for the perturbation flow generated by the presence of the particle, the effect on the flow of the structures of amplitude $O(\varepsilon)$ is expected to be of order $O(\varepsilon)$, so an order decomposition is performed as in equation (2.23)(a-b):

$$\mathbf{V}_s = \mathbf{V}_s^{(0)} + \varepsilon \mathbf{V}_s^{(1)} + O(\varepsilon^2) \tag{2.43a}$$

$$P_s = P_s^{(0)} + \varepsilon P_s^{(1)} + O(\varepsilon^2) \tag{2.43b}$$

Also, the technique of the "flattening of the surface" is again used to obtain an equivalent slip boundary condition on the flat surface, and following equation (2.17) we end up with the following boundary conditions:

$$\mathbf{V}_s^{(0)}\Big|_{x_3=0} = \mathbf{0} \qquad \mathbf{V}_s^{(0)}\Big|_{x_3\to\infty} = \mathbf{V}^\infty = \dot{\gamma} x_3 \mathbf{e}_1 \tag{2.44a}$$

$$\mathbf{V}_s^{(1)}\Big|_{x_3=0} = -aR(x_1,x_2)\left.\frac{\partial V_s^{(0)}}{\partial x_3}\right|_{x_3=0} \qquad \mathbf{V}_s^{(1)}\Big|_{x_3\to\infty} = \mathbf{0} \tag{2.44b}$$

The solution of the problem at order 0 is well known as it is a simple linear shear flow, with $\mathbf{V}_s^{(0)} = \mathbf{V}^\infty$ and therefore the boundary condition on the flat wall for the problem at order 1 is:

$$\mathbf{V}_s^{(1)}\Big|_{z=0} = -aR(x_1,x_2)\dot{\gamma}\mathbf{e}_1 \tag{2.45}$$

Under additional constraints that the structure pattern is periodic and does not depend on the x_2 coordinate such that $R(x_1+L,x_2) = R(x_1)$ with L the pattern period, the solution for the flow at order one is searched for in terms of a stream function $\Psi_s^{(1)}$ defined by :

$$\Psi_s^{(1)} = d_0 x_3 + f_0 + \sum_{n=1}^{\infty} \left[(d_n x_3 + f_n)\cos(n\omega x_1) + (e_n x_3 + g_n)\sin(n\omega x_1)\right]\exp(-n\omega x_3) \tag{2.46}$$

and the flow component in direction $\mathbf{e}_1$ and $\mathbf{e}_3$ are respectively :

$$U_s^{(1)} = \frac{\partial \Psi_s^{(1)}}{\partial x_3} \qquad W_s^{(1)} = -\frac{\partial \Psi_s^{(1)}}{\partial x_1} \tag{2.47}$$

Then the coefficients d_n, f_n, e_n and g_n are searched for by imposing the boundary conditions. The restriction to a periodic and unidirectional structure allows to approximate the shape function by a Fourier series:

$$R(x_1,x_2) = c_0 + \sum_{n=1}^{\infty} \left(c_n \cos(n\omega x_1) + s_n \sin(n\omega x_2)\right) \tag{2.48}$$

with $\omega = 2\pi/L$ and

$$c_0 = \frac{1}{L}\int_0^L R(x_1,x_2)dx_1, \quad c_n = \frac{2}{L}\int_0^L R(x_1,x_2)\cos(n\omega x_1)dx_1, \quad s_n = \frac{2}{L}\int_0^L R(x_1,x_2)\sin(n\omega x_1)dx_1 \tag{2.49}$$

In the end, [Assoudi *et al.* 2018] provides the velocity and pressure fields expression based on the Fourier series coefficients as :

$$U_s^{(1)} = a\dot{\gamma}\left(-c_0 + \sum_{n=1}^{\infty}\left[c_n\cos(n\omega x_1) + s_n\sin(n\omega x_1)\right]\left[n\omega x_3 - 1\right]\exp\left(-n\omega x_3\right)\right) \tag{2.50a}$$

$$W_s^{(1)} = -a\dot{\gamma}\omega x_3\sum_{n=1}^{\infty}\left[s_n\cos(n\omega x_1) - c_n\sin(n\omega x_1)\right]n\exp\left(-n\omega x_3\right) \tag{2.50b}$$

$$P_s^{(1)} = 2a\mu\dot{\gamma}\omega\sum_{n=1}^{\infty}\left[s_n\cos(n\omega x_1) - c_n\sin(n\omega x_1)\right]n\exp\left(-n\omega x_3\right) \tag{2.50c}$$

We found out that their expression does not respect the 0 velocity boundary condition (2.44b) at infinity and instead gives the value $U_s^{(1)} = -c_0 a\dot{\gamma}$. This expression becomes valid if the shape function has a mean amplitude of 0 which is not the case when the shape function is ranging from 0 to 1. If linear shape functions are used, they should therefore be defined ranging from -0.5 to 0.5 to ensure the c_0 coefficient is 0. This doesn't have any consequence on the previous calculations, as only changing the definition of the shape function fixes this issue. It happens that the amplitude of the structure being infinitely small, the distance between the particle and the equivalent flat surface changes barely when choosing to define the structure its mean value at $x_3 = 0$ or with the bottom of the structure at $x_3 = 0$. Therefore, the final value of the force acting on the particle using either definition of the shape function was observed to be equal.

As mentioned, this solution is valid for periodic patterns only. [Assoudi *et al.* 2018] also suggest another way to compute the integral involving $V_s^{(1)}$ by using a second application of the Lorentz reciprocal theorem and Euler's theorem, which can be computed for any structure pattern. They showed that:

$$\int_{\mathcal{S}}\mathbf{V}_s^{(1)}\underline{\underline{\sigma}}^*\mathbf{dS} = a\dot{\gamma}\int_{\mathcal{P}}R(x_1,x_2)\mathbf{e}_1\cdot\underline{\underline{\sigma}}^*\mathbf{dS} \tag{2.51}$$

Details of this calculation can be found in Appendix B of [Assoudi *et al.* 2018].

2.3.3 Numerical implementation

The computation of the vertical force (2.27) have been implemented in a python script. Details on the implementation, usage of the script as well as known limitations are presented here.

Initial parameters of the problem must be given in the first place. They are the particle radius, the fluid properties, the problem configuration (particle distance to wall, shear rate, imposed translational and angular velocity), as well as the strucured surface shape function.

From the particle size and distance to the wall, the bispherical coordinate system parameters α and c are computed, and the 3D grid is defined with a prescribed resolution and $(\xi,\eta,\phi) \in [0,\alpha]\times[0,\pi]\times[0,2\pi]$.

The 3 order zero flows and the adjoint flow field are then computed. The scripts runs in parallel on 4 processors where each processor is responsible for the calculation of one of the 4 flows. For each of these flows, the theoretical solution is detailed in sections 2.3.2.1 or 2.3.2.2. The output of this calculation is the velocity and pressure fields in the cylindrical coordinate system on the points defined previously using the bispherical coordinate system. Therefore, special care must be taken when numerical derivation will be performed to obtain the gradients of these flows. The output can also include the force and torque acting on the particle for each of the flow, obtained from the harmonic coefficients, which is used both for validation by comparing these forces to tabulated values as mentioned previously, as well as to determine the linear and angular velocities of a force-free and

torque-free particle in the shear flow.

From these flows, the computation of the integrals in (2.27) is then performed. Following [Assoudi *et al.* 2018], they are noted as follows:

$$L = \int_{\mathcal{P}} R(x_1, x_2) \left. \frac{\partial \mathbf{v}^{(0)}}{\partial x_3} \right|_{x_3=0} \underline{\underline{\sigma}}^* \cdot \mathbf{e}_3 dS \tag{2.52a}$$

$$I^{\infty} = \int_{\mathcal{S}} \mathbf{V}_s^{(1)} \underline{\underline{\sigma}}^* \mathbf{dS} = a\dot{\gamma} \int_{\mathcal{P}} R(x_1, x_2) \mathbf{e}_1 \cdot \underline{\underline{\sigma}}^* \cdot \mathbf{e}_3 dS \tag{2.52b}$$

In the end, the force acting on the particle is expressed as:

$$F_3^{(1)} = \frac{a}{U_3} L + \frac{1}{U_3} I_{\infty} \tag{2.53}$$

2.3.3.1 Computation of L

Following the decomposition of the flow at order 0 in 3 fundamental flows in equation (2.28), it is possible to define L_T, L_R and L_S such that:

$$L_T = \int_{\mathcal{P}} R(x_1, x_2) \left. \frac{\partial \mathbf{v}_T^{(0)}}{\partial x_3} \right|_{x_3=0} \underline{\underline{\sigma}}^* \cdot \mathbf{e}_3 dS \tag{2.54a}$$

$$L_R = \int_{\mathcal{P}} R(x_1, x_2) \left. \frac{\partial \mathbf{v}_R^{(0)}}{\partial x_3} \right|_{x_3=0} \underline{\underline{\sigma}}^* \cdot \mathbf{e}_3 dS \tag{2.54b}$$

$$L_S = \int_{\mathcal{P}} R(x_1, x_2) \left. \frac{\partial \mathbf{v}_S^{(0)}}{\partial x_3} \right|_{x_3=0} \underline{\underline{\sigma}}^* \cdot \mathbf{e}_3 dS \tag{2.54c}$$

with

$$L = L_T + L_R + L_S \tag{2.55}$$

Some of the dot products are simplified analytically before computing these integrals for easier implementation.

We know $\mathbf{v}_{\bullet}^{(0)}$ for $\bullet$ in $\{T, R, S\}$ in cylindrical coordinate system, the stress tensor in cylindrical coordinate system associated to flow $(\mathbf{v}, p)$ given by equation (2.56) is therefore used with $\mathbf{v} = u\mathbf{e}_r + v\mathbf{e}_\phi + w\mathbf{e}_z$, $\mathbf{e}_r = \cos(\phi)\mathbf{e}_1 + \sin(\phi)\mathbf{e}_2$, $\mathbf{e}_\phi = -\sin(\phi)\mathbf{e}_1 + \cos(\phi)\mathbf{e}_2$ and $\mathbf{e}_z = \mathbf{e}_3$.

$$\underline{\underline{\sigma}} = \begin{pmatrix} -p + 2\mu\frac{\partial u}{\partial r} & \mu\left(\frac{1}{r}\frac{\partial u}{\partial \phi} - \frac{\partial v}{\partial r} - \frac{v}{r}\right) & \mu\left(\frac{\partial u}{\partial z} + \frac{\partial w}{\partial r}\right) \\ \mu\left(\frac{1}{r}\frac{\partial u}{\partial \phi} - \frac{\partial v}{\partial r} - \frac{v}{r}\right) & -p + 2\mu\left(\frac{1}{r}\frac{\partial v}{\partial \phi} + \frac{u}{r}\right) & \mu\left(\frac{\partial v}{\partial z} + \frac{1}{r}\frac{\partial w}{\partial \phi}\right) \\ \mu\left(\frac{\partial u}{\partial z} + \frac{\partial w}{\partial r}\right) & \mu\left(\frac{\partial v}{\partial z} + \frac{1}{r}\frac{\partial w}{\partial \phi}\right) & -p + 2\mu\frac{\partial w}{\partial z} \end{pmatrix} \tag{2.56}$$

Developing the dot products in (2.54) yields relation (2.57) keeping in mind this is evaluated at $z = 0$.

$$\frac{\partial \mathbf{v}_{\bullet}^{(0)}}{\partial z} \underline{\underline{\sigma}}^* \mathbf{e}_z = \left(\frac{\partial u_{\bullet}^{(0)}}{\partial z} \mathbf{e}_r + \frac{\partial v_{\bullet}^{(0)}}{\partial z} \mathbf{e}_\phi + \frac{\partial w_{\bullet}^{(0)}}{\partial z} \mathbf{e}_z \right) \underline{\underline{\sigma}}^* \mathbf{e}_z \tag{2.57}$$

Also, from the incompressibility constraint at the wall and the fact that $\frac{\partial}{\partial r}$ and $\frac{\partial}{\partial \phi}$ are null at the wall, the vertical velocity gradient in the z direction $\frac{\partial w_{\bullet}^{(0)}}{\partial z}$ is also null at the wall.

Therefore, equation (2.57) becomes:

$$\begin{aligned}\frac{\partial \mathbf{v}_\bullet^{(0)}}{\partial z}\underline{\underline{\sigma}}^*\mathbf{e}_z &= \frac{\partial u_\bullet^{(0)}}{\partial z}\sigma_{rz}^* + \frac{\partial v_\bullet^{(0)}}{\partial z}\sigma_{\phi z}^* \\ &= \frac{\partial u_\bullet^{(0)}}{\partial z}\mu\left(\frac{\partial u^*}{\partial z}+\frac{\partial w^*}{\partial r}\right) + \frac{\partial u_\bullet^{(0)}}{\partial z}\mu\left(\frac{\partial v^*}{\partial z}+\frac{1}{r}\frac{\partial w^*}{\partial \phi}\right)\end{aligned} \tag{2.58}$$

Further simplpification can be done using the fact that $\frac{\partial}{\partial r}$ and $\frac{\partial}{\partial \phi}$ are null at the wall and that the velocity component v^* in direction $\mathbf{e}_\phi$ is zero for the case of the adjoint flow :

$$\frac{\partial \mathbf{v}_\bullet^{(0)}}{\partial z}\underline{\underline{\sigma}}^*\mathbf{e}_z = \mu\frac{\partial u_\bullet^{(0)}}{\partial z}\frac{\partial u^*}{\partial z} \tag{2.59}$$

In the end, the expression for L_T, L_R and L_S are given by:

$$L_T = \int_{\mathcal{P}} \mu R(x_1,x_2)\frac{\partial u_T^{(0)}}{\partial z}\frac{\partial u^*}{\partial z}dS \tag{2.60a}$$

$$L_R = \int_{\mathcal{P}} \mu R(x_1,x_2)\frac{\partial u_R^{(0)}}{\partial z}\frac{\partial u^*}{\partial z}dS \tag{2.60b}$$

$$L_S = \int_{\mathcal{P}} \mu R(x_1,x_2)\frac{\partial u_S^{(0)}}{\partial z}\frac{\partial u^*}{\partial z}dS \tag{2.60c}$$

This result is not in agreement with the one obtained by [Assoudi *et al.* 2018] for the case of the particle held fixed in the shear flow (2.60c). Indeed, they found similar expressions for the cases of the particle translating and rotating but for the resistance to the shear flow, they found an expression in the form of equation (2.61), (*c.f.* equation (43b) in [Assoudi *et al.* 2018]).

$$L_S^{+1} = \int_{\mathcal{P}} \mu R(x_1,x_2)\left(\frac{\partial u_S^{(0)}}{\partial z}+1\right)\frac{\partial u^*}{\partial z}dS \tag{2.61}$$

Note that we chose to keep the exact shape function for the structure while they expressed the shape function using modified Bessel functions so the expressions naturally differs but can nevertheless be compared as this difference only affects the definition of the structure and not the fluid flows.

From the details of the calculations above we are not able to explain the presence of this additional *+1* and because we made no particular assumption on the considered flow to obtain equations (2.60) we were not able to explain why it appears only for the case related to the resistance to shear in their expression. The impact of this difference on the computed force is discussed further in the validation section of this chapter.

In our script, equations (2.60) are implemented and for any $\bullet$ in $\{T,R,S\}$:

$$L_\bullet = \int_0^{2\pi}\int_0^{\infty} \mu R(x_1(r,\phi,0),x_2(r,\phi,0))\frac{\partial u_\bullet^{(0)}}{\partial z}\frac{\partial u^*}{\partial z}r dr d\phi \tag{2.62}$$

Numerical derivation is performed using relation (2.63b) provided by [Chaoui 1995] and a first order finite difference scheme.

$$\frac{\partial}{\partial r} = \frac{1}{c}\left((\cosh(\xi)\cos(\eta) - 1)\frac{\partial}{\partial \eta} - \sinh(\xi)\sin(\eta)\frac{\partial}{\partial \xi}\right) \tag{2.63a}$$

$$\frac{\partial}{\partial z} = -\frac{1}{c}\left(\sinh(\xi)\sin(\eta)\frac{\partial}{\partial \eta} + (\cosh(\xi)\cos(\eta) - 1)\frac{\partial}{\partial \xi}\right) \tag{2.63b}$$

Because all the quantities are defined over the bispherical coordinates grid, a change of variable is performed and integration is done over the coordinates (η, ϕ) instead of (r, ϕ) so that :

$$L_\bullet = \int_0^\pi \int_0^{2\pi} \mu R(x_1(0,\eta,\phi), x_2(0,\eta,\phi)) \frac{\partial u_\bullet^{(0)}}{\partial z} \frac{\partial u^*}{\partial z} r(0,\eta,\phi) \left|J_{r,\eta}\right| d\eta d\phi \tag{2.64}$$

with the Jacobian of the variable change given by equation (2.65) as ϕ remains the same for the two coordinate system.

$$J_{r,\eta} = \left.\frac{\partial r}{\partial \eta}\right|_{\xi=0} = \frac{c}{1-\cos(\eta)} \tag{2.65}$$

A 2nd order trapezoidal method is used to compute the integrals and integration of a Gaussian function using this change of variable has been done to confirm the integration is performed correctly.

2.3.3.2 Computation of I^∞

Two possible ways to compute I^∞ are available as shown in equation (2.52b). We begin with the expression in the right hand side of equation (2.52b) as it is very similar to the integration of L presented previously.

This way, I^∞ is defined by an integral over the plane surface:

$$I^\infty_{plane} = a\dot{\gamma} \int_{\mathcal{P}} R(x_1, x_2) \mathbf{e}_1 \cdot \underline{\underline{\sigma}}^* \cdot \mathbf{e}_3 dS \tag{2.66}$$

Simplification of the matrix product in the integral is performed beforehand as for the calculation of L, using the relation $\mathbf{e}_1 = \cos(\phi)\mathbf{e}_r - \sin(\phi)\mathbf{e}_\phi$ and $\mathbf{e}_3 = \mathbf{e}_z$ we have:

$$\mathbf{e}_1 \cdot \underline{\underline{\sigma}}^* \cdot \mathbf{e}_3 = \sigma^*_{rz}\cos(\phi) - \sigma^*_{\phi z}\sin(\phi) \tag{2.67}$$

and using the results from the simplification of L we know that $\sigma_{rz} = \mu\frac{\partial u^*}{\partial z}$ and $\sigma_{\phi z} = 0$ at the wall so that:

$$I^\infty_{plane} = a\dot{\gamma} \int_{\mathcal{P}} \mu R(x,y) \frac{\partial u^*}{\partial z} \cos(\phi) dS \tag{2.68}$$

The same change of variable is performed for the integration over the infinite plane as in (2.64) and derivation is again performed following (2.63b).

The second way to compute I^∞ following (2.52b) is to assess the following integral over the surface of the sphere :

$$I^\infty_{sphere} = \int_{\mathcal{S}} \mathbf{V}_s^{(1)} \underline{\underline{\sigma}}^* \mathbf{dS} \tag{2.69}$$

To perform this integration, the spherical coordinate system (r_s, θ, ϕ) is used and the normal of the

surface is $\mathbf{e}_{r_s}$. They are linked to the cylindrical coordinate system (r, ϕ, z) by the relations:

$$r_s = \sqrt{r^2 + z^2} \tag{2.70}$$

$$\theta = \tan^{-1}(\frac{r}{z-h}) \tag{2.71}$$

The integration on the sphere using these coordinates is given by:

$$I^{\infty}_{sphere} = \int_0^{\pi}\int_0^{2\pi} \mathbf{V}_s^{(1)} \underline{\underline{\sigma}}^* \mathbf{e}_{r_s} a^2 \sin(\theta) d\theta d\phi \tag{2.72}$$

and once again, using a change of variable to integrate over the bispherical coordinates results in the integration:

$$I^{\infty}_{sphere} = \int_0^{\pi}\int_0^{2\pi} \mathbf{V}_s^{(1)} \underline{\underline{\sigma}}^* \mathbf{e}_{r_s} r_s^2 \sin(\theta) \left|J_{\theta,\eta}\right| d\eta d\phi \tag{2.73}$$

with the Jacobian from spherical to bispherical coordinate system:

$$J_{\theta,\eta} = \left.\frac{\partial\theta}{\partial\eta}\right|_{\xi=\alpha} = \frac{cos(\eta)\sinh(\alpha) + \frac{h}{c}(1 - \cosh(\alpha)\cos(\eta))}{\left(\sinh(\alpha) - \frac{h}{c}(\cosh(\alpha) - \cos(\eta))\right)^2 + \sin^2(\eta)} \tag{2.74}$$

Calculation of the area of the sphere with integration over the bispherical coordinate system was used to confirm the integration was performed correctly as well as integration of the adjoint stress tensor over the surface of the sphere which was compared to tabulated values of the force acting on the particle provided by [Brenner 1961]. The undisturbed velocity field is computed following equations (2.50), with a Fourier series description of the structure defined with the shape function ranging from -0.5 to 0.5. When the structure contains very sharp angles such as a square pattern, up to 10 Fourier coefficients are required to accurately capture the structure but for smoother structures, only 3 fourier coefficients can be enough [Assoudi *et al.* 2018].

2.3.4 Results

First, comparison with the results obtained by [Assoudi *et al.* 2018] is performed. They provide the dimensionless force acting on a particle at any position over a periodic structure with triangular shape. The structure is of period $L = 4a$, with a ramp up between 0 and $3a$ where the maximum height is reached, and a ramp down between $3a$ and $4a$ as depicted on figure 2.4. The particle is placed at constant altitude $h = 1.57a$ and its position is varied across the period of the structure, the force being computed for each of the position of the particle. [Assoudi *et al.* 2018] provide the evolution of the force split into the 3 component related to the translation, the rotation and the resistance to the shear flow and from L_T, L_R, L_S and I^{∞} they give:

$$f_{3,T} = \frac{aL_T}{U_3^*}\frac{1}{-6\pi\mu a U} \tag{2.75a}$$

$$f_{3,R} = \frac{aL_R}{U_3^*}\frac{1}{6\pi\mu a^2\Omega} \tag{2.75b}$$

$$f_{3,S} = \frac{aL_S + I^{\infty}}{U_3^*}\frac{1}{6\pi\mu a h\dot{\gamma}} \tag{2.75c}$$

Figure 2.11 presents the dimensionless coefficients obtained by [Assoudi *et al.* 2018] and the ones obtained in this work. It appears that the amplitude of the forces is not accurately reproduced even though the evolution over the structure pattern is in good agreement.

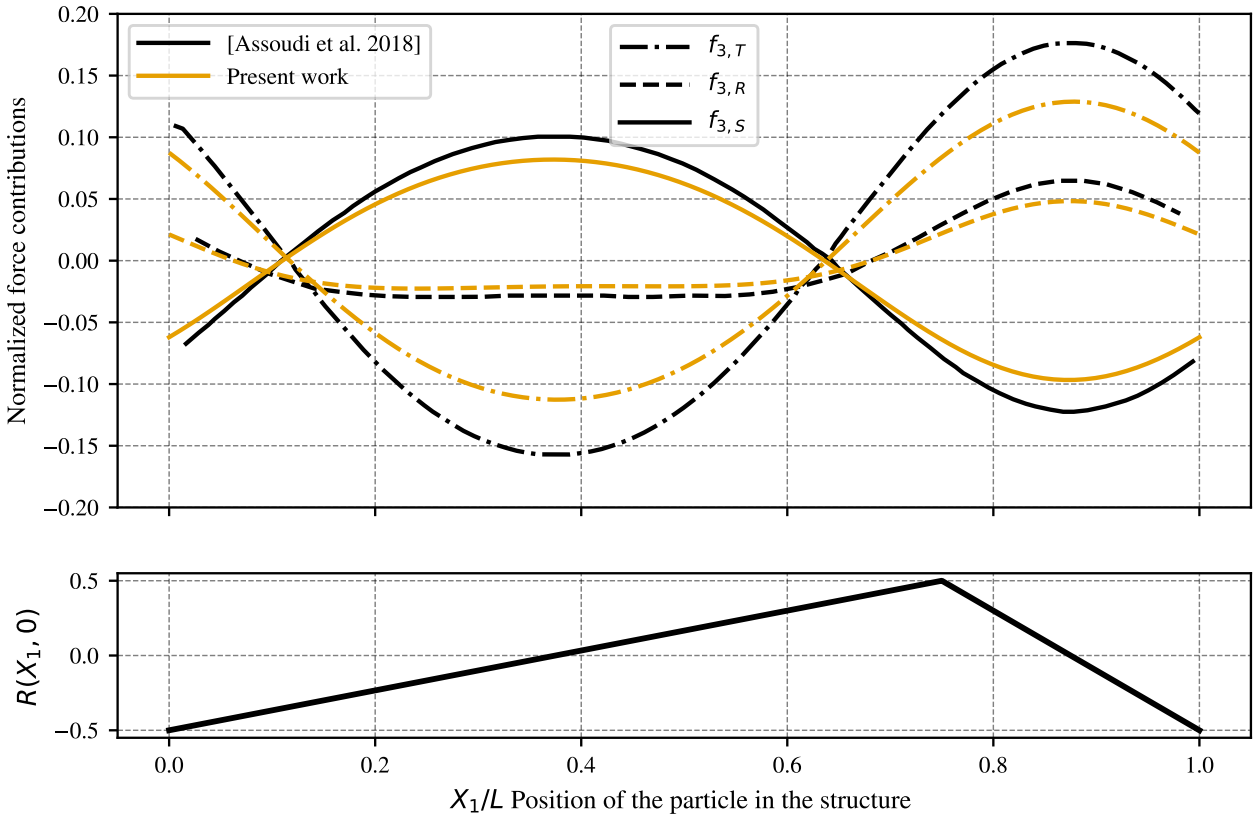

Figure 2.11: Evolution of the 3 contributions to the force acting on the particle at constant altitude $h = 1.57a$ over a triangular shape structure. (——) Results from [Assoudi *et al.* 2018] and (——) results obtained with the present implementation. The total force is divided into three contributions related to the particle (– · – ·) translation, (– – –) rotation and (——) resistance to shear as defined by equations (2.75).

The main difference between the two implementations is that we used I^{∞}_{sphere} using equation (2.69) while [Assoudi *et al.* 2018] used the expression of I^{∞}_{plane} at the plane wall via equation (2.66). When we use I^{∞}_{plane}, we obtain a result which is very different for the coefficient $f_{3,S}$, see orange curve in figure 2.12 which shows the contribution related to the resistance to shear for the different ways it can be computed. This is surprising as the two expressions are supposed to be equal following equation (2.52b).

Yet, it is possible to obtain the previous result (obtained using I^{∞}_{sphere}, blue dashed line in figure 2.12) if a second I^{∞}_{plane} is included, green curve in 2.12. This comes from the unexplained "+1" in the expression for L_S^{+1} from [Assoudi *et al.* 2018] which leads to the addition of an extra I^{∞}_{plane} compared to the expression of L_S (2.60c). Because we implemented the calculation of L_S as equation (2.60c), defining $f_{3,S}$ using I^{∞}_{plane} as equation (2.76) allows to obtain the same result as using I^{∞}_{sphere} as can be seen by the overlapping blue and green curves on figure 2.12.

$$f_{3,S} = \frac{aL_S + 2 \times I^{\infty}_{plane}}{U_3} \frac{1}{6\pi\mu a h \dot{\gamma}} \tag{2.76}$$

From this observation, we were not able to conclude whether we made a mistake in our development or implementation, or if there is a mistake in [Assoudi *et al.* 2018], as even though some expressions are different in both of our works, we are able to make up for these differences by considering extra terms, which we cannot explain.

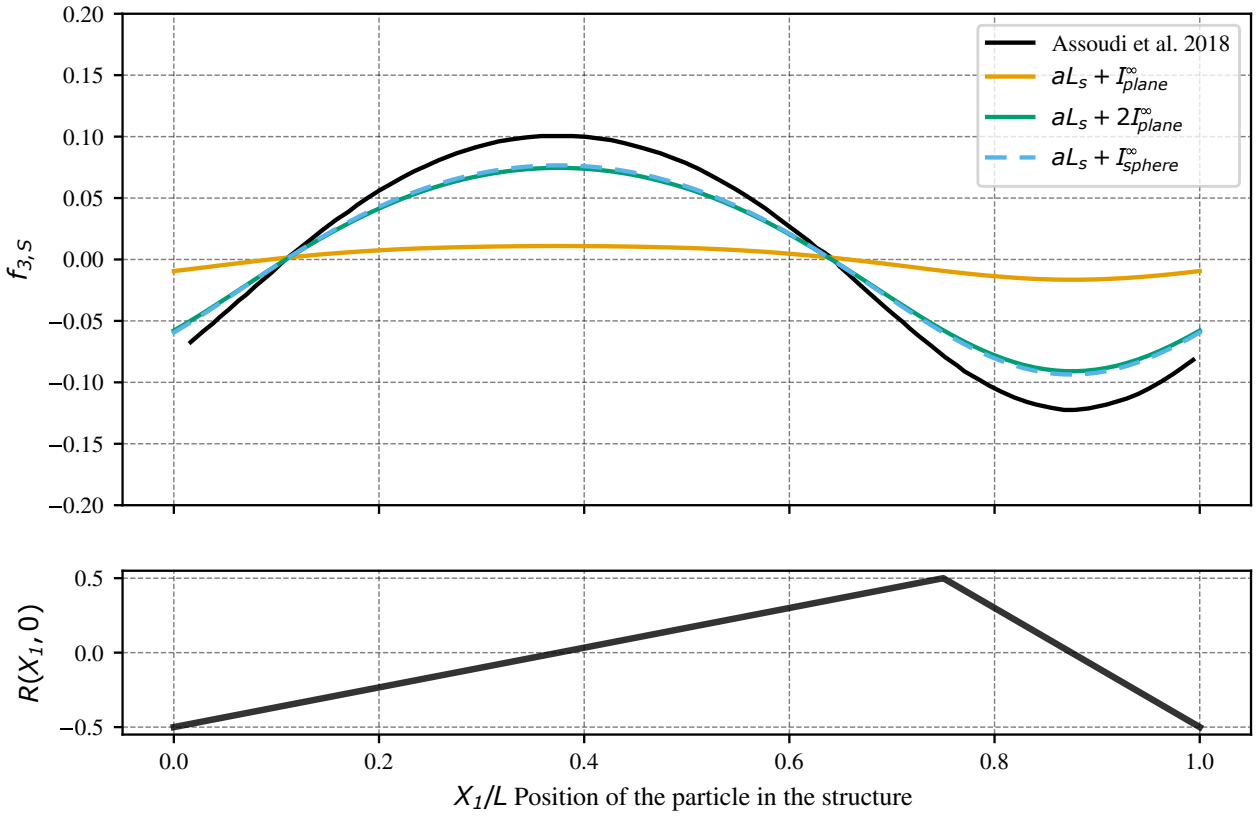

Figure 2.12: Evolution of the contribution of the resistance to the ambient shear on the force acting on the particle at constant altitude $h = 1.57a$ over a triangular shape structure. (——) Result from [Assoudi *et al.* 2018], (——) contribution computed using equation (2.75c) and $I^{\infty} = I^{\infty}_{plane}$ following equation (2.66). (- - -) contribution computed using equation (2.75c) and $I^{\infty} = I^{\infty}_{sphere}$ and (——) contribution computed with (2.76) where $I^{\infty} = I^{\infty}_{plane}$ is accounted for twice following [Assoudi *et al.* 2018].

To keep things under control, we decided to stick to using I^{∞}_{sphere} defined by equation (2.69), $L_{\bullet}$ defined by equations (2.60), and the total force defined by equation (2.53) for which we understand and are confident in the derivation. For the few cases presented further in this work (see chapter 5) where the structure pattern is not periodic anymore so that solution for $\mathbf{V_s}^{(1)}$ is not available and therefore direct computation of I^{∞}_{sphere} is not possible, I^{∞}_{plane} is used and accounted for twice in the total force following [Assoudi *et al.* 2018].

Even though some uncertainties remain regarding the amplitude of the different contributions, the average total force required to hold the particle at a constant altitude, taken over one pattern period of the structure, is zero. This indicates that this structure cannot generate any net particle drift.

Other structures were investigated to determine whether they could generate a net force on the particle. These structures were variations of the previous triangular shape, with the position of the maximum shifted across the pattern period, ranging from a downward sawtooth to an upward sawtooth and including intermediate shapes similar to the previous one. All these structures produce a zero mean force over a pattern period, which suggests that structures of negligible amplitude cannot generate a net mean force on the particle in a first-order approximation.

Based on this observation, the previous first-order development has been extended to second order. However, computing the force required to hold the particle at constant altitude at this order requires knowledge of the first-order flow field, just as the first-order force requires knowledge of the zeroth-

order flow field. Since the first-order flow field is not known analytically, the force generated by the second order flow cannot be assessed analytically.

In addition, because blood platelets are not spherical but are better represented by ellipsoidal particles, the analytical solution has been extended to account for the effect of small deviations from sphericity.

2.4 Extension to an ellipsoidal particle

2.4.1 Analytical expression of the force acting on the particle due to its non-sphericity

Because blood paltelets have a typical ellipsoidal shape, we tried to extend the previous result to the case of an ellipsoidal particle following [Masoud & Stone 2019]. They present the idea of flattening the surface of the slightly deformed sphere, as it was done for the wall structure, so that Lorentz reciprocal theorem can again be used with known sphere-wall interaction flow fields, leading to the expression of the force acting on the particle, due to its non-sphericity.

Consider the ellipsoid $\mathcal{E}$ defined as a slightly deformed sphere $\mathcal{S}$ following equation (2.77).

$$r|_{\mathcal{E}} = r|_{\mathcal{S}} + \tilde{\varepsilon}(a_1 - a_3)h(\theta, \phi) \tag{2.77}$$

where $a_1 = a_2 = a_3/AR$ are the semi axis of the ellipsoid of aspect ratio $AR = a_3/a_1$ and $h(\theta, \phi)$ is the added radius function ranging from 0 to 1 as shown on figure 2.13, $\tilde{\varepsilon}$ is a small dimensionless parameter and (r, θ, ϕ) are the spherical coordinates with origin taken at the center of the particle.

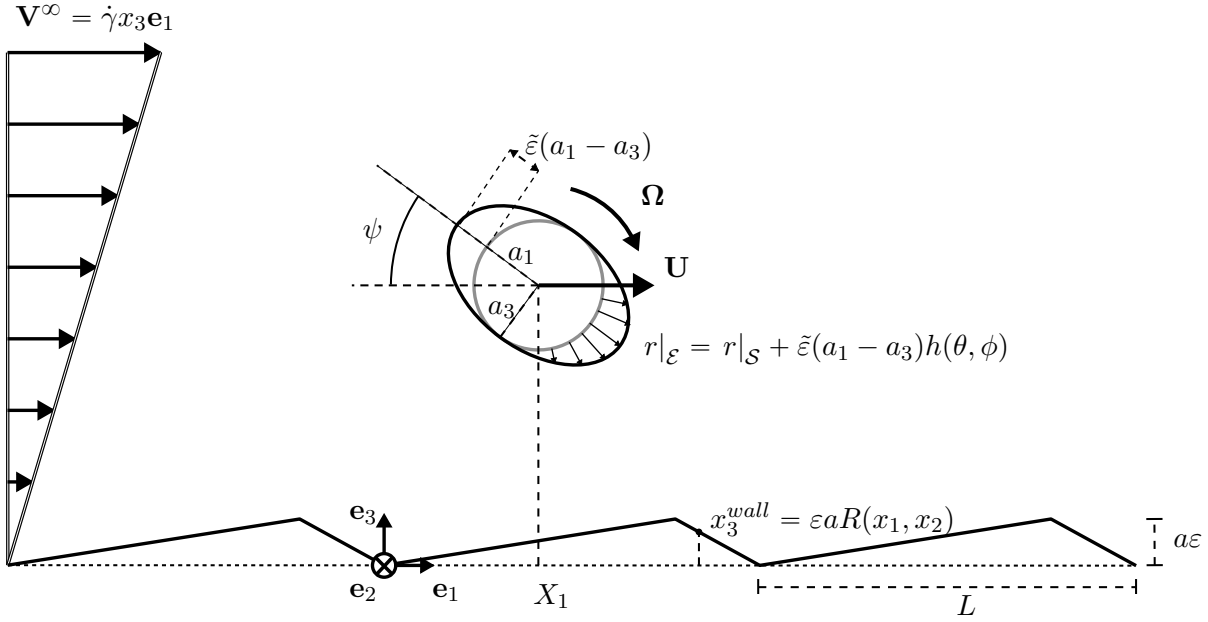

Figure 2.13: Configuration of the flow for an ellipsoidal particle translating, rotating and resisting the ambient shear over structured surfaces.

As for the surface structure, we consider that the force acting on the particle can be decomposed to the contribution of a sphere at order 0 and a contribution of order $\tilde{\varepsilon}$ which is proportional to the

non-sphericity of the particle as:

$$\mathbf{v} = \mathbf{v}^{(0)} + \tilde{\varepsilon}\mathbf{v}^{(1)} + O(\tilde{\varepsilon}^2) \tag{2.78a}$$

$$p = p^{(0)} + \tilde{\varepsilon}p^{(1)} + O(\tilde{\varepsilon}^2) \tag{2.78b}$$

By using a Taylor expansion and the previous decomposition, the domain with an ellipsoidal particle is reduced to the domain with a spherical particle allowing the use of the Lorentz reciprocal theorem.

$$\mathbf{v}|_{\mathcal{E}} = \mathbf{v}|_{\mathcal{S}} + \tilde{\varepsilon}(a_1 - a_3)h(\theta,\phi)\left.\frac{\partial \mathbf{v}}{\partial r}\right|_{\mathcal{S}} + O(\tilde{\varepsilon}^2) \tag{2.79}$$

$$= \left.\mathbf{v}^{(0)}\right|_{\mathcal{S}} + \tilde{\varepsilon}\left.\mathbf{v}^{(1)}\right|_{\mathcal{S}} + \tilde{\varepsilon}(a_1 - a_3)h(\theta,\phi)\left.\frac{\partial \mathbf{v}^{(0)}}{\partial r}\right|_{\mathcal{S}} + O(\tilde{\varepsilon}^2) \tag{2.80}$$

$$= \left.\mathbf{v}^{(0)}\right|_{\mathcal{S}} + \tilde{\varepsilon}\left(\left.\mathbf{v}^{(1)}\right|_{\mathcal{S}} + (a_1 - a_3)h(\theta,\phi)\left.\frac{\partial \mathbf{v}^{(0)}}{\partial r}\right|_{\mathcal{S}}\right) + O(\tilde{\varepsilon}^2) \tag{2.81}$$

The boundary condition on the sphere yields at order 0 and 1 :

$$\left.\mathbf{v}^{(0)}\right|_{\mathcal{S}} = \mathbf{U}^{(0)} + \mathbf{\Omega}^{(0)} \times \mathbf{r} - \mathbf{V}_s^{(0)} \tag{2.82a}$$

$$\left.\mathbf{v}^{(1)}\right|_{\mathcal{S}} = \mathbf{U}^{(1)} + \mathbf{\Omega}^{(1)} \times \mathbf{r} - \mathbf{V}_s^{(1)} - (a_1 - a_3)h(\theta,\phi)\left.\frac{\partial \mathbf{v}^{(0)}}{\partial r}\right|_{\mathcal{S}} \tag{2.82b}$$

Using the same arguments as for the surface structure, we consider only a motion at order 0, so that the motion is constrained to that of a spherical particle translating and rotating over a flat surface. The resulting force will be the one required to hold an ellipsoidal particle to this motion. Also, because we consider an ellipsoidal particle of negligible non-sphericity, the combined effect of the small surface structures of amplitude ε and the small particle non-sphericity of amplitude $\tilde{\varepsilon}$ will be negligible in comparison to the respective independent effect of the surface structure computed previously and the additional effect of the non-sphericity. Therefore, only the motion of the ellipsoidal particle over a flat surface is considered in this development. Contributions of the surface structures previously computed as well as the following contribution of non-sphericity can then be added to obtain the force acting on an ellipsoidal particle immersed in a shear flow over structured surfaces as depicted on figure 2.13. The no-slip boundary condition for the perturbation problem on the surface of the ellipsoid at order one expressed as a slip condition on the surface of the sphere is:

$$\left.\mathbf{v}^{(1)}\right|_{\mathcal{S}} = -(a_1 - a_3)h(\theta,\phi)\left.\frac{\partial \mathbf{v}^{(0)}}{\partial r}\right|_{\mathcal{S}} \tag{2.83}$$

Injecting this boundary condition into the Lorentz theorem (2.22) and using the same adjoint flow of the sedimenting particle, it results the force acting on an ellipsoidal particle over flat surface:

$$U_3^* F_3^{(1)} = (a_1 - a_3)\int_{\mathcal{S}} h(\theta,\phi)\frac{\partial \mathbf{v}^{(0)}}{\partial r}\underline{\underline{\sigma}}^* dS \tag{2.84}$$

The velocity field at order 0 and the adjoint stress field are known and have been detailed in the previous sections. Only the radial shape function $h(\theta,\phi)$ needs to be defined so that the contribution of the non-sphericity of the particle on the vertical force acting on the particle can be computed.

2.4.2 Definition of $h(\theta, \phi)$

First, let us define this function in the coordinate system attached to the particle, meaning the rotation of the particle is not considered yet. The rotation of the particle due to its motion is taken into account in a second time by applying the rotation to the coordinates in which we express the added radius function.

In the coordinate system attached to the ellipsoid, we define a Cartesian coordinate system $(O, \mathbf{e'}_1, \mathbf{e'}_2, \mathbf{e'}_3)$ aligned with the semi-axes a_1, a_2, and a_3 of the ellipsoid as well as a spherical coordinate system $(O, \mathbf{e'}_r, \mathbf{e'}_\theta, \mathbf{e'}_\phi)$ where O is the center of the sphere. In this coordinate system, the points on the surface of the ellipsoid are solutions of equation (2.85).

$$\frac{x_1'^2}{a_1^2} + \frac{x_2'^2}{a_2^2} + \frac{x_3'^2}{a_3^2} = 1 \tag{2.85}$$

The spherical coordinates are related to the Cartesian coordinates by the relations :

$$x_1' = r' \sin(\theta') \cos(\phi') \tag{2.86a}$$
$$x_2' = r' \sin(\theta') \sin(\phi') \tag{2.86b}$$
$$x_3' = r' \cos(\theta') \tag{2.86c}$$

Injecting this expressions in (2.85) allows to express the radius r of the surface of the ellipsoid for each point (θ, ϕ) :

$$\frac{r'^2 \sin^2(\theta') \cos^2(\phi')}{a_1^2} + \frac{r'^2 \sin^2(\theta') \sin^2(\phi')}{a_2^2} + \frac{r'^2 \cos^2(\theta')}{a_3^2} = 1 \tag{2.87}$$

$$r'_{ellipsoid}(\theta', \phi') = \left(\frac{\sin^2(\theta') \cos^2(\phi')}{a_1^2} + \frac{\sin^2(\theta') \sin^2(\phi')}{a_2^2} + \frac{\cos^2(\theta')}{a_3^2} \right)^{-1/2} \tag{2.88}$$

Therefore the expression of the added radius to transform a sphere of radius a_3 to the ellipsoid of radius $r_{ellipsoid}(\theta, \phi)$ is the function $h(\theta, \phi)$ such that:

$$h(\theta', \phi') = r'_{ellipsoid}(\theta', \phi') - a_3 \tag{2.89}$$

In the end the local coordinates x_1', x_2' and x_3' are obtained by performing a rotation of angle ψ around axis $\mathbf{e}_2$ following the particle orientation.

Due to time constraints, these developments could not be fully implemented and tested. Consequently, no definitive conclusion can yet be drawn from the analytical model regarding the interaction between small-amplitude structures and particle non-sphericity. This interaction will instead be examined for finite-amplitude structures using the numerical model presented in the next chapter.

Chapter 3

Numerical modelling of blood platelets dynamics

Contents

From the knowledge of blood and platelets physiology presented in section 1.2, this section presents the development of a numerical model describing the dynamics of blood platelets immersed in an ambient flow. As previously mentioned, the level of details in the platelets model should be sufficient so that their interaction with a structured wall is accurate but a lot of secondary elements of the platelets' physiology must also be discarded to ensure fast simulations. From this considerations, the platelets will be described as rigid ellipsoidal particle in this model. This is in agreement with most of the discrete models of blood platelets that consider platelets as rigid particle, most of the time spherical [Yazdani *et al.* 2017, Wang *et al.* 2020]. The ellipsoidicity of the particle will have an impact on its dynamic and it is also believed to play a role in platelets adhesion, justifying this choice. Also, platelets evolve in a rich environment which is dominated by the presence of red blood cells. In practical applications, interaction between the platelets and the red blood cells are not negligible however considering that the platelets are evolving in a cell free layer once they have marginated, the study of platelets as the only particle is relevant, at least as a first step towards a more comprehensive modelling effort. As the goal of this study is also to provide knowledge on the interactions between platelets adhesion and structured surfaces, restriction of the problem to the study of an isolated platelet is required. From these asumptions, the following model describes the evolution of a single platelet in blood plasma as the evolution of a rigid ellipsoidal particle in a homogeneous incompressible Newtonian fluid.

3.1 Numerical solution for Navier-Stokes equations

The evolution in time and space of the velocity and pressure field of an incompressible homogeneous Newtonian fluid is governed by the Navier-Stokes equations as introduced in section 2.1 and reminded here in their conservative form:

$$\frac{\partial \mathbf{u}}{\partial t} + \nabla \cdot (\mathbf{u} \otimes \mathbf{u}) = \frac{1}{\rho} \nabla \cdot \underline{\underline{\sigma}} + \frac{1}{\rho} \mathbf{f} \tag{3.1a}$$

$$\nabla \cdot \mathbf{u} = 0 \tag{3.1b}$$

and

$$\underline{\underline{\sigma}} = -p \mathbb{1} + \mu \left(\nabla \mathbf{u} + \nabla^T \mathbf{u} \right) \tag{3.2}$$

where $\mathbf{u}$ is the velocity, p is the pressure, ρ is the fluid density, μ is the dynamic viscosity, and $\mathbf{f}$ is the body force. Equation (3.1a) describes how pressure gradients, viscous forces, inertial forces and external forces affect the evolution of the velocity field following conservation of momentum and Equation (3.1b) states that the mass of the fluid in the domain is conserved at all times. To complete the description of a fluid dynamics problem, the geometry of the domain, the boundary conditions, and the initial conditions must be defined and from these, the resulting velocity and pressure field solution of the Navier-Stokes system of equation can be determined.

For simple problems (understand simple geometries, simple boundary conditions and simple initial conditions), analytical solutions can be found. However, for most practical applications, analytical solutions are not available and numerical methods must be used to solve the Navier-Stokes equations. Among the numerical methods available to solve partial differential equations, the Finite Volume Method (FVM) is the most popular for solving CFD problems as the equations to be solved arise from conservation laws and the FVM is naturally conservative.

This is the method implemented in the in-house code YALES2BIO developed at IMAG (UMR 5149) and dedicated to the simulation of blood flows at the micro and the macroscale [Mendez *et al.* 2022]. YALES2BIO is derived from the YALES2 library developed at CORIA (UMR 6614) for massively parallel simulations of combustion in multiphasic flows applications on large unstructured meshes reaching few billions elements. The availability of the code for this project, its relevance regarding the problem considered and the expertise and knowledge of our team on this code all favors its use and the following details on the numerical method are based on the implementation in YALES2BIO.

To be solved numerically, continuous PDE must be discretized both in space and time. The space discretization is done by dividing the domain of the problem in a grid of finite elements. The Finite Volume Method works by integrating the Navier-Stokes equations over these elements and solve the equations for the mean value of velocity and pressure. The time discretization is done by using a finite difference scheme of choice on the time derivative in equation (3.1a) and using a projection method. The next sections provide more details on the numerical method.

3.1.1 Spatial discretization

The continuous domain Ω over which the velocity and pressure fields are searched for is reduced to a discrete set of nodes at which a numerical solution is searched for, and interpolation between these discrete points is performed *a posteriori* to obtain the solution field at any point in the domain. The cost of the simulation and its precision are directly proportional to the number of these nodes. Indeed, if the distance between two discretization nodes is greater than the typical length of a domain or flow structure, it will be poorly resolved (see red arrows in Figure 3.1) and the resulting solution might be a bad description of the initial problem. However, increasing the number of nodes also increases the

required computational power to solve the problem. Therefore, there is a trade-off between numerical cost and precision to be found that dictates the definition of the subset of discretized nodes. These nodes are linked to each other through edges that themselves define faces and volumes which are called elements (Figure 3.1).

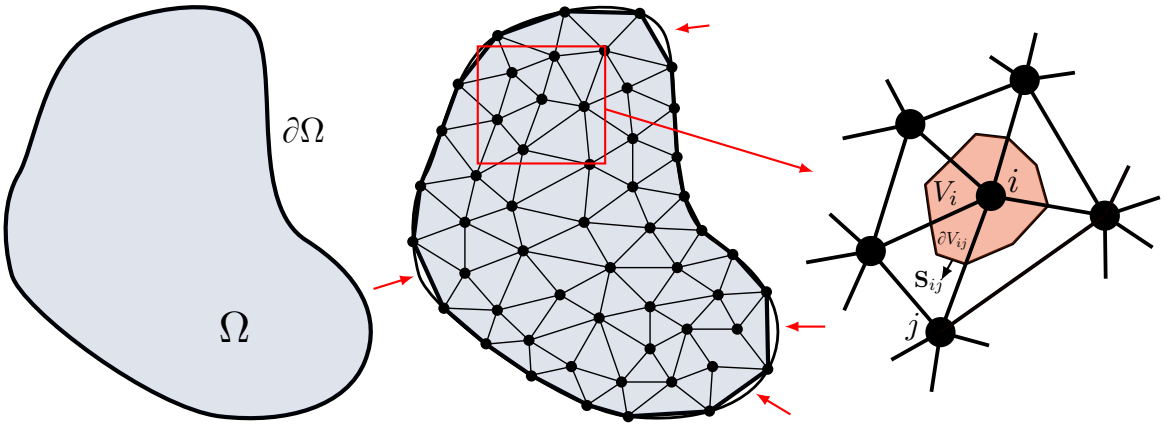

Figure 3.1: Discretization of a continuous 2D domain Ω (left) into a set of nodes, edges and faces (center). Red arrows indicate areas where the quality of the discretization is not sufficient to accurately describe the initial geometry and finer meshing could be required in such areas. (right) Definition of the control volume (CV) V_i in red around the discretization node i, and construction of the dual mesh by taking the center of the edge between node i and j and the barycenter of the element. The portion of the boundary of the CV between node i and j is noted ∂V_{ij} and the vector $\mathbf{S}_{ij}$ is oriented along the normal of the face and has the surface of the face as norm (or length of the edge here in 2D).

From this decomposition of the domain, control volumes (CV) are defined using the discretization nodes, the barycenter of the elements and the middle of the edges as depicted in figure 3.1 (right) forming a dual-mesh. In the FVM, the Navier-Stokes equations in their conservative form are integrated over each CV. Equation (3.3) presents the integration of the momentum equation (3.1a) over a CV V_i and the use of the divergence theorem to express the volume integral as fluxes through its boundary.

$$\int_{V_i} \frac{\partial \mathbf{u}}{\partial t} dV = \int_{V_i} \nabla \cdot \left(-\mathbf{u} \otimes \mathbf{u} + \underline{\underline{\sigma}}\right) + \frac{1}{\rho}\mathbf{f} dV \tag{3.3}$$

$$= \oint_{\partial V_i} \left(-\mathbf{u} \otimes \mathbf{u} + \underline{\underline{\sigma}}\right) \cdot \mathbf{n} dS + \int_{V_i} \frac{1}{\rho}\mathbf{f} dV \tag{3.4}$$

From a Taylor expansion in the vicinity of CV node i, the volume average of the unsteady term and the body forces are approximated form the nodal evaluation of the velocity $\mathbf{u}|_i$ and external force $\mathbf{f}|_i$ respectively such that:

$$\int_{V_i} \frac{\partial \mathbf{u}}{\partial t} dV \approx \tilde{V}_i \frac{\partial \mathbf{u}|_i}{\partial t} \tag{3.5}$$

$$\int_{V_i} \mathbf{f} dV \approx \tilde{V}_i \mathbf{f}|_i \tag{3.6}$$

where $\tilde{V}_i$ is the volume of CV V_i.

This approximation is first-order accurate on a general mesh but becomes second-order accurate if the CV center of mass is located at the CV node. The difference between the center of mass location and the node position is greatly influenced by the gradient of element size because as the dual mesh elements are defined from the middle of the edge between two nodes, increasing abruptly the element

size will lead to great increase in this difference. A smooth variation in mesh size is therefore required to reduce this approximation error.

The boundary ∂V_i of CV V_i is defined by a set of faces (or edges in 2D) ∂V_{ij} such that:

$$\partial V_i = \bigcup_{j \in \mathcal{N}_i} \partial V_{ij} \tag{3.7}$$

where $\mathcal{N}_i$ is the set of nodes connected to node i. From this decomposition, equation (3.4) can be expressed as a sum over each of these faces:

$$\tilde{V}_i \frac{\partial \mathbf{u}|_\mathbf{i}}{\partial t} = \sum_{j \in \mathcal{N}_i} \int_{\partial V_{ij}} \underline{\underline{\Psi}} \cdot \mathbf{n} dS + \frac{1}{\rho} \tilde{V}_i \mathbf{f}|_\mathbf{i} \tag{3.8}$$

where

$$\underline{\underline{\Psi}} = -\mathbf{u} \otimes \mathbf{u} + \underline{\underline{\sigma}} \tag{3.9}$$

It remains to approximate the integral of the flux over the face between two elements. Considering two nodes i and j connected by an edge and separated by face ∂V_{ij}, the flux $\underline{\underline{\Psi}}$ through the face ∂V_{ij} is approximated from its value at nodes i and j:

$$\int_{\partial V_{ij}} \underline{\underline{\Psi}} \cdot \mathbf{n} dS \approx \frac{\underline{\underline{\Psi}}|_i + \underline{\underline{\Psi}}|_j}{2} \mathbf{S}_{ij} \tag{3.10}$$

where $\mathbf{S}_{ij}$ is the vector normal to the face ∂V_{ij} and with norm equal to the area of the face. By definition, $\mathbf{S}_{ij} = -\mathbf{S}_{ji}$, indicating that for two adjacent elements, the quantity through the elements' common face is conserved providing the conservative property of the FVM.

It follows that equation (3.8) becomes:

$$\tilde{V}_i \frac{\partial \mathbf{u}|_\mathbf{i}}{\partial t} = \sum_{j \in \mathcal{N}_i} \frac{\underline{\underline{\Psi}}|_i + \underline{\underline{\Psi}}|_j}{2} \mathbf{S}_{ij} + \frac{1}{\rho} \tilde{V}_i \mathbf{f}|_\mathbf{i} \tag{3.11}$$

This scheme is second-order accurate over regular meshes but becomes only first-order accurate over irregular meshes. A fourth-order accurate scheme is also implemented in YALES2BIO to prevent numerical issues related to this scheme. This fourth-order scheme was used for all the simulations presented in the following chapters, but its derivation requires heavier work which is not detailed here. Interested readers can find more details in [Vantieghem 2011] as well as expressions for the approximation of the gradient, divergence and Laplacian operators similarly based on neighbor nodal values of the considered field.

As a result of these approximations, the problem is now defined by a set of coupled ODE in time where the unknowns are the nodal values of the velocity and pressure fields. Considering the initial values of these variables are known, the next step is to resolve the advancement in time of these approximated fields.

3.1.2 Temporal discretization

3.1.2.1 Projection method

In the case of an incompressible flow, the time evolution of the pressure gradient field is not described by the Navier-Stokes equation (3.1a). It can therefore be viewed as an auxiliary variable ensuring the incompressibility of the flow following the evolution of the velocity field through time. This property is used by the projection algorithm proposed by [Chorin 1968] to ensure the velocity field solution

of equation (3.1a) is also a solution of equation (3.1b) after advancement over a time step Δt. This is done by finding first a solution of the momentum equation that might not be divergence free, by advancing the velocity field from time t^n to an intermediate velocity field $\mathbf{u}^*$, here with a simple Euler forward scheme for simplicity:

$$\frac{\mathbf{u}^* - \mathbf{u}^n}{\Delta t} = \nabla \cdot \left(-\mathbf{u}^n \otimes \mathbf{u}^n - \frac{p^n}{\rho} \mathbb{1} + \nu \left(\nabla \mathbf{u}^n + \nabla^T \mathbf{u}^n \right) \right) + \frac{1}{\rho} \mathbf{f}^n \tag{3.12}$$

This advancement uses an old value of the pressure field p^n, which is not included in the initial method by Chorin but is used in YALES2BIO as it provides better accuracy of the solution [Guermond *et al.* 2006]. However, the velocity at the end of the time step is not related to p^n but rather p^{n+1}, therefore it follows:

$$\frac{\mathbf{u}^{n+1} - \mathbf{u}^*}{\Delta t} = -\frac{1}{\rho} \nabla \left(p^{n+1} - p^n \right) \tag{3.13}$$

Note that summation of equations (3.12) and (3.13) yields the correct advancement of the Navier-Stokes equation over a time step Δt. p^{n+1} being unknown at this point, the final value of the velocity field cannot be found yet. Taking the divergence of equation (3.13) and imposing $\nabla \cdot \mathbf{u}^{n+1} = 0$ allows for the computation of the pressure gradient field that ensures the velocity field $\mathbf{u}^{n+1}$ is divergence free:

$$\Delta \left(p^{n+1} - p^n \right) = \frac{\rho}{\Delta t} \nabla \cdot \mathbf{u}^* \tag{3.14}$$

This equation can be solved numerically using a linear solver adapted to Poisson equations. A Deflated Preconditioned Conjugate Gradient method (DPCG) [Nicolaides 1987] is typically used in YALES2BIO. Once the pressure gradient field is known, it is used to project the predicted velocity into the space of divergence free velocity fields during the correction step to obtain the velocity field solution of both equations (3.1a) and (3.1b) down to the tolerance prescribed for the linear solver of the Poisson equation on the pressure:

$$\mathbf{u}^{n+1} = \mathbf{u}^* - \frac{\Delta t}{\rho} \nabla \left(p^{n+1} - p^n \right) \tag{3.15}$$

Application of these relations on each CV and use of the discretized operators introduced in the previous section allows for the complete description of the space and time evolution of the velocity and pressure fields.

3.1.2.2 Implicit time advancement

The projection and correction steps were introduced previously using a 1st order Euler scheme for simplicity but a 4th order Runge-Kutta scheme is used in the code, providing better convergence and numerical stability. This numerical scheme is stable when the movement of the fluid during one time step is smaller than the typical mesh size. This is ensured in the solver by choosing a time step that depends on the mesh size, as well as the two transport mechanism : advection and diffusion. 2 dimensionless numbers can be defined from these mechanisms which are the Fourier number (Fo) and the Courant-Friedrichs-Lewy number (CFL) as defined by equation (3.16).

$$Fo = \frac{\nu \Delta t}{\Delta x^2} \qquad\qquad CFL = \frac{U \Delta t}{\Delta x} \tag{3.16}$$

For this explicit scheme to be stable, *i.e* the numerical error is not amplified at each time step, the time step is usually chosen so that $Fo < 0.1$ and $CFL < 0.3$ in 3D. This result in an upper limit in the time step which is most of the time dictated by Fourier number in the case of small Reynolds number flows which is our interest in this work. Indeed, Low flow and small length scales are both associated with a dominance of the diffusive terms and therefore the most restrictive transport mechanism is diffusion. This results in very small time steps that prevent the simulation of long physical times.

To alleviate this restriction on the time step due to the highly diffusive properties of the flow, an implicit scheme was used to advance the diffusion terms, after the advection terms are advanced in an explicit manner. Using again a simple Euler forward scheme for the explicit advection advancement and leaving out the diffusive terms in the first place yields :

$$\frac{\hat{\mathbf{u}} - \mathbf{u}^n}{\Delta t} = -\frac{\Delta t}{\rho}\nabla \cdot (\mathbf{u}^n \otimes \mathbf{u}^n + p^n \mathbb{1}) + \frac{1}{\rho}\mathbf{f}^n \tag{3.17}$$

The diffusion terms are then added in an implicit manner.

$$\frac{\mathbf{u}^* - \hat{\mathbf{u}}}{\Delta t} = \nu \left(\nabla \mathbf{u}^* + \nabla^T \mathbf{u}^*\right) \tag{3.18}$$

This requires the resolution of a linear system which can be expressed as follows :

$$\left(\mathbb{1} - \nu \Delta t \left(\nabla + \nabla^T\right)\right) \mathbf{u}^* = \hat{\mathbf{u}} \tag{3.19}$$

Once the predicted velocity field $\mathbf{u}^*$ has been found, typical projection over the divergence free velocity fields space is performed by solving for the pressure field. This implicit scheme alleviates the constraint on the time step due to the diffusive terms allowing to increase the timestep and therefore reduce the number of iteration to reach a given physical time. For this scheme to be usefull, the increase in the simulation time per time step following the need to solve a linear system must be lower than the increase in time step.

To test this, comparison between the explicit scheme and implicit diffusion scheme was performed in a simple configuration. The domain consists of a single square pillar in a periodic box, representing an isolated structure from an infinitely large microstructured surface. Dimensions of the periodic box were $4 \times 4 \times 30\ \mu m^3$ and the dimension of the pillar, placed at the center of the box and at the bottom surface, were $2 \times 2 \times 6\ \mu m^3$. The geometry design and the meshing were performed using the open source software GMSH [Geuzaine & Remacle 2009]. A $1000 s^{-1}$ shear flow is generated in the domain by imposing a translation velocity at the no-slip wall at the top of the box, and no-slip condition is imposed on the bottom and pillar surface. The initial velocity is set to a linear shear flow and simulation is performed during a physical time of $10\,\mu$s. The simulation time is compared between the explicit scheme at $Fo = 0.1$ and the implicit diffusion scheme for different values of Fo ranging from 0.1 to 100.

As shown on figure 3.2, at the same Fourier number of 0.1, the implicit diffusion scheme is slower than the explicit scheme, as the time step and therefore total iteration number are the same, but the resolution of each time step is more costly for the implicit diffusion scheme. For Fourier numbers higher than 0.1, the increase in the time step allowed by the implicit diffusion scheme leads to speeding up of the simulation. The accuracy of the solution for increasing values of the Fourier number using the implicit scheme have also been assessed. The wall shear stress errors compared to the explicit scheme at the top of the pillar all increased with increasing Fo, but remain below 10% error with the explicit scheme for $Fo = 10$, providing a reliable decrease by 10-fold of the simulation time.

When introducing the implicit diffusion scheme, some instabilities were observed in the simulation

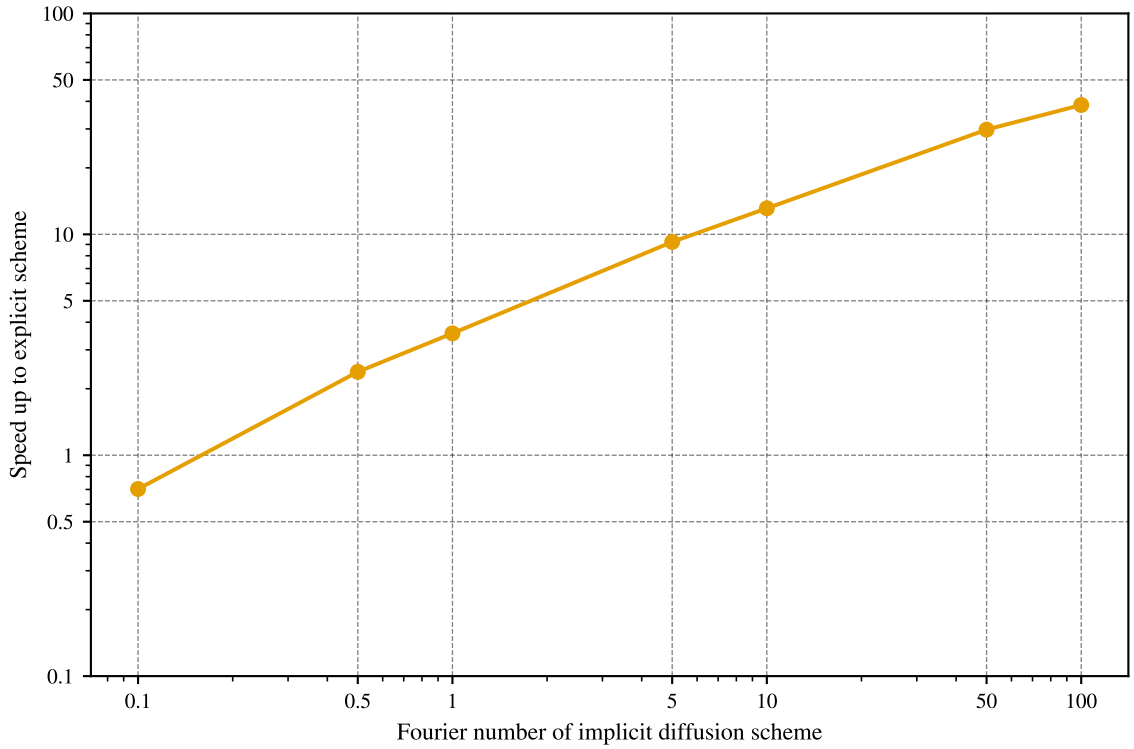

Figure 3.2: Speed up curve comparing the performance of the explicit scheme at $Fo = 0.1$ and the implicit diffusion scheme for values of the Fourier number ranging from 0.1 to 100.

when the flow was driven by an external body force to simulate a pressure driven Poiseuille flow. Near the sharp edge between the pillar side and the bottom wall, the pressure gradient was slowly diverging leading to the full crash of the simulation. This was resolved by using a Laplacian operator taking advantage of the simplicial property of the mesh [Specogna & Trevisan 2011] instead of the default nodal value based operator introduced in [Vantieghem 2011]. The issue as well as its resolution were not perfectly understood, but a proposed explanation was that at the junction between the two walls, some elements had all of their 4 nodes placed on a no-slip boundary leading to singularities using one method but not the other. The simplex based Laplacian operator is therefore used from now on.

3.2 Representation of a particle in a flow

The next step in the modelling of blood platelets dynamics in a flow is to accurately represent a rigid ellipsoidal particle dynamics in the immersed fluid previously resolved. To do so, several methods are available as detailed in [Maxey 2017] ranging from highly accurate direct numerical simulations (DNS) in an arbitrary Lagrangian-Eulerian (ALE) formulation with body fitted mesh, to point particles. Following previous discussion in chapter 1 on the choice of the modelling strategy for platelets, DNS as well as deformable resolved surfaces like the immersed boundary method are too expensive to be used for our problem. On the other hand, point particle lack the accurate description of the geometry of the particle and the way it disturbs the surrounding fluid. Methods are available at intermediate level of description that provide a good trade-off between single particle dynamics description and numerical efficiency.

Methods developed in the context of Stokes flows such as the Boundary Element Method (BEM) [Pozrikidis 2002], are very powerful as they take full advantage of the linearity of the Stokes equations.

However, they require the development of a full BEM solver from scratch, while other particle modelling strategies can be easily added on top of the existing YALES2BIO solver. Also, the need to solve dense systems makes it difficult to apply such method on simulations with multiple particles. Even though this is not a concern for this work, this can be restrictive for future use.

At finite Reynolds number, fictitious domain methods are of great interest as they rely on a fixed Eulerian grid over which the fluid equations are solved, on top of which Lagrangian particles are superimposed. The Lagrangian particles position is evolved on top of the eulerian grid without requiring remeshing such as in ALE, providing greater computational efficiency. For rigid particles, the force coupling method (FCM) and the distributed Lagrange multiplier (DLM) method are available and already extensively used. In both of these methods, the volume defined by the particle is filled with fluid described by the fixed Eulerian grid. To account for the presence of the particle, volumic forces are applied in the region of the particle disturbing the local flow and velocity of the particles are measured from the fluid grid, preceding the evolution of their position in time. The methods differ in the way the forces are applied to the fluid. In the DLM, the velocity of the fluid inside the particle is forced to be that of the rigid body motion of the particle, that is $\mathbf{u} = \mathbf{U} + \mathbf{\Omega} \times \mathbf{r}$ with $\mathbf{r}$ the vector between any point in the particle volume and the particle center of mass, through use of Lagrange multipliers [Glowinski 1999]. On the other hand, the FCM is derived from the multipole representation of particles in Stokes flow regularized over a Gaussian envelope that allows the method to works at Reynolds number up to unity [Lomholt & Maxey 2003]. Both of these methods seem suitable to our need as they allow the description of a rigid particle, and they are both available for ellipsoidal particles. In the end the FCM was chosen as it is initially developed for low Reynolds number flows which are our main target application. Yet, it is usable for Reynolds number up to unity. Also, the recommended mesh size of $\Delta x \approx a/6 - 8$ lies in the range of the mesh size used to represent the wall structures while the DLM method requires $\Delta x \approx a/10$ and up to $\Delta x \approx a/24$ for Reynolds number $20 - 400$ [Maxey 2017]. Additionally, the multipole representation of particles at the base of the FCM splits the contributions of external forces, external torques and resistance to deformation acting on the particles in a way that makes it practical for further extension of the method with adhesive bonds formation.

The main limitation of the FCM lies in the application of the volumic forces over a smoothly decaying Gaussian envelope resulting in a diffuse interface of the particle. Therefore, the resolution of the flow very close to the particle surface, closer than about 0.5 radius, is not very accurate. The lubrication forces are therefore poorly resolved with the FCM potentially resulting in a bad description of the particle near boundaries. This is mitigated by the fact that close to the boundaries, the biological adhesive bonds will dominate the dynamic of the particle and errors in the hydrodynamic description of the particle will be secondary.

The next sections present the theory behind the FCM for a spherical particle, starting from the multipole expansion for Stokes flows and its regularization, towards the extension of the method to ellipsoidal particles as well as its implementation in YALES2BIO and validation especially regarding the effect of the presence of a wall on the particle dynamic.

3.2.1 The multipole expansion

As the FCM is based on the multipole expansion, this method is briefly described here, but interested readers should look into [Kim & Karrila 1991] for an in depth description of this method and particles description in Stokes flows.

The idea behind the multipole expansion is to consider a spherical particle will transmit a given force to the fluid which is unknown *a priori*, and this force is therefore approximated by a Taylor expansion in the vicinity of the particle center of mass. For example, a particle centered at $\mathbf{Y}$ can be

represented by the following forces in a fluid governed by the Stokes momentum equation:

$$0 = -\frac{\partial p}{\partial x_i} + \mu \frac{\partial^2 u_i}{\partial x_j \partial x_j} + F_i \delta(\mathbf{x} - \mathbf{Y}) + F_{ij} \frac{\partial}{\partial x_j} \delta(\mathbf{x} - \mathbf{Y}) + F_{ijk} \frac{\partial^2}{\partial x_j \partial x_k} \delta(\mathbf{x} - \mathbf{Y}) + ... \tag{3.20}$$

where $\delta(\mathbf{x})$ is the Dirac delta function. In this case only the three first terms of the expansion are included and each of the term is related to different properties of the particle, so as more terms are included, the method becomes more accurate. Here the three first terms included are called the monopole F_i, dipole F_{ij} and quadrupole F_{ijk} and they are respectively related to the external forces acting on the particle, the external torques and incompressiblilty of the particle, and the finite size of the particle [Kim & Karrila 1991]. Note that if only the force monopole is included in the expansion, the method reduces to the point particle method.

One strength of this method is that it can be easily computed by using the linearity of the Stokes equation. The disturbance flow resulting from each of the expansion term can be obtained analytically before being summed up such that $\mathbf{u} = \sum_n \mathbf{u}^n$ and :

$$-\frac{\partial p^1}{\partial x_i} + \mu \frac{\partial^2 u_i^1}{\partial x_j \partial x_j} = -F_i \delta(\mathbf{x} - \mathbf{Y}) \tag{3.21a}$$

$$-\frac{\partial p^2}{\partial x_i} + \mu \frac{\partial^2 u_i^2}{\partial x_j \partial x_j} = -F_{ij} \frac{\partial}{\partial x_j} \delta(\mathbf{x} - \mathbf{Y}) \tag{3.21b}$$

$$-\frac{\partial p^3}{\partial x_i} + \mu \frac{\partial^2 u_i^3}{\partial x_j \partial x_j} = -F_{ijk} \frac{\partial^2}{\partial x_j \partial x_k} \delta(\mathbf{x} - \mathbf{Y}) \tag{3.21c}$$

$$\vdots$$

The starting point in solving these equations is the solution to equation (3.21a) which is called the Green's Function for the Stokes equation, that is the response of the Stokes equation to a point force. As the equation is linear, it is natural to express the relation between the point force and the fluid velocity via a matrix as in equation (3.22).

$$u_i = O_{ij} F_j \tag{3.22}$$

This matrix is called the Oseen tensor and its expression is given by [Kim & Karrila 1991]:

$$O_{ij} = \frac{1}{8\pi a} \left(\frac{\delta_{ij}}{r} + \frac{x_i x_j}{r^3} \right) \tag{3.23}$$

The solutions to the higher order terms of the expansion are obtained by differentiation of the Oseen tensor.

These analytical solutions are available in very simple geometries but when a more complex geometry is considered, numerical resolution of these equations is required. This is also true if the Reynolds number is not perfectly zero, meaning that the linear decomposition and summation of the expansion terms is not possible and the whole equation (3.20) must be solved at once also including inertia terms.

3.2.2 Regularization of the multipole expansion

Moreover, numerical solutions of a singular point force is often tricky [Maxey & Patel 2001] and regularization of the singular force distribution of the multipole expansion over a finite size Gaussian envelope is the solution proposed by the FCM. The equation for the presence of a single particle in a

Stokes flow now becomes, if only the monopole is included for simplicity:

$$0 = -\frac{\partial p}{\partial x_i} + \mu \frac{\partial^2 u_i}{\partial x_j \partial x_j} + F_i \Delta(\mathbf{x} - \mathbf{Y}) \tag{3.24}$$

with

$$\Delta(\mathbf{x}) = (2\pi\sigma^2)^{-3/2} exp\left(-\frac{\mathbf{x}^2}{2\sigma^2}\right) \tag{3.25}$$

and σ is the width parameter of the Gaussian.

The analytical expression for the flow field generated by this regularized point force will be useful later, so it is given here. Similarly to the singular point force case, an Oseen tensor can be derived relating the smoothed point force and the resulting velocity field as in (3.22). Its expression is provided by equation (3.26) and details of its computation can be found in [Lomholt 2001].

$$\tilde{O}_{ij} = \frac{1}{8\pi a}\left(\frac{\delta_{ij}}{r} + \frac{x_i x_j}{r^3}\right)\mathrm{erf}\left(\frac{r}{\sqrt{2}\sigma}\right) + \left(\delta_{ij} - \frac{3x_i x_j}{r^2}\right)\left[\frac{\sigma^2}{8\pi\mu r^3}\mathrm{erf}\left(\frac{r}{\sqrt{2}\sigma}\right) - \frac{\sigma^4}{2\mu r^2}\Delta(\mathbf{x},\sigma)\right] \tag{3.26}$$

Two question now arise: how to choose the width parameter σ of the Gaussian and how to measure the velocity of the particle ? Answer to these questions are the closing elements of the FCM and are presented in the next section.

3.2.3 The Force Coupling Method

The ways of measuring particle velocity and Gaussian envelope size are actually related. Indeed, the measurement of the particle velocity is chosen first, and it follows that there is only one correct way to apply external forces that will lead to the measurement of the correct velocity in a problem for which we know the theoretical velocity, such as a particle sedimenting under gravity in a quiescent unbounded fluid. A similar work is done for the matching between the theoretical value of the angular velocity of a particle when subjected to a contant torque in a quiescent unbounded fluid.

3.2.3.1 Monopole

Two different ways to measure the particle velocity are quite intuitive and the Gaussian size for each of them is briefly presented in the following section: taking the particle velocity as the underlying fluid velocity at the center of mass of the particle or taking the average velocity of the fluid in the particle volume through integration over the Gaussian envelope. Extensive details of these calculations can be found in [Lomholt 2001].

First we consider the measurement of the particle velocity $\mathbf{U}$ to be equal to that of the fluid velocity $\mathbf{u}$ at the center of mass of the particle $\mathbf{Y}$. The monopole is equal to the external forces acting on the particle, therefore in the case of particle sedimenting in a quiescent unbounded fluid under gravity, only the gravity force $\mathbf{F}_g$ is considered. Therefore, the fluid velocity at the center of mass of the particle is obtained from the evaluation of the Oseen tensor (3.26) at this same location, resulting from the application of a smoothed point force $\mathbf{F}_g$ following equation (3.22):

$$\mathbf{U} = \mathbf{u}(\mathbf{Y}) = \underline{\underline{\tilde{O}}}(\mathbf{Y})\mathbf{F}_g \tag{3.27}$$

The relation between the applied external force and the expected velocity of the particle $\mathbf{U}^{th}$ is given by the Stokes drag as the gravitational force balances the drag force:

$$\mathbf{U}^{th} = \frac{\mathbf{F_g}}{6\pi\mu a} \tag{3.28}$$

Therefore, by stating that the measured velocity $\mathbf{U}$ in equation (3.27) must be equal to the theoretical velocity $\mathbf{U}_{th}$ given by equation (3.28), and after evaluation of the Oseen tensor, equation (3.26), at the center of mass of the particle, we obtain a relation between the width of the Gaussian function σ and the particle radius a

$$6\pi\mu a \frac{1}{3\pi\mu\sigma}\frac{1}{\sqrt{2\pi}}\delta_{ij}U_j^{th} = U_i \tag{3.29}$$

and after simplifications we get the width of the Gaussian function required so that the application of the external force yields the expected sedimentation velocity when measured at the center of mass of the particle:

$$\sigma = \frac{a}{\sqrt{\pi/2}} \tag{3.30}$$

Now for the case where the particle velocity is measured as the average of the fluid velocity over the Gaussian function such that :

$$\mathbf{U} = \int_\Omega \mathbf{u}(\mathbf{x})\Delta(\mathbf{x}-\mathbf{Y})d\mathbf{x} \tag{3.31}$$

Similarly, the fluid veleocity is obtained from the Oseen tensor such that :

$$\mathbf{U} = \int_\Omega \underline{\underline{\tilde{O}}}(\mathbf{x}-\mathbf{Y})\mathbf{F}_g(\mathbf{x})\Delta(\mathbf{x}-\mathbf{Y})d\mathbf{x} \tag{3.32}$$

$$= 6\pi\mu a\mathbf{U}^{th}\int_\Omega \underline{\underline{\tilde{O}}}(\mathbf{x}-\mathbf{Y})\Delta(\mathbf{x}-\mathbf{Y})d\mathbf{x} \tag{3.33}$$

Use of Fourier Transform and convolution theorem allows to compute this integral, details can again be found in [Lomholt 2001], and the result is given by:

$$\mathbf{U} = \frac{a\mathbf{U}^{th}}{\sqrt{\pi}\sigma} \tag{3.34}$$

Once again, searching σ so that $\mathbf{U} = \mathbf{U}^{th}$ yields the correct width of the Gaussian function:

$$\sigma = \frac{a}{\sqrt{\pi}} \tag{3.35}$$

From there it appears that there are multiple valid ways to measure the particle velocity and corresponding width of the Gaussian function. However, [Maxey & Patel 2001] showed that even though the velocity field far from the particle is accurately reproduced by both velocity measurement and Gaussian width couple, the flow in the vicinity of the particle was best approximated for higher values of a/σ. Following this observation, the method of particle velocity measurement which is used in the FCM is to average the fluid velocity over the Gaussian function using equation (3.31), and using the appropriate width parameter $\sigma = a/\sqrt{\pi}$ to ensure matching of the particle sedimenting velocity in unbounded quiescent fluid.

Only the force monopole was included in this case, which means that only the external force acting on the particle have been taken into account. One consequence of the regularization of the singular forces over a finite size Gaussian is that the finite size of the particle is also taken into account whereas the finite size of the particle would require inclusion of a force quadrupole in the singular multipole expansion.

3.2.3.2 Dipole

Addition of a dipole is also possible with the FCM which enables to consider external torques acting on the particle as well as incompressibility of the particle. Indeed, the particle is represented by the

underlying fluid. However, this fluid is able to deform, so compensation for this local fluid deformation is required to accurately represent the behavior of a rigid particle. This dipole will be regularized in the same manner as the monopole (i.e. with the same gaussian function) but the width parameter of the gaussian for the dipole will not be the same as the one for the monopole.

The dipole amplitude $\underline{\underline{F}}$ can be divided into a symmetric and an antisymmetric part to outline better what it represents.

The antisymmetric part of $\underline{\underline{F}}$, labeled $\underline{\underline{G}}$ and called the Rotlet or antisymmetric torque dipole, is the resultant of all external torques acting at the center of mass of the particle, just like the monopole amplitude is linked to external forces. The relation between the external torques $\mathbf{T}$ and the dipole amplitude is given by equation (3.36) [Kim & Karrila 1991].

$$G_{ij} = \frac{1}{2}\varepsilon_{ijk}T_k \tag{3.36}$$

where $\underline{\underline{\underline{\varepsilon}}}$ is the Levi-Civita symbol.

This antisymmetric dipole will this time be spread over the gradient of the Gaussian function following the replacement of the singular Dirac with the smooth Gaussian in equation (3.21b) but the width of the Gaussian is expected to be different from the Gaussian width for the monopole. Indeed, the width parameter for the monopole Gaussian was chosen so that the measured linear velocity of a particle subjected to an external force matches the velocity predicted by the Stokes drag law. Because the dipole is not related to external force but rather external torques, the width parameter will be chosen so that the angular velocity $\mathbf{\Omega}$ of a particle subjected to an external torque $\mathbf{T}$ matches the angular velocity predicted by the Stokes drag law:

$$\mathbf{T} = 8\pi\mu a^3\mathbf{\Omega}^{th} \tag{3.37}$$

Similarly to the measureement of the linear velocity by averaging over the monopole Gaussian, the angular velocity of the particle is obtained by averaging the fluid vorticity ω over the dipole Gaussian of parameter σ_d:

$$\mathbf{\Omega} = \int_\Omega \omega(\mathbf{x})\Delta_d(\mathbf{x}-\mathbf{Y})d\mathbf{x} \tag{3.38}$$

Following a similar approach as for the monopole, equating the measured velocity and the theoretical one leads to the relation between the dipole Gaussian width parameter σ_d and the radius of the particle a so that the angular velocity of the particle subjected to an external torque is equal to the velocity predicted by Stokes drag law:

$$\sigma_d = \frac{a}{\sqrt[3]{6\sqrt{\pi}}} \tag{3.39}$$

The symmetric part of $\underline{\underline{F}}$, noted $\underline{\underline{S}}$ and called the Stresslet or symmetric dipole, is linked to the incompressibility of the particle. We have seen that the linear (respectively angular) velocity of the particle is linked to the underlying velocity (respectively vorticity) of the fluid. Similarly, the particle deformation is linked to the underlying strain rate of the fluid and because we expect the particle to be rigid, we want to ensure the underlying rate of strain is 0.

To do so we have to measure at each time step the average rate of strain at the particle location, using integration over the dipole Gaussian function:

$$\tilde{E}_{ij} = \int_\Omega E_{ij}(\mathbf{x})\Delta_d(\mathbf{x}-\mathbf{Y})d\mathbf{x} \tag{3.40}$$

with $\underline{\underline{E}} = \frac{1}{2}\left(\nabla\mathbf{u} + \nabla^T\mathbf{u}\right)$.

If nothing is done, and the underlying fluid strain rate is not zero, this average value will not be zero. From that, [Kim & Karrila 1991] gives the relation between the measured rate of strain and the stresslet required to ensure the rigidity of a spherical particle in an unbounded pure straining flow :

$$S_{ij} = \frac{20}{3}\pi\mu a^3 \tilde{E}_{ij} \tag{3.41}$$

However, in more general cases, the flow is not purely extensional, and the domain is bounded, therefore the exact value of the stresslet required to ensure 0 strain rate inside the particle is not known. An iterative process is then used by incrementing the stresslet step by step until the measured rate of strain is effectively zero, or actually below a given threshold as exact value of 0 is not achievable numerically. The step size is chosen to be that of the stresslet for the unbounded sphere in pure extensional force, which is considered to be a good first approximation of the real stresslet. The full algorithm is given by [Lomholt *et al.* 2002]:

1. Measure the averaged rate of strain $\tilde{E}$ over the dipole Gaussian following equation (3.40).
2. If its norm $||\tilde{E}|| = \sqrt{\tilde{E}_{ij}\tilde{E}_{ij}}$ is above a given threshold ε_s, the stresslet must be incremented using (3.41): $S_{ij}^{n+1} = S_{ij}^{n} + \frac{20}{3}\pi\mu a^3 \tilde{E}_{ij}$
3. Compute the velocity field resulting from this new stresslet and loop back to step 1.
4. Once $||\tilde{E}|| < \varepsilon_s$ the stresslet ensuring the rigidity of the particle for this configuration has been found. Move on to the next time step.

As mentioned in [Lomholt & Maxey 2003], this stresslet is supposed to have zero trace, as its trace is equal to the divergence of the fluid velocity, which is expected to be zero. Yet, direct implementation of this algorithm lead to numerical instabilities using our prediction-correction scheme related to the stresslet trace which was growing up to the crash of the simulation. This was a result of increasing the stresslet with a strain rate field which was not at perfectly zero trace, as the divergence free property of the velocity field is ensured up to the threshold given to the Poisson solver. In the end, the stresslet trace was increasing as residuals were summed over iterations, resulting in the generation of additional divergence, eventually leading to the crash of the simulation. To ensure the stresslet is correctly with zero trace, the strain rate field used to compute the stresslet was the measured strain rate field $\tilde{E}$ to which $\frac{1}{3}Tr(\tilde{E})\delta_{ij}$ was removed. This resulted in stable simulations, while the results remained the same.

To sum things up, the fluid flow around an immersed FCM particle for a Newtonian incompressible fluid is governed by equations

$$\rho\frac{\partial u_i}{\partial t} + \rho\frac{\partial u_i u_j}{\partial x_j} = -\frac{\partial p}{\partial x_i} + \mu\frac{\partial^2 u_i}{\partial x_j \partial x_j} + F_i\Delta(\mathbf{x}-\mathbf{Y},\sigma) + (G_{ij}+S_{ij})\frac{\partial}{\partial x_j}\Delta(\mathbf{x}-\mathbf{Y},\sigma_d) \tag{3.42a}$$

$$\frac{\partial u_i}{\partial x_i} = 0 \tag{3.42b}$$

with

$$\Delta(\mathbf{x},\sigma) = (2\pi\sigma^2)^{-3/2} exp\left(-\frac{\mathbf{x}^2}{2\sigma^2}\right) \tag{3.43}$$

$$F_i = F_i^{ext} \tag{3.44}$$

$$G_{ij} = \frac{1}{2}\varepsilon_{ijk}T_k^{ext} \tag{3.45}$$

$$\sigma = \frac{a}{\sqrt{\pi}} \tag{3.46}$$

$$\sigma_d = \frac{a}{\sqrt[3]{6\sqrt{\pi}}} \tag{3.47}$$

and S_{ij} are found iteratively to ensure the norm of the averaged rate of strain $\tilde{E}$ is below the given threshold ε_s following :

$$\tilde{E}_{ij} = \int_\Omega E_{ij}(\mathbf{x})\Delta_d(\mathbf{x}-\mathbf{Y})d\mathbf{x} \tag{3.48}$$

Once the flow field is computed, the linear and angular velocity of the particle are then obtained by averaging of the velocity and vorticity over the respective Gaussian functions:

$$\mathbf{U} = \int_\Omega \mathbf{u}(\mathbf{x})\Delta(\mathbf{x}-\mathbf{Y})d\mathbf{x} \tag{3.49}$$

$$\mathbf{\Omega} = \int_\Omega \omega(\mathbf{x})\Delta_d(\mathbf{x}-\mathbf{Y})d\mathbf{x} \tag{3.50}$$

These velocities are used to update the position of the center of mass $\mathbf{Y}$ and orientation angles θ of the particle using first order schemes:

$$\mathbf{Y}^{n+1} = \mathbf{Y}^n + \mathbf{U}\Delta t \tag{3.51}$$

$$\theta^{n+1} = \theta^n + \mathbf{\Omega}\Delta t \tag{3.52}$$

3.2.3.3 Extension to ellipsoidal particles

The extension of the FCM to ellipsoidal particles is quite straight forward. The idea is to change the shape of the spherically symmetric Gaussian to a new Gaussian of ellipsoidal shape. This is done by introducing 3 Gaussian width parameters instead of 1, labeled σ_1, σ_2 and σ_3, defining the width of the Gaussian in the principal axis of the ellipsoid x_1, x_2, x_3. The Gaussian is now defined in the particle coordinate system by equation (3.53).

$$\Delta(\xi,\sigma) = \frac{(2\pi)^{-3/2}}{\sigma_1\sigma_2\sigma_3}\exp\left[-\frac{1}{2}\left(\frac{\xi_1^2}{\sigma_1^2}+\frac{\xi_2^2}{\sigma_2^2}+\frac{\xi_3^2}{\sigma_3^2}\right)\right] \tag{3.53}$$

It appears that the previous relations between the particle radius and the Gaussian width parameter still holds between a particle semi-axis a_i in direction $\mathbf{e}_i$ and the width parameters σ_i and $(\sigma_d)_i$ [Liu *et al.* 2009], and therefore we have the relations:

$$\sigma_i = \frac{a_i}{\sqrt{\pi}} \tag{3.54}$$

$$(\sigma_d)_i = \frac{a_i}{\sqrt[3]{6\sqrt{\pi}}} \tag{3.55}$$

Equation (3.53) holds in the coordinate system attached to the particle as it rotates, however after rotation, the principal axes of the ellipsoid are not anymore aligned with the global coordinate system and a change of basis operation is required to obtain the expression of the Gaussian in the global coordinate given by equation 3.56.

$$\Delta(\mathbf{x},\sigma) = \frac{(2\pi)^{-3/2}}{\sigma_1\sigma_2\sigma_3}\exp\left[-\frac{1}{2}\mathbf{x}^T\underline{\underline{Q}}\begin{pmatrix}\sigma_1^{-2} & 0 & 0\\ 0 & \sigma_2^{-2} & 0\\ 0 & 0 & \sigma_3^{-2}\end{pmatrix}\underline{\underline{Q}}^T\mathbf{x}\right] \tag{3.56}$$

The orientation matrix $\underline{\underline{Q}}$ is derived from a unit quaternion $q = (q_0, q_1, q_2, q_3) = (q_0, \mathbf{q})$ which tracks the orientation of the particle over time and is given by equation (3.57) [Mignon & Mendez 2021].

$$\underline{\underline{Q}} = 2 \begin{pmatrix} q_0^2 + q_1^2 - \frac{1}{2} & q_1 q_2 - q_0 q_3 & q_1 q_3 + q_0 q_2 \\ q_1 q_2 + q_0 q_3 & q_0^2 + q_2^2 - \frac{1}{2} & q_2 q_3 - q_0 q_1 \\ q_1 q_3 - q_0 q_2 & q_0^2 q_1^2 + q_2^2 q_3^2 & q_0^2 + q_3^2 - \frac{1}{2} \end{pmatrix} \tag{3.57}$$

The advantage of using a unit quaternion over 3 orientation angles as introduced in equation (3.52) is that the time evolution of 3 independent angles can lead to singularities [Mignon & Mendez 2021].

The unit orientation quaternion is defined as follows:

$$q = \cos\frac{\theta}{2} + \sin\frac{\theta}{2}\mathbf{u} \tag{3.58}$$

where for any vector $\mathbf{v}$, $\tilde{v} = q\mathbf{v}\bar{q}$ is the image of vector $\mathbf{v}$ after rotation by an angle θ around axis $\mathbf{u}$, with $\bar{q} = (q_0, -\mathbf{q})$ is the conjugate of quaternion q.

The evolution through time of the orientation quaternion is governed by equation (3.59).

$$\frac{d\mathbf{q}}{dt} = \frac{1}{2}\mathbf{\Omega}\,\mathbf{q} \tag{3.59}$$

3.3 Implementation of the Force Coupling Method in YALES2BIO

In the YALES2BIO solver the FCM has been implemented on the basis of an existing solver developed to study the dynamics of red blood cells using an immersed boundary method (IBM). The computational elements of the immersed boundary method are not used in our case, however the already present data structures and parallelization algorithms are used and applied to the FCM. Also, the IBM relies on the displacement of a set of Lagrangian nodes forming a surface, on top of the Eulerian fluid grid, which will be used for visualization of the FCM particles.

The monopole and dipole Gaussians are defined over the Eulerian grid while all orther particle related informations are stored at the level of a Lagrangian particle, such as monopole and dipole amplitudes, particle center of mass or orientation quaternion. Initial position, initial orientation and semi-axes of the particle can be defined in the input file of a simulation case by using appropriately defined keywords. Inclusion of the stresslet iterative algorithm or not is also governed by an appropriate keyword, as well as convergence threshold ε_s and a maximum number of subiterations N_{sub}^{max}.

During each simulation time step, the Gaussian fields are computed based on particle center of mass and orientation quaternion following (3.56), (3.54) and (3.55). The gradient of the dipole Gaussian is obtained analytically by derivation of (3.56) to limit numerical errors. The monopole, antisymmetric dipole and the stresslet from the previous time-step are all regularized over the corresponding Gaussian function and summed yielding the external force field to be included in the Navier-Stokes equation. These equations are then solved following the prediction-correction algorithm introduced in 3.1.2.1, with a Runge-Kutta 4 scheme for the advection and an implicit diffusion scheme for the diffusion as discussed previously. 4th order scheme is used for the spatial operators. From this first computed flow field, the iterative process on the stresslet begins and subiterations until the average rate of strain is below the prescribed threshold is performed. After convergence of the stresslet, the particle velocity and angular velocity are measured following (3.49) and (3.50), and particle center of mass and orientation quaternion are updated with a 1st order explicit scheme. This scheme can lead to errors in the estimation of particle trajectory, however because the time step will be very small even with the implicit diffusion scheme, this error has been verified to be negligible.

3.4 Validation of the Force Coupling Method

First of all, three fundamental cases are used to validate the implementation of the three core components of the FCM for a spherical particle: the monopole, the anti-symmetric dipole and the symmetric dipole. These are validated independently by comparing simulated results and analytical results for the velocity of a sedimenting particle in unbounded fluid, angular velocity of a particle subjected to an external torque in unbounded fluid and value of the stresslet for a particle immersed in an unbounded extensional flow.

Following this fundamental validation, more practical simulations for which reference solutions are available are performed for ellipsoidal particles. In the first place, stationary simulations were used to compare the present implementation of the FCM against implementation by [Liu *et al.* 2009] as well as DNS simulations results they provide. Similar stationary simulations are performed to assess the validity of the FCM depending on the proximity of the particle with a plane wall using results from [Hsu & Ganatos 1994]. In the end, simulation of the full dynamic of a freely moving particle are performed, first in an unbounded shear flow by reproducing the Jeffery's orbits [Jeffery 1922]. Finally the dynamics of a particle immersed in a shear flow close to a flat surface is simulated and compared to results from [Hsu & Ganatos 1994] and [Mody & King 2005].

Throughout these validation cases, the effect of the mesh size, time step size (related to the Fourier Number) as well as aspect ratio of the ellipsoidal particle on the accuracy of the results are discussed leading to the definition of the validity range of the method before its application to the simulation of particle interaction with structured surfaces.

3.4.1 Implementation of the monopole

The validation case for the implementation of the monopole is the case of a spherical particle sedimenting under a constant gravitational force in an unbounded quiescent fluid. This is the configuration for which the width parameter of the monopole Gaussian has been calibrated for (see section 3.2.3.1). The evolution of the particle velocity in the direction of gravity U_p over time is given by the Basset-Boussinesq-Oseen equation (3.60) [Parmar *et al.* 2011] where the external forces acting on the particle are balanced by the hydrodynamic drag given by the Stokes drag law, the added mass of displaced fluid as well as viscous history forces.

$$m_p \frac{dU_p}{dt} = \underbrace{-6\pi\mu a U_p}_{\text{Stokes drag}} - \underbrace{\frac{2}{3}\rho\pi a^3 \frac{dU_p}{dt}}_{\text{Added mass}} + \underbrace{6\rho a^2\sqrt{\pi\nu}\int_0^t \frac{dU_p(\tau)/d\tau}{\sqrt{t-\tau}}d\tau}_{\text{Basset history force}} + F^{ext} \tag{3.60}$$

with m_p the mass of the particle with density ρ_p and radius a. μ, ν and ρ are the fluid dynamic viscosity, kinematic viscosity and density.

In the asymptotic regime, the terms which depends on particle acceleration vanish and only the Stokes drag law balances external forces so that the asymptotic velocity of the particle is given by relation (3.61).

$$U^{\infty} = \frac{F^{ext}}{6\pi\mu a} \tag{3.61}$$

For the case of the sedimenting particle under gravity, the external force is given by the sum of gravity force and buoyancy force resulting from density differences between the particle and the fluid

$$F^{ext} = -\frac{4}{3}\pi a^3(\rho_p - \rho)g \tag{3.62}$$

with g the gravitational acceleration.

For the Force Coupling Method, [Wang *et al.* 2018] states that the monopole F balances the added mass, drag and history forces therefore substituting F in equation (3.60) leads to the relation (3.63) between the monopole and the external forces acting on the particle.

$$m_p \frac{dU_p}{dt} = -F + F_{ext} \tag{3.63}$$

Also, if the Reynolds number is very small and inertial forces can be neglected, the inertia of the particle can also be neglected, therefore the monopole is equal to the external forces acting on the particle:

$$F = F^{ext} = -\frac{4}{3}\pi a^3(\rho_p - \rho)g \tag{3.64}$$

The simulation with the FCM is performed using a spherical particle of radius $a = 1\,\mu m$ and density $\rho_p = 2000\,kg.m^{-3}$ placed at the center of a cubic box of width $200a$ filled with water ($\rho = 1000\,kg.m^{-3}$, $\mu = 1\,mPa.s$). The mesh has a typical size of $\Delta x = a/3$ in the vicinity of the particle, as at least 2 elements per particle radius are required when only the monopole term is present [Liu *et al.* 2009], and a coarser mesh is set far from the particle where the flow is quiescent. The monopole (3.64) is applied in the vertical direction $\mathbf{e_3}$ and no dipole contribution is included. From this choice of parameters, the theoretical settling velocity is $U^\infty = 2.18\,\mu m/s$, so that the particle Reynolds number is small (here $Re = aU^\infty/\nu = 2.18 \times 10^{-6}$). The particle is free to move, and the simulation is performed until the velocity of the particle has converged to its settling value.

For this particular case, using a mesh size of $\Delta x = a/3$ and Fourier number $Fo = 10$ yielded a time-step of about $\Delta t \approx 1.1\,\mu s$ to ensure numerical stability of the fluid resolution while the characteristic timescale related to the acceleration of the particle is $\tau = \frac{m_p}{6\pi\mu a} \approx 0.44\,\mu s$ meaning it is poorly resolved using this time step. Therefore, the Fourier number and the time step were reduced to $Fo = 1$ and $\Delta t = 0.11\,\mu s$ for this first test, ensuring the transient evolution of the particle velocity is well resolved.

The time evolution of the particle velocity computed from the FCM simulation is compared to a numerical solution of the ODE (3.60) in figure 3.3. Details on the numerical resolution of this ODE are provided in appendix A.1.

We can observe a very good agreement between the FCM simulation and the theory both for the transient evolution of the velocity and for the asymptotic value which is reached with 0.13% of error, confirming the correct implementation of the monopole.

3.4.2 Implementation of the anti-symmetric dipole

A similar work is done for the case of the particle subjected to an external torque in an otherwise quiescent fluid. The particle and domain configuration are the same, except this time the monopole is zero and a constant external torque is applied to the particle. The expected asymptotic angular velocity of the particle is once again given by Stokes' drag law $\mathbf{\Omega}^\infty = \mathbf{T}^{ext}/8\pi\mu a^3$.

The temporal evolution of the angular velocity is much less discussed in the literature than the translational case and, to the best of our knowledge, only [Feuillebois & Lasek 1978] provides a clear relation between the torque and the angular velocity of a particle with inclusion of history terms. They showed that the angular velocity $\Omega(t)$ of the particle subjected to an external torque $T^{ext} = -T_h$ is solution of equation (3.65).

$$\begin{aligned} T_h(t) = -8\pi\mu a^3\Big(\Omega(t) + \frac{a}{3\sqrt{\nu\pi}}\int_0^t \frac{d\Omega/d\tau}{\sqrt{(t-\tau)}}d\tau \\ - \frac{1}{3}\int_0^t \frac{d\Omega}{d\tau}\exp(\nu(t-\tau)/a^2)\mathrm{erfc}(\sqrt{\nu(t-\tau)/a^2})d\tau\Big) \end{aligned} \tag{3.65}$$

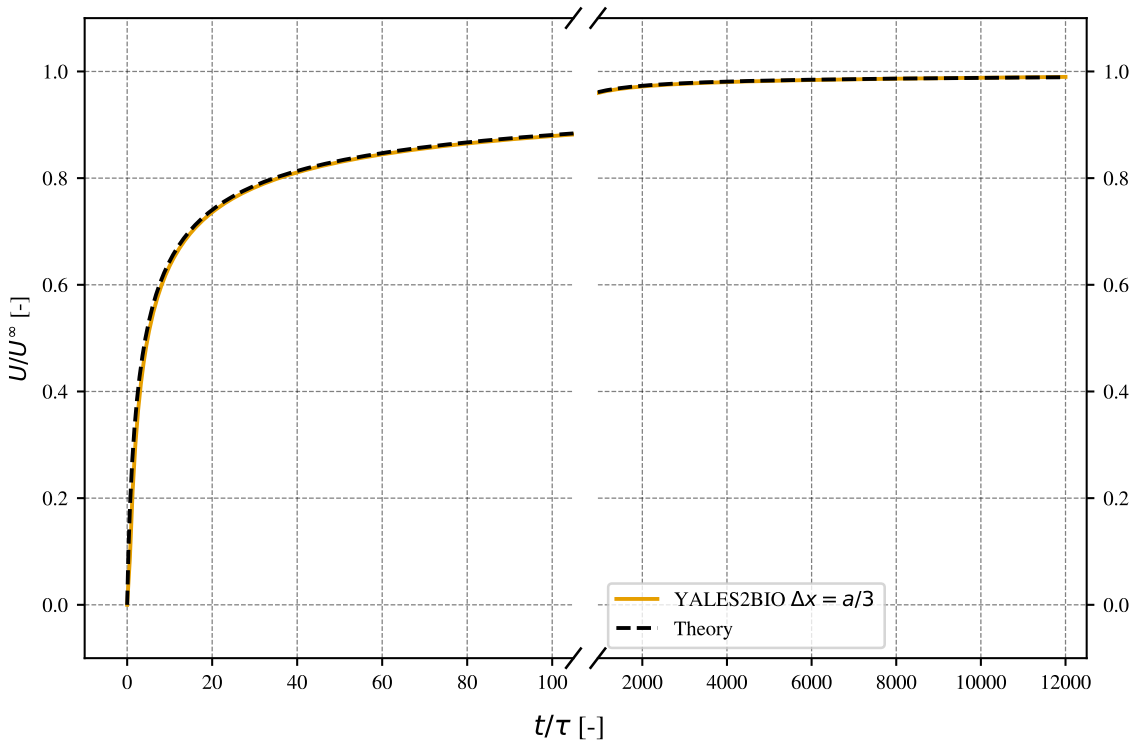

Figure 3.3: Evolution of the velocity of a spherical particle subjected to a constant gravitational force in quiescent fluid over time. (– – –) Theory given by a numerical solution of equation (3.60) detailed in appendix A.1, (——) Numerical simulation using the FCM and a mesh size of $\Delta x = a/3$. The velocity is made dimensionless using the asymptotic velocity U^∞ and the time by using the characteristic timescale of the particle defined by $\tau = m_p/6\pi\mu a$.

where the first term is the Stokes drag, and the two other terms are history terms and the complementary error function is given by:

$$\text{erfc}(x) = \frac{2}{\sqrt{\pi}} \int_x^\infty e^{-y^2} dy \tag{3.66}$$

The evolution of the angular velocity over time is then given by Newton's law as:

$$I \frac{d\Omega}{dt} = T_h + T^{ext} \tag{3.67}$$

where I is the moment of inertia of a sphere $I = \frac{2}{5}\rho_p V_p a^2$. Because this moment of inertia scales as a^5, it ended up causing numerical issues when performing numerical resolution of equation (3.67) as it is very small. Therefore, for this case of the external torque acting on the particle, a scale up by a factor 1000 is applied on the particle radius and domain size to prevent such issues. Also, as for the monopole, the characteristic timescale of the acceleration defined as $\tau = I/8\pi\mu a^2$ is small (about $66\,ms$), and use of the Fourier number $Fo = 10$ and $\Delta x = a/3$ results $\Delta t \approx 1.1\,s$, which is too big to accurately resolve the acceleration of the particle. Therefore, a Fourier number of 0.1 yielding a time step of $\Delta t \approx 11\,ms$ has been used for this case.

In the end, solution of equation (3.67) is obtained numerically as detailed in appendix A.2 and serves as a reference for the FCM simulation where, neglecting inertia, the dipole T balances the hydrodynamic forces. The applied external torque was $T = T^{ext} = 1\,pN.m$.

Figure 3.4 presents the comparison between the theory and the FCM simulation.

It can be seen that for the grid size of $\Delta x = a/3$ that was shown to be sufficient when only the

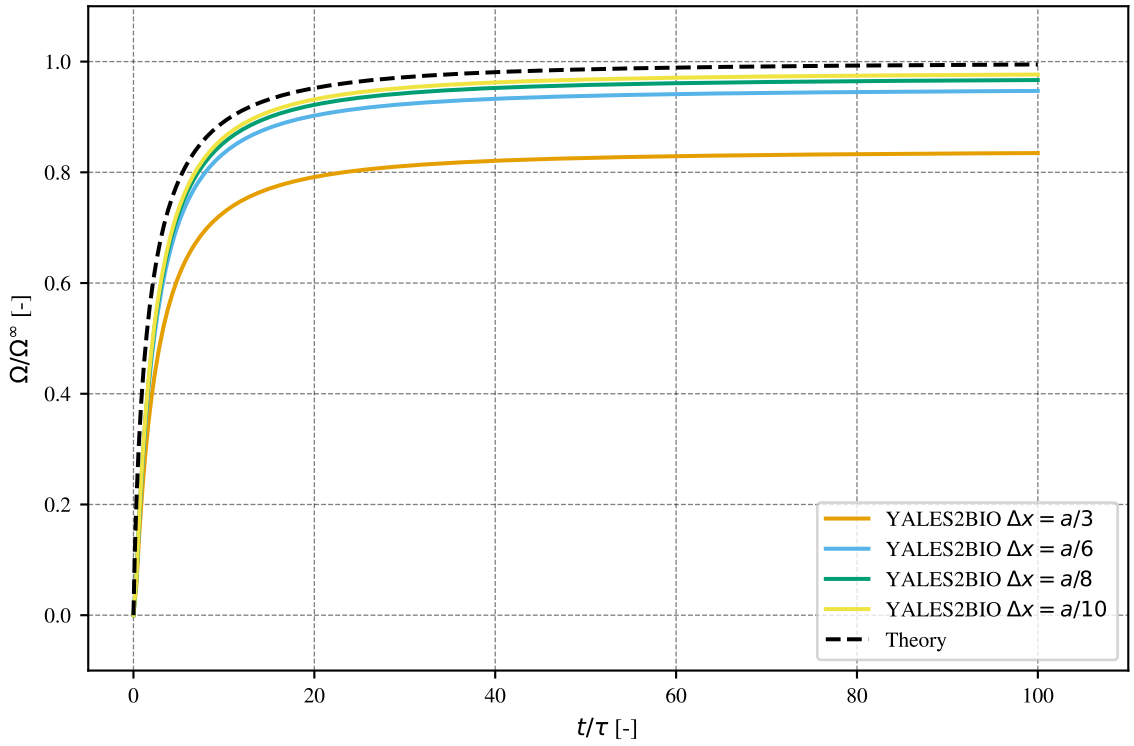

Figure 3.4: Evolution of the angular velocity over time for a particle subjected to a constant external torque in quiescent fluid. The angular velocity is made dimensionless using the asymptotic angular velocity Ω^{∞} and the time by a typical timescale of the particle defined by $\tau = I/8\pi\mu a^3$. (– – –) Theory given by a numerical solution of equation (3.67) detailed in appendix A.2, Continuous lines are results for numerical simulations using the FCM for mesh sizes (——) $\Delta x = a/3$, (——) $\Delta x = a/6$, (——) $\Delta x = a/8$, (——) $\Delta x = a/10$.

monopole was included, both the acceleration and asymptotic velocity of the particle are not accurately reproduced. This is actually expected as [Liu *et al.* 2009] mention that when the dipole term is included a mesh size of at least $\Delta x = a/4$ is required.

To observe the effect of the mesh size independently, the timestep was kept constant at $\Delta t = 11\,ms$ corresponding to a Fourier number of $Fo = 0.1$ for the mesh size $\Delta x = a/3$, while the mesh size was decreased at $\Delta x = a/6$, $\Delta x = a/8$ and $\Delta x = a/10$ yielding respectively Fourier numbers of 0.4, 0.7 and 1.1. The results for these different mesh sizes are presented in figure 3.4 alongside the result for $\Delta x = a/3$ and the theoretical angular velocity.

Reducing the mesh size greatly improves the quality of both the transient and asymptotic velocity of the particle, as decreasing the mesh size from $\Delta x = a/3$ to $\Delta x = a/6$ divided the error by more than 2. Further decrease down to $\Delta x = a/8$ shown slight decrease in the error while further decrease down to $\Delta x = a/10$ did not provide a significant improvement related to the increase in computational cost. Therefore, it appears that the mesh size of $\Delta x = a/8$ provides a good balance between performance and precision, where for this mesh size, the error on the asymptotic angular velocity is around 3% which remains acceptable.

This difference between the grid resolution of $\Delta x = a/4$ prescribed by [Liu *et al.* 2009] and the grid resolution required here probably comes from the differences in the numerical method used. Indeed, they implemented the FCM in a spectral/hp element method solver while a finite volume method with a prediction-correction schemes were used in the present case.

The mesh grid size of $\Delta x = a/8$ is used in all the following FCM simulations.

3.4.3 Implementation of the symmetric dipole

The validation case for the implementation of the symmetric dipole is the case of a particle immersed at the center of a planar extensional flow. The value of the stresslet needed to counter the deformation and ensure rigidity of the particle should be matching the theoretical value of $S_{ij} = \frac{20}{3}\pi\mu a^2 E_{ij}$ [Lomholt & Maxey 2003]. The same particle and the same domain is used with the previously chosen grid size of $\Delta x = a/8$ in the vicinity of the particle, where this time the background fluid velocity is set to a planar extensional flow, that is $\mathbf{u} = (-x_1, x_2, 0)$, by imposing this velocity as Dirichlet boundary conditions on the faces of the domain and as the initial velocity field. Fourier number of 10 was used in this simulation.

The effect of the stresslet convergence threshold ε_S as well as the effect of the maximum number of stresslet subiterations N_{sub}^{max} on the stresslet convergence were investigated. The convergence threshold was tested at both 1% and 0.1% of the norm of the background strain $||E|| = \sqrt{E_{ij}E_{ij}}$, that is $\varepsilon_S = \sqrt{2} \times 10^{-2}$ or $\varepsilon_S = \sqrt{2} \times 10^{-3}$ in this case and maximum subiterations per time step of $N_{sub}^{max} = 5$ and 20 have been tested. This value means that even if the norm of the averaged rate of strain has not reached the threshold after N_{sub}^{max} subiterations, the solver moves on to the next time step to prevent infinite looping. Note that the effective number of subiterations per time step can be lower than this maximum value if the norm of the averaged strain rate reaches the threshold value before the subiterations limit.

The resulting convergence of the component S_{11} of the stresslet is presented in figure 3.5 as well as the evolution of the effective number of subiterations per temporal iteration.

First, we can see that higher value of N_{sub}^{max} leads to higher variations in the stresslet value over a time step. Indeed, both simulations with $N_{sub}^{max} = 20$ yield a value for S_{11} twice as high as the theoretical value after the first time step while the simulation with $N_{sub}^{max} = 5$ slightly overshoots by 25%. From then, the two simulations with $N_{sub}^{max} = 20$ oscillate around the theoretical value until convergence while the simulation at $N_{sub}^{max} = 5$ decreases monotonously. Also, the effect of the convergence threshold can be seen to be very small, and the asymptotic values agree with the theory with a 2.81% error for the threshold at 1% of the background strain norm and $N_{sub}^{max} = 5$, while error is only decreased to 2.63% when the threshold is divided by 10 and $N_{sub}^{max} = 20$. Reducing the threshold also results in the need for more subiterations to converge. Indeed, a simulation with $N_{sub}^{max} = 5$ and $\varepsilon_S/||E|| = 0.1\%$ was performed but was not able to converge to the theoretical value while being stuck at performing the maximum number of subiterations at each timestep (not shown).

Figure 3.6 presents qualitative comparison of the streamlines in the vicinity of the particle between an FCM simulation with parameters $\varepsilon_S/||E|| = 1\%$ and $N_{sub}^{max} = 5$, and the exact Stokes flow provided by [Lomholt & Maxey 2003], highlighting the perturbation of the streamlines as a result of the presence of the rigid particle. Note that in the YALES2BIO simulation the actual domain is much larger than depicted as mentioned previously, and this figure is only a close-up on the particle.

This figure highlights very well the idea behind the FCM that is to impose some forces inside the particle volume which will result in disturbance of the surrounding flow. Here, vortices inside the particle volume generated by the stresslet provide a recirculating area inside the particle, ensuring the surrounding fluid is going around the particle and not through.

From this comparison we conclude that using a convergence threshold of 1% of the background strain rate norm and a maximum subiteration number of 5 provides a good trade off between performance and precision for our case. These values are in good agreement with the values of 6 to 20 subiterations reported by [Lomholt *et al.* 2002] for a threshold of 0.1%. Decreasing the convergence threshold must be carefully associated with an increase in the maximum number of subiterations allowed to ensure correct convergence is achieved.

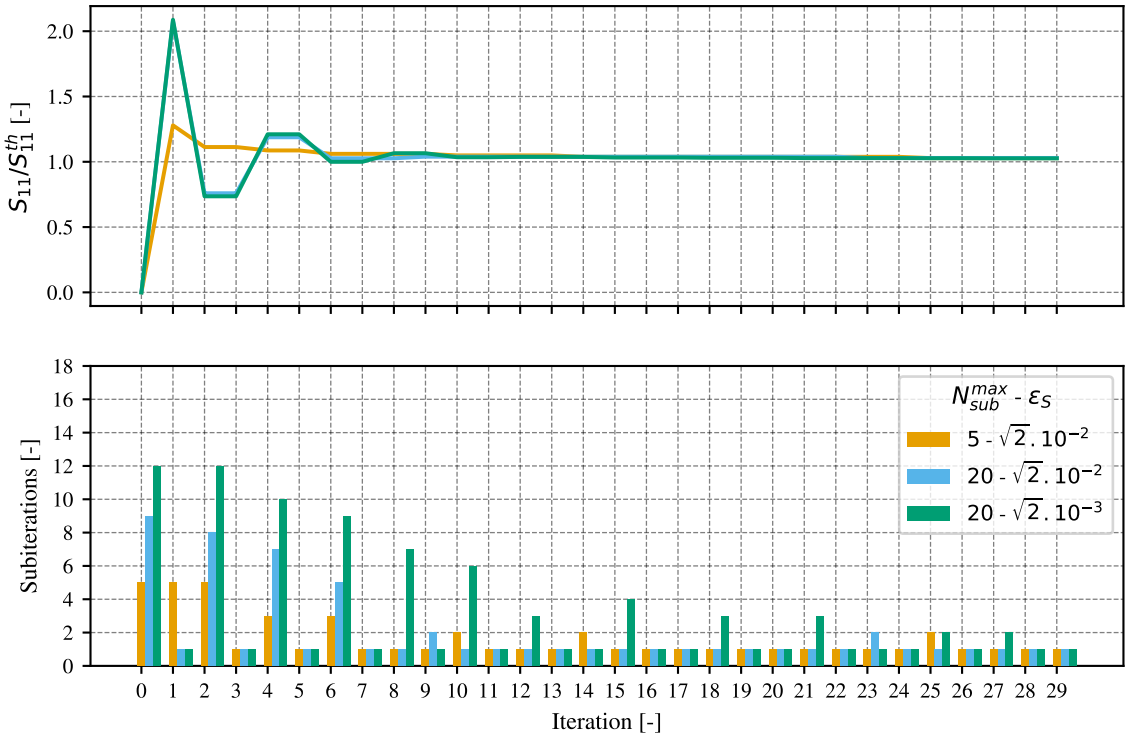

Figure 3.5: Effect of the stresslet algorithm parameters on the convergence of the component S_{11} for a spherical particle immersed in a planar extensional flow. (——) $N_{sub}^{max} = 5$ and $\varepsilon_S/||E|| = 1\%$, (——) $N_{sub}^{max} = 20$ and $\varepsilon_S/||E|| = 1\%$, (——) $N_{sub}^{max} = 20$ and $\varepsilon_S/||E|| = 0.1\%$. (Top) Evolution of the component S_{11} of the stresslet normalized by the theoretical value $S_{11}^{th} = 20\pi\mu a^3 E_{11}/3$ over the temporal iterations. (Bottom) Evolution of the effective subiterations number of the stresslet algorithm over the temporal iterations. All the simulations were performed with a fixed time step yielding a Fourier number of approximately 10 ($\Delta t = 1.778E-7\,s$), so that the iterations can be compared between simulations.

It must be noted that changing the time step might influence this transient behavior of the evolution of the stresslet. However, for the considered applications, we expect the stresslet to be converged for the entirety of the simulation. Even if the transient evolution is not accurate, we confirm here that using a Fourier number of 10, which was shown to be suitable for fluid only simulations, is also suitable to obtain the correct value of the stresslet. To prevent this transient to alter the results of the following dynamic cases with a moving particle, the particle will be initially kept at the same position during a small physical time, to ensure the flow field around the particle is established and the stresslet has converged to the correct value before the *real* simulation starts. During the simulations, only slight correction to the stresslet requiring small number of subiterations are required every other time step as can be seen on the bottom pannel in figure 3.5, for number of iteration higher than around 15.

3.4.4 Static simulation cases

3.4.4.1 Comparison with other FCM implementation and DNS results

The considered cases are that of a particle held fixed in a channel with a pressure driven flow for various geometric configurations where the forces and torques acting on the particle are measured and compared with resolved DNS simulations. These forces are natural results for the DNS simulations, however because the FCM uses forces as an input and outputs measured velocities, the force and

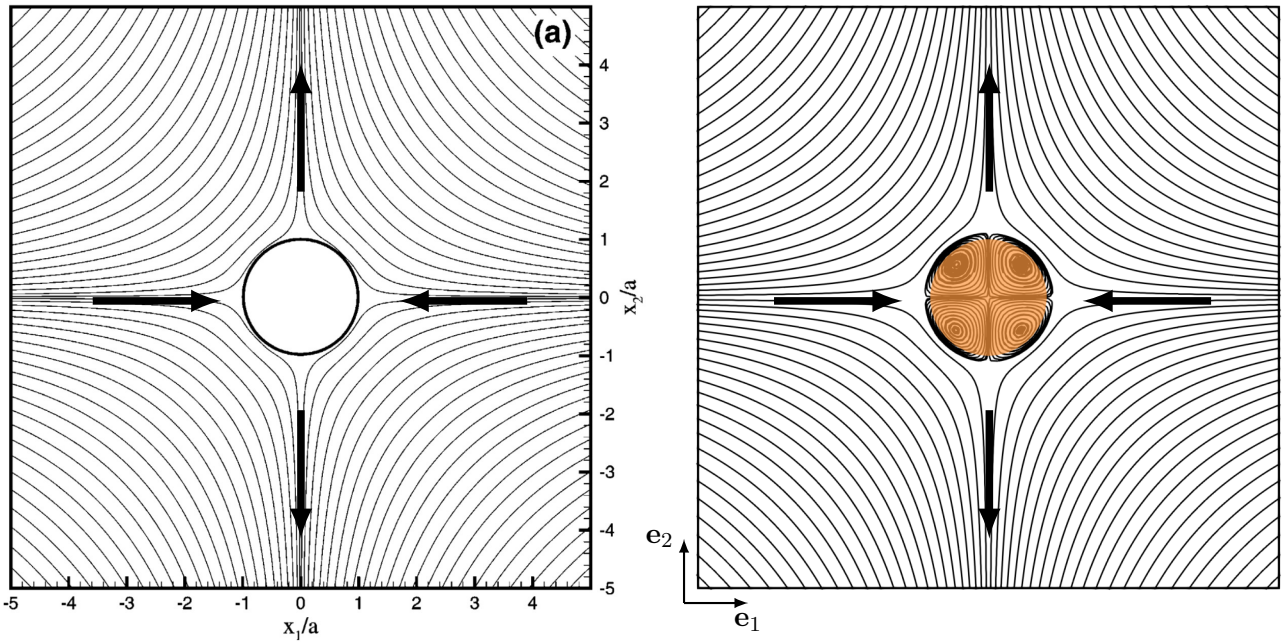

Figure 3.6: Close-up view of the perturbation of the background strain flow streamlines due to the rigidity of the particle in a $10a \times 10a$ region around teh particle. (Left) Theoretical streamlines from Stokes theory, reproduced from [Lomholt & Maxey 2003]. (Right) Simulation result from the FCM implemented in YALES2BIO with parameters $\varepsilon_S/||E|| = 1\%$ and $N_{sub}^{max} = 5$. The orange circle depicts the real size of the particle.

torque measurements are done by imposing the monopole and the dipole terms to be proportional to the difference between the target velocity (0 for a static particle) and the measured one. After convergence, the measured forces and torques are exactly the one that compensate the effort the fluid is acting on the particle yielding the quantity of interest.

Different configurations are presented in [Liu *et al.* 2009] and have been used for comparison with our implementation, but only one of them is presented here. This is the case of an ellipsoidal particle held fixed in a square Poiseuille flow, where the particle is placed close to a wall and its axes are not aligned with the flow resulting in a non-symmetric configuration. The particle has semi-axes $a_1 = 1.5a$, $a_2 = 0.9a$ and $a_3 = 1.2a$ and the channel has dimensions $16a$, $7a$ and $7a$ in directions $\mathbf{e}_1$, $\mathbf{e}_2$ and $\mathbf{e}_3$ respectively. The particle is placed at position $x_1 = 7a$, $x_2 = 2a$ and $x_3 = 0$, and it is tilted by 15° around axis $\mathbf{e}_3$. No-slip boundary conditions are imposed at the side walls in directions $\mathbf{e}_2$ and $\mathbf{e}_3$ and periodic boundary conditions are imposed in direction $\mathbf{e}_1$. A uniform pressure gradient is applied in the flow to generate momentum and the forces are measured after the full convergence of the flow and the forces, as well as the centerline velocity u_{cl} of the fluid used to normalize the forces. In our case, the centerline velocity was $u_{cl} = 1.39\,\mu m.s^{-1}$, resulting in a Reynolds number of around 10^{-5} using the channel width, centerline fluid velocity, water viscosity and $a = 1\,\mu m$.

Horizontal force, vertical force and torque acting on the particle are shown in table 3.1 for the DNS and FCM results of [Liu *et al.* 2009], as well as our results with the FCM. From this results we can conclude that our implementation compares quite well with that of [Liu *et al.* 2009] as the relative errors to the DNS results are comparable. Also, the error with the DNS results are quite small ($< 10\%$) considering the resolution of the DNS simulation required 40 times more elements than the FCM simulations.

	$F_1/(\pi\mu a u_{cl})$	$F_2/(\pi\mu a u_{cl})$	$T_3/(\pi\mu a^2 u_{cl})$
DNS [Liu *et al.* 2009]	35.34	2.182	5.517
FCM [Liu *et al.* 2009]	37.69 (6.6%)	2.256 (3.4%)	5.857 (6.2%)
FCM YALES2BIO	37.59(6.4%)	2.238 (2.6%)	6.001 (8.7%)

Table 3.1: Normalized forces and torque acting on an ellipsoidal particle held fixed close to the wall and tilted by 15° in a square Poiseuille flow. Results using the FCM implemented in YALES2BIO are compared to DNS and FCM values from [Liu *et al.* 2009]. Error between the FCM and DNS simulation in parantheses.

3.4.4.2 Effect of particle distance to the wall

A more general validation for such static case is performed following [Hsu & Ganatos 1994] which provides values for the velocity of an ellipsoidal particle immersed in a shear flow for different orientation angles and different distances to a plane wall. To do so they used boundary element methods, so the results are very accurate and can be used as trusted references. The validation against this case is very important as it is known that the precision of the FCM decreases when the particle gets close to a wall [Lomholt & Maxey 2003]. This is caused by the smooth regularization of the multipole expansion over the Gaussian envelopes which results in a blurry interface between the particle and the fluid instead of the real sharp interface, resulting in a layer close to the particle surface where the flow field is not matching the theoretical solution. This blur zone is approximately from a quarter to half of a radius [Lomholt & Maxey 2003] and if the wall is interacting with this zone, then the effect of the wall on the particle will be poorly resolved. Incorporating additional lubrication forces which are not resolved by the FCM as external forces improved the accuracy of the results close to a wall but at the expense of a doubled simulation time [Dance & Maxey 2003]. The goal here is to evaluate how the accuracy of the FCM depends on the distance between the particle and the wall. Since we are interested in particle-wall interactions, this will help determine the minimum reliable working distance for using the FCM with confidence.

The considered case is that of an ellipsoidal particle placed with its center of mass at a distance h from a flat wall in a surrounding shear flow. The particle has dimensions $2a_1 = a_2 = a_3 = 1\,\mu m$ and the shear rate is $\dot{\gamma}$. The cubic simulation domain for the FCM has dimensions $20a_3$ while the results of [Hsu & Ganatos 1994] are obtained for a half-infinite domain. In our simulation, the shear flow is imposed by the translating top wall while the 4 side walls have periodic boundary conditions. Different orientations of the particle are investigated by performing rotations of an angle α around axis $\mathbf{e}_2$, as well as different particle to wall distances h as shown on figure 3.7.

For each configuration, longitudinal and vertical velocities as well as the angular velocity are measured. Note that no external forces or torques are acting on the particle, and only the rigidity of the particle is ensured via application of the stresslet. The particle position and orientation are not updated over the time steps to reach the asymptotic values of the velocities, due to the transient establishment of the perturbation flow around the particle.

The slip velocity U_s of the particle is derived from its longitudinal velocity as $U_s = U_1 - h\dot{\gamma}$ and is plotted on figure 3.8 where the continuous lines are the reference results of [Hsu & Ganatos 1994] and the dots are numerical results using the FCM implemented in YALES2BIO.

The first observation is that the slip velocity is always negative meaning that the particle is slower than the undisturbed fluid at the same distance from the wall. The amplitude of this lagging velocity decreases as the distance to the wall increases, indicating that the lag is due to the presence of the wall. When comparing the results of FCM simulations and the theory of [Hsu & Ganatos 1994] we

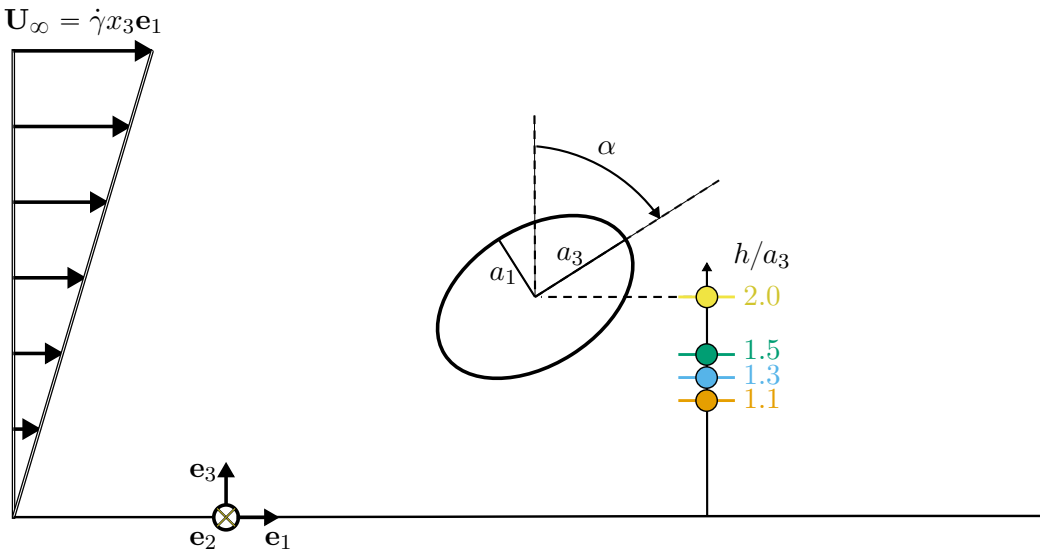

Figure 3.7: Configuration for the static particle test case as done by [Hsu & Ganatos 1994]. The particle is placed in a shear flow and its velocity and angular velocity are measured for different orientations α and distances to the wall h. The simulation domain is $20a_3$ and the shear rate of $1000\,s^{-1}$ is imposed by the top translating wall. Periodic boundary conditions are applied on the sides.

obtain confirmation that far from the wall the results are very accurate, as can be seen for particle to wall distances of $2.0a_3$ or $1.5a_3$, however when we get closer to the wall, the accuracy of the FCM decreases as expected.

Indeed, when considering a particle to wall distance of $1.3a_3$, the FCM agrees well with the theory for most of the angles except for the range $[-30°, 30°]$ where slight discrepancies begin to appear. This is the range for which the gap between the particle surface and the wall is the smallest and in the case $\alpha = 0°$ this gap is exactly $0.3a_3$ meaning the wall is right at the edge of the FCM blur zone, explaining the small errors in this range of configurations. When decreasing the distance between the particle and the wall down to $1.1a_3$, accuracy further drops for the angle range $[-50°, 50°]$, once again corresponding to the range for which the particle surface to wall gap is the smallest. This time at $\alpha = 0°$ the gap is $0.1a_3$ meaning the wall is fully in the blur region around the particle, resulting in a very bad consideration of the wall effect on the particle. The quality of the FCM is retrieved for the bigger angles as the gap width is around $0.4a_3$ for $\alpha = 50°$ and increasing up to $0.6a_3$ for $\alpha = 90°$.

The exact same observation can be made for the vertical velocity as shown on figure 3.9.

As a side note, it seems important to outline the antisymmetric property of this vertical velocity profile over the orientation angles. Indeed, this results in a mean vertical velocity over a full rotation of the particle which is zero as the positive contribution to the vertical velocity of the negative angles is compensated by the positive angle and their negative contribution. Consequently, a particle which would not be constrained to these configurations but rather free to move, would perform a rotation initiated by the surrounding shear flow and therefore follow a similar vertical velocity curve over one movement period. The resulting motion will be that of a particle rotating and moving in the vertical direction during its rotation finally coming back to its original altitude after a period of the movement, that is a half rotation of the particle. This is in agreement with the reversibility of Stokes flows and makes us believe that one key property required by the microstructures to generate a net vertical movement of the particle would be to break the fore-aft symmetry, which will be discussed further in chapter 4.

Considering the evolution of the angular velocity of the particle over the orientations and particle

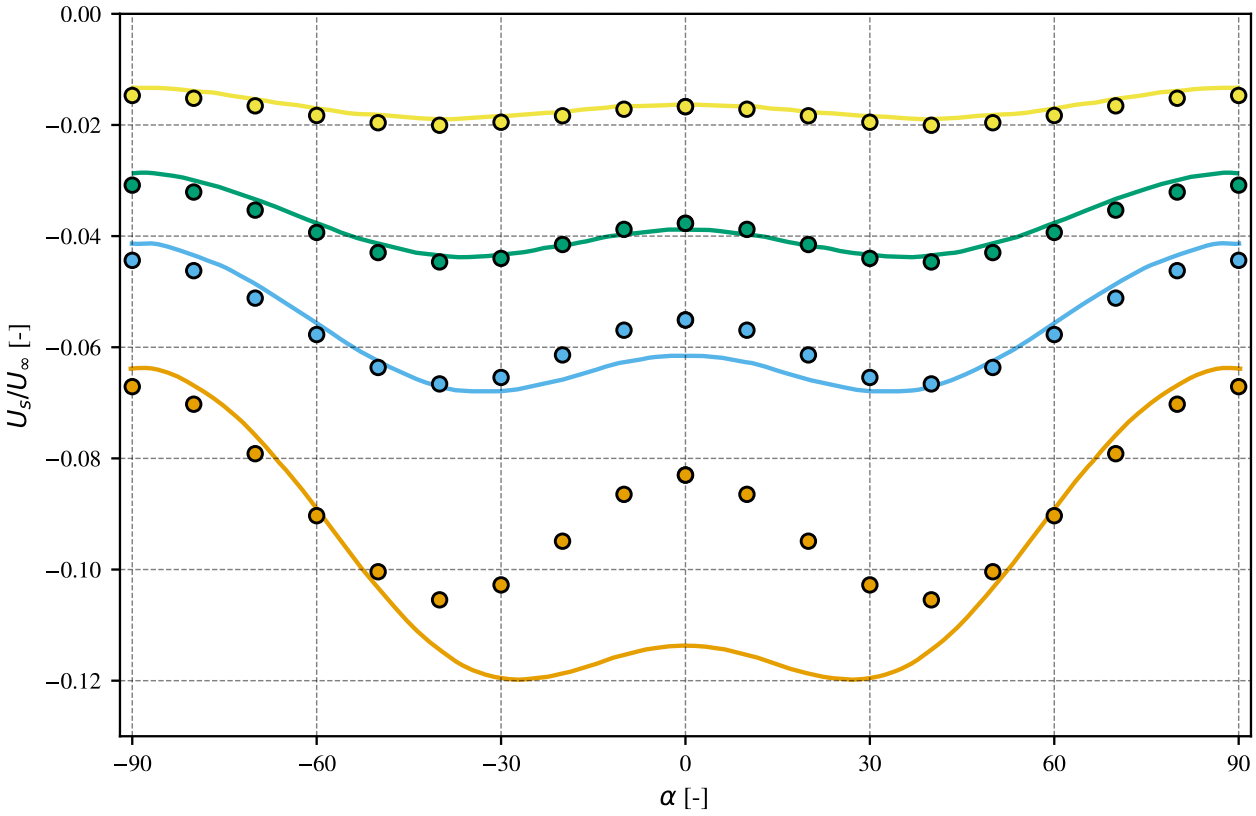

Figure 3.8: Evolution of the normalized slip velocity $U_s = U_1 - h\dot{\gamma}$ over particle orientation angles. The slip velocity is normalized by the undisturbed velocity at the center of the particle $U_\infty = h\dot{\gamma}$. The evolution is plotted for 4 different particle center to wall distances: $1.1a_3$, $1.3a_3$, $1.5a_3$ and $2a_3$. The continuous lines are the theoretical results from [Hsu & Ganatos 1994] and the color matching dots are the results from FCM simulations using YALES2BIO at the corresponding particle to wall distance. Theoretical results for negative angle are obtained by duplicating the positive values as [Hsu & Ganatos 1994] only plotted the results for $\alpha \in [0, 90]$ using the fact that U_1 is an even function of α.

to wall distances, the error is still maximal for the smallest distance to the wall $h = 1.1a_3$. However, the error is much smaller than for the translational velocities, so is the variation between the different curves, indicating that the effect of the wall have a small effect on the angular velocities compared to its effect on the translational velocities. This effect is to slow down the rotation of the particle which should have a mean angular velocity of $0.5\dot{\gamma}$ in an unbounded shear flow while the mean values here for distances to the wall from $h = 1.1a_3$ to $h = 2a_3$ ranges from about $0.46\dot{\gamma}$ to $0.48\dot{\gamma}$.

This whole comparison allows us to draw some conclusion on the validity of the FCM when the particle is interacting with a wall. We consider that for distances greater than $1.3a_3$, the FCM is very accurate and is able to account for the effect of the wall. On the other hand, for distances below $1.3a_3$, the error resulting from the bad resolution of the fluid in the immediate surrounding of the particle results in poor description of the particle-wall interaction. As this error is increasing as the particle is getting close to the wall, simulations around $h = 1.3a_3$ are possible as the error introduced is still small, however for values down to $h = 1.1a3$ the error might greatly influence the overall dynamics of the particle and the results will be misleading.

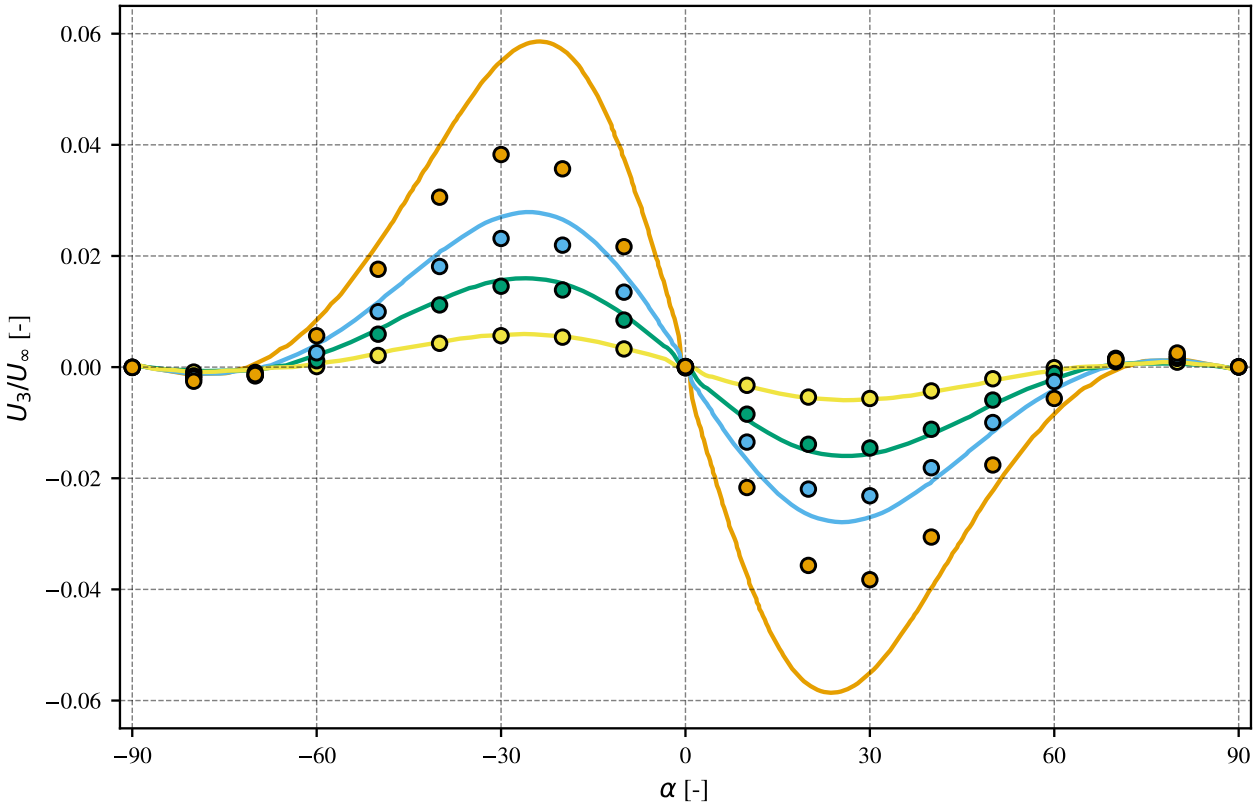

Figure 3.9: Evolution of the normalized vertical velocity U_3 over particle orientation angles. The vertical velocity is normalized by the undisturbed velocity at the center of the particle $U_\infty = h\dot{\gamma}$. The evolution is plotted for 4 different particle center to wall distances: $1.1a_3$, $1.3a_3$, $1.5a_3$ and $2a_3$. The continuous lines are the theoretical results from [Hsu & Ganatos 1994] and the color matching dots are the results from FCM simulations using YALES2BIO at the corresponding particle to wall distance. Theoretical results for negative angle are obtained by taking the opposite of the values for positive angle as [Hsu & Ganatos 1994] only plotted the results for $\alpha \in [0, 90]$ using the fact that U_3 is an odd function of α.

3.4.5 Dynamic simulation cases

3.4.5.1 Jeffery's orbit

The first results that comes to mind when speaking about ellipsoidal particle dynamics in flow is the result of Jeffery's orbits, which is typically used as a validation for models of ellipsoidal particle dynamics [Mody & King 2005, Wang *et al.* 2018]. [Jeffery 1922] derived an analytical expression of the angular velocity of an ellipsoidal particle immersed in an unbounded shear flow, depending on its orientation. In a shear flow, a spherical particle would rotate at the same angular velocity for all its orientations as the particle is isotropic, which would be equal to the vorticity of the fluid, that is $\dot{\gamma}/2$. In the case of an ellipsoidal particle, on top of the vorticity contribution, the strain component of the shear flow tends to orient the particle axes with the principal directions of strain, resulting in an additional hydrodynamic torque acting on the particle and which depends on its orientation. This strain contribution is increasingly important as the particle aspect ratio $AR = a_3/a_1$ with $a_3 < a_1$ decreases [Kim & Karrila 1991].

Consider an oblate spheroid of major semi-axes $a_1 = a_2$ and minor semi-axis a_3 in an unbounded shear flow of shear rate $\dot{\gamma}$. If the minor semi-axis of the particle, which is also its axis of revolution, is

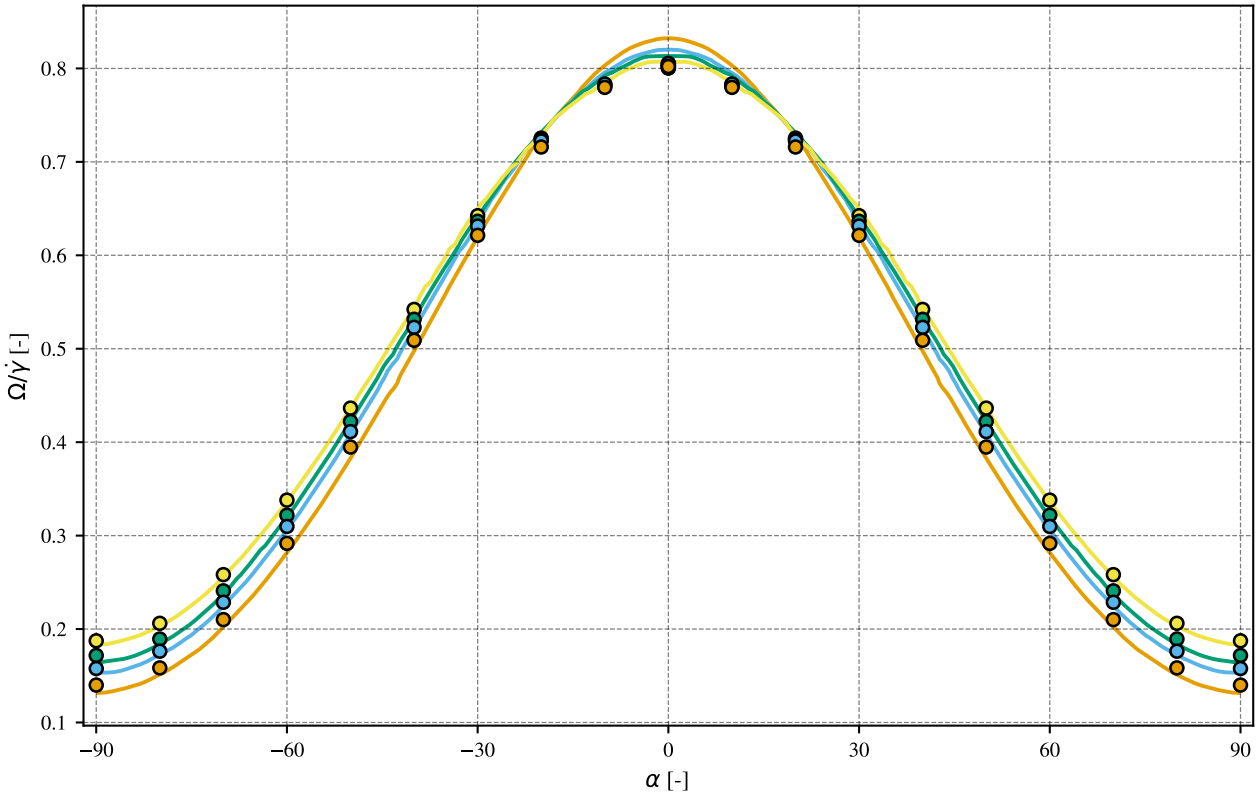

Figure 3.10: Evolution of the normalized angular velocity Ω over particle orientation angles. The angular velocity is normalized by the shear rate $\dot{\gamma}$. The evolution is plotted for 4 different particle center to wall distances: $1.1a_3$, $1.3a_3$, $1.5a_3$ and $2a_3$. The continuous lines are the theoretical results from [Hsu & Ganatos 1994] and the color matching dots are the results from FCM simulations using YALES2BIO at the corresponding particle to wall distance. Theoretical results for negative angle are obtained by duplicating the positive values as [Hsu & Ganatos 1994] only plotted the results for $\alpha \in [0, 90]$ using the fact that Ω is an even function of α.

initially placed in the shear plane, the particle will rotate around the vorticity axis and the revolution axis will remain in the shear plane during the whole rotation of the particle. A single angle θ is therefore needed to describe the rotation of the particle and its evolution over time is given by equation (3.68) [Jeffery 1922].

$$\dot{\theta} = \dot{\gamma} \frac{a_3^2 \cos^2\theta + a_1^2 \sin^2\theta}{(a_3^2 + a_1^2)} \tag{3.68}$$

The corresponding FCM simulation was performed by placing a particle with dimensions $a_1 = a_2 = 2a_3 = 1\,\mu m$ at the center of a cubic domain of width $40a_1$ initialized with a linear shear flow driven by two moving walls translating in opposite direction, imposing a shear rate of $\dot{\gamma} = 10,000\,s^{-1}$. The 4 other boundaries of the domain are set to be periodic. The particle position and orientation are not updated for the first $50\,\mu s$ (≈ 4000 iterations) so that the stresslet reaches a converged value before the particle is released at $t = 0$, and its angular velocity is tracked through time. Blood plasma fluid properties are used in this case with $\rho = 1023.9\,kg.m^{-3}$ and $\nu = 1.1719 \times 10^{-6}\,m^2.s^{-1}$ [Mody & King 2005].

The Jeffery's orbit equation (3.68) can be integrated to find the evolution of the particle orientation θ through time. This analytical result is presented in Figure 3.11 alongside numerical result obtained with the FCM for an aspect ratio of $a_1/a_3 = 0.5$ and a rotation of 180° of the particle.

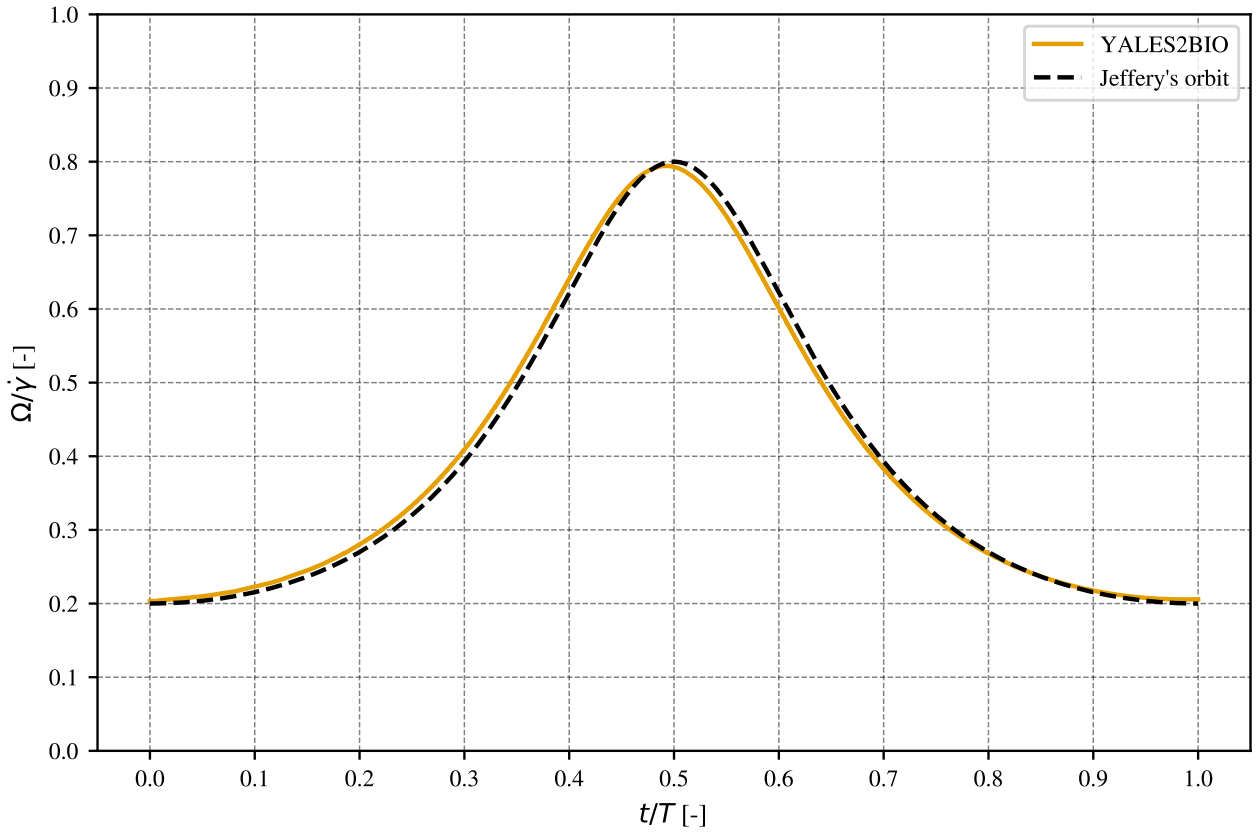

Figure 3.11: Comparison between an FCM simulation and theoretical evolution of the angular velocity of an ellipsoidal particle of aspect ratio 0.5 immersed in a shear flow. (– – –) Jeffery's orbit theory, (——) Numerical simulation with the FCM. The time is normalized by the Jeffery's orbit half period $T = \pi \frac{a_1^2+a_3^2}{\dot{\gamma} a_1 a_3}$ corresponding to a 180° rotation of the particle.

From this result, the FCM is able to reproduce accurately the motion of the ellipsoidal particle in shear flow, as the error on the angular period is around 1.20% which is considered acceptable.

Now, because we are interested in the simulation of blood platelets, the aspect ratio to be considered is not 0.5 but rather 0.25 [Mody & King 2005, Pozrikidis 2006]. The same study was therefore conducted for a particle of aspect ratio 0.25 and is compared with Jeffery's theory in figure 3.12.

In this case, the amplitude of the angular velocity variations is again well reproduced however the angular period is smaller by around 8%. Degradation of the results due to the aspect ratio of the particle can be explained by two elements. First, the FCM has been indicated to be working best for aspect ratios higher than 0.5 for oblate spheroids, while for smaller aspect ratios, the resulting thin and smooth Gaussian envelope along the major axis of the particle cannot accurately capture the sharp edge of the particle [Liu *et al.* 2009]. Additionally, as mentioned in the introduction of this simulation case, the hydrodynamic torque resulting from the strain rate acting on the particle becomes increasingly important as the particle aspect ratio is small. Due to the worse description of the FCM particle at these smaller aspect ratios but the increasing importance of the strain rate hydrodynamic torque which is badly captured, the resulting motion of the particle is not accurately reproduced.

Even though this error can be considered acceptable as the overall dynamics of the movement is quite well reproduced, the cost of this simulation is much greater than that of the particle at aspect ratio 0.5. Indeed, the mesh size required to obtain an accurate resolution of the FCM particle

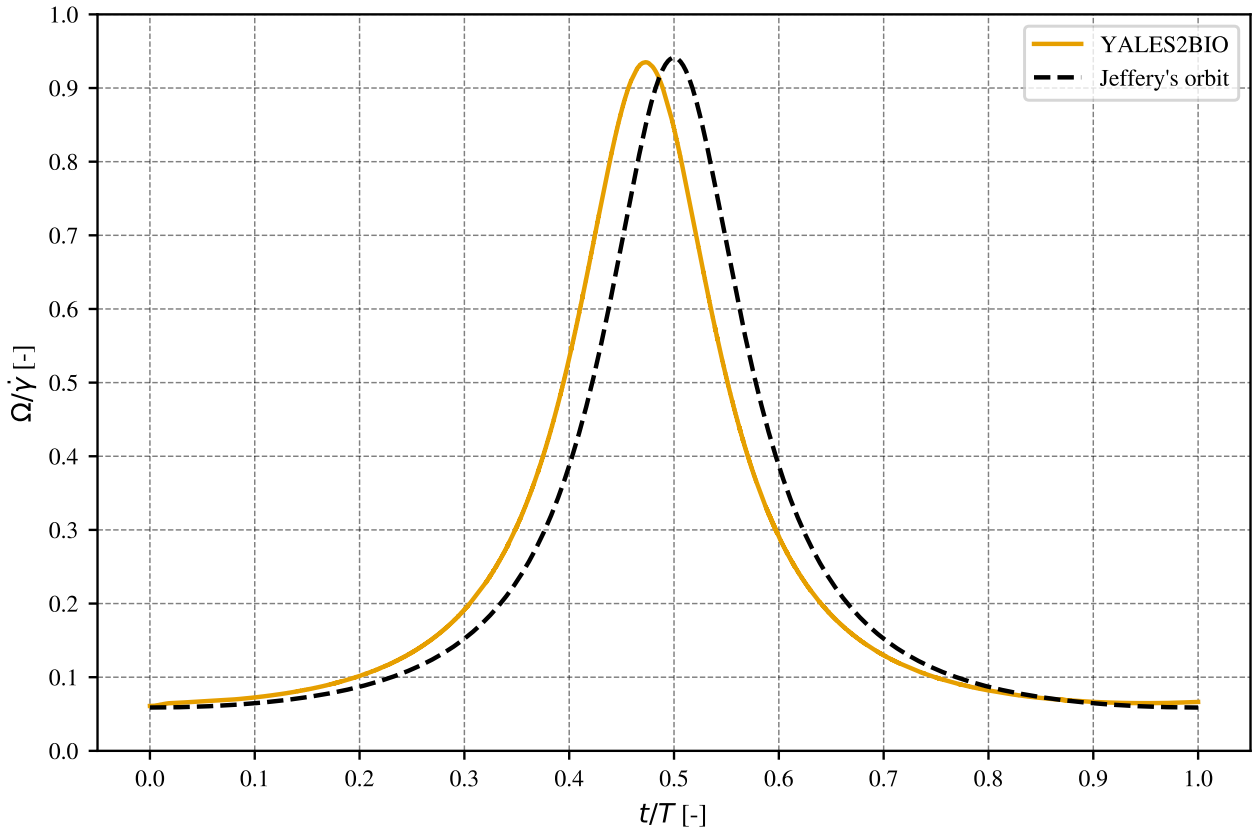

Figure 3.12: Comparison between an FCM simulation and theoretical evolution of the angular velocity of an ellipsoidal particle of aspect ratio 0.25 immersed in a shear flow. (– – –) Jeffery's orbit theory, (——) Numerical simulation with the FCM. The time is normalized by the Jeffery's orbit half period $T = \pi \frac{a_1^2+a_3^2}{\dot{\gamma} a_1 a_3}$ corresponding to a 180° rotation of the particle.

that is $\Delta x = a/8$ must be defined based on the smallest particle semi-axis for an ellipsoidal particle [Liu *et al.* 2009], therefore the mesh size is divided by 2 when transitioning from aspect ratio 0.5 to 0.25. This leads to about 8 times more mesh nodes in the domain as well as 4 times smaller time steps, if the Fourier number is kept constant, resulting in a simulation about 24 times more costly in computational resources.

3.4.5.2 Dynamics over a flat plate

The final validation case we present here is the one of a particle freely moving close to a plane wall in a shear flow. This experiment is the closest to the simulations we aim at performing, regarding the interaction between an ellipsoidal particle and structured surfaces, for which results are available in the literature. This validation case is therefore key to ensure the model is able to capture correctly these interactions. This case has been treated using boundary elements method by [Mody & King 2005] and [Pozrikidis 2006] for a particle of aspect ratio 0.25 and different particle to wall distances, but we showed in the previous case that using an aspect ratio smaller than 0.5 can lead to errors with the FCM. Ideally this same experiment should be performed for a particle of aspect ratio 0.5 but to our knowledge, the only result for a particle of aspect ratio 0.5 has been presented by [Hsu & Ganatos 1994] where they only considered particle to wall distance of $h/a_1 = 1.25$ for which we know the FCM starts to be less accurate. Also, in their work, the particle trajectory was obtained by integrating the velocity

of static particles, obtained for seven particle orientation at a given distance to the wall, and not dynamic simulations, so comparisons with this reference must be done carefully as the configurations are not identical.

The simulation with the FCM at aspect ratio 0.5 was performed by placing the particle of dimensions $a_1 = a_2 = 1.0\,\mu m$ and $a_3 = a_1/2$, with its axes initially aligned with the global coordinate system and at a distance $x_3 = 1.25a_1$ from the bottom no-slip wall. The domain is a cube of $20a_1$ side length where the ambient shear rate of $2000\,s^{-1}$ is imposed by the translating top wall and periodic boundary conditions are applied on the sides of the domain. The mesh has a prescribed size of $\Delta x = a_3/8$ in a cylinder encapsulating the particle trajectory, while the mesh is coarser away from the particle. The particle is again kept at its initial position and orientation for $50\,\mu s$ so that the stresslet and the disturbance flow are converged before the particle is released and free to move. The resulting particle trajectory in the shear plane is plotted on figure 3.13 alongside the trajectory obtained by [Hsu & Ganatos 1994].

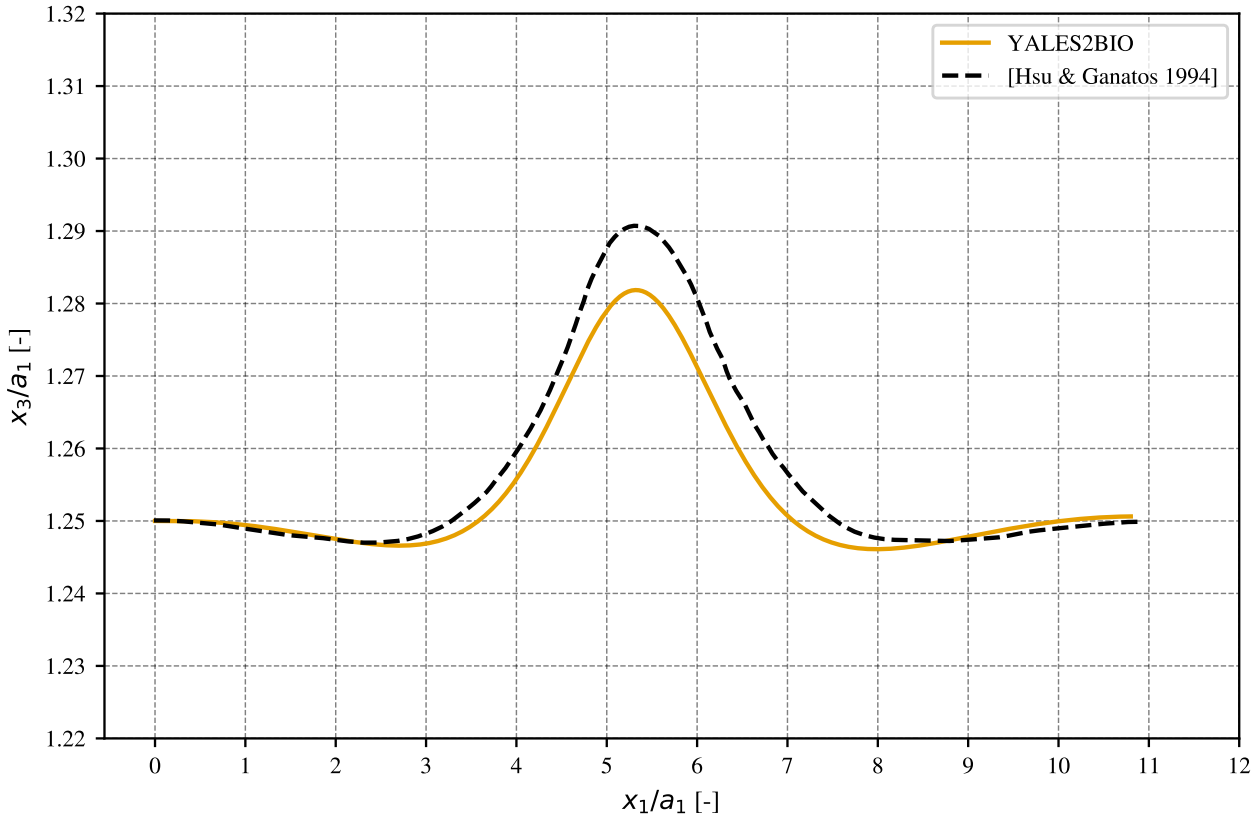

Figure 3.13: Dynamic of an ellipsoidal particle of $AR = 0.5$ over a flat surface in shear flow. (– – –) Reference trajectory corresponding to a particle initially oriented at $\alpha = 90°$ in figure 3.7 [Hsu & Ganatos 1994] and (——) FCM simulation with YALES2BIO.

It can be seen that the overall trajectory of the particle is well reproduced, notably the vertical movement of the particle caused by the presence of the wall agrees well with the reference. Some discrepancies can be observed at the apex of the motion, for which the gap between the particle and the wall is the smallest, in agreement with the previous observations on static cases. Yet these discrepancies are small in relation to the quality of the overall particle trajectory.

The same experiment was conducted for a particle of aspect ratio 0.25 so that $a_3 = a_1/4$ by comparing FCM simulation with results from [Mody & King 2005]. They provide particle trajectories

for different initial particle to wall distances so we can perform the FCM simulation at a distance for which the effect of the wall is well captured by the FCM. The results for the FCM simulation and the corresponding reference trajectory for a particle initially placed at $x_3 = 1.4a_1$ is presented in figure 3.14.

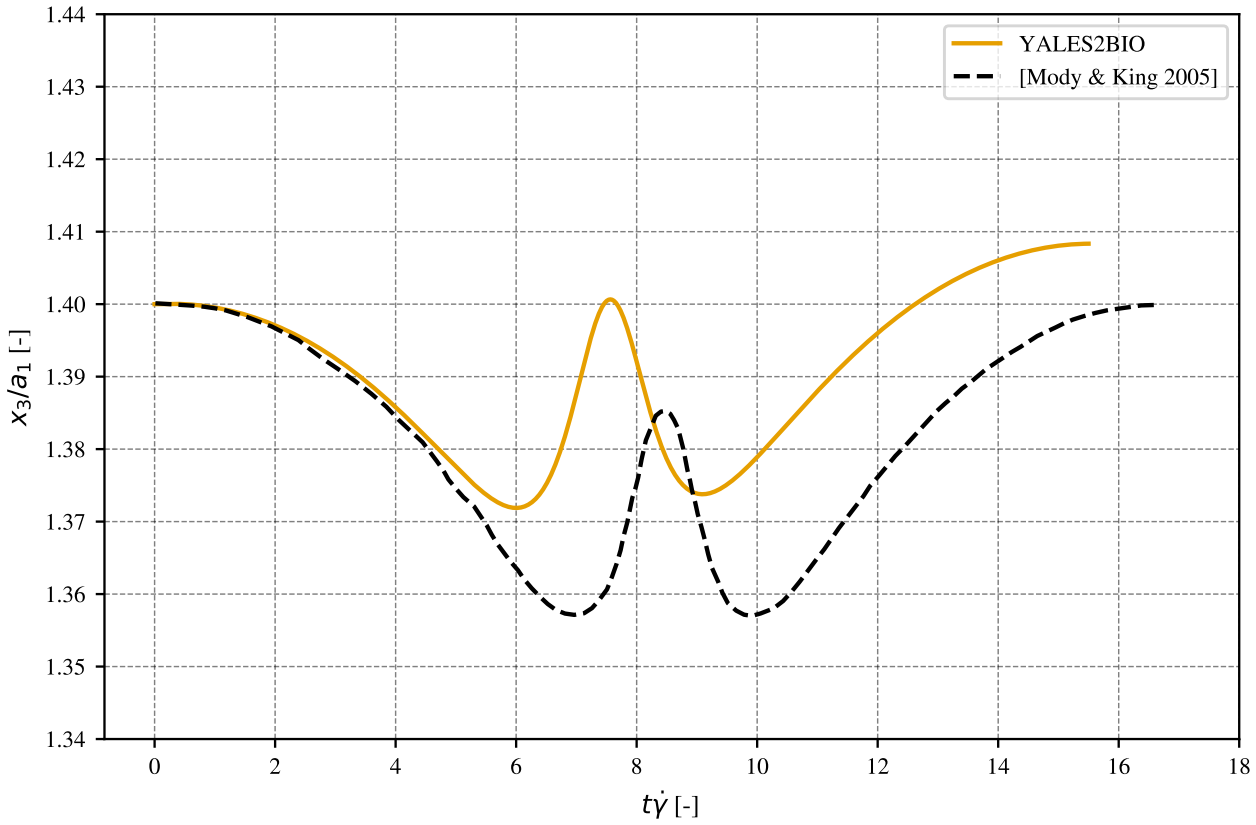

Figure 3.14: Dynamic of an ellipsoidal particle of $AR = 0.25$ over a flat surface in shear flow. (– – –) Reference trajectory [Mody & King 2005], (——) FCM simulation with YALES2BIO.

It appears that the FCM is performing very badly in this case, where the particle is rotating faster than expected, as already observed in the case of Jeffery's orbits, and also the vertical movement of the particle is not correct at all. This leads to the conclusion that the FCM can be used to study the interaction of ellipsoidal particles and walls if the particle has an aspect ratio of at least 0.5 and is not too close to the wall.

It feels intuitive that the interactions between a spherical particle and structured surfaces will be altered by a non-sphericity of the particle and that the amplitude of this alteration will be related to the aspect ratio of the particle. Even though it is probably not linear, we do not expect the effect of the non-sphericity to be completely the opposite between a particle with aspect ratio 0.5 or 0.25, so that observations on the interaction of an ellipsoidal particle of aspect 0.5 should provide some valuable insight on the interaction between an ellipsoidal particle of aspect ratio 0.25 and the same structures. From these remarks, we decided to keep the particle aspect ratio at 0.5, ensuring more precise simulations as well as higher throughput.

In the end, we are confident in the implementation of the FCM in YALES2BIO to perform dynamic simulations for such ellipsoidal particle immersed in a shear flow and interacting with a nearby surface, as long as this surface is at a distance of $1.25a_1$ from the particle center of mass.

Following this extensive validation, the model can be exploited in two directions. The first one,

which was the most extensively studied during this work is the use of the model in its current state to investigate purely hydrodynamic interactions between ellipsoidal particles and structured surfaces. Results of such study are presented in chapter 4 and exploratory work to explain these results are presented in chapter 5. On the other hand, the model can be further enriched by incorporating adhesive bonds mechanisms, in an attempt to reproduce the adhesion mechanism of blood platelets. The biological mechanisms of platelets adhesion and the way they are implemented into the numerical model is presented in chapter 6 with qualitative comparison on the effect of the surface structuration on platelet adhesion.

Chapter 4

Hydrodynamic interaction of ellipsoidal particles and structured artificial surfaces

Contents

Now that the numerical model has been validated, the hydrodynamic interaction of a blood platelet, represented by a rigid ellipsoidal particle of aspect ratio 0.5, with structured surfaces can be investigated. An analytical estimation of the force acting on a spherical particle over such structures is also available, even though it is restricted to structures of negligible amplitude. First, comparison between the numerical model and the analytical solution is performed, for the case of a spherical particle. Then, simulation of the dynamics of an ellipsoidal particle over structures of finite amplitude are performed using the FCM model implemented in YALES2BIO.

Two different structure shapes were investigated: a symmetric square groove structure for which we expect no drift of the particle, following the reversibility principle of Stokes flows, and a sawtooth structure which is expected to break this symmetry of the flow configuration and eventually could lead to a net force acting on the particle. The effect of the structure pattern period, structure amplitude and Reynolds number are discussed in this chapter.

4.1 Validation against the analytical method

The numerical model allows the simulation of a much more complex dynamics than the theoretical framework, that is the dynamics of an ellipsoidal particle near structures of finite amplitude as opposed to spherical particles near structures of negligible amplitude with respect to the particle radius. However, the theoretical model can first be used to assess the validity of the numerical model in the context of a sphere moving close to structures of small amplitude. This was done by performing a numerical simulation of a spherical particle with radius $a = 0.75\,\mu$m placed at an initial distance of $3a$ from the middle of a structured surface, using the FCM model. The domain dimensions are $15a \times 10a \times 30a$ respectively in directions $\mathbf{e}_1$, $\mathbf{e}_2$ and $\mathbf{e}_3$. An ambient shear flow with $\dot{\gamma} = 2000\,s^{-1}$ is generated by imposing a translation velocity at the top wall and periodic boundary conditions are imposed on each opposing side. No-slip boundary condition is imposed on the bottom wall which is a structured surface. The different patterns of the considered structures are detailed below.

Following the methodology of the analytical framework, the movement of the particle in the FCM simulations is constrained to the motion of the same particle which is freely evolving at a distance $\tilde{h}$ of

a flat surface[1]. This leads to an imposed constant translational velocity, constant angular velocity and zero vertical velocity. They are imposed by incrementing the monopole and the anti-symmetric dipole at each time step to counter the deviation from the target velocities. The velocity and angular velocity are obtained from the forces and torques acting on a particle translating or rotating in quiescent fluid, or resisting the ambient shear flow. These forces and torques are obtained from the bispherical harmonic coefficients of the flows at order 0 presented in chapter 2, see table 2.3. From these, the velocity and angular velocities which results in a force free and torque free particle are obtained by searching for U_1 and Ω_2 such that:

$$\begin{cases} -U_1 f_1^T - a\Omega_2 f_1^R + \tilde{h}\dot{\gamma} f_1^S = 0 \\ -U_1 t_2^T - a\Omega_2 t_2^R + \frac{1}{2} a\dot{\gamma} t_2^S = 0 \end{cases} \tag{4.1}$$

For this specific configuration, this corresponds to a particle velocity of $U_1 = 4.45\, mm.s^{-1}$ and angular velocity of $\Omega_2 = 977.10\, s^{-1}$.

Three different structure amplitudes h were tested in the FCM simulation. When compared to equation (2.10), a given amplitude of the structure can be understood as a given ε which is not perfectly 0 as it is in the analytical theory. The simulated structures with height $h = a$, $h = 0.4a$ and $h = 0.2a$ correspond to $\varepsilon = 1$, $\varepsilon = 0.4$ and $\varepsilon = 0.2$ respectively, moving towards a structure of negligible amplitude as assumed in the analytical model. Reducing further the amplitude of the structure would require a reduction in the mesh size as the height of the structure reaches the current size of a mesh element. The amplitude was varied by keeping the mean altitude of the structures constant, so that the distance between the particle and the equivalent flat surface is the same between the simulations, ensuring an accurate comparison with the analytical result.

In the analytical model, the force acting on the particle in the vertical direction was searched for in the decomposed form:

$$F_3 = F_3^{(0)} + \varepsilon F_3^{(1)} + O(\varepsilon^2) \tag{4.2}$$

Because in the simulations we impose the motion of a particle to be that of a force free and torque free particle over a flat surface it results that $F_3^{(0)} = 0$. Also, the analytical model provides us the contribution of the structured surface on the force $F_3^{(1)}$ directly while the FCM simulation gives the total force F_3 required to impose the velocity of the particle. To compare the results of the analytical model and the FCM simulations, scaling of the FCM forces by ε of the corresponding structure amplitude is required following equation (4.2).

The first structure investigated is that of square corrugations perpendicular to the flow direction, with equal length at the top and the bottom of the structure equal to $2a$ so that the pattern period is $L = 4a$.

Figure 4.1 presents the evolution of the force needed to hold the particle at constant altitude for the numerical simulation and the analytical model according to the position of the particle in a single pattern of this structure. The shear rate and the velocity of the particle are imposed so that a freely moving particle is transported from left to right in figure 4.1.

The negative forces for the first half of the pattern indicate that a freely moving particle would rise upward due to the step in the structure patterns, and the opposite sign is observed for the force on the second half where the free particle would go back down. The locations where the force is zero corresponds to the positions of the particle for which the geometry is symmetric, considering both the particle and the structure. However, because the external shear is forcing the particle to translate sideways, these positions are not stable equilibrium positions.

[1]The distance bewteen the particle and the surface is noted here $\tilde{h}$, instead of h which was used during chapter 2, to avoid confusion with the amplitude of the structure discussed further in this section, which is labeled h.

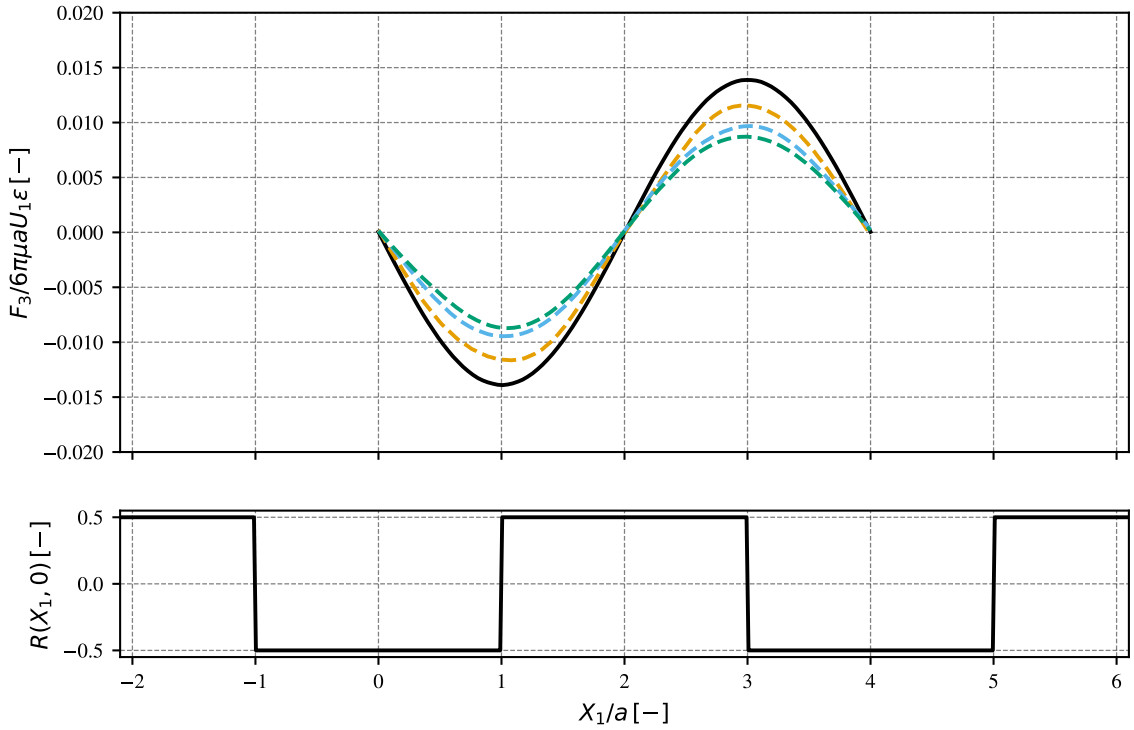

Figure 4.1: Force needed to hold the particle at a constant altitude along a square groove pattern of period $L = 4a$ with equal length at the top and the bottom of the groove. Comparison between numerical simulation using the YALES2BIO-FCM model for (– – –) $\varepsilon = 0.2$, (– – –) $\varepsilon = 0.4$, (– – –) $\varepsilon = 1.0$ and (——) analytical theory ($\varepsilon \ll 1$).

Comparing the results of the FCM simulations in dashed lines and the analytic model in continuous line, it appears that even for the smallest structures at $\varepsilon = 0.2$, the amplitude of the force in the FCM simulation is still not matching the values of the analytical model, suggesting that the amplitude of the structures is still too high. Nevertheless, when the amplitude of the simulation structure are decreased, it can be clearly seen that the amplitude of the force obtained in the FCM simulations converges towards the analytical force. On the other hand, when the amplitude of the structure is increased, the amplitude of the force drifts away from the analytical solution as effects due to the finite size of the structure start to arise. However, even though the amplitude is not matched, the extrema and the points of zero force agree between the models.

It must be noted that the mean force acting on the particle is zero for all the simulation curves and the analytic result, as indicated by the anti-symmetry of the curves over a period, which is in agreement with the reversibility of Stokes flows. Indeed, during the first half of the period $X_1 \in [0, 2a]$ the particle is subjected to a step-up resulting in a vertical force. From then, reversibility states that if the movement of the particle is reversed, the forces acting on it will also be reversed, and it will go back to its initial position eventually. In this reversed scenario, the particle would be confronted to the same step down as if it had continued its motion over the second half of the pattern period, indicating that such symmetric pattern cannot generate any net lift force on a spherical particle. This can also be explained by Purcell's Scallop theorem [Purcell 1976] which exposes the conditions for a microsmiwer in an unbounded viscous flow to generate movement through a swimming motion. The theorem states that if the swimming motion is reversed, and this reversed motion is the same as the mirror image of the initial motion, then no net displacement can be achieved through this swimming motion. Even though we do not study microswimmers in unbounded fluid, the considered movement

of the particle over the square corrugations is the same whether the movement is reversed or observed through a mirror perpendicular to the direction of the particle, suggesting that the particle must be back to its initial altitude after translating a pattern period.

Following this observation, similar comparison between FCM simulations and the analytical model were conducted for an upward sawtooth structure of period $L = 6a$. In this case, the principle of reversibility cannot conclude on the amplitude of the lift force acting on the particle. This does not necessary mean a net force will be present, but all can be said is that if a lift force is present, then reversing the motion of the particle will lead to a lift force in the opposite direction. The Scallop theorem is not able to conclude neither, as the mirror image of the particle motion is still the same particle translating over the upward sawtooth structure, while the reversed motion is that of a particle translating over downward sawteeth.

The resulting forces are plotted in figure 4.2.

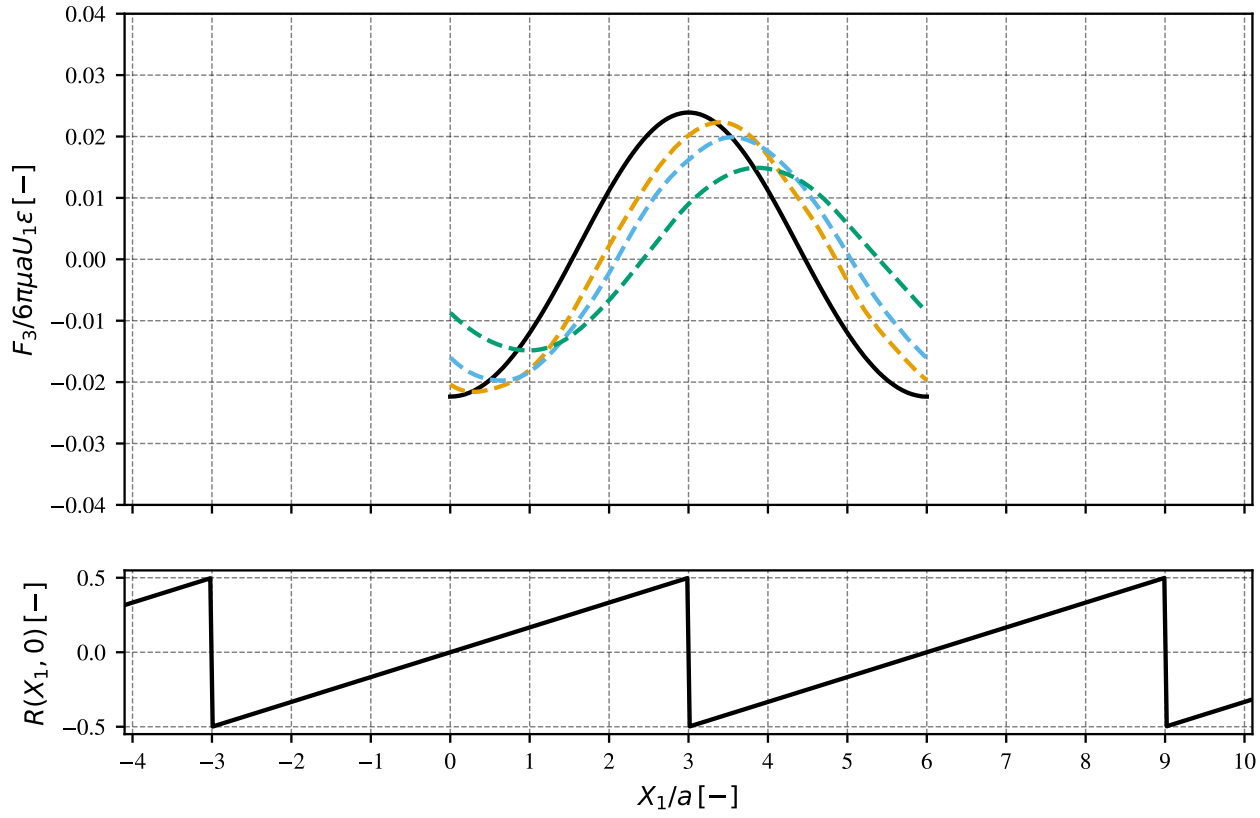

Figure 4.2: Force needed to hold the particle at a constant altitude along a sawtooth groove pattern with period $L = 6a$. Comparison between numerical simulation using the YALES2BIO-FCM model for (– – –) $\varepsilon = 0.2$, (– – –) $\varepsilon = 0.4$, (– – –) $\varepsilon = 1.0$ and (——) analytical theory.

As for the square corrugations, decreasing the amplitude of the structure tends to make the amplitude of the force converge towards the analytical results, even though the structure $\varepsilon = 0.2$ is not small enough to match the analytical result. In this case however, a shift in the location of the extrema and points of zero force is also observed when the amplitude of the structure is increased, which was not observed for the square corrugations. This suggests that changing the size of the structure also changes the behavior of the fluid and the particle in the longitudinal direction, as the pattern is not symmetric anymore.

However, the mean force exerted on the particle over one period of the pattern remains zero, both in the FCM simulations and in the analytical solution. To investigate whether a net drift can arise

when the particle is not constrained, it is necessary to consider the case of freely moving particles. Also, the non-sphericity of the particle can play a role in the breaking of the symmetry of the pattern. The following section is therefore dedicated to the study of the dynamics of freely moving ellipsoidal particles interacting with structured surfaces, in order to evaluate the influence of particle shape on the emergence of a net drift.

4.2 Ellipsoidal particles interacting with structured surface

From the previous comparison between the analytical method and the FCM simulations, it seems that no net force will be acting on the particle when it is flowing at constant altitude past a period of the structure pattern, at least for a spherical particle. In this section, we investigate the case of a freely moving ellipsoidal particle with the FCM model. The simulation configuration is presented in figure 4.3 where an ellipsoidal particle with semi-axis $a_1 = a_2 = 2a$ and $a_3 = a$ is initially placed at a distance $h_0 = 2.5a$ from the top of the investigated structures corresponding to $x_3 = 0$ as if the structures were carved into the flat surface. A linear shear flow with shear rate $\dot{\gamma} = 2000\, s^{-1}$ is driven by the translating top wall located at $x_3 = 40a$, no slip boundary condition is applied to the structured bottom wall. The side boundaries located at $x_2 = \pm 10a$ and $x_1 = \{0, 5L\}$ are set with periodic boundary conditions, where L is the period of a surface structure pattern. The surrounding fluid has the properties of blood plasma so that $\rho = 1023.9\, kg.m^{-3}$ and $\mu = 1.2\, mPa.s$ [Mody & King 2005]. The resulting particle Reynolds number for these simulations is $Re_p = 4a^2\dot{\gamma}/\nu = 3.83 \times 10^{-3}$.

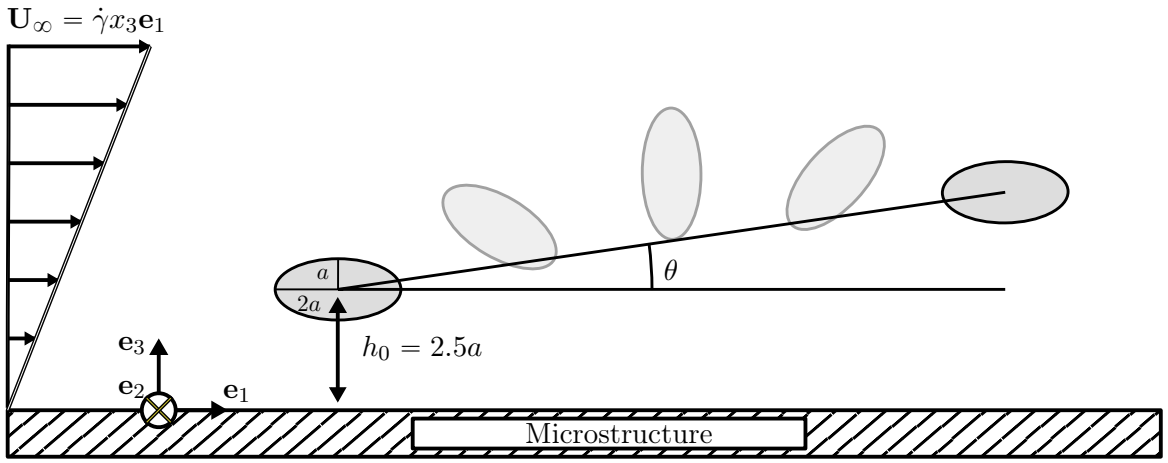

Figure 4.3: Configuration for the simulation of ellipsoidal particle interacting with a structured surface. The drift angle θ is measured from the change in altitude between the initial position of the particle and its position after performing a 180° rotation. The depicted movement of the particle and resulting drift angle are overly exaggerated for clarity. Different microstructure patterns are investigated, each time positionned so that the top of the structure is at $x_3 = 0$, resulting in an initial particle to top of the structure distance of $h_0 = 2.5a$.

To measure the effect of the structure on the particle, the particle is let free to move after a static initialization time of $50\,\mu s$ as discussed in the previous chapter, and its position is tracked through a 180° rotation around axis $\mathbf{e}_2$. The result is a drift angle defined by $\theta = \tan^{-1}(\Delta x_3/\Delta x_1)$ where Δx_3 is the change in the particle altitude between its final and initial position, and Δx_1 is the longitudinal displacement over the flipping motion.

As mentioned in the introduction of the chapter and in the previous comparison with the analytical model, two different structure shapes are investigated. First, a symmetric square groove perpendicular to the flow direction with 2 different sizes of the pattern were tested where the length of the top of

the grooves was kept constant, but the length of the bottom part was either equal or twice as large as the top. Then a sawtooth pattern is investigated, for which the orientation was changed so that the reversibility of the flow is observed. The amplitude of all the structures were $h = 4a$ while their pattern period were $L = 6a$ except for the simple groove structure for which $L = 4a$ as indicated in figure 4.4.

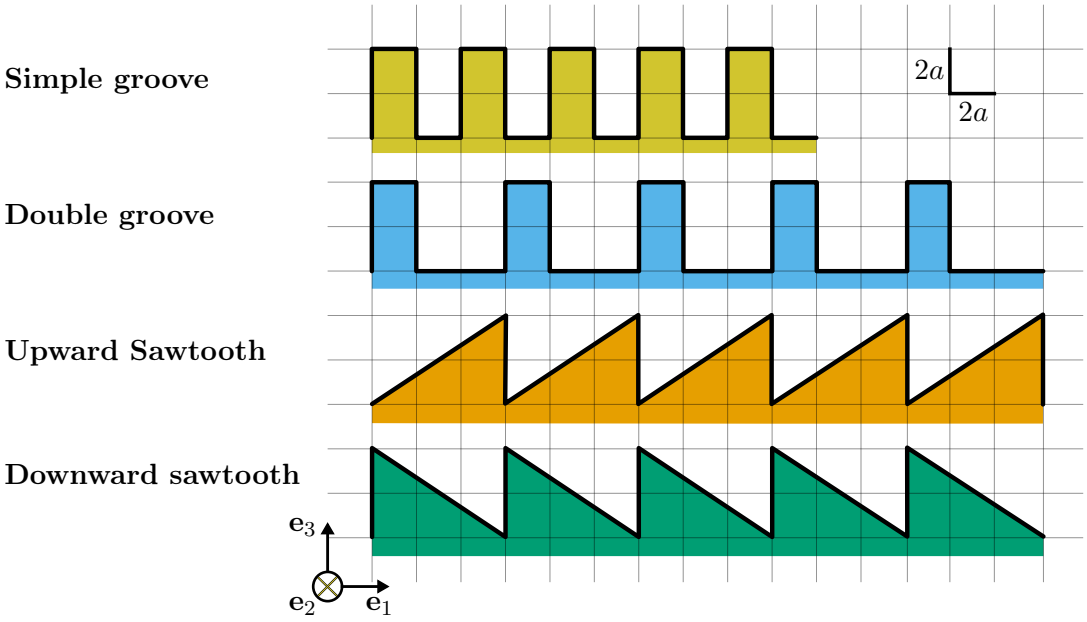

Figure 4.4: 2D slice of the geometries investigated for the study of ellipsoidal particle dynamics over the structured surface. This 2D slice is extruded in direction $\mathbf{e}_2$ to obtain the surface microstructure pattern. The grid squares have dimensions $2a \times 2a$.

Also, because we fix the initial altitude of the particle, the longitudinal position of the particle in the structure pattern determines the streamline it is deposited on as well as the position in the pattern where the particle flipping will occur (*i.e.* when the particle will be oriented at 90°). To smooth out the effect of the initial position, the simulation is performed for 10 initial particle positions in the pattern period, at the same initial altitude, so that the average drift angle over the initial positions is obtained. This mean drift angle is particularly useful to extend the trajectory of the particle to multiple consecutive flipping. Indeed, as the particle will perform one flip, it might not land at the same position in the structure pattern as the one it originates from. Therefore, the drift angle of the second flip might be different of the first one, and so will be the third and following ones. Using the mean drift angle is therefore an easy way to know the average gain in altitude for a given travel distance of the particle.

4.2.1 Symmetric pattern - Square grooves

The first structure is a square groove pattern, oriented perpendicular to the flow direction. This geometry was chosen first for its simplicity, but considering the structure is symmetric, the reversibility of Stokes flows suggests that no net drift should be observed as already discussed. The resulting drift angles for the different initial particle positions in the pattern are shown on figure 4.5 by markers as well as a fitted line which is used to compute the mean drift angle with more accuracy than the discrete points.

For each structure, the drift angle measured for an ellipsoidal particle over a flat surface is used as a reference and indicated by a black horizontal line. This drift angle is supposed to be zero at perfectly

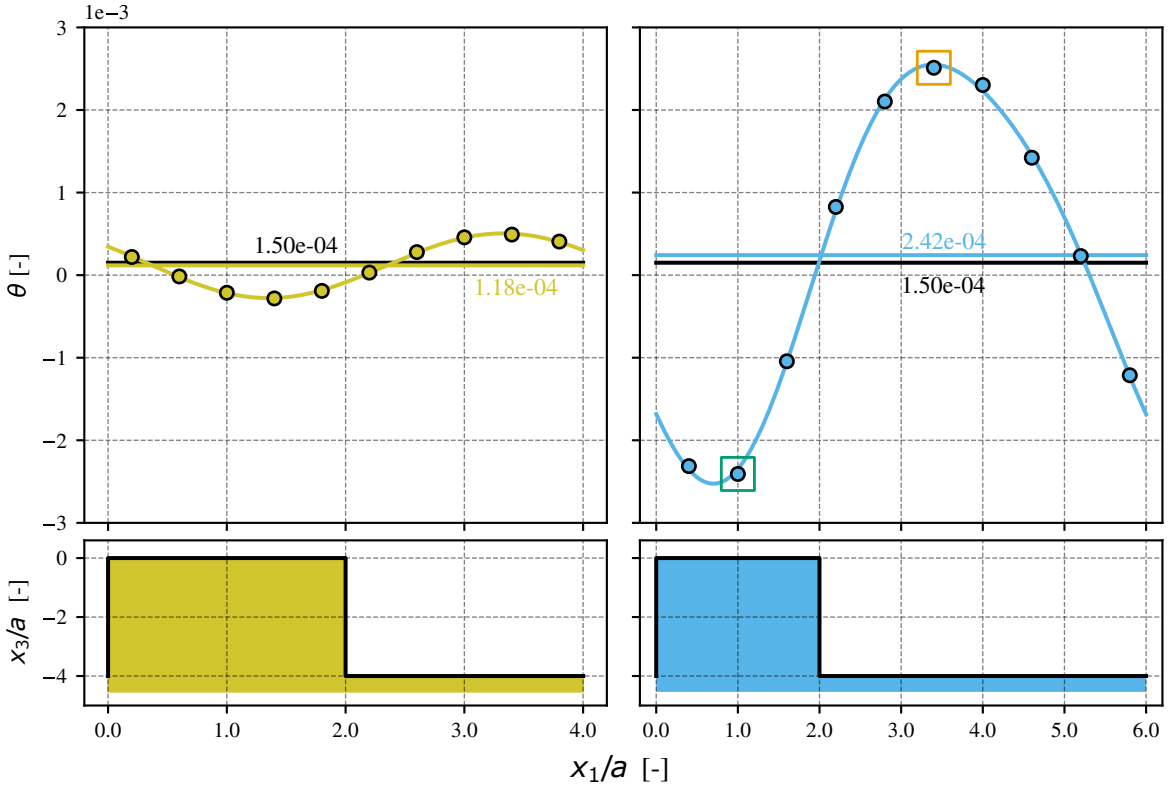

Figure 4.5: Drift angle for different initial positions of an ellipsoid with aspect ratio 0.5 initially placed at a distance $x_3 = 2.5a$ from (——) a flat surface, (—●—) a simple-spaced groove surface, (—●—) a double-spaced groove surface. The dots indicate the drift angle in radians for the corresponding initial position of the particle obtained with the FCM model and the first two terms of a Fourier series are fitted through the points to obtain the mean value over the initial positions with more accuracy. The mean value is shown as a horizontal line of the corresponding color as well as its value. The trajectories for the particles yielding the maximal and minimal drift angle, indicated by colored squares, are plotted on figure 4.6.

zero Reynolds number. However, these simulations are performed at $Re_p = 3.83 \times 10^{-3}$ which is small but not exactly zero, therefore some inertial effects are still present. Note that the fluid properties, particle dimensions, and shear rate all lies in physiological range for blood platelets, therefore residual inertial effects are indeed present for platelets, even though they are small.

Regarding the drift angle over the structured surfaces, the first observation is that it is not always zero as expected. Indeed, the resulting drift angle is sometimes positive or negative, with amplitude almost 20 times that of the drift angle over a flat surface for the double groove structure.

Such drift must come from the ellipsoidal shape of the particle, as the structures do not induce any dissymetry. This leads to interferences between the oscillatory motion caused by the translation over the structures, and the oscillation due to the flipping of the particle discussed previously on a flat surface. The trajectories for the initial positions yielding the maximal and minimal drift angle over the double groove structure, indicated by colored squares on figure 4.5, are plotted on figure 4.6.

The first observation is that the initial position of the particle effectively determines the streamlines the particle will follow, as the particle initially at the top of the structure will start to move downward as it first faces the downward step, while the particle initially placed close to the middle of the groove will initially rise upwards as it faces the upward step. On these trajectories, the combination of the oscillatory motion due to flowing above the structures can be observed as well as the rise of the particle when it is approaching 90°, indicated by the vertical ellipse marker. Around the flipping location, a

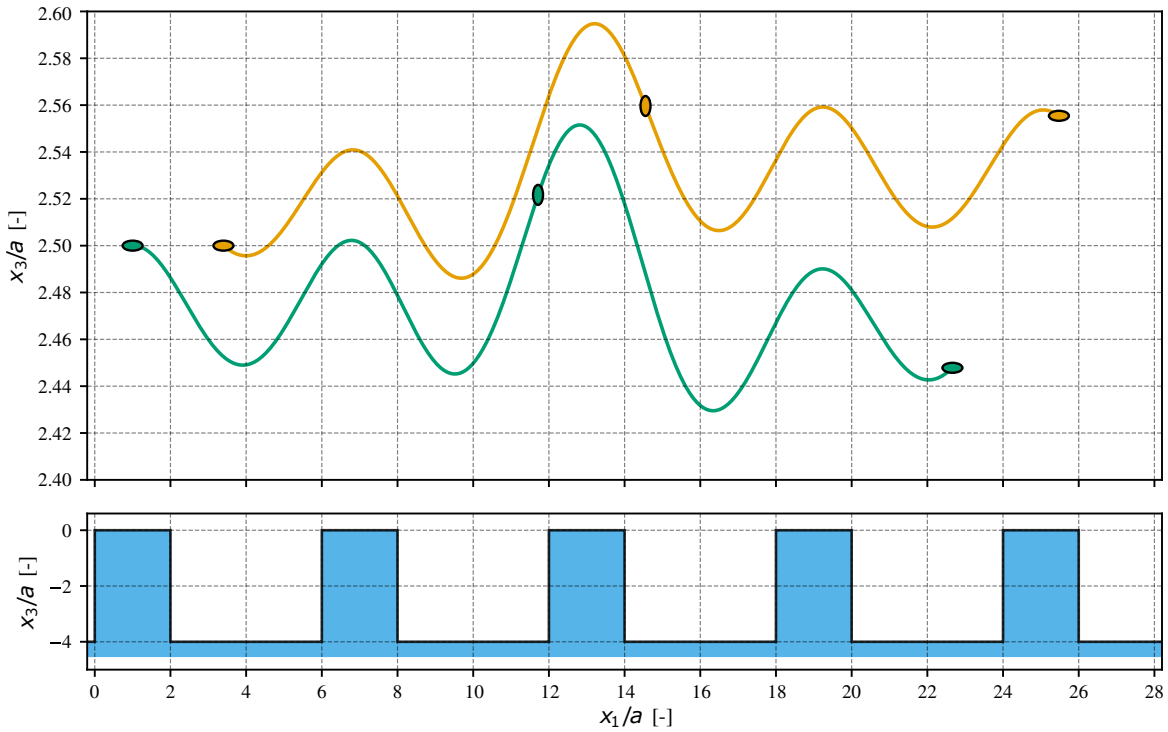

Figure 4.6: Trajectories of ellipsoidal particles over the double groove structure resulting in (——) maximal drift angle, (——) minimal drift angle. The orientation of the particle along the trajectories is indicated by the markers, highlighting the location of the particle flipping in the structure pattern.

clear step in the mean particle altitude can be observed, suggesting that the drift angle is related to the flipping of the particle. Indeed, it seems that the particle flipping nearby the downward step, will not be going down as much as it went up. The opposite observation can be made for the particle flipping around the upward step, which will sink deeper after its flipping and crossing of the structure.

Such interaction between the particle flipping and the structure oscillations lead to a net drift of the particle over one flipping motion. Note that if these two particles' final position is used as an initial position, the resulting drift angle is of opposite sign which is in agreement with the reversibility of Stokes flows.

However, the mean value of the drift angles over the initial positions of the particle is very close to the drift angle over a flat surface as shown on figure 4.5. This indicates that these structures, because of their symmetry, will generate as much lift upward as downward, resulting in no other net effect than an inertial lift due to small yet non-zero Reynolds number. This further suggest that using an asymmetric surface structure can be the key to generate a net lift force on the particle which is discussed in the next section by investigating the interaction between the same ellipsoidal particle and sawtooth shaped structures.

4.2.2 Symmetry breaking pattern - Sawtooth

Following the same protocol as introduced for square corrugations, triangular corrugations referred to as sawtooth patterned structures are investigated. As discussed previously, the Stokes reversibility principle tells us that reversing the flow should also reverse any lift force acting on the particle, so that a structure which is symmetric should produce the same force on the particle in either direction, indicating this force must be zero. Now, when the reversed flow is not the same as the initial flow, the principle still states that the force should be reversed, but it cannot be used to conclude on the amplitude of this force. To highlight this principle, the sawtooth shape is investigated both in an upward orientation and a downward orientation which is the same as a reversed motion over the upward sawtooth.

Result of the drift angle for the different initial positions in the structure pattern are presented for these two structures on figure 4.7, again with the first two terms of the Fourier series used to obtain the mean drift angle as well as the drift angle over a flat surface used as a reference.

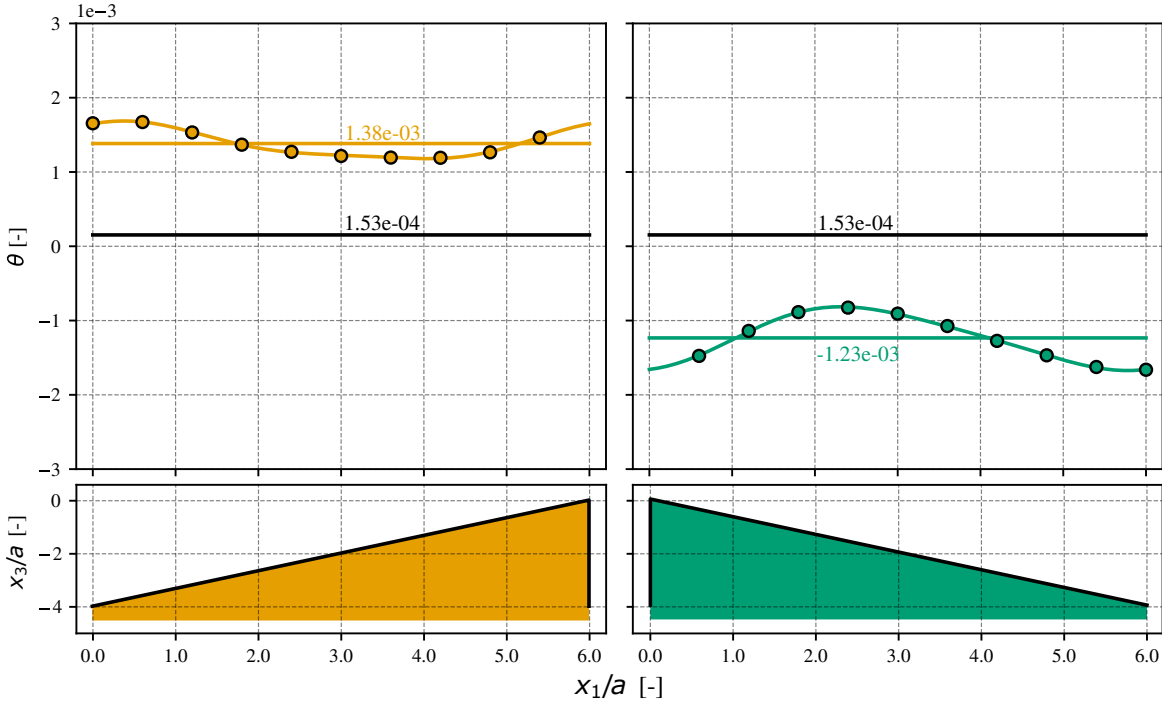

Figure 4.7: Drift angle for different initial positions of an ellipsoid with aspect ratio 0.5 initially placed at a distance $x_3 = 2.5a$ from (——) a flat surface, (—●—) an upward sawtooth structure, (—●—) a downward sawtooth structure. The dots indicate the drift angle in radians for the corresponding initial position of the particle obtained with the FCM model and the first two terms of a Fourier series are fitted through the points to obtain the mean value over the initial positions with more accuracy. The mean value is shown as a horizontal line of the corresponding color as well as its value.

The most notable observation is that the drift angle has a constant sign over the different initial positions, whether it is strictly positive for the upward sawtooth or strictly negative for the downward sawtooth. This results in a non-zero mean drift angle for both of these structures that is 8 to 9 times that of a particle over a flat surface and induced by inertia. Also, the variations of drift angle around the mean value from the different initial positions are much less important for these structures than for the double groove structure previously described, even though the amplitude and the period of the structures are the same.

Comparison between the mean drift angle for the upward and downward sawtooth are also in

agreement with the reversibility principle, up to the small inertia effects. Indeed, the difference between the magnitudes of the mean drift angle of the upward and the downard sawtooth structures is around 1.5×10^{-4} radians, which is in the range of the drift angle over a flat surface due to inertial effects.

From these simulations, it appears that an upward sawtooth structure is beneficial in the context of reducing blood platelet interactions with the surface, as platelets would be repelled. As a broad estimate, taking the drift angle of a platelet as the mean drift angle of the ellipsoidal particle (1.38×10^{-3}), it would take the platelet about $75, \mu$m, or about $100a$, to drift away from the wall by a distance of $100\,nm$, which is a typical length scale for blood platelet adhesive bond formation [Ruggeri 2009].

Another way to estimate how meaningful this structure-induced drift is is to compare it to a gravity-induced drift. Indeed, gravity was not accounted for in the simulations, but a gravitational drift angle based on the horizontal particle velocity and the vertical sedimentation velocity due to gravity can be computed. Taking the density of a blood platelet as $\rho_{PLT} = 1064.5\,kg.m^{-3}$ [Martin *et al.* 2008], and the mobility of a sphere of radius a in an unbounded fluid, the sedimentation velocity is expressed as

$$U_{settling} = \frac{(\rho_{PLT} - \rho)\frac{4}{3}\pi a^3 g}{6\pi\mu a}. \tag{4.3}$$

Defining the gravitational drift angle as $\theta_g = \frac{U_{settling}}{2.5a\dot{\gamma}}$, with the horizontal velocity taken as the undisturbed fluid velocity at the center of mass of the particle, and matching it with the structure-induced drift angle suggests that gravitational sedimentation overcomes the effect of the structures only when the flow is sufficiently slow, that is, for shear rates lower than around $15\,s^{-1}$. At the considered shear rates ($2000\,s^{-1}$), the effect of structures largely overcomes the effect of gravity.

Lastly, the structure-induced drift is compared to the margination drift of platelets in red blood cell suspensions. [**?**] provides trajectories of platelets marginating in red blood cells for different hematocrits. Taking the margination drift angle as the angle between a horizontal line and the line formed by the initial and final positions of the platelet in each trajectory yields $\theta_{\phi=0.20} = 0.92 \times 10^{-3}$, $\theta_{\phi=0.30} = 1.66 \times 10^{-3}$, and $\theta_{\phi=0.40} = 2.33 \times 10^{-3}$ for the 0.20, 0.30, and 0.40 hematocrits, respectively. Taking the structure-induced drift angle as 1.38×10^{-3}, it appears to be of similar magnitude to the margination drift at the lowest hematocrits.

The end of this chapter is dedicated to the investigation of the effect of various structure parameters on this drift angle considering an upward sawtooth only. In the next chapter, the interaction between the particle and the structure is studied in more details to provide an explanation for this drift angle.

4.2.2.1 Effect of the pattern height

In the previous section, the structure height was fixed at $h = 4a$. In this section, the effect of the height of the structure on the drift angle is investigated. As it was shown on figure 4.7, the variations of the drift angle from the different initial positions around the mean drift angle are small, so we restrict this study to a single initial position for each structure height to limit the computational cost.

The amplitude of the structures is varied by keeping the altitude of the top of the structure at $z = 0$, corresponding to a structure carved more or less deeply into the flat surface. The particle initial distance to the top of the structure is again $x_3 = 2.5a$ and the height of the structure ranged from $0.5a$ to $6a$. The resulting drift angle for each structure height is plotted on figure 4.8.

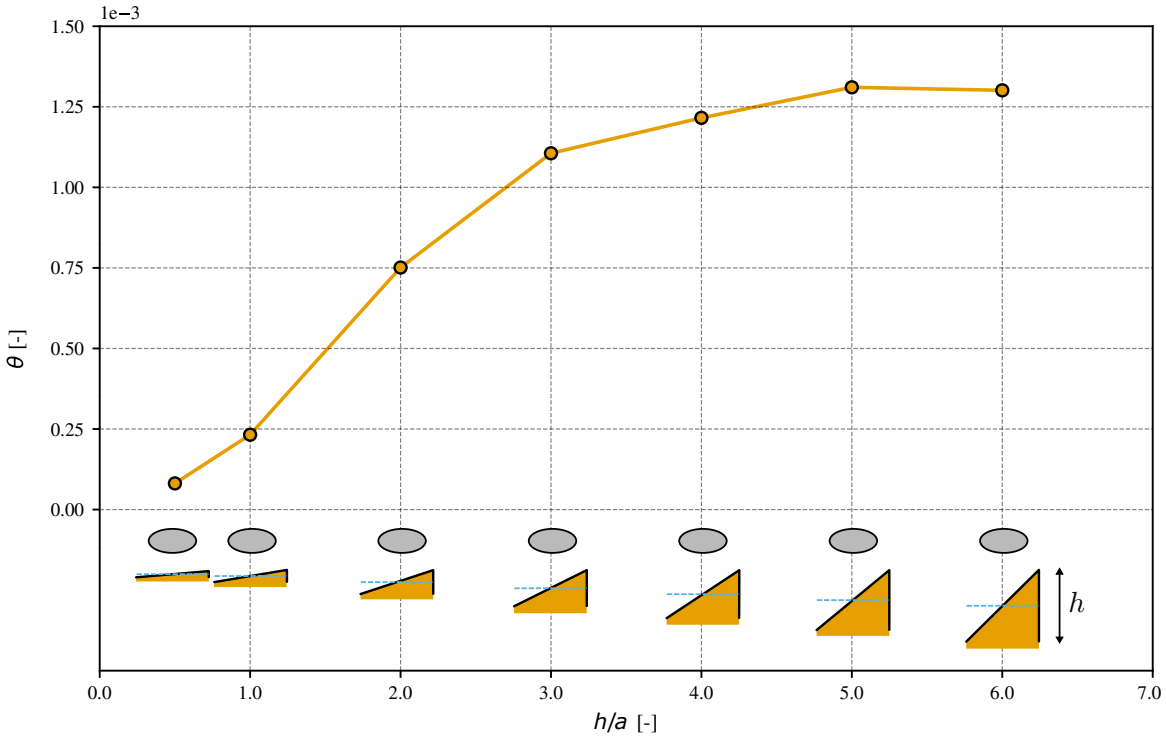

Figure 4.8: Evolution of the drift angle for a particle placed initially in the middle of the upward sawtooth pattern with the height of the structure. The corresponding particles size, distance to the top of the structure and sawtooth height and width are depicted with the real scale. The dashed blue line indicate the equivalent flat surface of the structure.

Two observations can be done regarding the effect of the height of the structure. First, when the height of the structure is decreased towards zero, the drift angle is also decreasing towards zero. This is in agreement with the fact that no lift is present over a flat surface, which corresponds to the case $h = 0$, up to the inertial effects. This is also in agreement with the analytical solution which indicates no net force was acting on the spherical particle over structures of negligible amplitude compared to the particle radius (section 4.1). This result shows that the observed drift is due to the finite size of the structures or the ellipsoidal shape of the particle.

On the other hand, when the structure amplitude is increased, the drift angle reaches a threshold, and does not increase any more past $h = 5a$. This can be explained by two mechanisms. First, by imposing that the top of the structures remains at the same altitude, the equivalent flat surface at the mean height of the structure is forced to be lowered as the height is increased, resulting in an increase in the distance between the particle and the equivalent flat surface. This leads to reduced interaction between the particle and the structure that can explain why the drift angle is not increasing anymore.

Also, regarding the fluid dynamics around the structure, when the size of the structure increases, there is an increase in the vertical velocity of the fluid in the vicinity of the top of the structures, but this also reaches a threshold. This is depicted on figure 4.9 where the first non-recirculating streamline is plotted over the structures of different sizes. It can be seen that past a certain structure height, the volume of fluid entering the structures is not increasing anymore and only the recirculating region is increased. This indicates that the increase in structure height does not lead to additional effects above the structures.

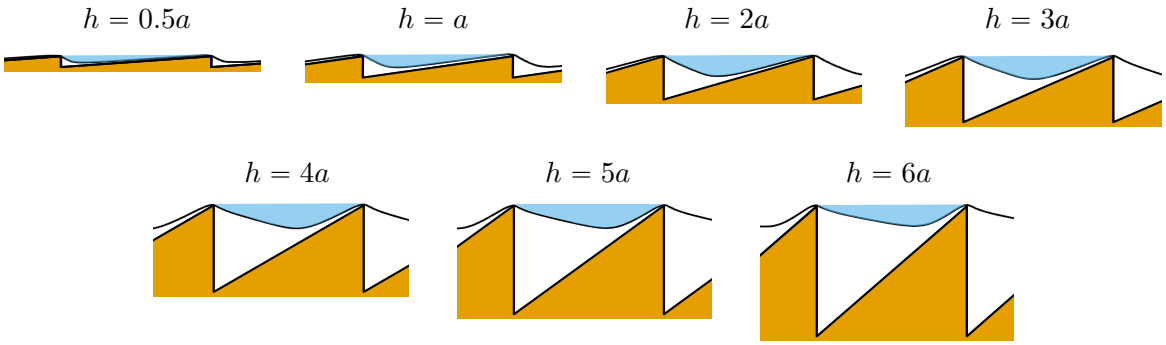

Figure 4.9: (——) Lowest non-recirculating streamline. ( ) Region where fluid enters the core of the structure but is not trapped. The fluid between the structure and the streamline is trapped and recirculating.

Note that when the structure amplitude is increased, the minimum of the streamline is shifted towards the right. A similar shifting was observed when comparing the force required to hold a spherical particle fixed at constant altitude over such structures and the amplitude of the structure was increased similarly.

Increasing the height of the structures while keeping the pattern period constant also leads to the increase of the slope of the sawtooth. This tends to make the upward ramp stiffer and converging towards a vertical step as the height tend to infinity. This would result in a symmetric geometry and therefore no particle drifting is expected, confirming the drift angle should not keep increasing with the structure height but rather reach a plateau and eventually decrease back down to zero.

4.2.2.2 Effect of the pattern period

The effect of the pattern period is investigated by performing simulations for both a smaller and larger pattern than the previous case, with period $L = 4a$ and $L = 8a$ respectively. Again, because the effect of the initial position is quite small, we only conducted a reduced number of simulations to limit the computational cost, therefore only 3 initial positions are tested so that a mean value and variations around the mean value can still be observed and are presented on figure 4.10.

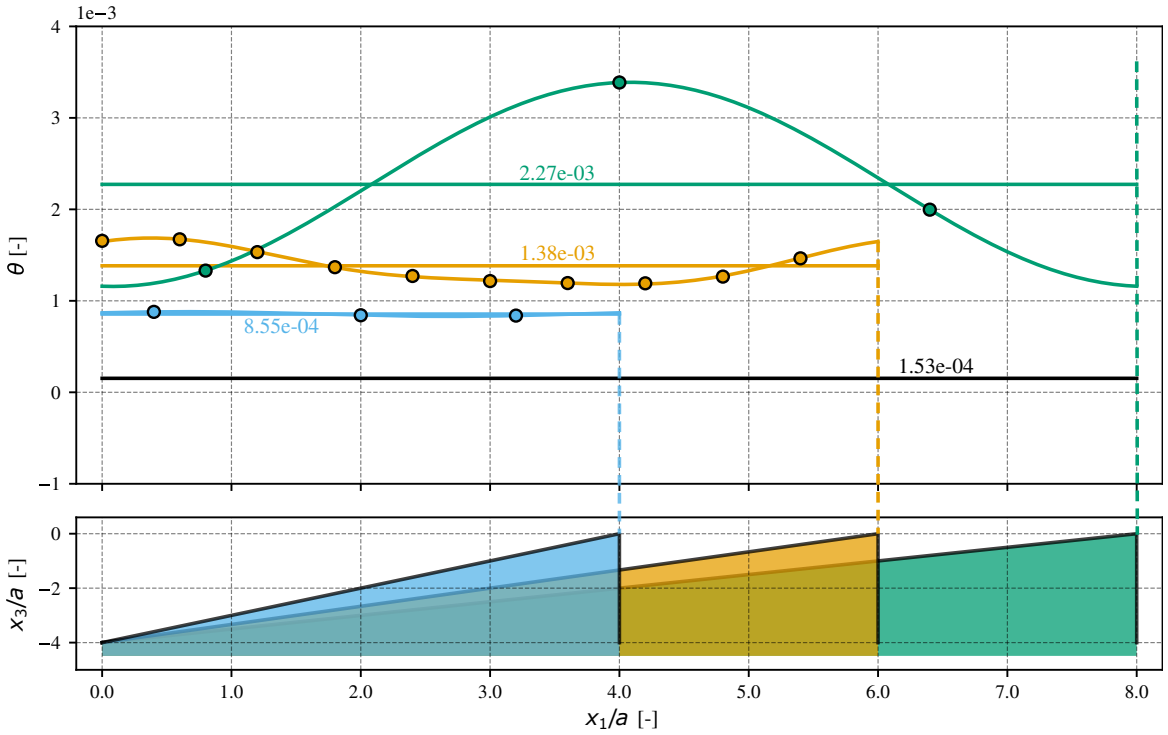

Figure 4.10: Drift angle for different initial position and different pattern period of an ellipsoid with aspect ratio 0.5 initially placed at a distance $x_3 = 2.5a$ from (——) a flat surface, (—●—) an upward sawtooth structure with period $L = 6a$, (—●—) an upward sawtooth structure with period $L = 3a$ and (—●—) an upward sawtooth structure with period $L = 8a$. The dots indicate the drift angle in radians for the corresponding initial position of the particle obtained with the FCM model. For the structure with period $L = 6a$ the first two terms of a Fourier series are fitted through the points to obtain the mean value over the initial positions with more accuracy, only the first term of the Fourier series is used for the structures with $L = 4a$ and $L = 8a$ as less data points were available. The mean value is shown as a horizontal line of the corresponding color as well as its value.

The first observation is that the mean drift angle is increasing with increased pattern period. As for the effect of the amplitude of the structures, if the structure period tends towards zero or infinity, the structure will tend to a flat surface where the drift angle should be zero, indicating that there must be a period which maximizes the mean drift angle. Therefore, the observed increase in mean drift angle here indicates that this maximum has not been reached. If we want to maximize the drift angle to minimize particle interaction with the surface we might want to increase further the pattern period but on the other hand, keeping the pattern period in the range of the particle size also provide a reduction of the available interaction surface if the particle cannot enter the core of the structure. Therefore, there might be a trade-off to find between a drift angle and a reduction in available adhesive surface.

Increasing the structure period also increases the drift angle variations over the initial positions, while we observe an almost constant drift angle for the structure with period $L = 4a$. The maximum

drift angle is also not achieved with the same initial position in the structure, as the frequency of the oscillations due to the structures have changed with the pattern period, but the frequency of the platelet flipping motion remained the same.

4.2.2.3 Effect of the Reynolds number

Lastly the effect of the Reynolds number on the drift angle is investigated. Once again, the trajectory for a single particle initially positioned in the middle of the ramp is simulated to reduce computational costs as the variation over the initial positions is small compared to the mean drift angle. The Reynolds number was varied by changing the shear rates to values of 1000, 2000, 4000 and 8000 s^{-1}. The resulting particle Reynolds numbers are respectively 1.92×10^{-3}, 3.84×10^{-3}, 7.68×10^{-3} and 15.35×10^{-3}. The evolution of the drift angle for the particle initially placed at the center of the ramp of the upward sawtooth structure is plotted on figure 4.11.

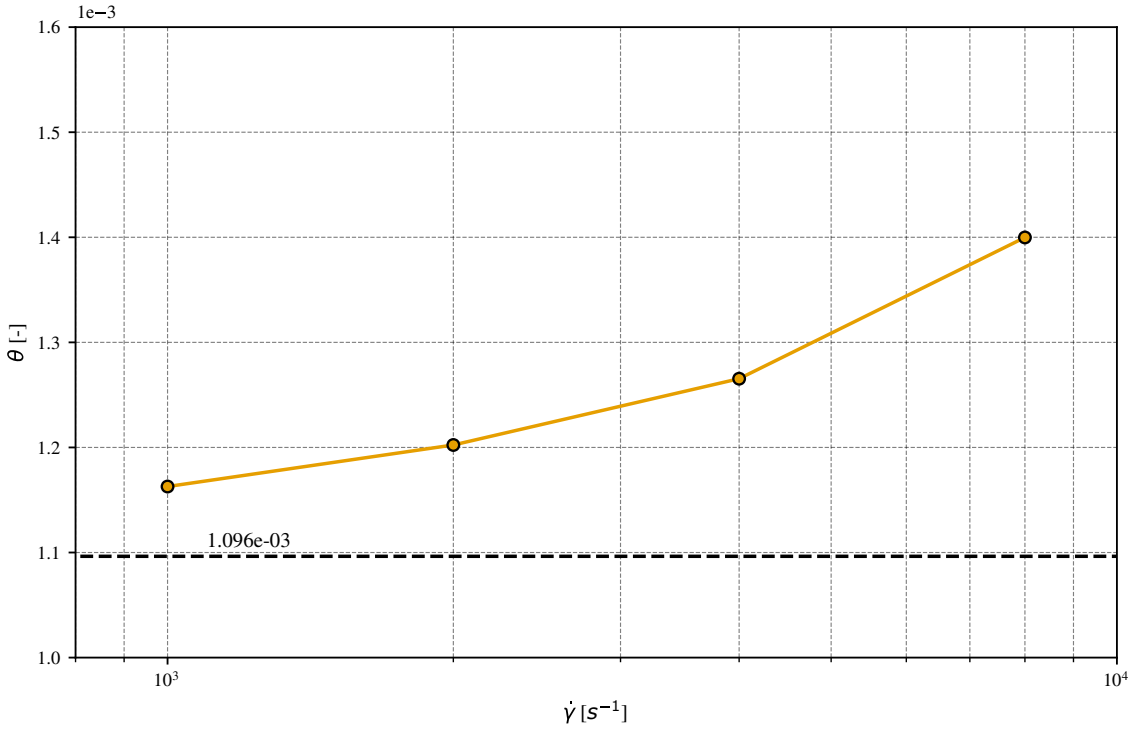

Figure 4.11: (—●—) Evolution of the drift angle with the shear rate for a particle initially placed at the center of the ramp over an upward sawtooth structure. (– – –) Asymptotic extrapolation of the drift angle in the case of perfectly zero Reynolds number.

The drift angle is decreasing with the shear rate, but we can see it is not converging towards zero. To estimate the drift angle at zero Reynolds number, an extrapolation is performed following [Sigüenza *et al.* 2016] which gives the apparent convergence order towards the zero Reynolds number as well as an estimation of the asymptotic value by using three data points. The convergence order is given by equation (4.4) where $r = 2$ is the ratio between two shear rate values and θ_{1000}, θ_{2000} and θ_{4000} are the drift angle with subscript indicating the corresponding shear rate.

$$p = \frac{1}{\ln(r)} \left| \ln \left| \frac{\theta_{4000} - \theta_{2000}}{\theta_{2000} - \theta_{1000}} \right| \right| \tag{4.4}$$

Once the apparent convergence order is found ($p \approx 0.67$), the asymptotic extrapolation of the drift angle towards Reynolds number of zero is obtained with relation 4.5 and plotted as a dashed horizontal

line on figure 4.11.

$$\theta_0 = \frac{r^p \theta_{4000} - \theta_{2000}}{r^p - 1} \tag{4.5}$$

This non-zero asymptotic value of $\theta_0 = 1.096 \times 10^{-3}$ suggests that the drift angle observed from the interaction between an ellipsoidal particle and an upward sawtooth structure pattern is not an inertial effect.

The next chapter is dedicated to the presentation of the various tests that were conducted to better understand the origin of this drift angle.

Chapter 5

Investigation of the particle drift over sawtooth structures

Contents

Following the observation of a drift angle for an ellipsoidal particle transported by a shear flow over sawtooth structures, as discussed in the previous chapter, this chapter focuses on identifying the mechanisms responsible for this drift. To achieve this, the problem is progressively simplified while retaining the essential features that produce the drift, thereby reducing the number of parameters involved. The first step is to consider a spherical particle, which removes the complex rotational dynamics associated with the ellipsoidal shape of blood platelets. We demonstrate that, although the drift is weaker than in the ellipsoidal case, it is still present for spherical particles. Next, the wall geometry is reduced to its simplest elements: instead of a periodic array of sawtooth patterns, we analyze the particle motion over an isolated ramp or step. On the other hand, for the periodic sawtooth configuration, we compute the particle's mobility matrix at different positions in a pattern to characterize the spatial variations in mobility and the resulting lift force.

5.1 Spherical particle transported over sawtooth structures

As mentioned in the introduction, the problem is first reduced to the study of the dynamics of a spherical particle transported by the ambient shear flow over the sawtooth structures. Compared to section 4.2.2, the structure is kept the same that is an upward and downward sawtooth structures with pattern period $L = 6a$ and height $h = 4a$. The particle is now a sphere with radius $a = 0.75\,\mu m$ instead of the ellipsoid of semi axes $a_1 = 2a$, $a_2 = 2a$ and $a_3 = a$. As for the case of the ellipsoidal particles, the initial position of the particle is varied in a structure pattern and the resulting drift angles are compared to the inertial drift of a spherical particle transported over a flat surface. The motion of the particle is now simulated for a single pattern period instead of a half flipping motion of the particle. This single pattern period distance is also used to compute the inertial drift angle over the flat surface for the spherical particle. The same shear rate and fluid properties are used as in section 4.2.2 so that $\dot{\gamma} = 2000\,s^{-}1$, $\rho = 1023.9\,kg.m^{-3}$ and $\mu = 1.2mPa.s$ yielding a particle Reynolds number of $Re \approx 10^{-3}$.

For the particle initially placed at $x_3 = 2.5a$ from the top of the structures, as in section 4.2.2, the mean drift angle is $\theta = 4.20 \times 10^{-4}$ radians for the upward sawtooth and $\theta = -3.59 \times 10^{-4}$ for the downward sawtooth and the drift over a flat surface is $4.15e-5$ radians (not shown). This indicates

that the observed drift is still present when the particle is spherical, even though it is about 3 times smaller than for the ellipsoidal particle ($\theta = 1.38 \times 10^{-3}$ radians for the upward sawtooth structure).

Figure 5.1 presents the same result for an initial particle to structure distance of $x_3 = 3a$, as the following experiments were conducted at this initial distance, ensuring easier comparisons.

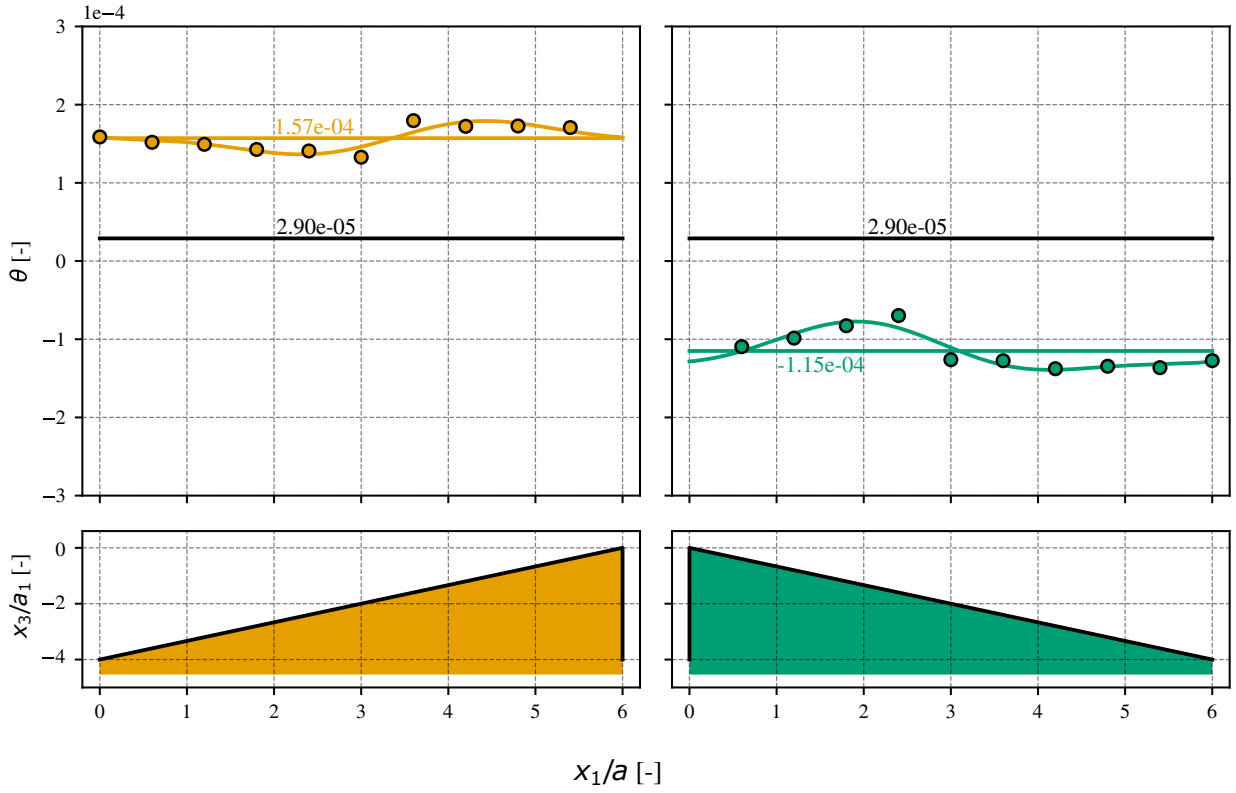

Figure 5.1: Drift angle for different initial positions of a spherical particle initially placed at a distance $x_3 = 3a$ from (——) a flat surface, (—●—) an upward sawtooth structure, (—●—) a downward sawtooth structure. The dots indicate the drift angle in radians for the corresponding initial position of the particle obtained with the FCM model and the first two terms of a Fourier series are fitted through the points to obtain the mean value over the initial positions with more accuracy. The mean value is shown as a horizontal line of the corresponding color as well as its value.

We can observe that increasing the distance between the particle and the structure leads to the decrease in the mean drift angle by about 2.5 folds, while the drift angle over the flat surface has only reduced by 1.5 folds. This suggests that the drift angle due to the structured surface is evolving quicker than the inertial drift with the particle distance to the structure.

Overall, these two results mean that the interaction of the spherical particle with the structures is enough to study the underlying mechanisms of this drift, which makes it easier to isolate the cause.

5.2 Isolated step and ramp

From previous observations (section 4.1), no net lift force is generated by the translation of a spherical particle over a small amplitude sawtooth pattern. Therefore, our intuition to explain the observed drift with structures of finite amplitude (figure 5.1) was that at negligible amplitude, considering either a ramp or a vertical step affected the spherical particle similarly, while on finite amplitude structures, a different effect was generated by these two elementary geometrical feature of the sawtooth pattern. Especially, we expected the threshold length scale to be of the order of a particle radius, where a ramp of length greater than a radius would be "felt" by the whole particle, while a ramp of smaller

length such as a vertical step, would only affect a part of the particle resulting in a smaller drift. This would explain why a combination of a long ramp-up and a short step-down generated a net drift of the particle.

To investigate this hypothesis, the sawtooth structure was decomposed into elementary geometrical features, which are a ramp-up and a step-down. The particle motion over these elementary features of the sawtooth was simulated with the FCM model by having the ramp or step placed between two flat surfaces as depicted on figure 5.2. The simulation domain was of size $4l$ in the direction of the particle motion, with l the distance bewteen the initial particle position and the middle of the ramp. The domain is symmetric and periodic boundary conditions are applied. The same simulation was carried with Dirichlet inlet boundary condition and stress-free outlet boundary condition, but the influence region of the boundary conditions were very big and required a very large domain so that the particle was not interacting with them. Therefore, the periodic domain was used, where periodic boundary condition is imposed on boundaries located at $x_1 = \{0, 4l\}$. The size of the domain is also increased in directions x_2 and x_3 to ensure no undesirable effect is present. Periodic boundary conditions are imposed on the side walls located at $x_2 = \pm 50\,\mu m$ and the ambient shear rate of $\dot{\gamma} = 2000\,s^{-1}$ is imposed via translation of the top wall located at $x_3 = 100\,\mu m$. The fluid properties remained the same as in chapter 4.

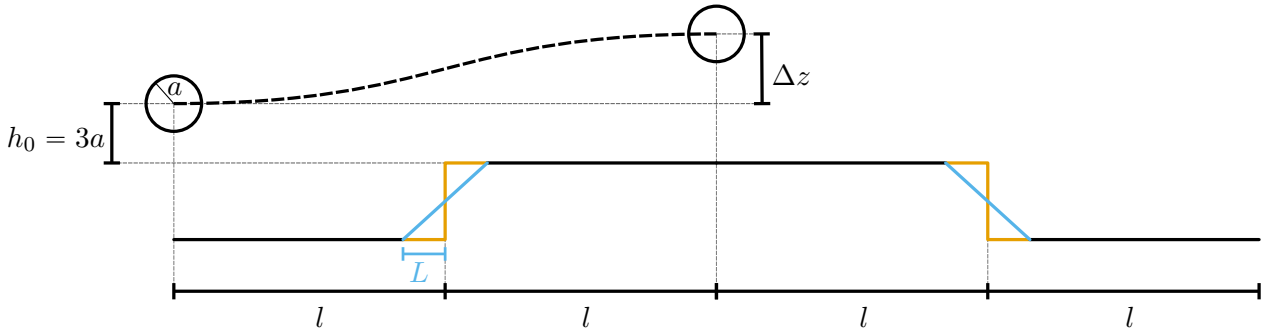

Figure 5.2: Configuration for the study of a spherical particle dynamics over an isolated ramp-up of different length L. The spherical particle of radius a is initially placed at a distance l from the middle of the ramp and at an altitude $h_0 = 3a$ from the top of the ramp. The vertical displacement Δz of the particle is measured after it is transported by a distance $2l$, and the resulting drift angle can be measured as $\theta = \tan^{-1}(\Delta z/2l)$.

The distance l between the initial particle position and the middle of the ramp was determined using the analytical model. It allowed to find the minimal distance l for which the particle experiences 0 force in the vertical direction for a brief period around its initial position, ensuring it is initially placed on an apparently flat surface from a hydrodynamic point of view before interacting with the step. Because the size of the step is very short compared to the overall period of the geometry, the description of the structure with a Fourier series decomposition requires a lot of terms and a lot of noise is generated around the step, degrading the quality of the computation. Therefore, following the discussion in chapter 2 on the two available methods for calculating the coefficient I_∞, for this particular case the calculation of I_∞ on the wall is used (equation (2.66)), which utilizes the exact expression of the structure and not a Fourier series decomposition, instead of the calculation of I_∞ on the surface of the sphere (equation (2.69)). As discussed and following [Assoudi *et al.* 2018], calculated this way, I_∞ must be accounted for twice in the total force given by equation (2.76). The force required to hold the particle at constant altitude over a vertical step for $l = 25a$, $l = 50a$ and $l = 100a$ is plotted on figure 5.3.

The vertical force required to hold the particle at constant altitude does not reach a plateau when

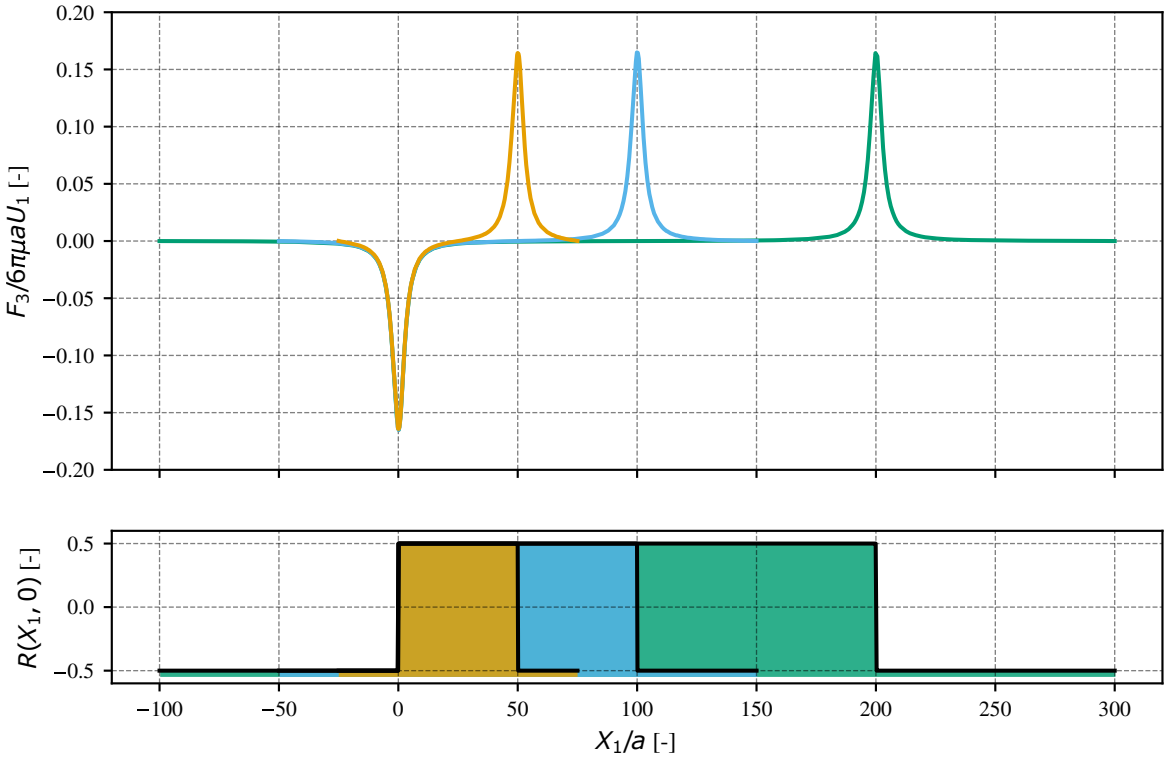

Figure 5.3: Evolution of the force required to hold a spherical particle at a constant altitude over a step-up and a step-down for different length l as depicted on figure 5.2. (——) $l = 25a$, (——) $l = 50a$ and (——) $l = 100a$. The results for the three geometries are shifted so that the step-up is aligned at $X_1 = 0$ between the geometries.

the particle is the furthest from both the upward and downward step ($X_1 = 25a$) for the domain with $l = 25a$, drawn in orange. On the other hand, taking a domain with $l = 100a$ results in a long period of apparent flat surface which is shown in green, but to minimize the computational time which is directly related to the size of the domain and the distance that the particle must travel, we take a domain with $l = 50a$ as a trade-off between a large enough flat surface but a particle trajectory as short as possible. In the introduction of this section, it was suggested that the origin of the drift could come from the localized force when the ramp is smaller than the particle radius, but this is contradicted by the very large range of action of the step on the particle shown on figure 5.3.

Using this geometry (see figure 5.2, with $l = 50a$), the analytical model is first used to confirm the effect of a ramp or a step is the same on the spherical particle if the amplitude of the structures is negligible. The force required to hold the particle at a constant altitude when it is transported over the upward ramp for different ramp length is plotted on figure 5.4.

The apparent effect of increasing the ramp length in the analytic model is to spread out the force exerted on the particle over a wider region, resulting in a smaller maximal force at the middle of the ramp. However, the mean value of the force remains constant between the different ramp length (less than 10^{-4}% of variation in the mean force) suggesting that a combination of a ramp-up and a step-down will result in zero mean force as expected.

Also, using this domain size, the particle trajectory is simulated with the FCM model for structures of finite height $h = 4a$, starting at a distance l upstream from the step-up and for a travel distance of $2l$. This is performed for different size of the ramp L which is varied by keeping the step height constant as well as the center of the ramp. The vertical step corresponds to the case $L = 0$.

The resulting trajectories for the different ramp length are shown on figure 5.5 with the color

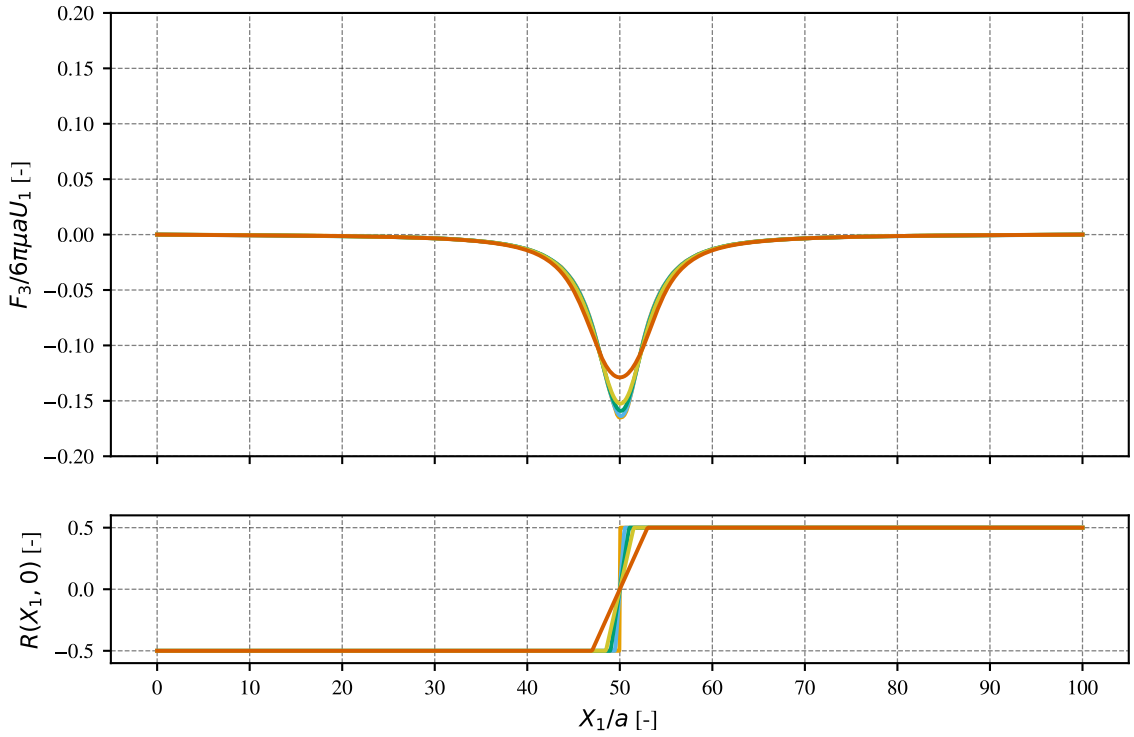

Figure 5.4: Analytical solution of the force required to hold the particle at a constant altitude over a ramp up of negligible amplitude and length (——) $L = 0$, (——) $L = a$, (——) $L = 2a$, (——) $L = 3a$ and (——) $L = 6a$.

matching structure on the bottom panel.

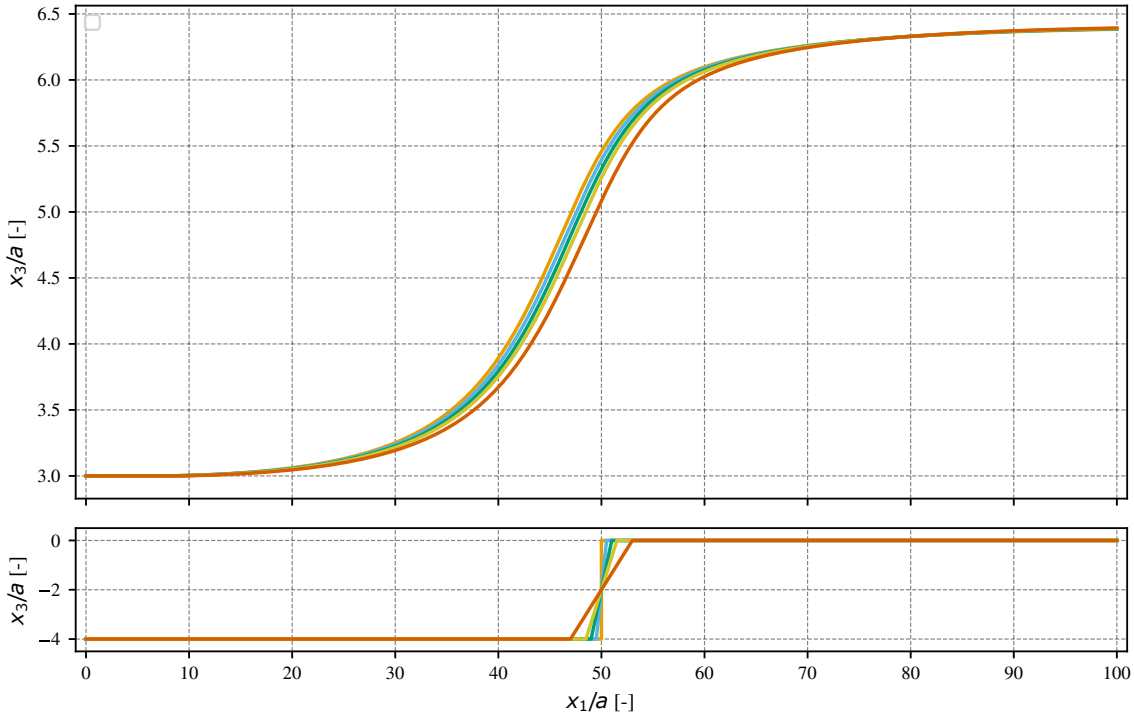

Figure 5.5: Particle trajectories for over an isolated ramp-up for different length of the ramp. (——) $L = 0$, (——) $L = a$, (——) $L = 2a$, (——) $L = 3a$ and (——) $L = 6a$.

The first observation is that the particle vertical displacement is of much greater amplitude than the one observed on the patterned structures. Indeed, for the case of an ellipsoid flipping over the square groove structure presented on figure 4.6, the amplitude of the particle movement is about 10% of a particle radius while for these long trajectories the particle has gained about $3.4a$ in altitude. This is due to the simulation of the trajectories over a much longer distance as well as the absence of the downward motion caused by the step-down in the structure.

From these trajectories it also appears that the final altitude is the same for all the ramp length. As depicted on figure 5.6, the change in particle altitude only varies by about 1% of the particle radius between the different ramp length. This is expected because the drift angles we found previously are very small, indicating that the effect of a ramp-up is almost balanced by a step-down. However, this value is very small compared to the overall dynamics of the particle suggesting that the measure can be heavily influenced by numerical errors or inertial effects accumulated over the long trajectory of the particle. This makes us believe that this configuration is not ideal to measure precisely the observed drift and to investigate its origin.

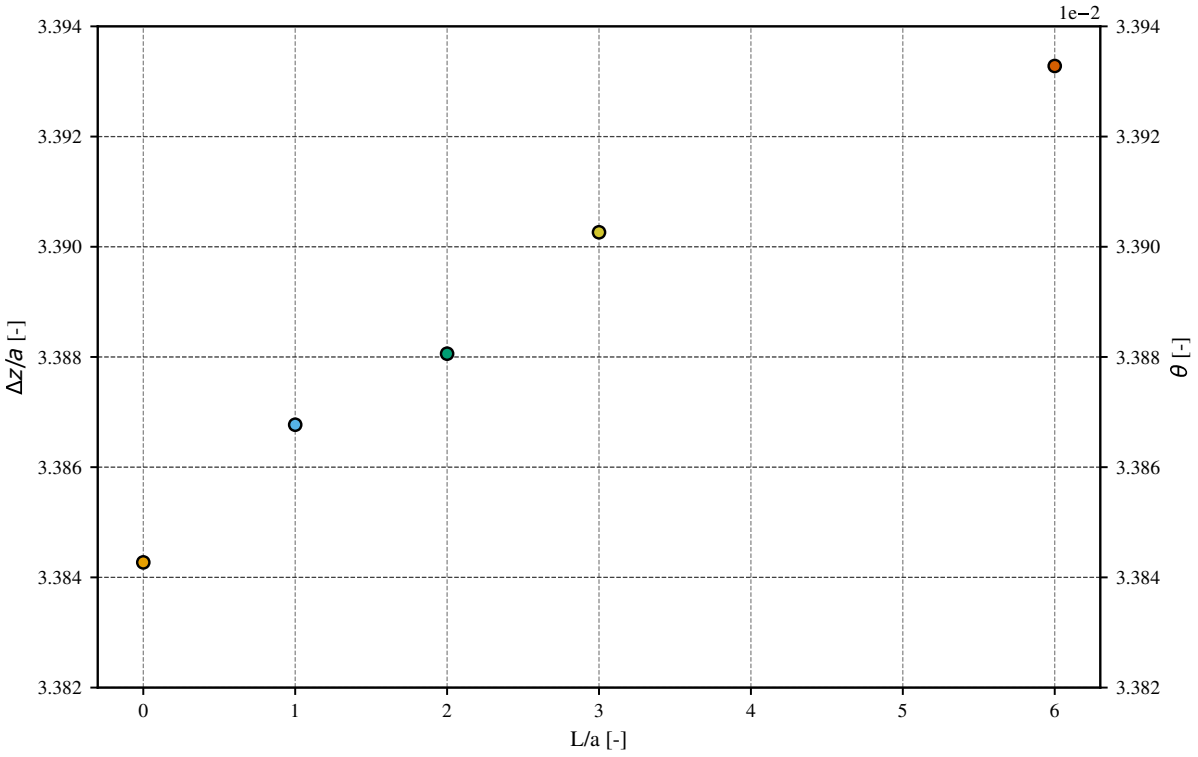

Figure 5.6: Evolution of the particle gain in altitude Δz and corresponding drift angle $\theta = \tan^{-1}(\Delta z/2l)$ of a spherical particle transported over an isolated ramp with varying ramp length L. (●) $L = 0$, (●) $L = a$, (●) $L = 2a$, (●) $L = 3a$ and (●) $L = 6a$.

Nevertheless, if we assume the flow is reversible, the drift angle over a sawtooth of length $L = 6a$ can be reconstructed by taking the drift angle associated with the long trajectory over the upward ramp of length $L = 6a$ and the opposite of the drift angle associated with the long trajectory over the upward vertical step $L = 0$. These values are respectively $\theta_{L=6} = 3.393 \times 10^{-2}$ and $\theta_{L=0} = 3.384 \times 10^{-2}$ radians, therefore the estimated drift angle over the sawtooth from these isolated features is $\tilde{\theta} = \theta_{L=6} - \theta_{L=0} = 0.9 \times 10^{-4}$ which is comparable to the values obtained over the patterned structures.

Also, figure 5.5 presents a shift in the particle trajectory. Even though the particles end up almost at the same altitude, they did not achieve it by following the same trajectory. From the vertical

step, increasing the ramp length tends to make the particle react later resulting in a shifting of the point of maximal force experienced by the particle towards the flow direction, as was already observed previously when comparing analytical results and FCM simulations over sawtooth structures (section 4.1). In this case, the analytical results do not predict this shifting as shown on figure 5.4 which again suggests this shifting is caused by the finite size of the structure.

From the previously discussed uncertainties regarding the amplitude of the measured effect compared to the amplitude of the particle dynamics, the same domain and geometries are used, but we now focus on the force exerted on the particle placed at the middle of the ramp.

The force required to hold the particle at constant altitude at this location is obtained with the FCM model for the different ramp lengths, as well as for different heights of the ramp, towards structures of negligible amplitude. This allows comparison with the analytical model so that the effect of the finite size of the structure is highlighted. The resulting forces are presented on figure 5.7.

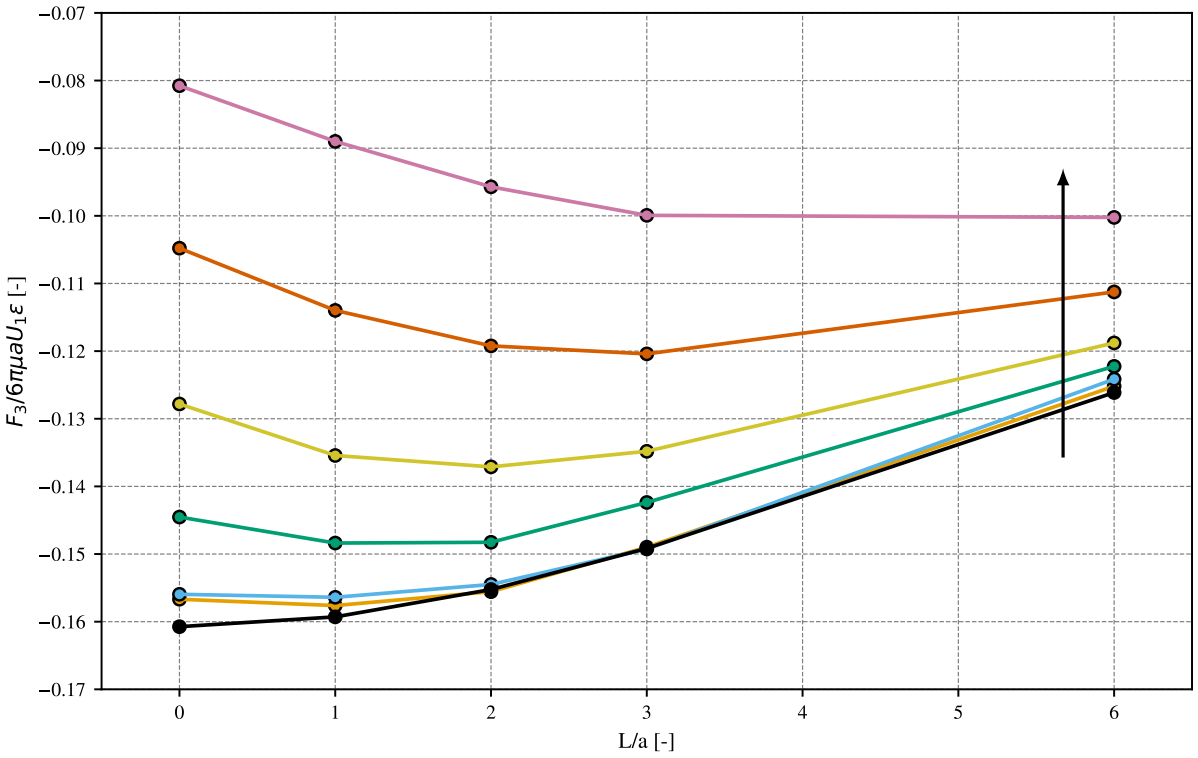

Figure 5.7: Evolution of the vertical force required to hold a spherical particle in the center of a ramp as a function of the ramp length, for different ramp height. (—●—) Analytic result for $h \to 0$, (—●—) $h = 0.1a$, (—●—) $h = 0.2a$, (—●—) $h = 0.5a$, (—●—) $h = 1a$, (—●—) $h = 2a$ and (—●—) $h = 4a$. The black arrow indicates the direction of increasing h. The force from the FCM simulations are scaled by $\varepsilon = h/a$ as detailed in section 4.1

The first thing to notice is again a very good agreement between the FCM model with structures of small amplitudes and the analytic model. The FCM converges indeed towards the analytical model which is reached almost exactly by the structures of height $0.1a$ and $0.2a$. For these cases, the magnitude of the force required to hold the particle at a constant altitude is greater for the vertical step $L = 0$ than for the inclined ramp. This was already observed from figure 5.4 which indicated that lengthening the ramp resulted in a smaller maximal force at the center of the ramp but an increased range of interaction.

Now when the structure height is increased, we observe a progressive shifting of the difference between the force required to hold the particle over a ramp of length $L = 6$ and the force required

to hold the particle over a vertical step $L = 0$. This difference is negative for structures of small amplitude, but ultimately becomes positive for the bigger structures, transitioning from negative to positive around the structure height equal to the particle radius. The maximal force is also shifted towards the bigger ramp length as the structure height is increased. This observation heavily suggests that the finite size of the structure plays a key role in the generation of the particle drift.

However, the study of this force at the middle of the ramp is not an accurate representation of the overall dynamics of the particle. Indeed, for the case of the smaller structures, the non-zero difference between the force needed to hold the particle over a ramp or a vertical step structure suggests that a net force would be acting on a particle translating over a sawtooth, which is not true, as was shown in section 4.1.

These results therefore highlights the importance of the size of the structure on the drift of the particle but do not explain the origin of this drift.

Another approach was then chosen to understand the underlying mechanisms. Back to the study of the motion of a spherical particle over patterned structures as in section 5.1, we observed no mean force acting on the particle held fixed at a constant altitude while transported over a pattern period (section 4.1), yet the same freely moving particle was experiencing a drift (section 5.1). This suggests that the origin of this drift might not lie in the vertical force exerted on the particle, which has zero mean value over a pattern, but in the way the overall forces (not only vertical) experienced by the particle convert into velocity; this information is included in the mobility matrix.

5.3 Mobility matrix of the particle over the patterned structure

In Stokes flows, the velocities (both translational and angular) of a particle are directly proportional to the forces exerted on the particle. This is usually expressed as a matrix-vector product where the matrix $\underline{\underline{M}}$ relating external forces and torques $\mathbf{F}$ to the resulting velocities and angular velocities $\mathbf{U}$ of a particle in quiescent fluid following equation (5.1) is referred to as the mobility matrix.

$$\mathbf{U} = \underline{\underline{M}}\mathbf{F} \tag{5.1}$$

For the case where the motion of the particle lies in the plane $(\mathbf{e}_1, \mathbf{e}_3)$, this relation can be expanded to equation (5.2).

$$\begin{pmatrix} U_1 \\ U_3 \\ \Omega_2 \end{pmatrix} = \begin{pmatrix} M_{U_1F_1} & M_{U_1F_3} & M_{U_1T_2} \\ M_{U_3F_1} & M_{U_3F_3} & M_{U_3T_2} \\ M_{\Omega_2F_1} & M_{\Omega_2F_3} & M_{\Omega_2T_2} \end{pmatrix} \begin{pmatrix} F_1 \\ F_3 \\ T_2 \end{pmatrix} \tag{5.2}$$

U_1 and U_3 are the velocities in direction $\mathbf{e}_1$ and $\mathbf{e}_3$ respectively, Ω_2 is the angular velocity around $\mathbf{e}_2$, F_1 and F_3 are the external forces acting on the particle in direction $\mathbf{e}_1$ and $\mathbf{e}_3$ respectively and T_2 is the external torque around axis $\mathbf{e}_2$.

The coefficient $M_{U_1F_1}$ therefore encapsulates the relation between the external force F_1 acting on the particle and the resulting velocity U_1 in this same direction. The total velocity of the particle in direction $\mathbf{e}_1$ from the contributions of the external forces and torque is then given by equation (5.3).

$$U_1 = M_{U_1F_1}F_1 + M_{U_1F_3}F_3 + M_{U_1T_2}T_2 \tag{5.3}$$

However, for the case of interest, the background shear flow results in a particle velocity and angular velocity even for a force free and torque free particle. This force free and torque free particle velocity

is noted $\mathbf{U}^0$ so that equation (5.1) now writes as equation (5.4) ensuring $\mathbf{U} = \mathbf{U}^0$ when $\mathbf{F} = \mathbf{0}$.

$$\mathbf{U} - \mathbf{U}^0 = \underline{\underline{M}}\mathbf{F} \tag{5.4}$$

This relation can also be written the other way around by using the inverse of the mobility matrix, called the resistance matrix and noted $\underline{\underline{R}} = \underline{\underline{M}}^{-1}$, so that:

$$\mathbf{F} - \mathbf{F}^0 = \underline{\underline{R}}\mathbf{U} \tag{5.5}$$

and $\mathbf{F}^0$ is the force required to hold the particle fixed ($\mathbf{U} = \mathbf{0}$) in the background flow.

When $\mathbf{F} = \mathbf{F}^0$, we also have $\mathbf{U} = 0$ so that equations (5.4) leads to relation (5.6) between the velocities and angular velocity of the force free particle and the forces and torque required to hold the particle still in the background flow:

$$\mathbf{U}^0 = -\underline{\underline{M}}\mathbf{F}^0 \tag{5.6}$$

The negative sign indicates that the forces required to hold the particle fix in the background flow are in the opposite direction to the movement of the force free and torque free particle in this same background flow.

The mobility and resistance matrices fully encapsulate the configuration of the flow such as the geometry and the boundary conditions. For example a spherical particle immersed in an unbounded resting fluid must be subjected to the following external forces F_1, F_3 and torque T_2 to move at velocities U_1, U_3 and Ω_2:

$$\begin{pmatrix} F_1 \\ F_3 \\ T_2 \end{pmatrix} = \begin{pmatrix} 6\pi\mu a & 0 & 0 \\ 0 & 6\pi\mu a & 0 \\ 0 & 0 & 8\pi\mu a^3 \end{pmatrix} \begin{pmatrix} U_1 \\ U_3 \\ \Omega_2 \end{pmatrix} \tag{5.7}$$

Note that the resistance matrix in this case is diagonal, indicating that only a force (or torque) in direction $\mathbf{e}_i$ can generate a translation (or a rotation) in this direction. Now when the same particle is in the vicinity of a flat wall, some cross-terms arise due to the interaction with the wall:

$$\begin{pmatrix} F_1 \\ F_3 \\ T_2 \end{pmatrix} = \begin{pmatrix} 6\pi\mu a\lambda_1(h/a) & 0 & R_{F_1\Omega_2}(h/a) \\ 0 & 6\pi\mu a\lambda_3(h/a) & 0 \\ R_{T_2U_1}(h/a) & 0 & 8\pi\mu a^3\lambda_2(h/a) \end{pmatrix} \begin{pmatrix} U_1 \\ U_3 \\ \Omega_2 \end{pmatrix} \tag{5.8}$$

In equation (5.8), $\lambda_i(h/a)$ is the correction of the Stokes drag law in direction $\mathbf{e}_i$ which depends on the distance to the wall and the particle radius [Brenner 1961, Goldmans *et al.* 1966]. The terms outside the diagonal indicates that a particle which is translating parallel to the wall will be subjected to an external torque as well as the drag force. Similarly, a particle rotating around $\mathbf{e}_2$ will be subjected to a drag force parallel to the wall as well as the torque. In this case, these two cross-terms contributions are related by $R_{F_1\Omega_2} = \frac{4}{3}R_{T_2U_1}$ [Goldmans *et al.* 1966]. Note that a rotation or translation of the particle parallel to the wall do not generate any lift force due to the symmetry of the problem, as already discussed. Also, the coefficients $\lambda_i(h/a)$ tend to 1 as $h/a \to \infty$ and the cross-terms vanish far from the wall, so that the Stokes drag law in unbounded fluid given by equation (5.7) is retrieved when the wall is sufficiently far away from the particle.

Regarding the interaction of a spherical particle with a structured surface, we observed in section 4.1 that the vertical force required to hold the particle at a constant altitude over the sawtooth pattern had zero mean value. Yet the particle is experiencing a non-zero average vertical velocity over a pattern period when let free to move. We therefore suggest that the explanation of the drift lies in the mobility matrix which depends on the geometry and therefore on the position of the particle in the pattern,

so that even if the force averages to zero, the product of the force and the mobility matrix does not necessarily.

From this intuition, we computed the mobility matrix associated with the spherical particle over the upward structures with the FCM model, for different fixed positions of the particle in a structure pattern to observe its evolution as presented on figure 5.8.

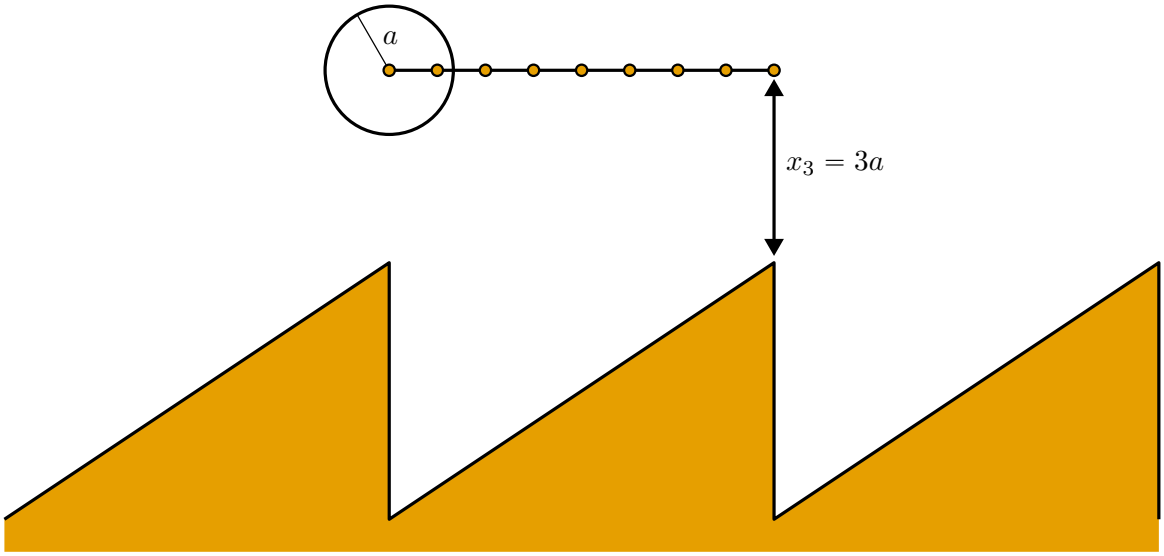

Figure 5.8: Positions of spherical particle of radius $a = 0.75\,\mu m$ over an upward sawtooth structure with dimensions $L = 6a$ and $h = 4a$ at which the mobility matrix was computed with stationary FCM simulations. The particle center of mass distance to the top of the structures is $x_3 = 3a$.

The computational domain is the same as for the freely moving spherical particle in section 5.1 and the fluid properties are still that of blood plasma such that $\rho = 1023.9\,kg.m^{-3}$ and $\mu = 1.2\,mPa.s$. However, because the mobility matrix decomposition is only valid in Stokes flow, the previously imposed shear rate of $\dot{\gamma} = 2000\,s^{-1}$ has been reduced to $\dot{\gamma} = 2\,s^{-1}$ to ensure inertial effects are negligible. The resulting particle Reynolds number is then of the order of $Re \approx 10^{-6}$.

Following equation (5.4), imposing the external forces and torque successively as $\mathbf{F} = (F_1, 0, 0)$, $\mathbf{F} = (0, F_3, 0)$ and $\mathbf{F} = (0, 0, T_2)$ via the FCM monopole and dipole, we can obtain the coefficients of the mobility matrix from the resulting measured particle velocities for each position in the structure as:

$$\mathbf{F} = \begin{pmatrix} F_1 \\ 0 \\ 0 \end{pmatrix} \Rightarrow \begin{cases} M_{U_1F_1} = \frac{U_1 - U_1^0}{F_1} \\ M_{U_3F_1} = \frac{U_3 - U_3^0}{F_1} \\ M_{\Omega_2F_1} = \frac{\Omega_2 - \Omega_2^0}{F_1} \end{cases} \tag{5.9a}$$

$$\mathbf{F} = \begin{pmatrix} 0 \\ F_3 \\ 0 \end{pmatrix} \Rightarrow \begin{cases} M_{U_1F_3} = \frac{U_1 - U_1^0}{F_3} \\ M_{U_3F_3} = \frac{U_3 - U_3^0}{F_3} \\ M_{\Omega_2F_3} = \frac{\Omega_2 - \Omega_2^0}{F_3} \end{cases} \tag{5.9b}$$

$$\mathbf{F} = \begin{pmatrix} 0 \\ 0 \\ T_2 \end{pmatrix} \Rightarrow \begin{cases} M_{U_1T_2} = \frac{U_1 - U_1^0}{T_2} \\ M_{U_3T_2} = \frac{U_3 - U_3^0}{T_2} \\ M_{\Omega_2T_2} = \frac{\Omega_2 - \Omega_2^0}{T_2} \end{cases} \tag{5.9c}$$

The force free and torque free velocities and angular velocity $\mathbf{U}^0$ of the particle at the same locations are also needed and are obtained by performing the simulation with no external forces and torques,

but not updating the particle position so that the flow and the stresslet establishes, and the resulting asymptotic velocity is measured once the flow is stationary. Also, the forces and torques $\mathbf{F}^0$ required to hold the particle fixed are computed by updating the monopole and dipole at each iteration by an increment which is proportional to the difference between the measured and the target velocity ($\mathbf{U} = \mathbf{0}$).

This measured force $\mathbf{F}^0$ required to hold the particle fixed in the background shear flow is used to obtain the force free and torque free particle velocity via equation (5.6), which was then compared to the simulated value of $\mathbf{U}^0$ for the different positions. This comparison was used as a validation of the calculation of the mobility matrix coefficients. Across the eight particle positions, the worst error was obtained on the vertical velocity of the particle placed in the middle of the ramp, for which this vertical velocity is very small. Yet this error was limited to 0.2% indicating the mobility matrix have been accurately computed.

The evolution of each coefficient of the mobility matrix over the positions in the structure pattern is presented on figure 5.9.

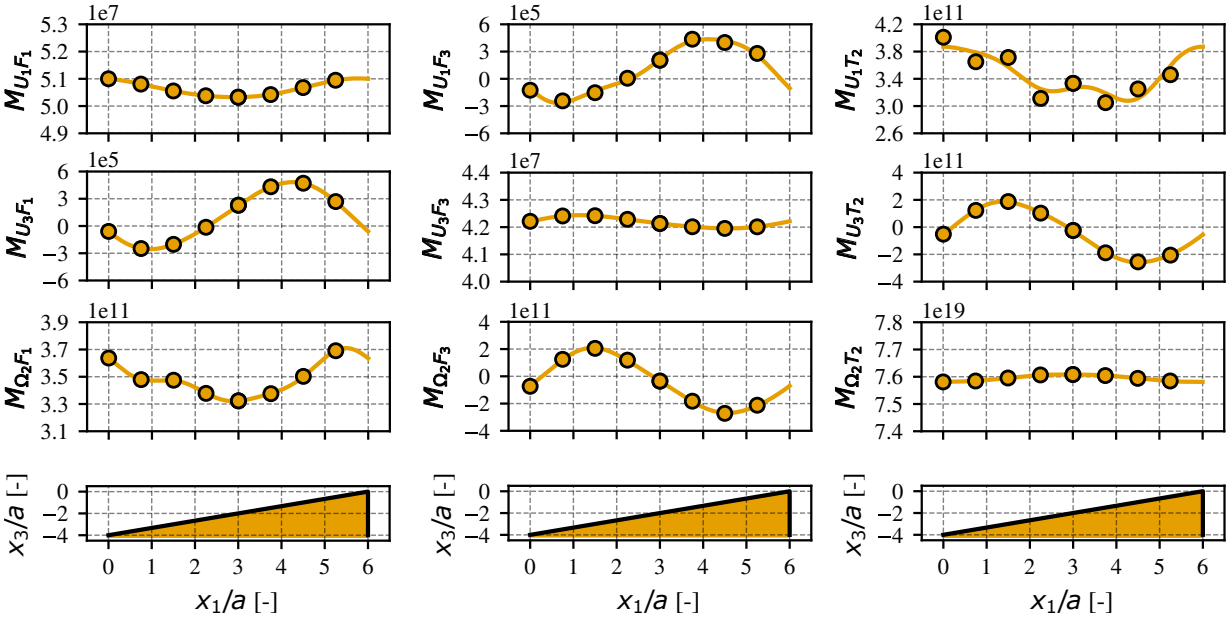

Figure 5.9: Evolution of the mobility matrix coefficients over an upward sawtooth pattern, at $Re \approx 10^{-6}$. The first three terms of a Fourier series decomposition are fitted through the data points.

First, the diagonal terms are all positive which is expected because the imposed force will generate a movement of the particle in the direction of the force, and not opposite to it. On the other hand, some off diagonal terms are oscillating around zero, changing sign according to the considered position of the particle in the structure.

The drift angle θ that was previously measured for a freely moving particle as $\theta = \tan^{-1}(\Delta z/\Delta x)$ when considered over the whole particle movement can also be defined as a local drift angle expressed from the local velocities of the freely moving particle as:

$$\theta(X_1) = \frac{U_3^0(X_1)}{U_1^0(X_1)} \tag{5.10}$$

From this local drift angle, an estimation of the mean drift angle for the particle over a structure pattern is obtained as follows:

$$\tilde{\theta} = \frac{1}{L}\int_0^L \theta(X_1)dX_1 \tag{5.11}$$

Following equation (5.6), the local drift angle can be expressed with the mobility matrix and the forces and torque required to hold the particle fixed:

$$\theta(X_1) = \frac{-\left(\underline{\underline{M}}(X_1)\mathbf{F}^0(X_1)\right)\mathbf{e}_3}{-\left(\underline{\underline{M}}(X_1)\mathbf{F}^0(X_1)\right)\mathbf{e}_1} \tag{5.12}$$

When developing the product between the mobility matrix and the force vector, the different contributions of the translational force, the vertical force and the torque acting on the particle are appearing in the resulting equation (5.13).

$$\theta(X_1) = \frac{-M_{U_3F_1}F_1^0 - M_{U_3F_3}F_3^0 - M_{U_3T_2}T_2^0}{-M_{U_1F_1}F_1^0 - M_{U_1F_3}F_3^0 - M_{U_1T_2}T_2^0} \tag{5.13}$$

The resulting drift angle can therefore be decomposed into the three contributions:

$$\theta(X_1) = \theta_{F_1}(X_1) + \theta_{F_3}(X_1) + \theta_{T_2}(X_1) \tag{5.14}$$

associated respectively to the translational force, the vertical force and the torque exerted on the particle by the background flow:

$$\theta_{F_1}(X_1) = \frac{-M_{U_3F_1}F_1^0}{-M_{U_1F_1}F_1^0 - M_{U_1F_3}F_3^0 - M_{U_1T_2}T_2^0} \tag{5.15a}$$

$$\theta_{F_3}(X_1) = \frac{-M_{U_3F_3}F_3^0}{-M_{U_1F_1}F_1^0 - M_{U_1F_3}F_3^0 - M_{U_1T_2}T_2^0} \tag{5.15b}$$

$$\theta_{T_2}(X_1) = \frac{-M_{U_3T_2}T_2^0}{-M_{U_1F_1}F_1^0 - M_{U_1F_3}F_3^0 - M_{U_1T_2}T_2^0} \tag{5.15c}$$

By neglecting the effect of particle change in altitude over its trajectory, we can estimate this integral with the previously computed mobility matrices at the different locations in the structure at constant altitude. To increase the accuracy of the integration, the integral is computed with the fitted Fourier series through the data points as presented on figure 5.9. The resulting value is $\tilde{\theta} = 1.59 \times 10^{-4}$ radians, which is in good agreement with the value measured with the freely moving particle of $\theta = 1.57 \times 10^{-4}$ radians (figure 5.1), even though the Reynolds number is a thousand times smaller. This indicates that the drift generated by the structure does not depend on the Reynolds number, at least in the low Reynolds number range.

Moreover, the drift angle of a particle for which the translational velocity was imposed to be constant and equal to the mean value of the translational velocity of the freely moving particle was computed in the same way as in section 5.1, with its vertical and angular velocity let free. The resulting drift angle was increased by around 10% compared to the fully free particle, indicating that the origin of the drift angle does not lie in the variations of the translational velocity (the denominator of equation (5.15)) over a pattern of the structure but rather in the variations of the vertical velocity (the numerator of equation (5.15)).

Following expressions (5.15), the contributions of the horizontal force, the vertical force and the external torque on the generation of a vertical velocity can be investigated independently.

First, the contribution of the force in the horizontal direction is discussed, with figure 5.10 showing the evolution of the horizontal force required to hold the particle fixed in the background shear flow F_1^0, the evolution over the sawtooth structure pattern of the mobility matrix coefficient $M_{U_3F_1}$ and the opposite of their product $-M_{U_3F_1}F_1^0$ which is proportional to the drift angle $\tilde{\theta}_{F_1}$ once divided by the translational velocity U_1^0.

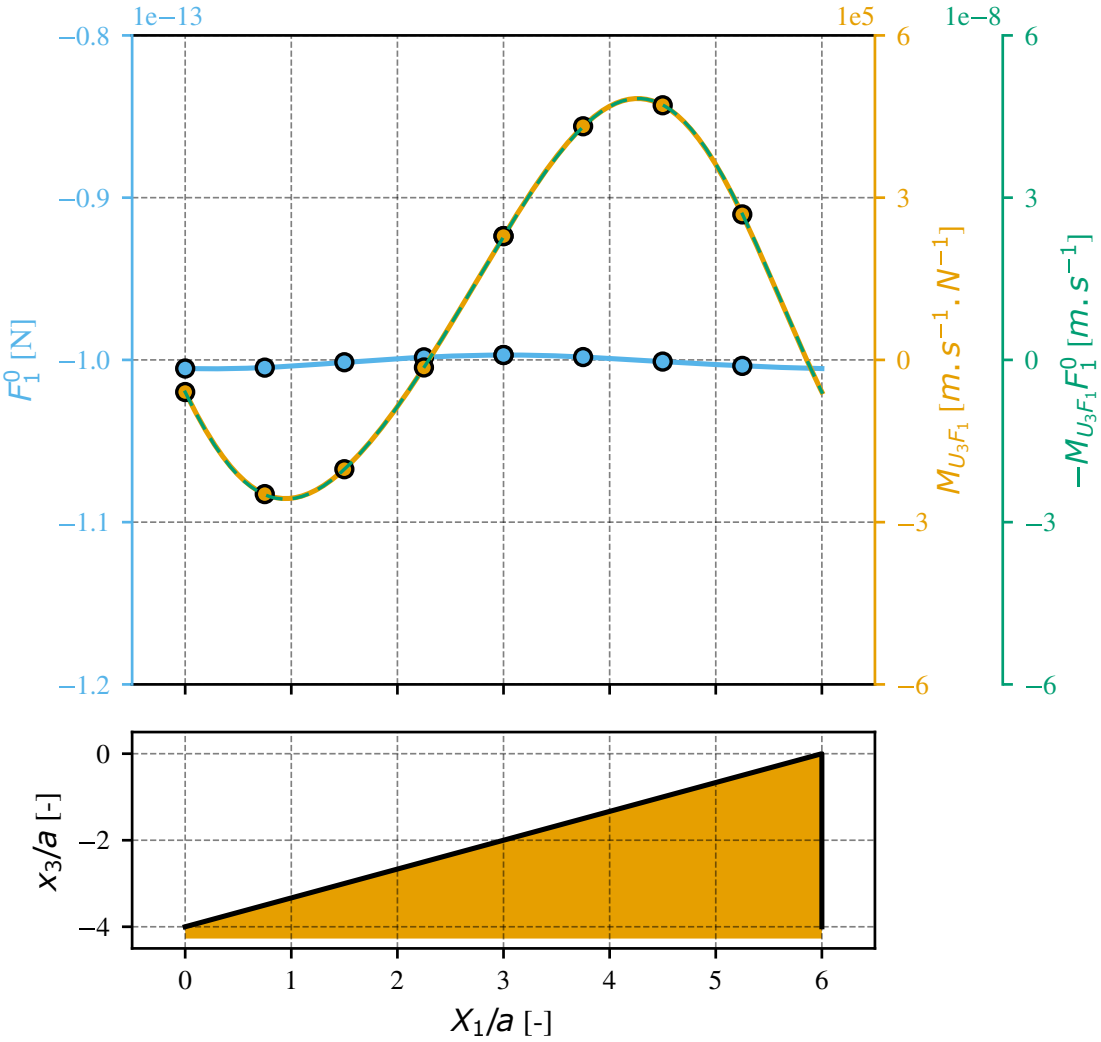

Figure 5.10: Evolution over the upward sawtooth pattern of the contribution from the horizontal force acting on the particle on the generation of a vertical velocity, at $Re \approx 10^{-6}$. The dots indicate the exact measure obtained for the corresponding position and the line is the fitted Fourier series decomposition with the first 3 terms of the serie. (—o—) Horizontal force required to hold the particle fixed in the background shear flow, (—o—) Mobility matrix coefficient relating the horizontal force to the vertical velocity and (- - -) opposite of the product between the force and the matrix coefficient which is proportional to the drift angle $\tilde{\theta}_{F_1}$.

The first observation is that the force required to hold the particle fixed in the horizontal direction is almost constant over the structure pattern indicating the pattern has very little effect on the translational force exerted on the particle due to the ambient shear flow. This is in agreement with the previous observation on the particle with its translational velocity being imposed to be the mean value of the freely moving particle, which resulted in a very small change in the resulting drift angle.

Then, the mobility matrix coefficient $M_{U_3F_1}$, which relates the horizontal force exerted on the particle to the generation of a vertical velocity of the particle, is changing sign over the structure

pattern but it has got a non-zero and positive mean value. It follows that the product of the two terms is following the same variations as the mobility matrix coefficient and taking its opposite following equation (5.13) indicates that the mean contribution of this translational force will generate a positive vertical velocity over a period pattern.

Secondly, the contribution of the vertical force acting on the particle is presented in figure 5.11 where again the evolution of the force required to hold the particle fixed in the vertical direction F_3^0, the mobility matrix coefficient $M_{U_3F_3}$ relating this force to the generated vertical velocity and the opposite of their product are shown over a structure pattern.

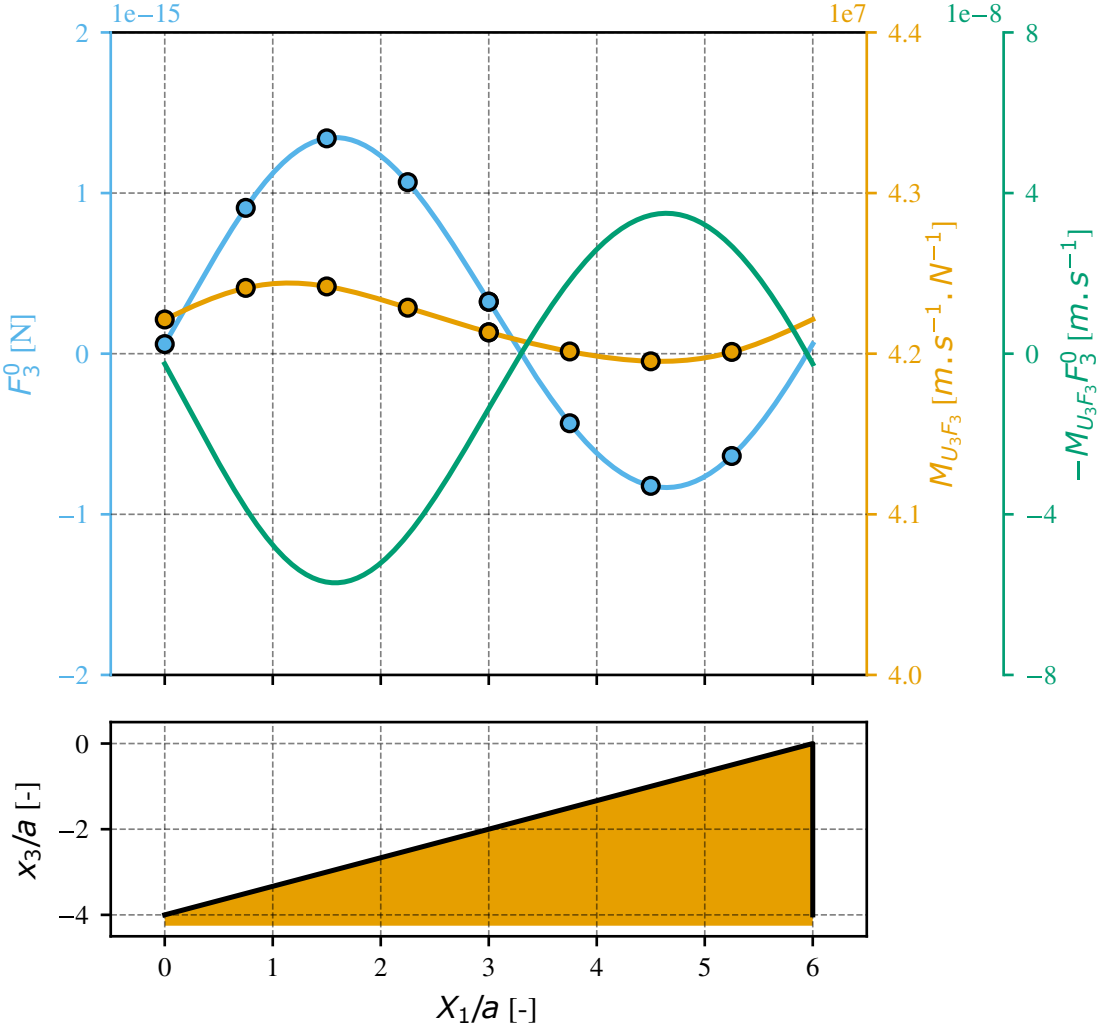

Figure 5.11: Evolution over the upward sawtooth pattern of the contribution from the vertical force acting on the particle on the generation of a vertical velocity, at $Re \approx 10^{-6}$. The dots indicate the exact measure obtained for the corresponding position and the line is the fitted Fourier series decomposition with the first 3 terms of the serie. (—o—) Vertical force required to hold the particle fixed in the background shear flow, (—o—) Mobility matrix coefficient relating the vertical force to the vertical velocity and (——) opposite of the product between the force and the matrix coefficient which is proportional to the drift angle $\tilde{\theta}_{F_3}$.

In this case, the vertical force required to hold the particle fixed changes sign due to the oscillations of the fluid, which alternately moves downward after the vertical step and upward during the ramp-up. Interestingly, the curve does not have a zero mean value, indicating that a net vertical force acts on the particle over the upward sawtooth pattern which was not previously observed. At first sight, this result may appear inconsistent with the one reported in section 4.1, where the vertical

force required to maintain the particle at constant altitude was obtained while allowing it to move freely in the horizontal direction and to rotate around the vorticity axis. However, in the present case, the particle is completely fixed in all three degrees of freedom, preventing any lateral displacement or reorientation that could partially compensate the vertical load. The two configurations therefore probe different physical constraints, which explains why their vertical force responses differ without being contradictory.

From figure 5.11, the mean value of the force required to hold the particle at constant altitude is positive indicating that the mean external force exerted by the fluid on the particle is negative. The associated mobility matrix coefficient $M_{U_3F_3}$ being strictly positive, the opposite of the product between the force required to hold the particle fixed and the mobility matrix coefficient indeed have a negative mean value.

Finally, the contribution of the external torque on the generation of a vertical velocity of the particle is presented on figure 5.12.

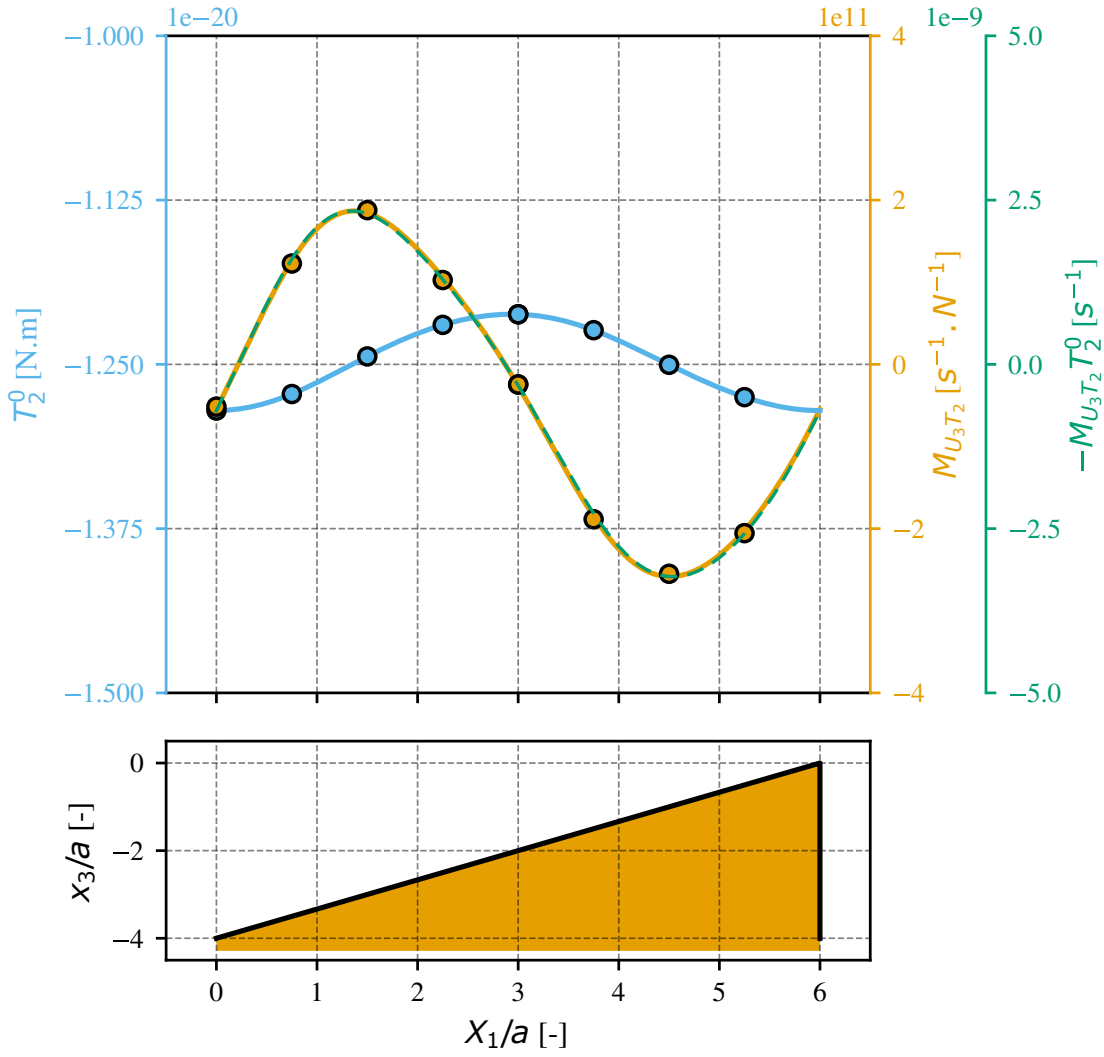

Figure 5.12: Evolution over the upward sawtooth pattern of the contribution from the torque acting on the particle on the generation of a vertical velocity, at $Re \approx 10^{-6}$. The dots indicate the exact measure obtained for the corresponding position and the line is the fitted Fourier series decomposition with the first 3 terms of the series. (—o—) Torque required to hold the particle fixed in the background shear flow, (—o—) Mobility matrix coefficient relating the torque to the vertical velocity and (- - -) opposite of the product between the torque and the matrix coefficient which is proportional to the drift angle $\tilde{\theta}_{T_2}$.

In this case, just as with the translational force contribution, the torque fluctuates slightly around a strictly negative mean value, while the corresponding mobility matrix coefficient oscillates around zero over the pattern period. However, in this case its mean value is close to zero. The resulting product between the torque and the matrix coefficient is also close to having a zero mean value, which indicates that the contribution of the external torque on the vertical velocity generation is quite small, at least compared to the contribution of the translational and vertical forces.

The evolution of the three contributions $\theta_{F_1}(X_1)$, $\theta_{F_3}(X_1)$ and $\theta_{T_2}(X_1)$ are plotted on figure 5.13 as well as the evolution of their sum $\theta(X_1)$. Their mean value obtained by integration over the pattern is also written on the right side.

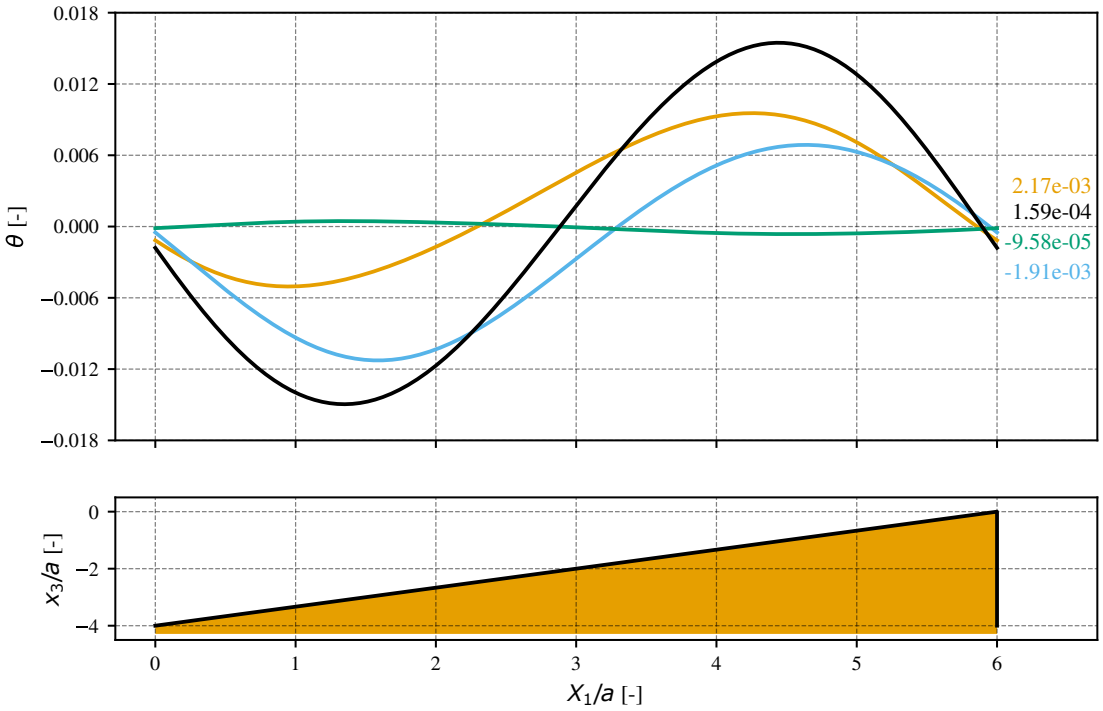

Figure 5.13: Evolution of the different contributions to the drift angle over the upward sawtooth pattern obtained from the mobility matrix decomposition, at $Re \approx 10^{-6}$. (——) Contribution of the horizontal force $\theta_{F_1}(X_1)$, (——) Contribution of the vertical force $\theta_{F_3}(X_1)$, (——) Contribution of the torque $\theta_{T_2}(X_1)$ and (——) sum of the three contributions $\theta(X_1)$. The mean values obtained by integration over a structure pattern are written on the right side with the corresponding color.

In agreement with the previous observations, the contribution of the horizontal force has a positive mean value and the contribution of the vertical force has a negative mean value. Also, the contribution of the torque is negative but much smaller than the other two. It appears that the translational contribution has greater magnitude than the vertical and rotational contributions combined, resulting in the positive value of the total mean drift angle which is comparable to the observed drift angle of a freely moving particle. This is better highlighted by figure 5.14 (first row), where the mean amplitude of the different contributions are compared, showing that the observed effect results from a slight imbalance between larger quantities.

This allows to conclude that the observed drift angle of a freely moving spherical particle transported over upward oriented sawtooth structures is due to the effect of the horizontal translation of the particle, which generates a mean velocity of the particle repelling the particle away from the wall. Note that the vertical contribution of the shear flow tends to push the particle down towards the surface but with a smaller amplitude.

For a downward sawtooth structure, the mobility matrix at a given location is expected to remain

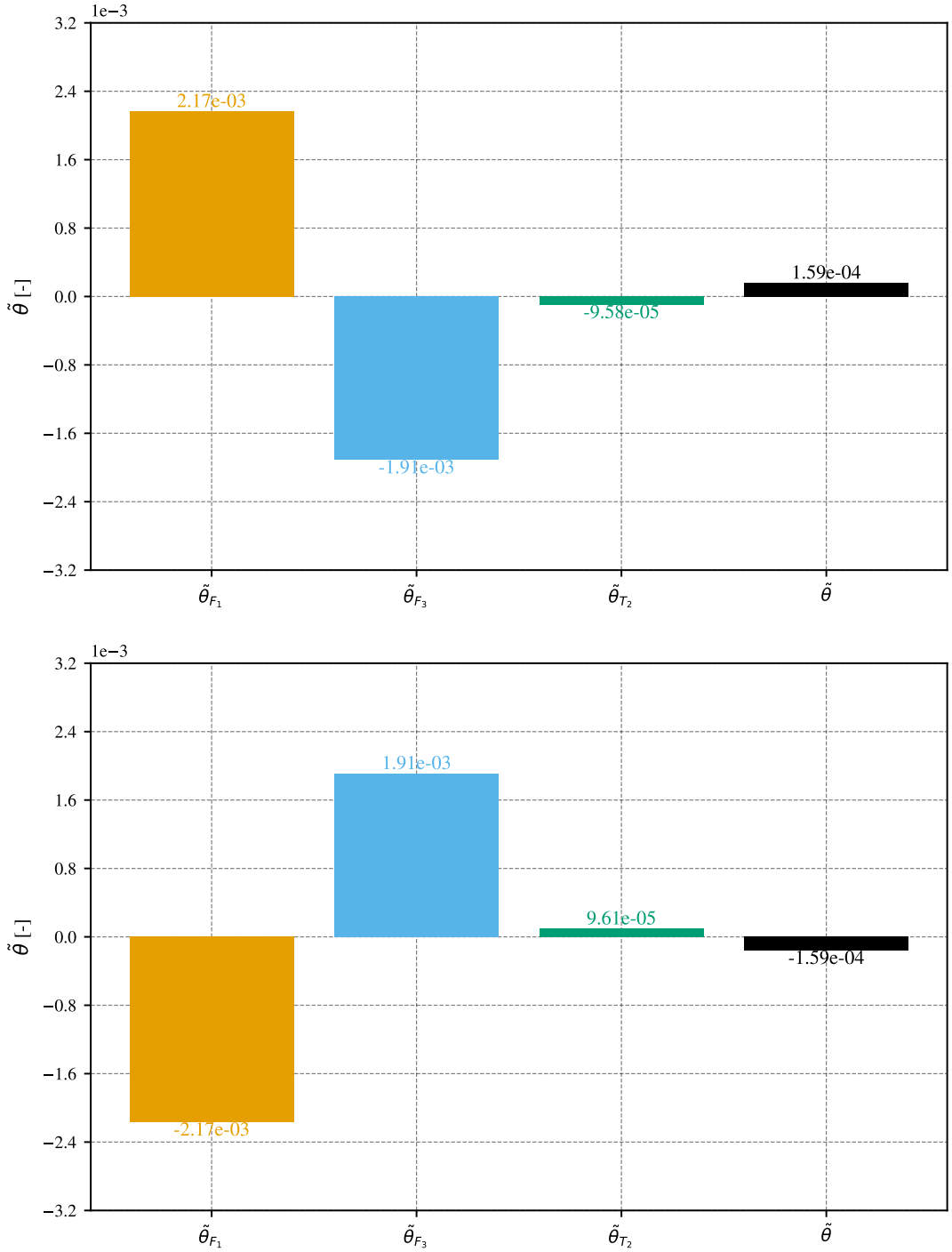

Figure 5.14: Mean values of the different contributions to the drift angle over an upward (first row) and a downward (second row) sawtooth pattern obtained from the mobility matrix decomposition, at $Re \approx 10^{-6}$. ( ) Contribution of the horizontal force $\tilde{\theta}_{F_1}$, ( ) Contribution of the vertical force $\tilde{\theta}_{F_3}$, ( ) Contribution of the torque $\tilde{\theta}_{T_2}$ and ( ) sum of the three contributions $\tilde{\theta}$.

unchanged. This becomes clearer when the downward sawtooth is viewed as a reversal of the flow over the upward sawtooth. Consequently, the only difference between the upward and downward sawtooth cases is a sign change in both the force-free and torque-free particle velocity $\mathbf{U}^0$ and the forces and torques $\mathbf{F}^0$ required to hold the particle fixed. From this perspective, the local drift angle (given by equation (5.10)) remains identical, since both the numerator and denominator change sign. However,

the integral in equation (5.11) is evaluated from L to 0, following the trajectory of the freely moving particle. As a result, the average drift angle is expected to reverse sign, such that $\theta_{upward} = -\theta_{downward}$. To verify this reversibility, the mobility matrix was computed using the same methodology as before, but applied to the downward sawtooth configuration. The resulting contributions to the drift angle averaged over the structure pattern are shown on figure 5.14 (second row), where we can observe each of the contribution is equal to the one for the upward sawtooth (first row), with opposite sign.

Now, blood platelets are not evolving at perfectly zero Reynolds number, even though this is a common assumption for platelet numerical models [Mody & King 2005, Pozrikidis 2006]. The previous analysis, conducted at a reduced Reynolds number of 10^{-6} to ensure Stokes flow conditions, is now performed at the physiological platelets Reynods number of 10^{-3} by raising the shear rate back to $\dot{\gamma} = 2000\, s^{-1}$. This physiological flow conditions were used in chapter 4 where the drift angle of the ellipsoidal particles over the sawtooth structures were initially observed.

The mobility matrix is computed following the same methodology and the quality of its computation is again assessed by computing the force free and torque free particle velocities from the obtained mobility matrix and the forces and torque required to hold the particle fixed, following (5.6). Comparison between this computed and the measured force free and torque free velocities yielded errors as high as 5%, indicating a less accurate computation of the mobility matrix at this Reynolds number even though this error could be considered acceptable.

The different contributions to the drift angle obtained via this mobility matrix, as well as their sum are presented in figure 5.15 for the particle over the upward sawtooth (first row) and the downward sawtooth (second row) at $Re \approx 10^{-3}$.

It can be clearly seen that the reversibility is not ensured anymore as a result of small but non-zero inertia. It also turns out that taking the mean of the drift angle's absolute value between the upward and the downward structure at $Re \approx 10^{-3}$ gives the amplitude of the contribution at $Re \approx 10^{-6}$. This is explained by the fact that the structure generates a drift which changes sign according to the direction of the particle, while the inertial drift is always acting in the same direction for any structure. If the drift generated by the upward structure at $Re \approx 10^{-6}$ is labeled $\tilde{\theta}_{sawtooth} > 0$ and the drift caused by the inertia is labeled $\tilde{\theta}_{inertia} > 0$, then we have for the upward structure at $Re \approx 10^{-3}$:

$$\tilde{\theta}_{upward} = \tilde{\theta}_{sawtooth} + \tilde{\theta}_{inertia} > 0 \tag{5.16}$$

Similarly for the downward sawtooth:

$$\tilde{\theta}_{downward} = -\tilde{\theta}_{sawtooth} + \tilde{\theta}_{inertia} < 0 \tag{5.17}$$

From figures 5.14 and 5.15, the drift angle induced by the structure at zero Reynolds number should write:

$$\tilde{\theta}_{sawtooth} = \frac{|\tilde{\theta}_{upward}| + |\tilde{\theta}_{downward}|}{2} \tag{5.18}$$

For example, the contribution of the translational force $\tilde{\theta}_{F_1}$ is 1.54×10^{-3} and -2.76×10^{-3} for the upward and downward sawtooth at $Re \approx 10^{-3}$ respectively. The mean of their absolute value yields 2.15×10^{-3} which matches the absolute value of this contribution at $Re \approx 10^{-6}$.

Using the mobility matrix at $Re \approx 10^{-3}$ therefore provides a direct measure of the inertial effects. In this case, they are quite significant, indicating that platelets are not evolving in a zero Reynolds number environment as it is often assumed.

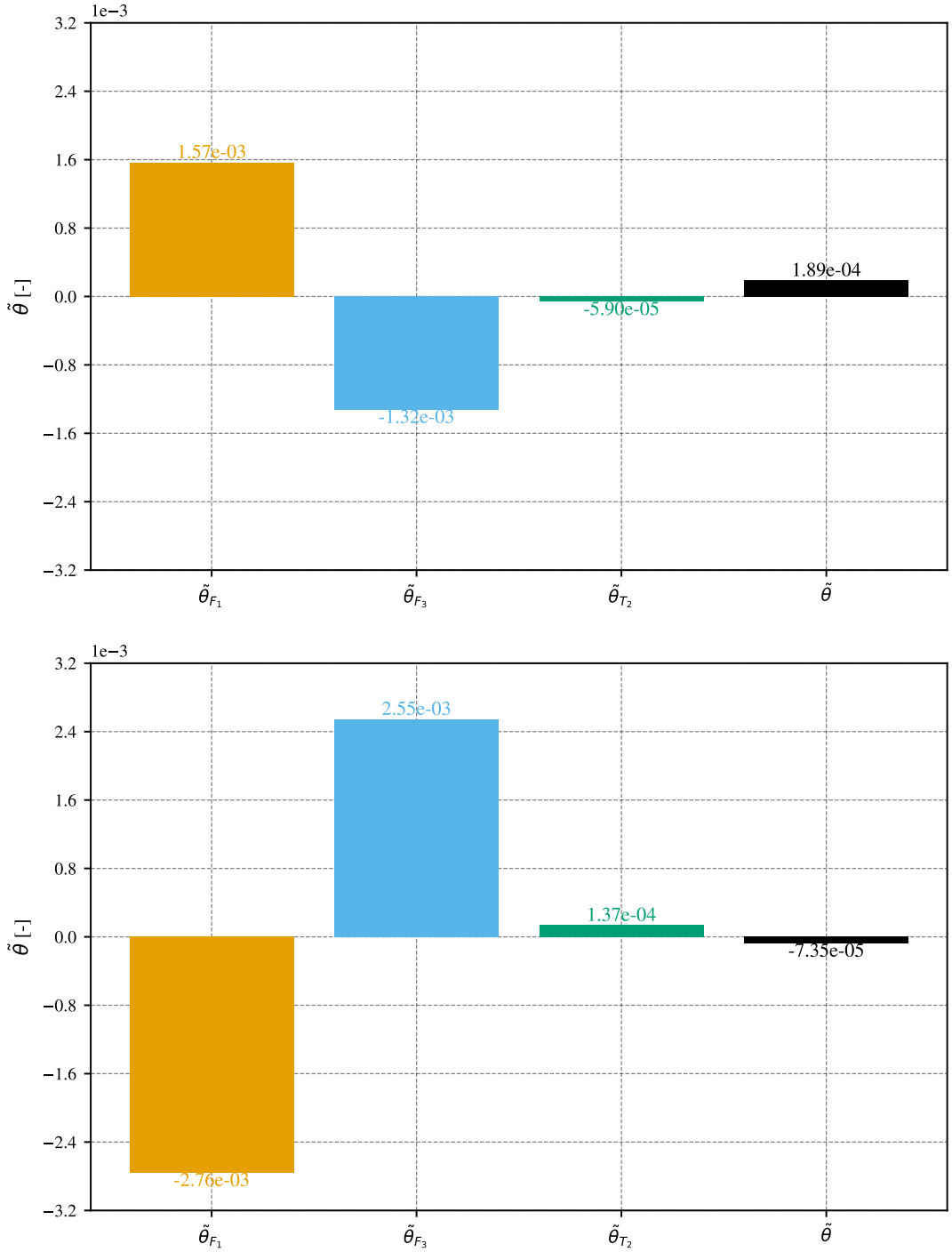

Figure 5.15: Mean values of the different contributions to the drift angle over an upward (first row) and downward (second row) sawtooth pattern obtained from the mobility matrix decomposition, at $Re \approx 10^{-3}$. ( ) Contribution of the horizontal force $\tilde{\theta}_{F_1}$, ( ) Contribution of the vertical force $\tilde{\theta}_{F_3}$, ( ) Contribution of the torque $\tilde{\theta}_{T_2}$ and ( ) sum of the three contributions $\tilde{\theta}$.

Following this discussion, the configuration of the flow is changed to investigate the evolution of the drift angle obtained with the mobility matrix and the FCM. In the following sections, the effect of bringing the particle closer to the surface and the effect of the structure height on the mobility matrix are presented, both at $Re \approx 10^{-3}$ corresponding to a physiological Reynolds number for platelets and $Re \approx 10^{-6}$ for which the inertial effects are negligible compared to the measured drift angle.

5.3.1 Effect of the particle-structure distance

In the previous section, the particle was placed at a distance of $x_3 = 3a$ from the top of the structure as in figure 5.8. It was shown in section 5.1 that by moving the particle from $x_3 = 3a$ to $x_3 = 2.5a$, the drift angle was increased by about 2.5 folds, so we expect a similar observation when computing an estimated drift angle with the mobility matrix.

In the exact same manner as the previous section, the mobility matrix for the particle placed initially at $x_3 = 2.5a$ from the top of the upward sawtooth structure with dimensions $L = 6a$ and $h = 4a$ is computed following equations (5.9c) by imposing successively the forces and torque in each direction, and measuring the resulting velocities. The results are first presented for $Re \approx 10^{-6}$ and the effect of inertia at the platelet physiological Reynolds number $Re \approx 10^{-3}$ is discussed afterwards.

For the translational contribution shown on figure 5.16, we can first observe that the force required to hold the particle fixed is still almost constant and negative, but with a smaller amplitude than the case where the particle was placed at $x_3 = 3a$.

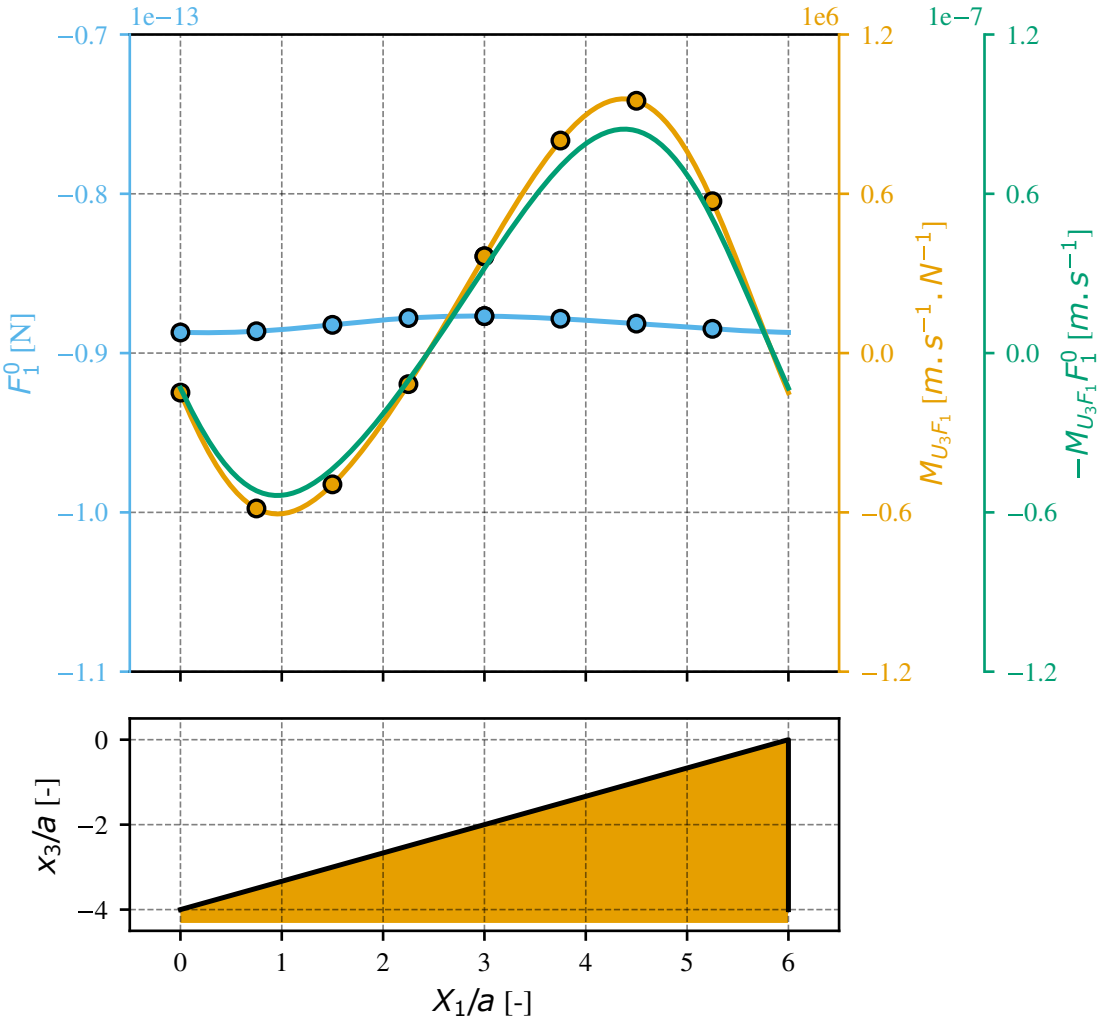

Figure 5.16: Evolution over the upward sawtooth pattern of the contribution from the horizontal force acting on the particle on the generation of a vertical velocity, for a particle placed at $x_3 = 2.5a$, at $Re \approx 10^{-6}$. The dots indicate the exact measure obtained for the corresponding position and the line is the fitted Fourier series decomposition with the first 3 terms of the serie. (—o—) Horizontal force required to hold the particle fixed in the background shear flow, (—o—) Mobility matrix coefficient relating the horizontal force to the vertical velocity and (——) opposite of the product between the force and the matrix coefficient which is proportional to the drift angle $\tilde{\theta}_{F_1}$.

This is expected as the background flow being a linear shear flow which vanishes at the wall, the surrounding velocity decreases as the particle is closer to the wall, so the drag force acting on the particle is subsequently decreased. For the associated mobility matrix coefficient $M_{U_3F_1}$, the coefficient changes sign at the same location as for the previous case, the only difference being that the amplitude of the variations over the positions in the pattern are about twice as big. This means that applying the same translational force on a particle placed at $x_3 = 3a$ or $x_3 = 2.5a$ will result in a greater vertical velocity generation for the particle placed at $x_3 = 2.5a$. Even though the external horizontal force that is applied to the particle has decreased as discussed previously, the increase in the mobility matrix coefficient $M_{U_3F_1}$ leads to an increased mean contribution of the translation on the generation of a vertical velocity.

Then for the contribution of the vertical force presented on figure 5.17, the vertical force required to hold the particle fixed is very similar to the one observed for the particle placed at $x_3 = 3a$ (see figure 5.11) only with a little increase in amplitude.

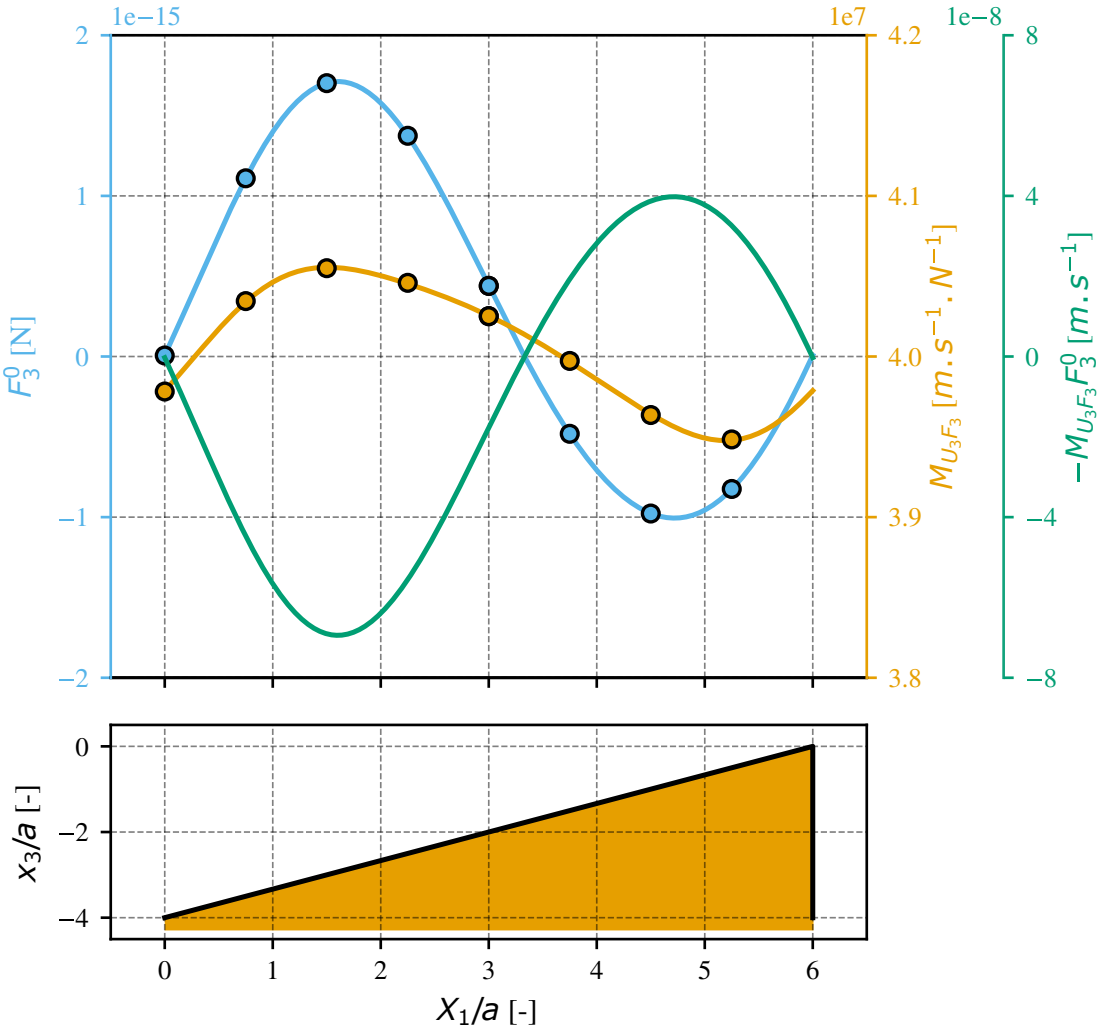

Figure 5.17: Evolution over the upward sawtooth pattern of the contribution from the vertical force acting on the particle on the generation of a vertical velocity, for a particle placed at $x_3 = 2.5a$, at $Re \approx 10^{-6}$. The dots indicate the exact measure obtained for the corresponding position and the line is the fitted Fourier series decomposition with the first 3 terms of the series. (—o—) Vertical force required to hold the particle fixed in the background shear flow, (—o—) Mobility matrix coefficient relating the vertical force to the vertical velocity and (——) opposite of the product between the force and the matrix coefficient which is proportional to the drift angle $\tilde{\theta}_{F_3}$.

The associated mobility matrix coefficient $M_{U_3F_3}$ is also evolving similarly but with a slight decrease in amplitude. This means that bringing the particle closer to the wall results in an increase in the effective resistance of the wall on the particle movement, which is expected.

Finally, the contribution of the torque is presented on figure 5.18 where we can see the torque required to hold the particle fixed is exactly the same for the two particle distance to the structure. This is explained by the rotational part of the shear flow being the same everywhere in the domain except very close to the structures. The associated mobility matrix coefficient $M_{U_3T_2}$ is evolving similarly but has increased in amplitude when the particle is closer to the wall, implying an increased contribution of the torque on the mean drift angle of the particle.

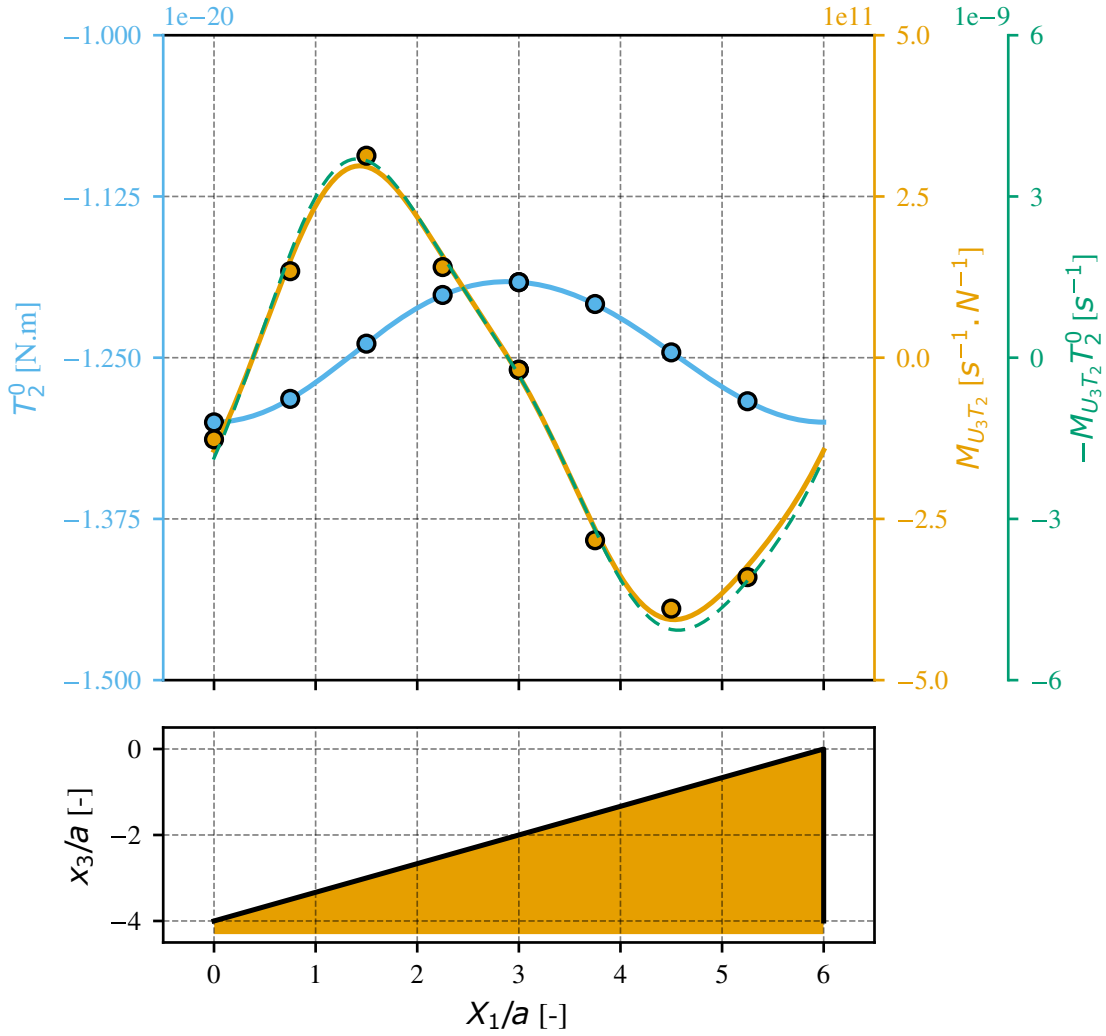

Figure 5.18: Evolution over the upward sawtooth pattern of the contribution from the torque acting on the particle on the generation of a vertical velocity, for a particle placed at $x_3 = 2.5a$, at $Re \approx 10^{-6}$. The dots indicate the exact measure obtained for the corresponding position and the line is the fitted Fourier series decomposition with the first 3 terms of the series. (—o—) Torque required to hold the particle fixed in the background shear flow, (—o—) Mobility matrix coefficient relating the torque to the vertical velocity and (- - -) opposite of the product between the force and the matrix coefficient which is proportional to the drift angle $\tilde{\theta}_{T_2}$.

The mean values of the drift angle for the different contributions are compared in figure 5.19 (first row) for which the conclusion is very similar to the previous case, that is the translational and vertical contributions have very large variations in amplitude and their mean values are respectively positive and negative and almost balance each other, while the contribution of the torque is very small compared

to these two. In the end the mean drift angle from the sum of the three contribution at $Re \approx 10^{-6}$ of $\theta = 4.06 \times 10^{-4}$ radians is again in very good agreement with the drift angle of the freely moving particle initially placed at $x_3 = 2.5a$ and at $Re \approx 10^{-3}$ which was $\theta = 4.20 \times 10^{-4}$ radians.

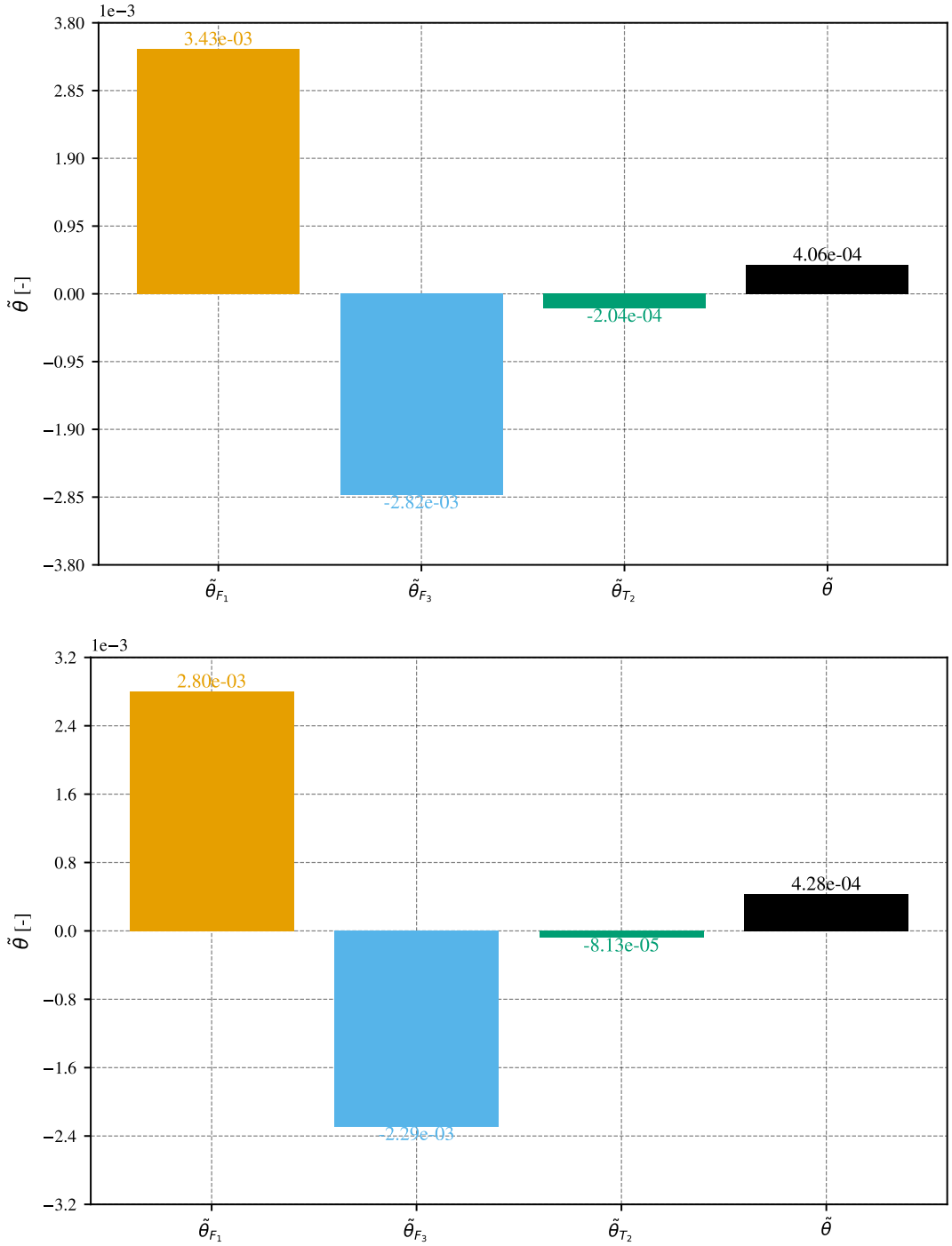

Figure 5.19: Mean values of the different contributions to the drift angle over the upward sawtooth pattern obtained from the mobility matrix decomposition, for a particle placed at $x_3 = 2.5a$ at $Re \approx 10^{-6}$ (first row) and $Re \approx 10^{-3}$ (second row). ( ) Contribution of the horizontal force $\tilde{\theta}_{F_1}$, ( ) Contribution of the vertical force $\tilde{\theta}_{F_3}$, ( ) Contribution of the torque $\tilde{\theta}_{T_2}$ and ( ) sum of the three contributions $\tilde{\theta}$.

The result of reducing the particle distance to the wall is to increase all the contributions by a similar factor, so that the difference between the contribution of the translational force and the vertical force is also increased by a similar factor, resulting in the observed increase in the drift angle.

The same experiment has also been conducted at $Re \approx 10^{-3}$ to highlight the effect of inertia. The mean value of the different contributions to the drift angle are presented on figure 5.19 (second row) for this higher Reynolds number case. As observed in the previous section for the particle placed at $x_3 = 3a$ from the top of the structures, when inertia is included, all the contributions are reduced in amplitude but the sum of all the contributions remains in a similar order of magnitude. This indicates that the effect of inertia remains small in comparison to the structure induced drift at zero Reynolds number.

5.3.2 Effect of the structure amplitude

Similarly, the mobility matrix is computed for structures of decreasing amplitude, down to a negligible value where the drift angle is expected to vanish. As in the tests presented in section 4.1, the structure amplitude is varied around its mean altitude, which is kept constant so that the particle–structure distance remains unchanged across simulations as presented on figure 5.20 *a*). The particles are positioned at a distance of 5a from this mean altitude. The amplitudes considered are $4a$, $2a$, a, $0.4a$ and $0.2a$ corresponding to a distance of $3a$, $4a$, $4.5a$, $4.8a$ and $4.9a$ between the particle center and the top of the structure respectively.

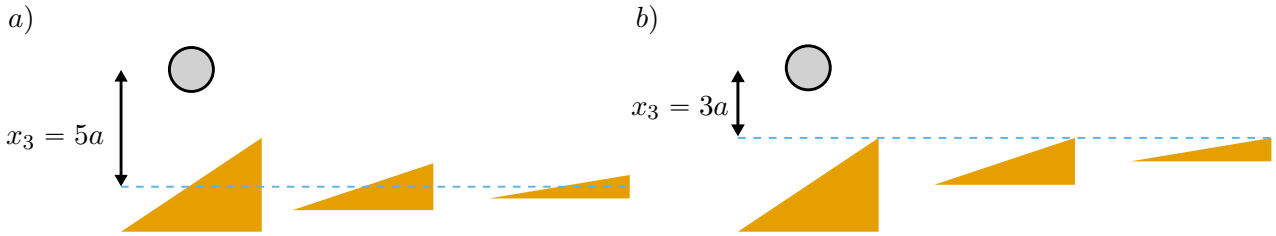

Figure 5.20: Configuration for the study the effect of structure amplitude. *a*) The amplitude of the structure is varied by keeping the mean altitude of the structure constant indicated by the blue line. *b*) The amplitude of the structure is varied by keeping the top of the structure at the same altitude indicated by the blue line.

First, figure 5.21 presents the average drift angle over a pattern period with $L = 6a$ for the different structure heights computed with the mobility matrix following equation (5.11) at the pysiological platelet Reynolds number $Re \approx 10^{-3}$. For clarity, all the results at $Re \approx 10^{-3}$ are presented with triangle markers and all the results at $Re \approx 10^{-6}$ are presented with a circular marker.

We can observe the drift angle vanishes almost instantly when the amplitude of the structure is only divided by 2, from $h = 4a$ to $h = 2a$. Indeed, comparing all the estimated drift angles for structures of amplitude $h \leqslant 2a$ with the drift angle measured over a flat surface indicated by the black marker at $h = 0$ we can observe that these drift angles are all comparable in amplitude to the inertial effects. This indicates that the mobility matrix is indeed able to accurately reproduce the result that structures of smaller amplitude generate smaller particle drift. It must be noted that the obtained mobility matrices resulted in very large error (around 20-50% for most locations but up to 300% for the locations where the vertical velocity is very small) between the calculated and predicted force free and torque free particle velocity for the smallest structures, as inertial effects become increasingly important compared to the structure effect when the amplitude of the structure decreases.

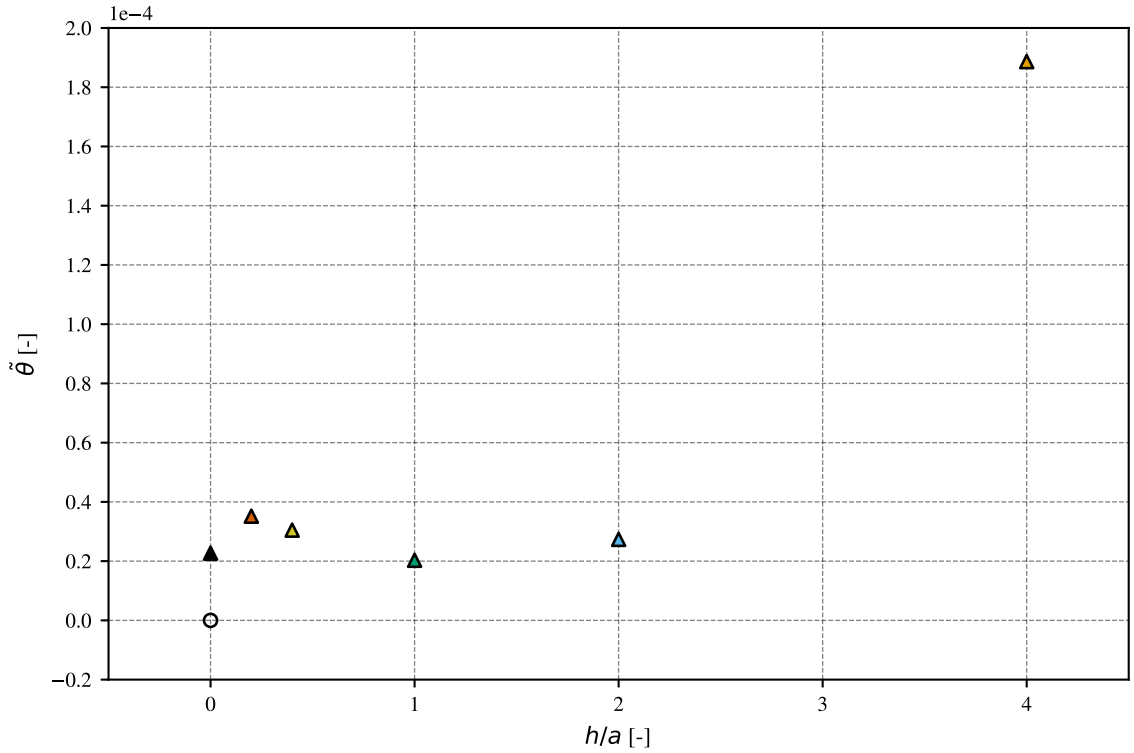

Figure 5.21: Averaged drift angle over a pattern period of the upward sawtooth structure for the different structure amplitudes investigated, at $Re \approx 10^{-3}$. The structure amplitude is varied by keeping the mean amplitude at a constant altitude. The inertial drift angle at $h/a = 0$ (▲) has been obtained by performing a simulation of a freely moving sphere of radius a initially placed at a distance of $5a$ from the surface corresponding to the distance between the particle and the mean altitude of the structures, and measuring its change in altitude after it has travelled the length of a structure pattern. The empty marker at ($h/a = 0$, $\tilde{\theta} = 0$) indicates the theoretical drift over a flat surface at $Re = 0$.

Also, the very sharp decrease (about 10 folds) in drift angle when the structure amplitude is reduced from $h = 4a$ to $h = 2a$ is not what has been observed previously in section 4.2.2.1. Even though in this case the particle was ellipsoidal, we observed that the drift angle was decaying much slowly, for example with only a twofolds reduction between the structures with $h = 4a$ and $h = 2a$. Also, apart from the particle shape, the key difference between the present structure amplitude effect investigation and the one performed on the ellipsoidal particle is that in the present case the amplitude of the structure was varied by keeping the mean structure altitude constant, while in the previous case, the top of the structure was kept at constant altitude. Therefore, in the present case, the gap between the particle and the top of the structure is varied with the structure amplitude, while in the former study, the mean structure altitude was varied with the structure amplitude. Observing a greater reduction in drift angle with the present study might suggest that the gap between the particle and the top of the structure has a greater importance than the distance to the mean structure altitude. To confirm this hypothesis, the same study is conducted, but with the structures amplitude varied with their top at constant altitude as shown on figure 5.20 *b*).

The corresponding average drift angle evolution over the structures' amplitudes at $Re \approx 10^{-3}$ is presented in figure 5.22 with the triangle markers.

Once again, the mobility matrix estimation of the mean drift angle is converging towards the value of the inertial drift over a flat surface, indicated by the value at $h/a = 0$, when the amplitude is decreased. Also, the drift angle is decaying slower, with about 2.5-fold decrease between the structure

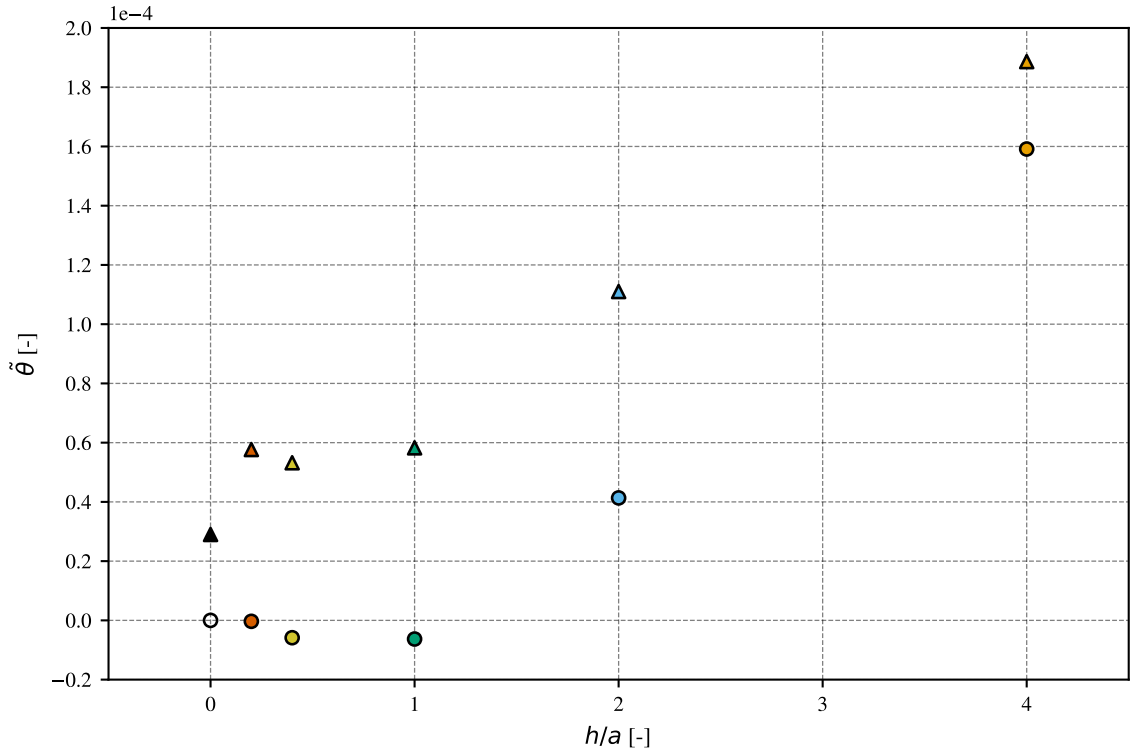

Figure 5.22: Average drift angle over a pattern period of the upward sawtooth structure for the different structure amplitudes with the top at constant altitude. (▲) $Re \approx 10^{-3}$, (●) $Re \approx 10^{-6}$. The drift angle at $h/a = 0$ due to inertial effects at $Re \approx 10^{-3}$ is the same as in figure 5.1 as the configuration is the same. The empty marker at ($h/a = 0$, $\tilde{\theta} = 0$) indicates the theoretical drift over a flat surface at $Re = 0$.

with $h = 4a$ and $h = 2a$. This confirms that the variation of the gap between the particle and the top of the structure plays a more important role than the variation of the distance between the particle and the mean structure. For the structures with amplitude $h \leqslant a$, the mean drift angle is again comparable with the drift generated by inertial effects, but in this case, the mobility matrix are obtained with better accuracy, as for all the structure amplitude, the error between the computed force free and torque free particle and the one obtained from the product of the mobility matrix and the forces and torques required to hold the particle fixed against the shear flow, were all below 5% error.

Similarly, the mean drift angle for the different structures' amplitudes, varied by keeping the top of the structure at the same altitude, is obtained from the mobility matrix computed at $Re \approx 10^{-6}$. These drift angles are presented on figure 5.22 with the circular markers. In this case, the average drift angle is converging towards zero as the amplitude of the structure decreases. In particular, no drift angle is expected below the threshold amplitude $h = a$. Note that this agrees with the analytical model for the case $h \ll a$ (see chapter 2).

Regarding the evolution of the individual contributions, the evolution of the mean horizontal force required to hold the particle fixed for the different structure amplitude is presented on figure 5.23.

Because the value of the force varies very little over the structure pattern, only this mean value is shown for the different structure amplitudes. Also, as these mean values are directly proportional to the Reynolds number, they are presented in a dimensionless form, using a characteristic fluid velocity $U_c = a\dot{\gamma}$ so that both the force for $Re \approx 10^{-6}$ and $Re \approx 10^{-3}$ can be compared on the same graph.

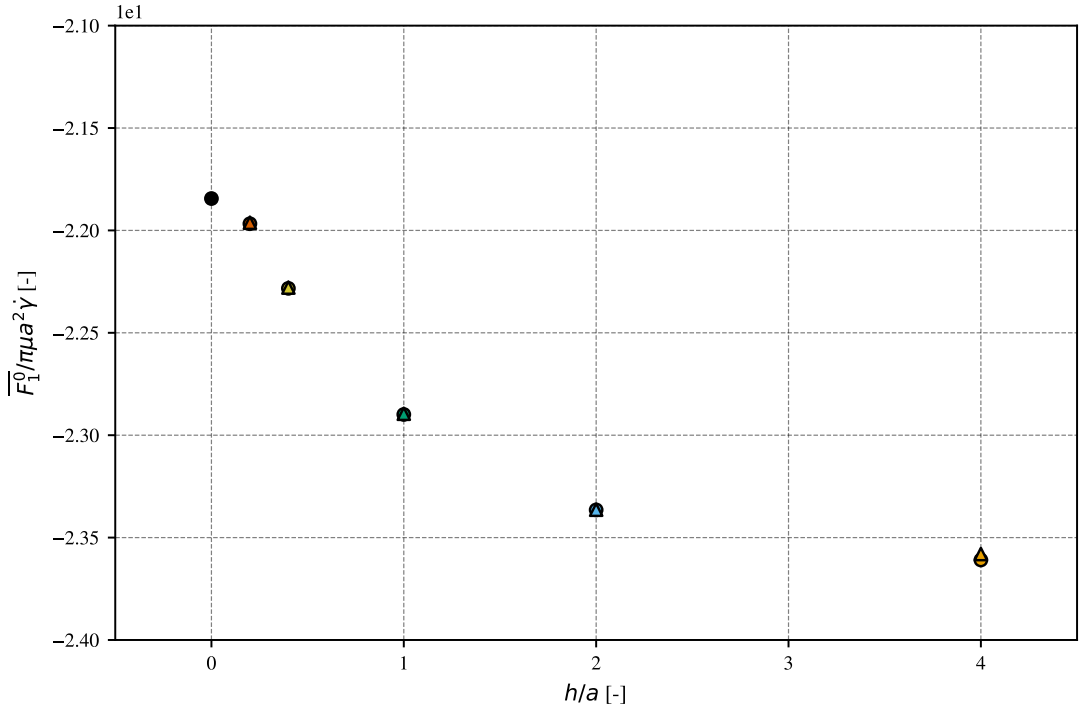

Figure 5.23: Mean force over the structure pattern required to hold the particle fixed in the horizontal direction for different structures amplitude. (▲) $Re \approx 10^{-3}$, (●) $Re \approx 10^{-6}$. The value at $h/a = 0$ corresponds to the analytical value of the force at $Re = 0$ computed using the analytical model (equation (2.34a)) for a particle placed at $x_3 = 3a$. The force is made dimensionless by using a characteristic fluid velocity $U_c = a\dot{\gamma}$.

We can observe that the force is correctly converging towards the theoretical value of the force for a particle placed at $x_3 = 3a$ from a flat surface, obtained with the analytical model (equation (2.32a)), for both flow regimes. This indicates that inertia plays a very little role regarding this force component. We also expect the associated mobility matrix coefficient $M_{U_1F_1}$ tends to zero, as a horizontal force should produce no vertical velocity on a particle close to a flat surface at zero Reynolds, see equation (5.8). The mean value over a structure period of this mobility matrix coefficient for the different structure amplitudes is presented on figure 5.24.

We can observe that at $Re \approx 10^{-6}$ (circle markers), its mean value indeed decreases with the amplitude of the structure, and tends towards 0 as expected. Now when inertia is present at $Re \approx 10^{-3}$ (triangle markers), this value is not converging towards zero anymore. The coefficient converges toward a negative value which indicates that a particle close to a flat surface will gain a negative vertical velocity due to the horizontal force acting on the particle, taking the opposite of the product between the force and the mobility matrix coefficient following equation (5.6). When the amplitude of the structure is increased, this coefficient changes sign and the resulting particle velocity becomes positive.

Also the evolution over the structure amplitudes for both $Re \approx 10^{-6}$ and $Re \approx 10^{-3}$ is remarkably similar, with only a shifting by a constant between the two curves. As we concluded from previous observations that the Reynolds number had a relatively small effect on the drift generated by the structure, the constant shifting of the curves suggests that the inertial effects are of similar amplitude for all structures amplitudes. Additionnaly, figure 5.25 presents the evolution of this coefficient over the structure pattern for the different altitudes at $Re \approx 10^{-6}$, highlighting once again the shifting in the extremas of the coefficient when the amplitude is varied, as was previously observed for the extremas of the vertical force required to hold the particle fixed (section 4.1).

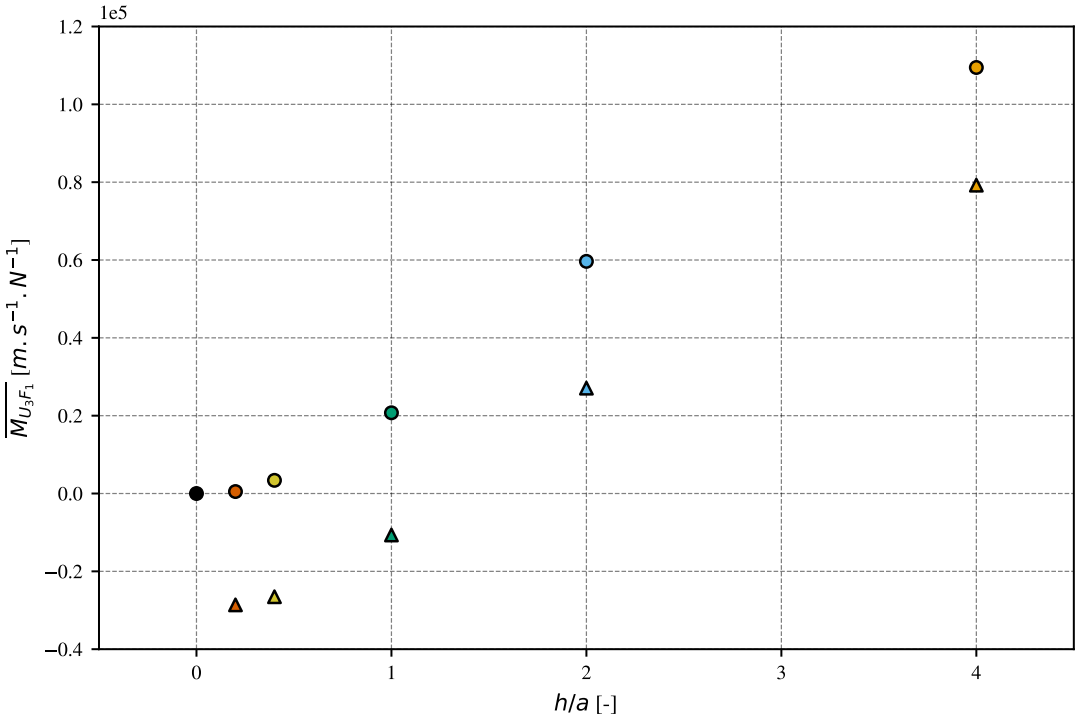

Figure 5.24: Evolution of the mean value of the mobility matrix coefficient relating the translational force to the vertical velocity over the upward sawtooth structure for different structures amplitude. (▲) $Re \approx 10^{-3}$, (●) $Re \approx 10^{-6}$. This mobility matrix coefficient should be zero over a flat surface at zero Reynolds number, which is indicated by the black dot at $h/a = 0$.

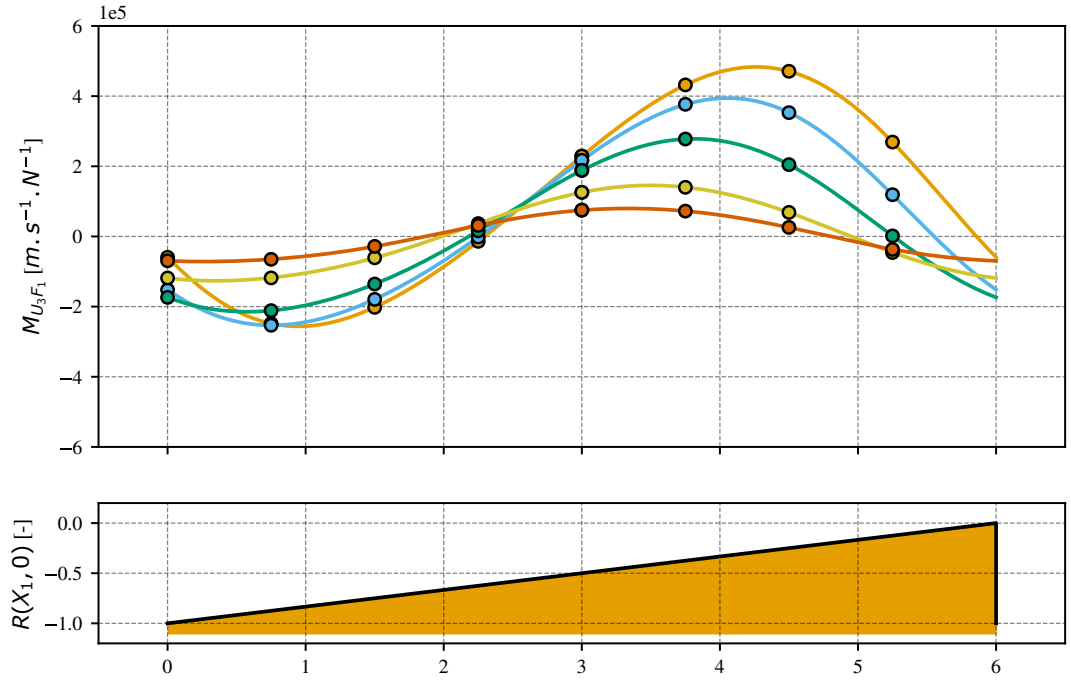

Figure 5.25: Evolution over the upward sawtooth pattern of the mobility matrix coefficient relating the translational force to the vertical velocity for different structures amplitude, at $Re \approx 10^{-6}$. The dots indicate the exact measure obtained for the corresponding position and the line is the fitted Fourier series decomposition with the first 3 terms of the series. (—●—) $h = 4a$, (—●—) $h = 2a$, (—●—) $h = 1a$, (—●—) $h = 0.4a$, and (—●—) $h = 0.2a$.

Regarding the vertical force required to hold the particle fixed, the evolution of its mean value is shown on figure 5.26 for both Reynolds numbers.

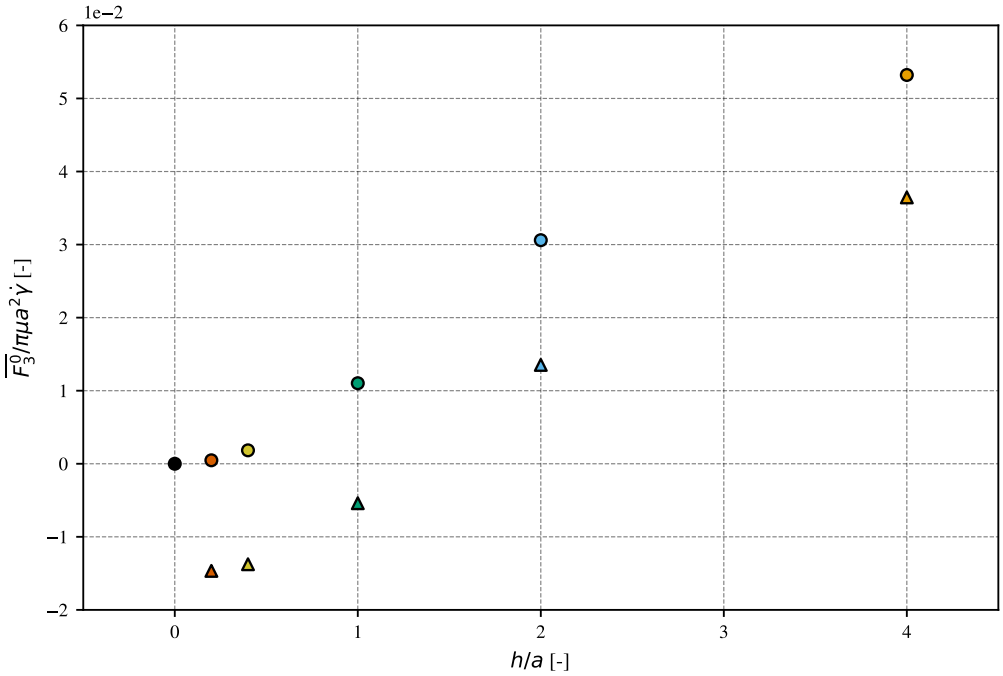

Figure 5.26: Evolution of the mean value of the force required to hold the particle fixed in the vertical direction over the upward sawtooth structure for different structures amplitude. (▲) $Re \approx 10^{-3}$, (●) $Re \approx 10^{-6}$. This force is expected to be zero on a flat surface at zero Reynolds number as indicated by the black dot at $h/a = 0$. The force is made dimensionless by using a characteristic fluid velocity $U_c = a\dot{\gamma}$.

The observation is very similar to the mobility matrix relating the horizontal force to the vertical velocity $M_{U_3F_1}$ discussed previously. Indeed, the vertical force is decreasing in amplitude progressively with the smaller structures, and converges towards 0 at $Re \approx 10^{-6}$ but towards a negative value at $Re \approx 10^{-3}$. This non-zero and negative vertical force required to hold the particle fixed over the flat surface is the force required to compensate the inertial lift generated by the translation of the particle. Also, the shifting between the curves for the two Reynolds number is again constant over the structure amplitude indicating a superposition of the two independent effects of the structure and inertia.

The mean value of the coefficient of the mobility matrix associated to the vertical force and the vertical velocity is shown on figure 5.27, where we can see that both simulation at $Re \approx 10^{-6}$ and $Re \approx 10^{-3}$ converges towards the theoretical value over a plane surface at zero Reynolds number. Reducing the size of the structure decreases the coefficient, indicating that for the same external force applied to the particle in the vertical direction, the particle will have a smaller vertical velocity over the flat surface than the structured surface. This is probably due to the fact that the mean altitude of the sawtooth structure is getting closer to the particle as the amplitude decreases, increasing the interaction with the particle.

Finally, the contribution of the torque on the generation of a vertical velocity is presented.

The evolution of the mean value of the torque required to hold the particle fixed is shown on figure 5.28. It can be seen that the value of the torque for both Reynolds numbers is evolving similarly with the structure amplitude, but does not converge exactly towards the theoretical value obtained with the analytical model. The value of the torque for the smallest structure amplitude nevertheless remains within a 1% error of the theoretical value, which is still acceptable.

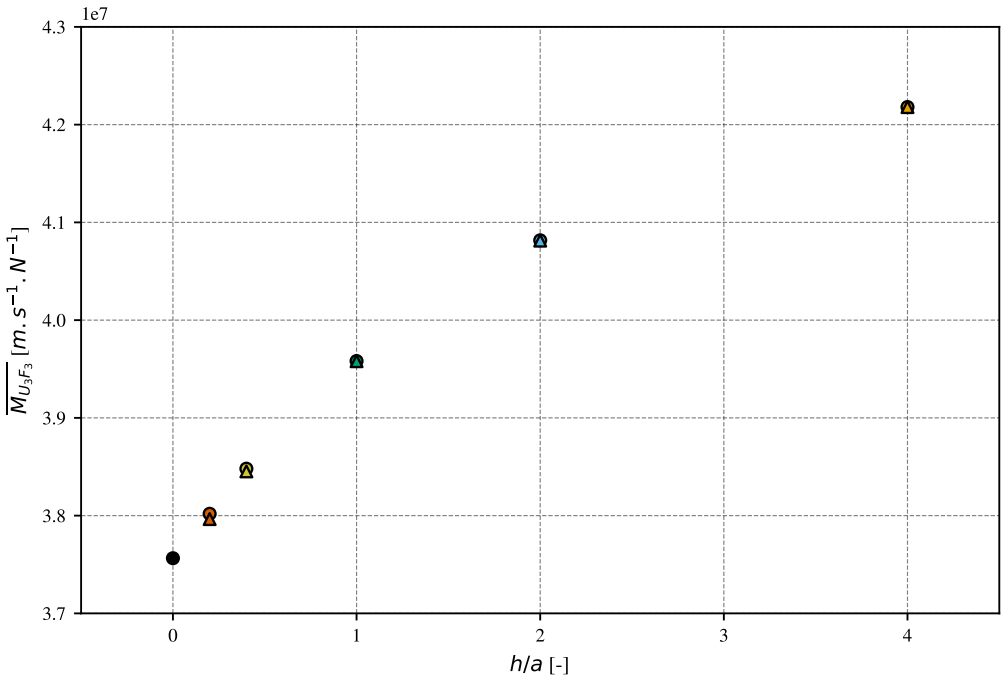

Figure 5.27: Evolution of the mean value of the mobility matrix coefficient relating the vertical force to the vertical velocity over the upward sawtooth structure for different structures amplitude. (▲) $Re \approx 10^{-3}$, (●) $Re \approx 10^{-6}$. The theoretical value over a flat surface and at zero Reynolds number is obtained from [Brenner 1961].

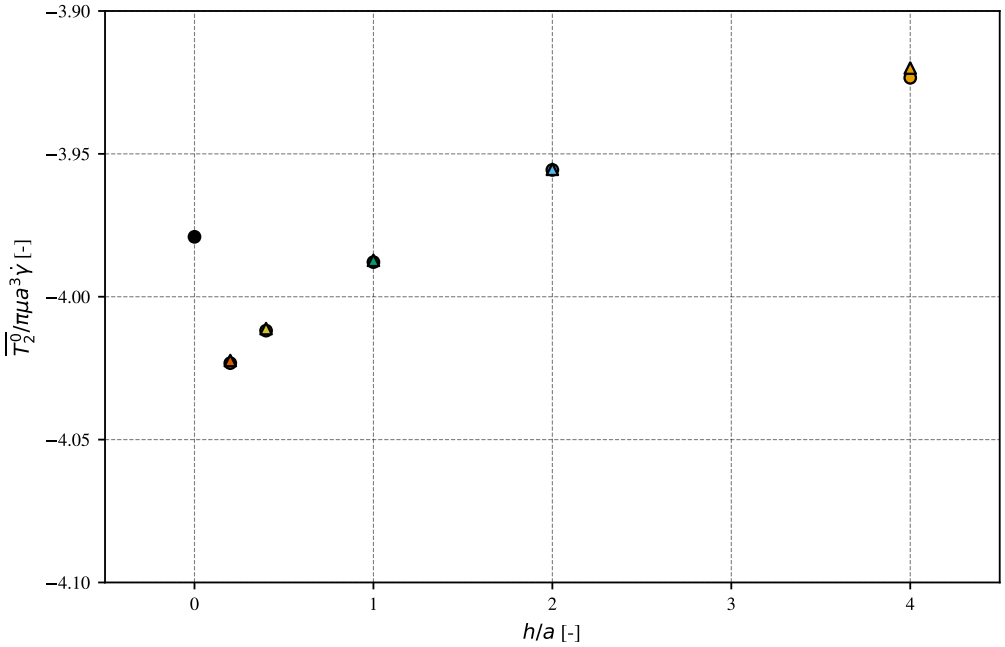

Figure 5.28: Evolution of the mean value of the mobility matrix coefficient relating the vertical force to the vertical velocity over the upward sawtooth structure for different structures amplitude. (▲) $Re \approx 10^{-3}$, (●) $Re \approx 10^{-6}$. The value at $h/a = 0$ corresponds to the analytical value of the force at $Re = 0$ computed using the analytical model (equation (2.34b)) for a particle placed at $x_3 = 3a$. The torque is made dimensionless by using a characteristic fluid velocity $U_c = a\dot{\gamma}$.

Regarding the associated mobility matrix coefficient $M_{U_3T_2}$ presented on figure 5.29, the simulation at $Re \approx 10^{-6}$ converges towards the theoretical value of 0 for a flat surface at $Re = 0$ as expected, ensuring no lift is generated by the rotation of a particle close to a flat wall when no inertia is present. However, when the Reynolds number is increased and inertial effects are becoming dominant, this mobility matrix coefficient converges towards a non-zero value.

Moreover, as for the two previous contributions (see the analysis of $M_{U_3F_1}$ and F_3^0), the introduction of inertia results in a constant shifting of the coefficient $M_{U_3T_2}$ over the structure amplitudes compared to the case without inertia.

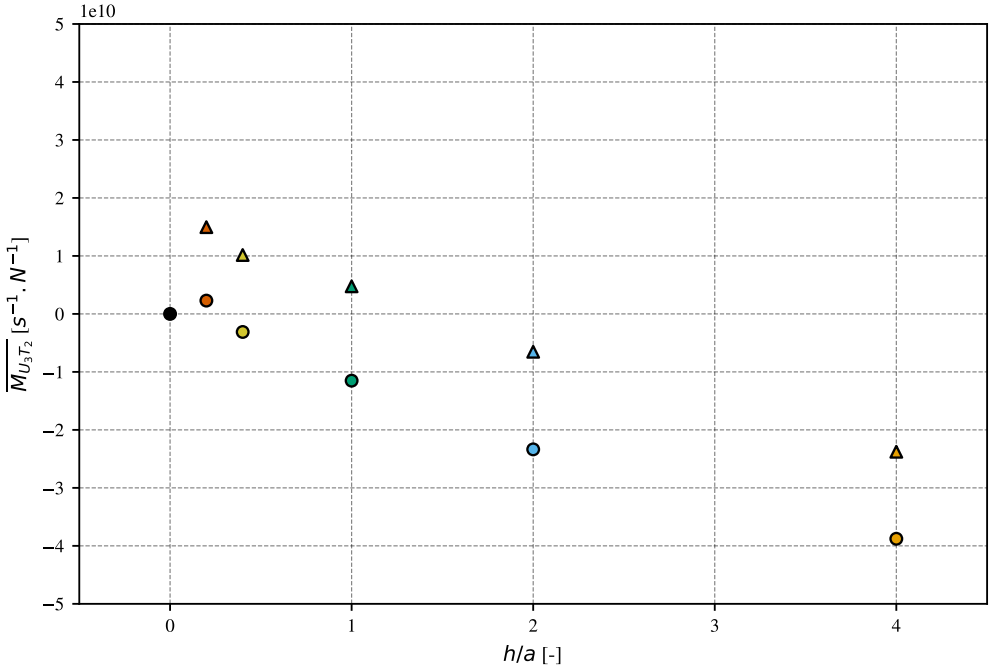

Figure 5.29: Evolution of the mean value of the mobility matrix coefficient relating the vertical force to the vertical velocity over the upward sawtooth structure for different structures amplitude. (▲) $Re \approx 10^{-3}$, (●) $Re \approx 10^{-6}$. This mobility matrix coefficient should be zero over a flat surface at zero Reynolds number, which is indicated by the black marker at $h/a = 0$.

Figure 5.30 (first row) presents the evolution of the average of the 3 contributions to the vertical velocity and their sum, over the different structure amplitudes at $Re \approx 10^{-6}$. The different contributions decrease in amplitude with the decrease in structure amplitude. Especially, the sum of the contributions seems to be vanishing at $h = a$ even though the individual contributions have not vanished yet. For example, between $h = 4a$ and $h = a$, the sum of the contributions (*i.e.* the average drift angle of the particle) has decreased by about 25 folds (from 1.59×10^{-4} to 6.29×10^{-6} radians), while the contribution of the horizontal force has only been reduced by 5 folds (from 2.16×10^{-3} to 4.18×10^{-4} radians).

When inertia is present, the contributions to the drift angle do not vanish when the structure amplitude is decreased as shown on figure 5.30 (second row). Instead, the contributions change sign around $h = a$ and some residual drift which is attributed to inertia remains. Note that a similar change in sign was already observed when the force required to hold the particle in the middle of an isolated ramp was measured (section 5.2).

In the end, we showed that the drift of the particle translating over the sawtooth structures is caused by the horizontal force acting on the particle which is generating a positive vertical velocity due to the particular geometry of the surface, which is not balanced by the negative vertical velocity

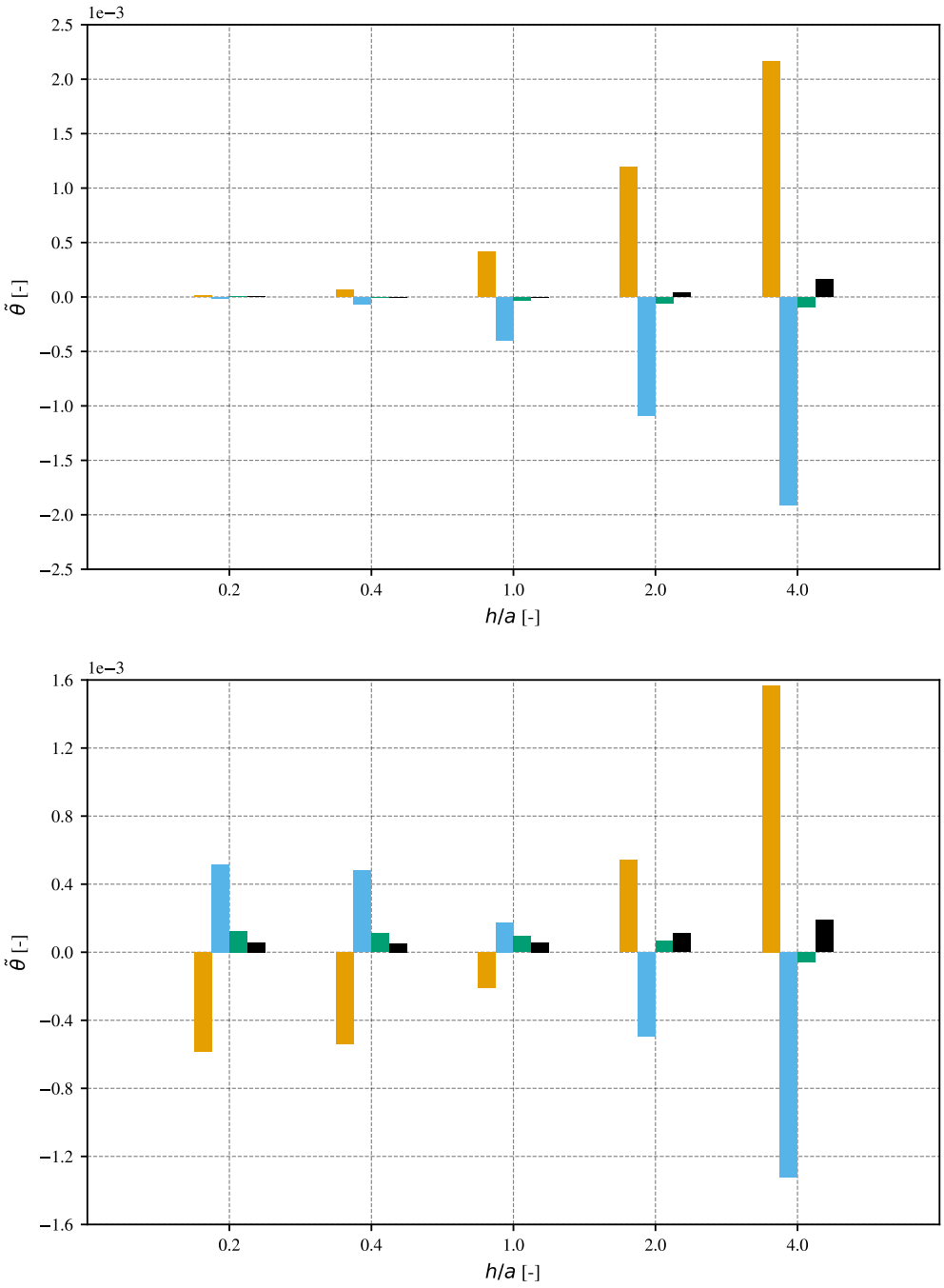

Figure 5.30: Mean values of the different contributions to the drift angle over the upward sawtooth pattern obtained from the mobility matrix decomposition, for different structure amplitude, at $Re \approx 10^{-6}$ (first row) and $Re \approx 10^{-3}$ (second row). ( ) Contribution of the horizontal force $\tilde{\theta}_{F_1}$, ( ) Contribution of the vertical force $\tilde{\theta}_{F_3}$, ( ) Contribution of the torque $\tilde{\theta}_{T_2}$ and ( ) sum of the three contributions $\tilde{\theta}$.

generated by the vertical force acting on the particle. Decomposing the motion as a sum of these individual contributions allowed to reconstruct an estimated drift angle in very good agreement with the freely moving particle. The fact that the mobility matrices and the forces were obtained at a constant altitude shows that the variations of particle distance to the surface are not at the origin of this drift. Also, at a physiological Reynolds number of $Re \approx 10^{-3}$, inertial effects are not negligible and are dominant for structures smaller than $h = a$.

Chapter 6

Platelets adhesion modelling

Contents

The previous chapters were focusing on the hydrodynamic interaction between a single particle and different surface structures, without considering any collision or adhesive mechanisms. This is the focus of this chapter, which first reminds the biological adhesion mechanisms of blood platelets already presented in chapter 1, as well as the way they have been modeled and coupled with the Force Coupling Method. The adhesive particle model is then used to investigate the adhesion on a flat surface at different Reynolds number and interaction with the sawtooth structured wall which was shown in the previous chapters to be of particular interest in reducing the interaction between the particle and the structure.

6.1 Platelets adhesion mechanisms

As blood platelets are circulating in the blood stream, they need to be brought to rest at the site of injury to fulfill their hemostatic role. They are thus able to form bonds with external ligands released upon endothelium injury or adsorbed on an artificial surface, ultimately leading to their complete stop.

Over physiological surfaces, platelets primarily bind to collagen, either directly through the GPVI receptor or indirectly via collagen-bound von Willebrand factor (vWF) [Fogelson & Neeves 2015]. In contrast, adhesion on artificial surfaces is mainly mediated by fibrinogen, which is the first protein to adsorb onto the surface and interacts with platelets through the integrin $\alpha IIb\beta 3$ [Jaffer *et al.* 2015]. vWF can also adsorb onto artificial surfaces and contribute to platelet adhesion.

vWF is a polymer, which is found in a globular shape at rest but have an average size of 1 to 2 μm when fully stretched [Fogelson & Neeves 2015], making it the longest protein in the human body. It is found circulating in the plasma, in the subendothelium matrix as well as in platelets granules which are released upon platelet activation [Fogelson & Neeves 2015]. In its globular form, vWF is inert to platelets adhesion and needs to be stretched by the surrounding flow to reveal its adhesive sites [Ruggeri 2009]. [Schneider *et al.* 2007] showed that a shear rate of $5.000\,s^{-1}$ was required to unfold a non-tethered vWF in water.

Regarding platelets adhesion, platelet GP1bα receptors will first bind to vWF that is unfolded due to flow. [Fu *et al.* 2017] suggest that the vWF A1 domain must be subjected to inner tensile forces greater than $10\,pN$ to favor binding with the GP1bα receptor. This implies greater affinity closer to the tethered end of the vWF multimer where the tensile force is greater than the free end. The GP1bα-vWF bonds are fast to form but are also easy to break so they are not sufficient to fully stop the motion

of platelets under high shear rates. However, they allow the platelet to slow down in a rolling motion as bonds rapidly form and break [Fogelson & Neeves 2015]. They also trigger mechanical activation of the platelet resulting in conformational change of the $\alpha IIb\beta 3$ receptor to its high affinity state. This receptor can also bind vWF but requires longer time to form so initial slow down of the platelet due to GP1bα-vWF bonds is key to allow the secondary $\alpha IIb\beta 3$-vWF bonds to form. These bonds are much stronger than the GP1bα-vWF bonds and ultimately result in firm platelet adhesion.

Additionnaly, the GP1bα-vWF bond is referred to as a catch-slip bond, presenting both slip bond and catch bond properties [Fogelson & Neeves 2015]. Intuitively, as the force exerted through a slip bond increases, the probability of the bond to break increases accordingly, resulting in a reduced bond lifetime. On the other hand, when the force exterted on a catch bond increases, the probability of the bond to break decreases, increasing the bond lifetime. Indeed, [Yago *et al.* 2008] showed that below $10\,pN$, the GP1bα-vWF bond lifetime presents a catch bond behavior, followed by a slip bond behavior past this value. This catch bond property of the GP1bα-vWF bond could further explain the low affinity between vWF and platelets in the circulation [Ruggeri 2009], as well as a minimum shear stress below which no vWF mediated platelet adhesion is observed [Fogelson & Neeves 2015].

6.2 Adhesive particle model

The implemented model is based on the two-step mechanisms of adhesion to vWF, coupled to the FCM model presented in chapter 3. The full dynamics of the vWF is not modelled yet but is expected to be implemented in the future. Springs are therefore used between the particle and the adhesion sites in this first platelet adhesion modeling effort. In particular, it was mentioned in chapter 3 regarding the implementation of the FCM in the YALES2BIO solver that even though the particles are represented by a Gaussian function over the fluid grid in the FCM framework, a meshed surface with the dimensions of the particle was still transported and oriented following the particle movements for visualization purpose. This meshed surface is also at the center of the adhesive model. Indeed, the nodes of the surface are used as platelets receptor anchor points, from which it is easy to compute a distance towards an adhesion site, such as a labeled wall or another particle if aggregation is desired.

Bond formation is triggered when a node on the particle surface comes under a threshold distance to a wall node. This threshold distance is chosen to be $0.5\,\mu m$, in agreement with a typical vWF size. It also ensures a reasonable gap between the particle surface and the wall, allowing the particle to be accurately resolved by the FCM during the initial formation of bonds, as discussed in section 3.4.4.2. After bonds form, the particle may be attracted closer to the surface, leading to a lower resolution of the hydrodynamic interaction. However, in this regime, the particle dynamics are predominantly governed by bond and collision forces.

Once a bond is formed, the link between the wall node and the particle surface node is following a linear spring behavior. The stiffness of the bonds in the model is derived from [Zhang *et al.* 2015] where traction of a GP1bα-vWF A1 domain was performed using optical tweezers, and force-displacement curves were obtained. From these force-displacement curve, a linear fit is used to derive a linear spring stiffness for a single GP1bα-vWF bond of $5\times10^{-5}\,N.m^{-1}$. In our model, this stiffness was used initially but was reduced to $2\times10^{-5}\,N.m^{-1}$ after various tests, so that the model is reproducing qualitatively the translocation phenomenon of blood platelets presented in the next section. The spring rest length is taken to be the same as the bond formation length, that is $0.5\,\mu m$.

The bonds are allowed to stretch under the displacement of the particle, which will induce a tensile force in the bond that will be applied in the direction of the bond. No compression force can arise from the bonds as the biological bonds are not generating any compressive forces, and no angular resistance in the bending of the bond at its anchor point is included. Only one bond can be formed for each

particle surface node, but no restriction is set on the number of bond per wall node.

To account for this force on the particle movement, the tensile force is transported at the center of mass of the particle and applied via the monopole of the Force Coupling Method. A torque is also generated if the force is not applied in the direction of the center of mass. This resulting torque is applied at the center of mass of the particle via the dipole of the FCM from a lever-arm computation between the receptor anchor point on the surface of the particle and the center of mass.

According to [Zhang *et al.* 2015], bonds are able to extend up to $0.225\,\mu m$ from their rest length before they rupture. This value is used in our model, meaning that a spring with length greater than $0.725\,\mu m$ will break, considering a $0.225\,\mu m$ stretching from the $0.5\,\mu m$ rest length. Once the bond is broken, the bond site on the particle surface is now free to form a new bond and no more force is applied at this point until a new bond is formed.

Also [Fu *et al.* 2017] states that around 8 GP1bα receptor can bind per micrometer of vWF, or a density of $64\text{GP1b}\alpha.\mu m^{-2}$ due to geometrical constraints. This indicates that not all the platelet surface receptors are able to bind even though they are in the bond formation range. This means that a spherical particle with radius $0.75\mu m$ and total surface $7.07\mu m^2$ can only form around 450 bond at the same time among the $25,000$ GP1bα receptors present on a platelet surface [Gremmel *et al.* 2016]. Because the meshed surface in the numerical model has 571 nodes, we assumed each of the node was representing a GP1bα bond, so that a total of 571 bonds could be formed at the same time.

Each bond formation time is also tracked which allows the state of the bond to evolve through time. The objective is to reproduce the two-step adhesion process of platelet on vWF, where initial GP1bα-vWF transient bonds forms allowing the formation of slower but stronger $\alpha IIb\beta 3$-vWF bonds. To do so, the stiffness of the bonds in our model is set to evolve when a bond is formed for a threshold time. To our knowledge, no data is available on the bond strength between $\alpha IIb\beta 3$ and vWF, so the increase in stiffness was just based on the increase in available bond site. Indeed, $\alpha IIb\beta 3$ are the most numerous platelet receptor with about $100,000$ copies while around $25,000$ GP1bα receptors are found on a platelet surface [Gremmel *et al.* 2016]. Therefore, an increase in the stiffness by a factor 4 was chosen, taking into account they are 4 times more $\alpha IIb\beta 3$ receptors than GP1bα. The time delay before increase in bond stiffness is chosen to be 3 ms following [Yazdani *et al.* 2017].

Because no compression forces are generated by the bond and lubrication forces are not resolved by the FCM, a repulsion force is also included between the particle surface and the surface walls to account for possible collisions. To do so, a Lennard-Jones potential have been tuned to prevent overlap between the particle and the wall while keeping the interaction distance small compared to the adhesive bonds (collision only occurs below a distance of $0.3\,\mu m$ and bonds form at $0.5\,\mu m$ and break at $0.725\,\mu m$). The resulting collision force is applied at the center of mass of the particle and added to the FCM monopole.

Table 6.1 sums up the parameters of the adhesion model.

6.3 Single platelet adhesion over a flat surface

Over a flat surface, we examine how the two-step adhesion model influences particle dynamics. At low shear rates, the particle can be brought to rest quickly, as slowly forming but strong bonds have sufficient time to establish. At higher shear rates, however, an initial slowdown of the particle is required before these stronger bonds can form.

To investigate these distinct mechanisms, two simulations are performed and compared. In both cases, an ellipsoidal particle with semi-axes $a_1 = 1.5, \mu m$, $a_2 = 1.5, \mu m$, and $a_3 = 0.75, \mu m$ is placed at a distance $h = 2.5a_3$ from a flat wall located at $x_3 = 0$. A shear rate of $\dot{\gamma} = 2000, s^{-1}$ is imposed

Parameter	Value
Number of surface receptor	571
Bond formation threshold distance	$0.5\,\mu m$
Bond breaking threshold distance	$0.725\,\mu m$
Stiffness	$2 \times 10^{-5}\,N.m^{-1}$
Rest length	$0.5\,\mu m$
Bond activation time	$3\,ms$
Stiffness increase factor	4
Max number of bonds per surface node	1
Max number of bonds per wall node	∞
Lennard-Jones zero force distance	$0.3\,\mu m$
Lennard-Jones repulsive energy	10^{-26}

Table 6.1: Parameters of the adhesion model.

by a translating top wall at $x_3 = 40a_3$, while periodic boundary conditions are applied on the lateral walls at $x_1 = 0, 30a_3$ and $x_2 = \pm 10a_3$.

The particle is initialized with its semi-axes aligned with the coordinate system, such that the minimal gap between its surface and the wall is $1.5a_3$. At this distance, no bond can form, since the bond-formation threshold is $0.66a_3$. To initialize the flow, the particle position is held fixed for the first $100\,\mu s$, ensuring that the flow is fully developed and the stresslet has converged.

To assess particle dynamics under different flow regimes, the bond activation time is varied. Reducing this parameter while keeping the shear rate fixed effectively mimics a slower flow, without the need to simulate longer particle trajectories. Two cases are considered: an activation time of 3 ms, taken from the literature (see table 6.1), and a ten times faster activation of 0.3 ms.

Representative snapshots of the particle dynamics are presented in figures 6.1 and 6.2, for the faster and slower activation times, respectively.

For the case of the faster activation time, mimicking a slower flow, the particle initially form soft bonds with the wall which very quickly transform into stronger bonds, resulting in the immediate arrest of the particle on the surface. On the other hand, when the activation time is longer or that the flow is faster, the particle is flowing too fast for the strong bonds to form in the first place. Only soft bonds are formed but are not able to counter the hydrodynamic force acting on the particle, resulting in the breaking of the bonds. Each time the particle is forming these bonds with the surface, the particle is brought closer to the wall and slowed down, which ultimately leads to a point where the slower but stronger bonds are able to form, stabilizing the adhesion of the particle.

Time: 0.00 ms

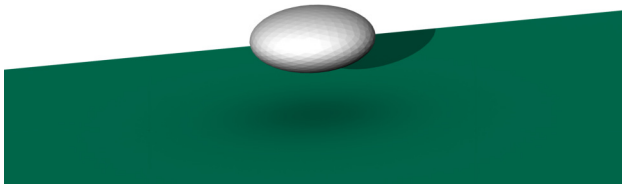

Time: 1.00 ms

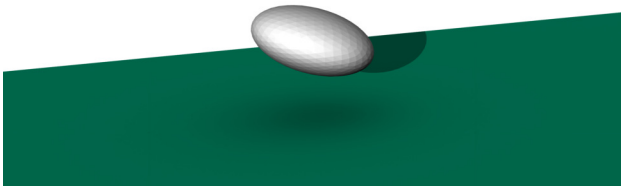

Time: 2.10 ms

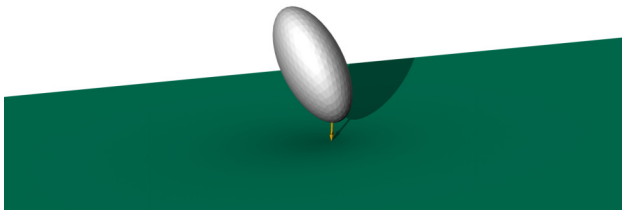

Time: 2.25 ms

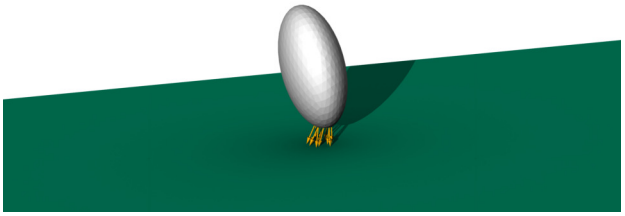

Time: 2.50 ms

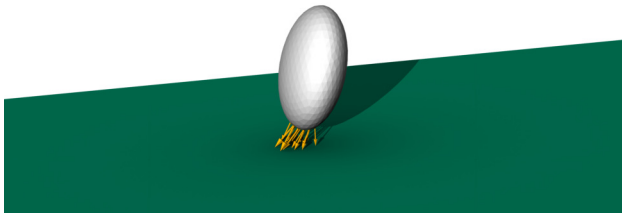

Time: 2.75 ms

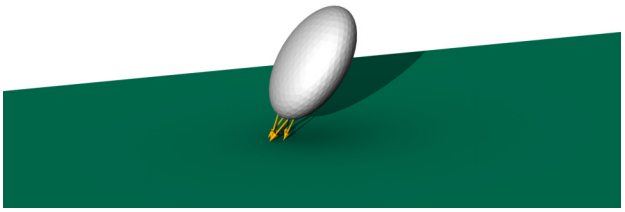

Time: 3.00 ms

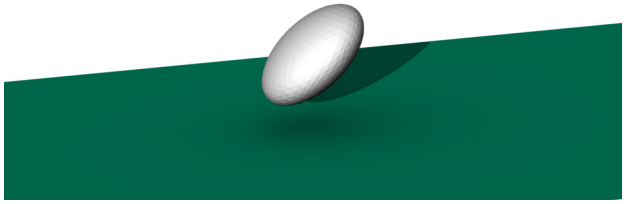

Time: 4.50 ms

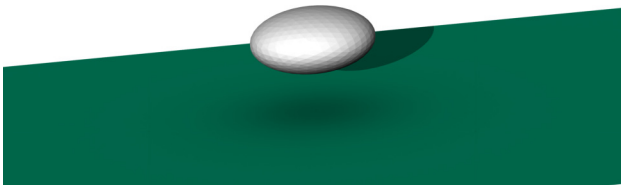

Time: 6.60 ms

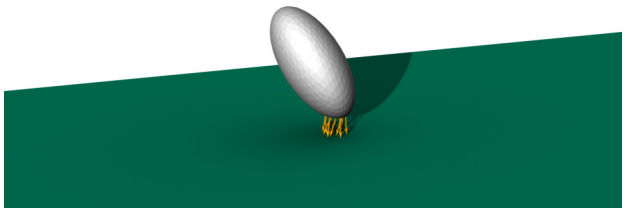

Time: 6.95 ms

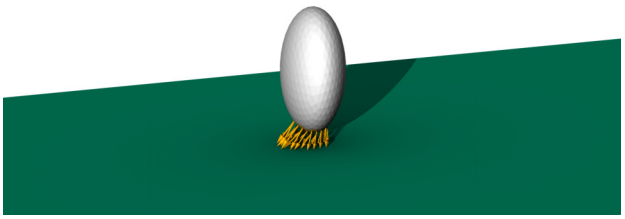

Time: 7.45 ms

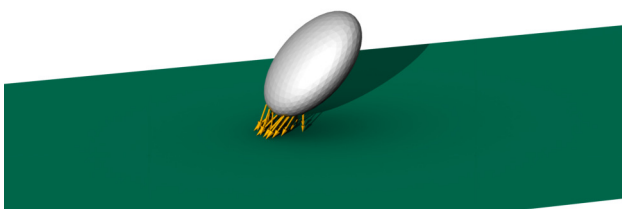

Time: 7.95 ms

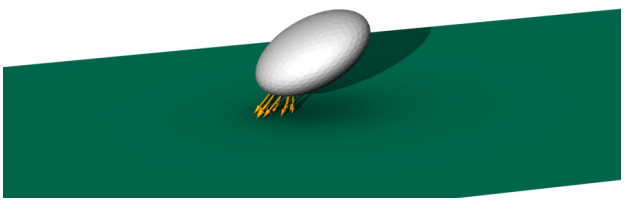

Figure 6.1: Particle adhesion over a flat surface with activation time 3 ms. (⟶) Instantaneous soft bond. (⟶) Strong bond, resulting from the activation of a soft bond formed for over 3 ms. The movie of the simulation can be viewed at the following link:

https://youtu.be/RpXevmhFc0M

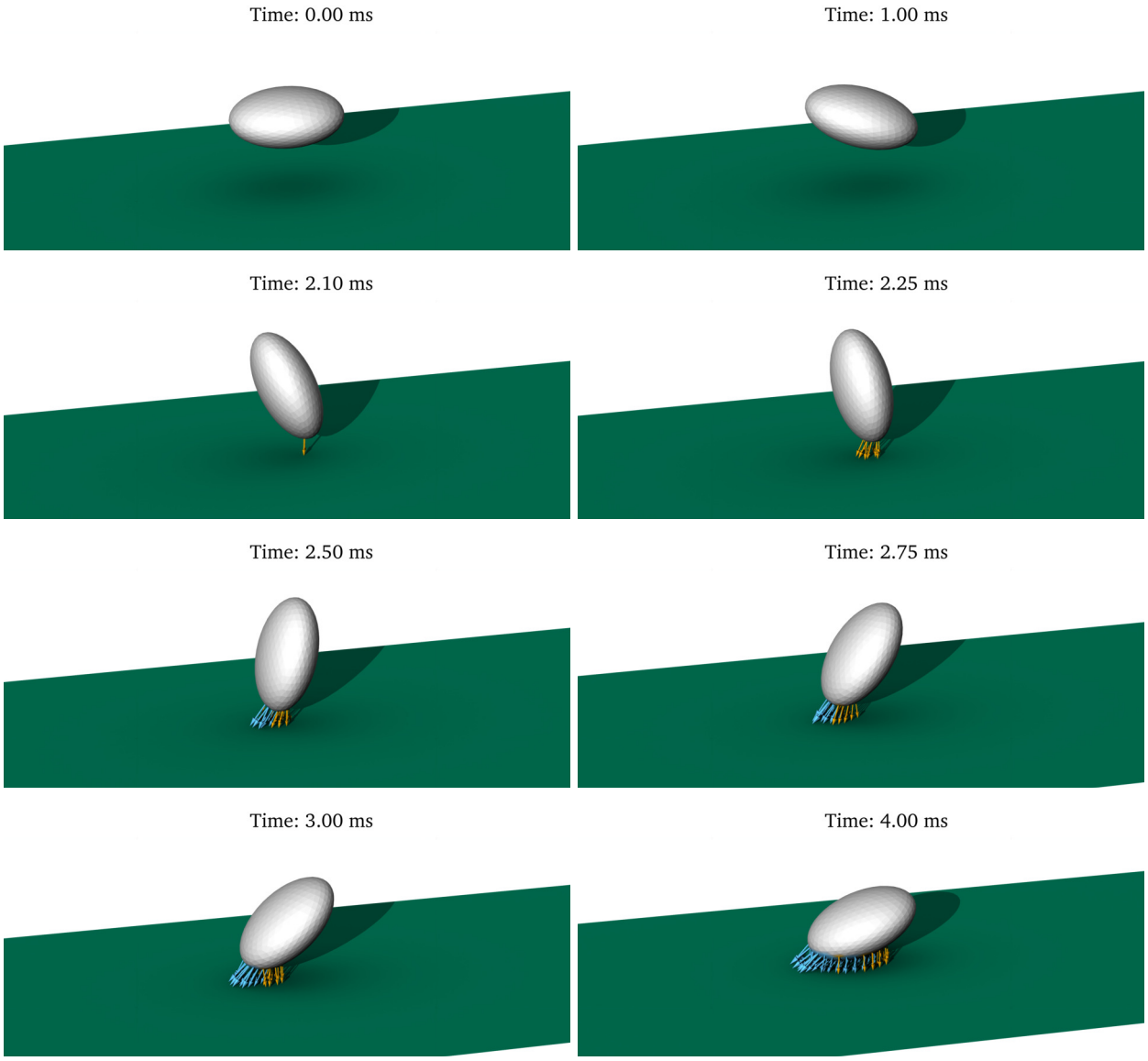

Figure 6.2: Particle adhesion over a flat surface with activation time 0.3 ms. (⟶) Instantaneous soft bond. (⟶) Strong bond, resulting from the activation of a soft bond formed for over 0.3 ms. The movie of the simulation can be viewed at the following link:

https://youtu.be/BBAtBb7uJdQ

Figure 6.3 shows the evolution of the particle center of mass position over time, in the direction of the flow, which is used to compute the translocation distance of both particles after shifting the curves so that the first bond formation occurs at $t = 0$ and $X_1 = 0$.

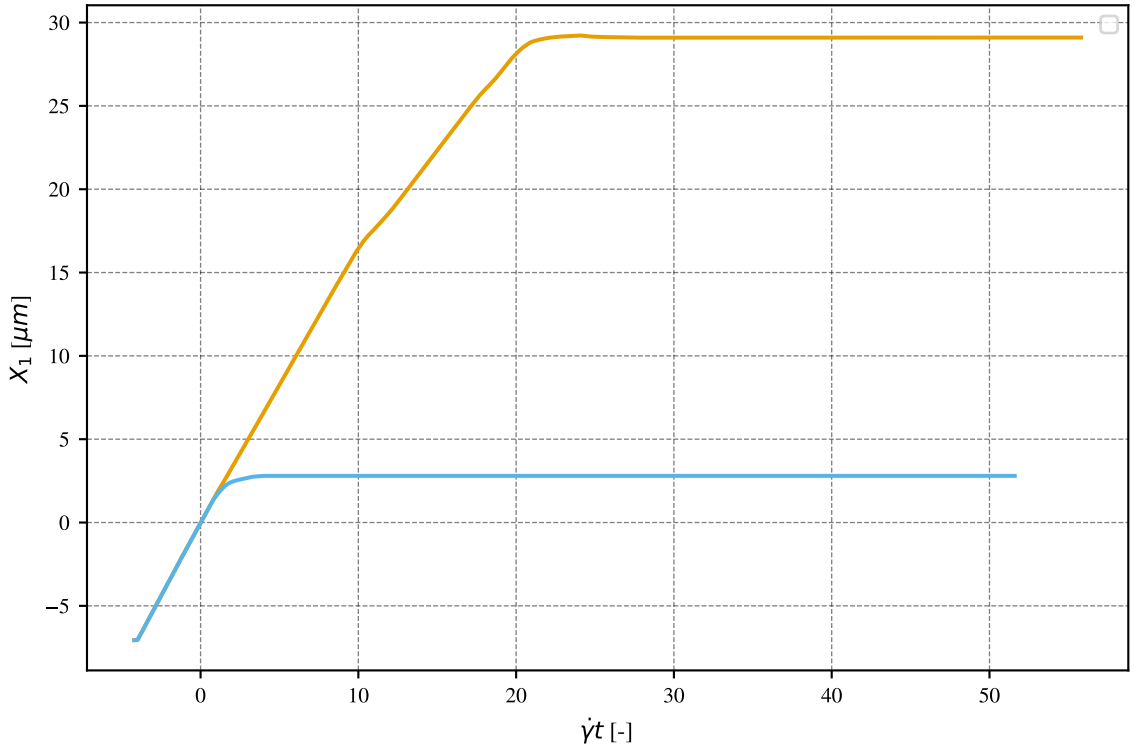

Figure 6.3: Evolution of the particle center of mass position over time in the flow direction. The time and position are shifted so that the first bond formation happens at $t = 0$ and $X_1 = 0$. (——) Activation time $\tau_{act} = 3$ ms. (——) Activation time $\tau_{act} = 0.3$ ms.

The resulting translocation distances are 2.8 μm and 29 μm for the faster and slower activation times, respectively. These values are in reasonable agreement with the experimental and numerical results of [Fitzgibbon *et al.* 2015] who observed a mean translocation distance of 8 μm at a shear rate of $\dot{\gamma} = 1500\, s^{-1}$. [Fitzgibbon *et al.* 2015] also observed that the translocation distance depends almost linearly on the shear rate, with a slope of approximately 3/8. In our case, reducing the activation time by a factor of 10 yields a translocation distance that is also reduced by a factor of 10, corresponding to a linear dependence with slope 1 between activation time and translocation distance. This suggests a limitation in interpreting changes in apparent shear rate solely through variations in activation time. Nonetheless, the model successfully captures the qualitative features of the translocation mechanism.

6.4 Single platelet adhesion over a sawtooth structure

The previous section confirmed the model represents correctly the translocation mechanism of platelet adhesion over a flat surface, using parameter values derived from biological information. This section now focuses on the usage of this model to investigate the adhesion of a particle on structured surfaces and in particular the upward sawtooth structure which was shown in section 4.2.2 to generate a repulsion of the particle.

Using the same geometry and domain as in section 4.2.2, the investigated structure has a period pattern of $L = 6a_3$ and height $h = 4a_3$. The particle is initially placed at a distance of $2.5a_3$ from the top of the structure as if the sawtooth were carved into the flat surface of section 6.3. The same adhesive model parameters are used which are summed up in table 6.1. The shear rate of $\dot{\gamma} = 2000\,s^{-1}$ is again imposed by the translating top wall, and periodic boundary conditions are imposed on the sides.

Selected snapshots of the particle dynamics are presented on figure 6.4

It can be seen that the particle only form soft bonds during its first flipping motion, when the particle is vertical right above the top of a sawtooth. However, because of the reduced available surface, fewer bonds are formed compared to the flat surface at the same instants. Consequently, the particle is not slowed down as much and is not brought closer to the wall which is also a consequence of the drift generated by the structure. From this reduced slow down and difficulty to bring the particle closer to the wall, as well as a reduced surface area, the particle will not form any other bonds for the rest of its motion, as already seen on the second flip shown on figure 6.4. It is slowly drifting away due to the structure and eventually reaches an altitude where it cannot form any bonds, whatever its orientation and position in the structure.

An argument which is often used to justify a reduced platelet adhesion on structured surfaces in experimental observations is the reduction of available adhesive surface (see section 1.3.2). To distinguish the effect of the reduced available adhesive surface from the hydrodynamic repulsion of the sawtooth structure, the adhesion of the particle over a flat surface with reduced available adhesive surface is performed. To do so, the flat surface from section 6.3 is used, but adhesive regions of width $1.33a_3$, spaced by $4.66a_3$ to obtain the same pattern period of $L = 6a_3$ as the sawtooth structure. The resulting geometry therefore yields a reduced surface area comparable to that of the sawtooth structure, while ignoring the hydrodynamic effect of the structure. Snapshots of the particle dynamics are presented on figure 6.5.

The particle can be seen regularly forming bonds with the adhesive areas, being pulled slightly closer to the surface each time and reducing its velocity. As it is closer to the surface and slowed down, more and more bonds are able to form. However, the reduction of adhesive surface results in a reduced number of formed bonds, so that even when the particle is in contact with the surface, the soft bonds do not counter the hydrodynamic forces enough to allow the activation of the stronger bonds. The particle is therefore never fully arrested on the surface and keeps translocating for the whole simulated time.

This highlights the effect of a reduced adhesive area, which indeed prevents complete stop of the particle on the surface. Nevertheless, the particle is still interacting a lot with the surface, which could lead to platelet activation from mechanical signaling or high interaction rates with surface bound chemicals. On the other hand, the sawtooth structure, while reducing the available adhesive surface also repulses the particle away from the wall, minimizing the interactions between the particles and the surface.

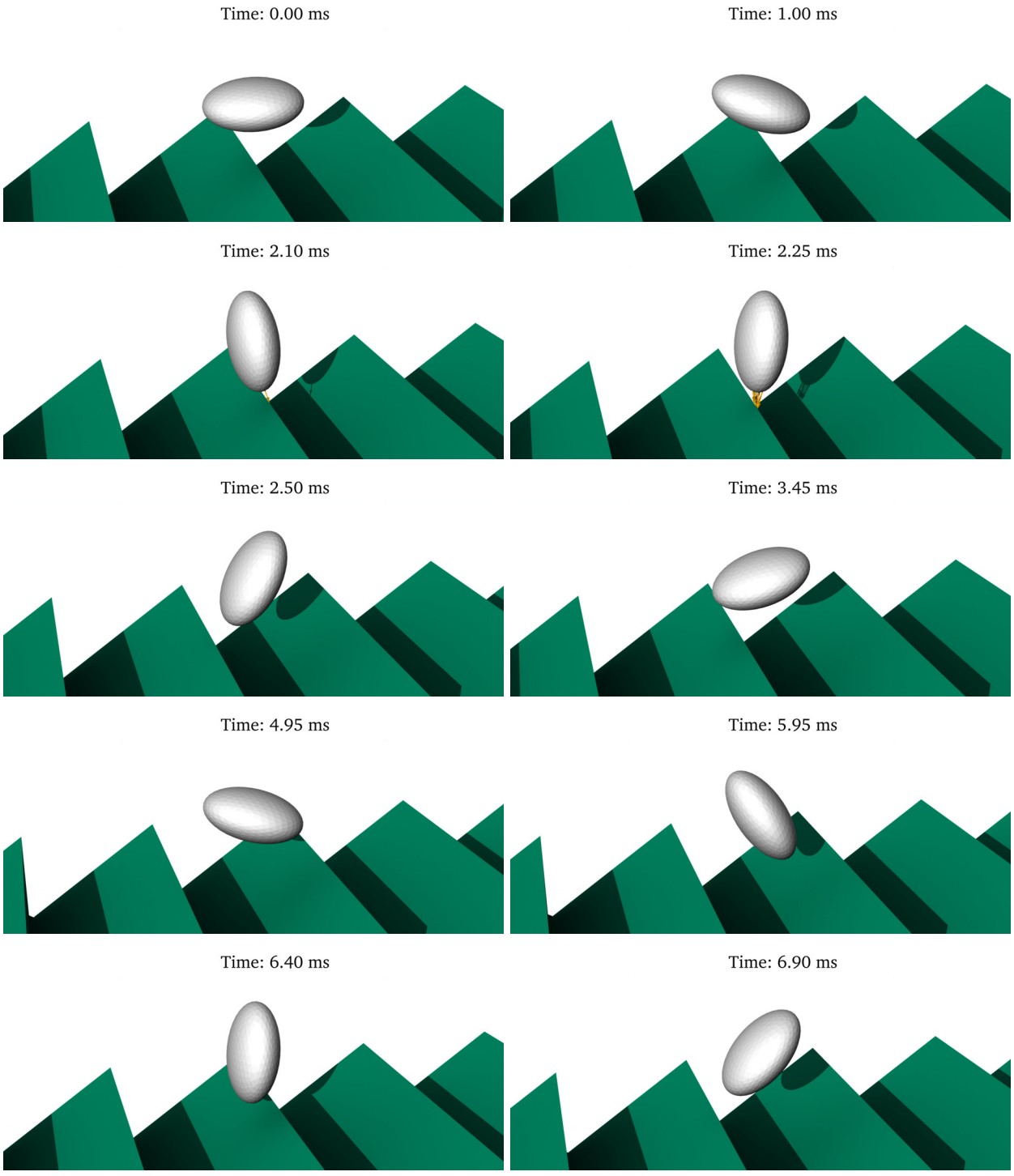

Figure 6.4: Particle adhesion over a sawtooth structure. (→) Instantaneous soft bond. (→) Strong bond, resulting from the activation of a soft bond formed for over 3 ms. The movie of the simulation can be viewed at the following link:

https://youtu.be/q3M5eiCwxEg

Time: 0.00 ms

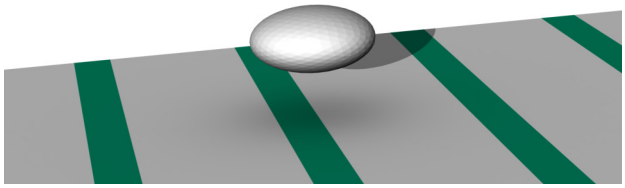

Time: 1.00 ms

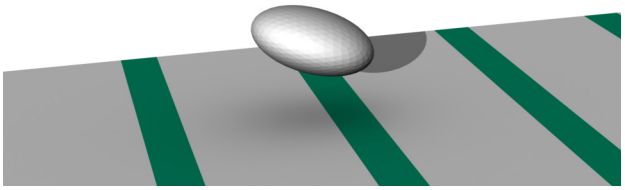

Time: 2.10 ms

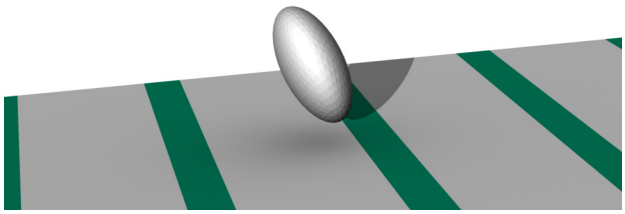

Time: 2.25 ms

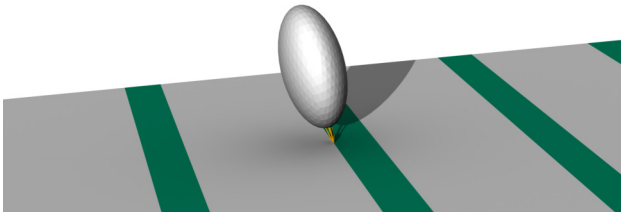

Time: 2.50 ms

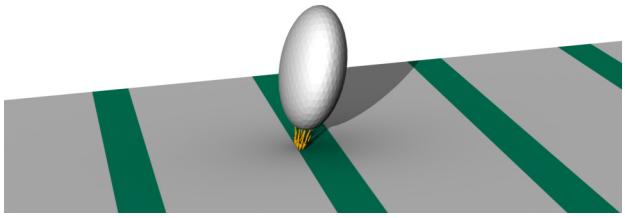

Time: 2.75 ms

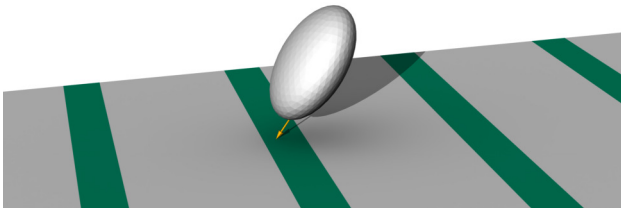

Time: 4.50 ms

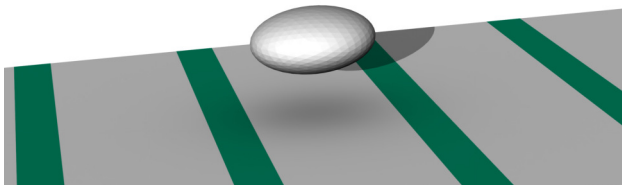

Time: 6.60 ms

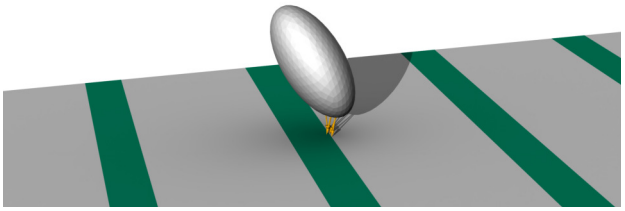

Time: 6.95 ms

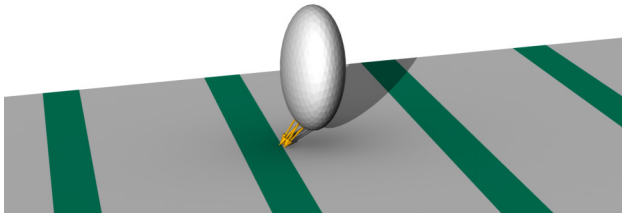

Time: 7.95 ms

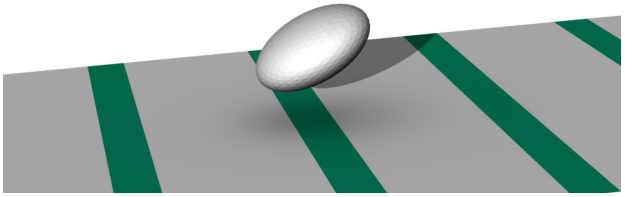

Time: 8.95 ms

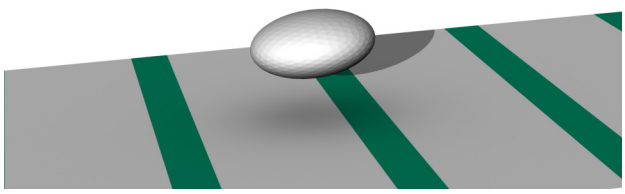

Time: 11.10 ms

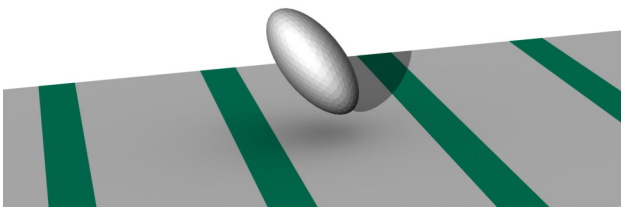

Time: 12.40 ms

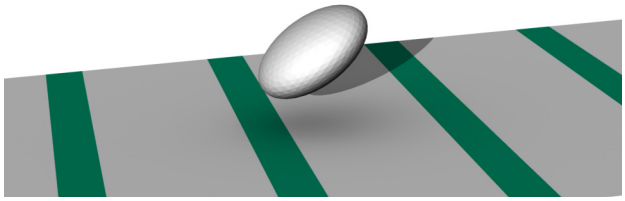

Time: 14.90 ms

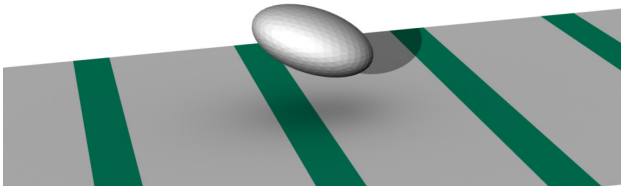

Time: 15.90 ms

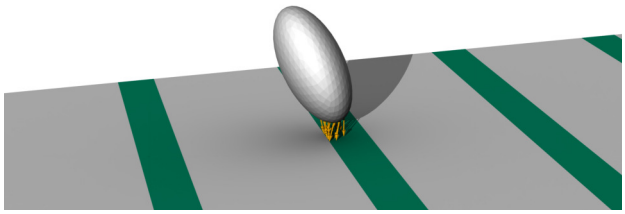

Time: 16.40 ms

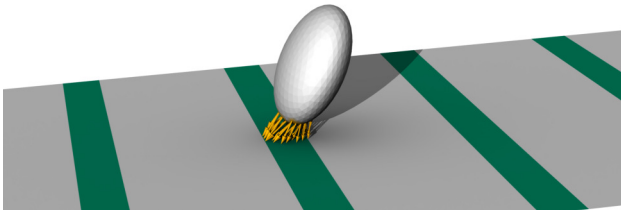

Time: 16.85 ms

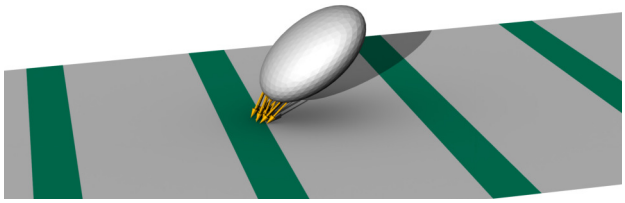

Time: 17.35 ms

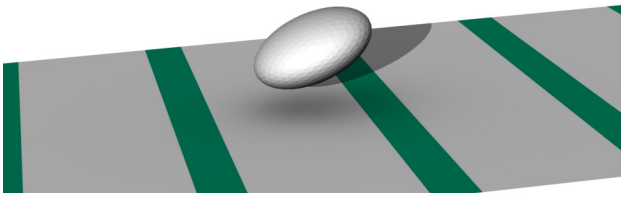

Time: 18.35 ms

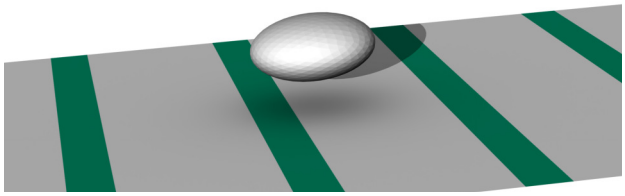

Time: 20.35 ms

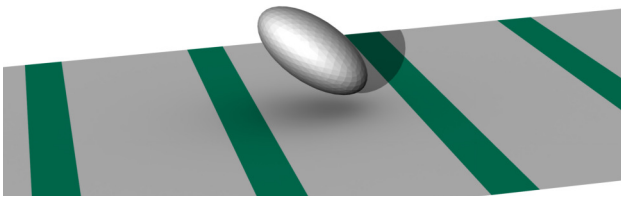

Time: 20.85 ms

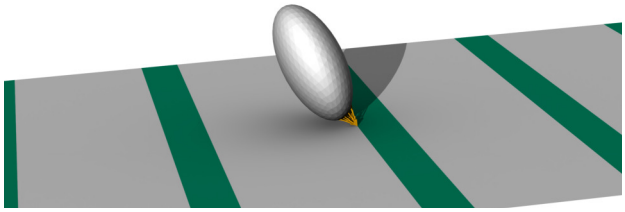

Time: 21.35 ms

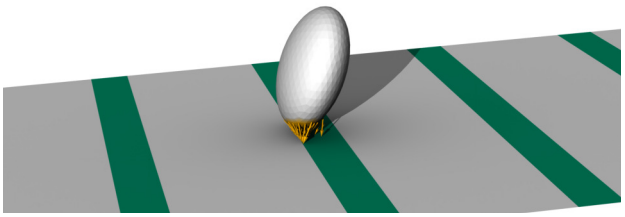

Time: 21.80 ms

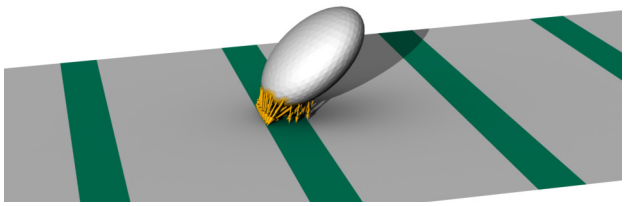

Time: 22.30 ms

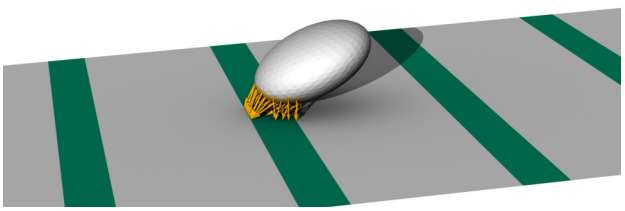

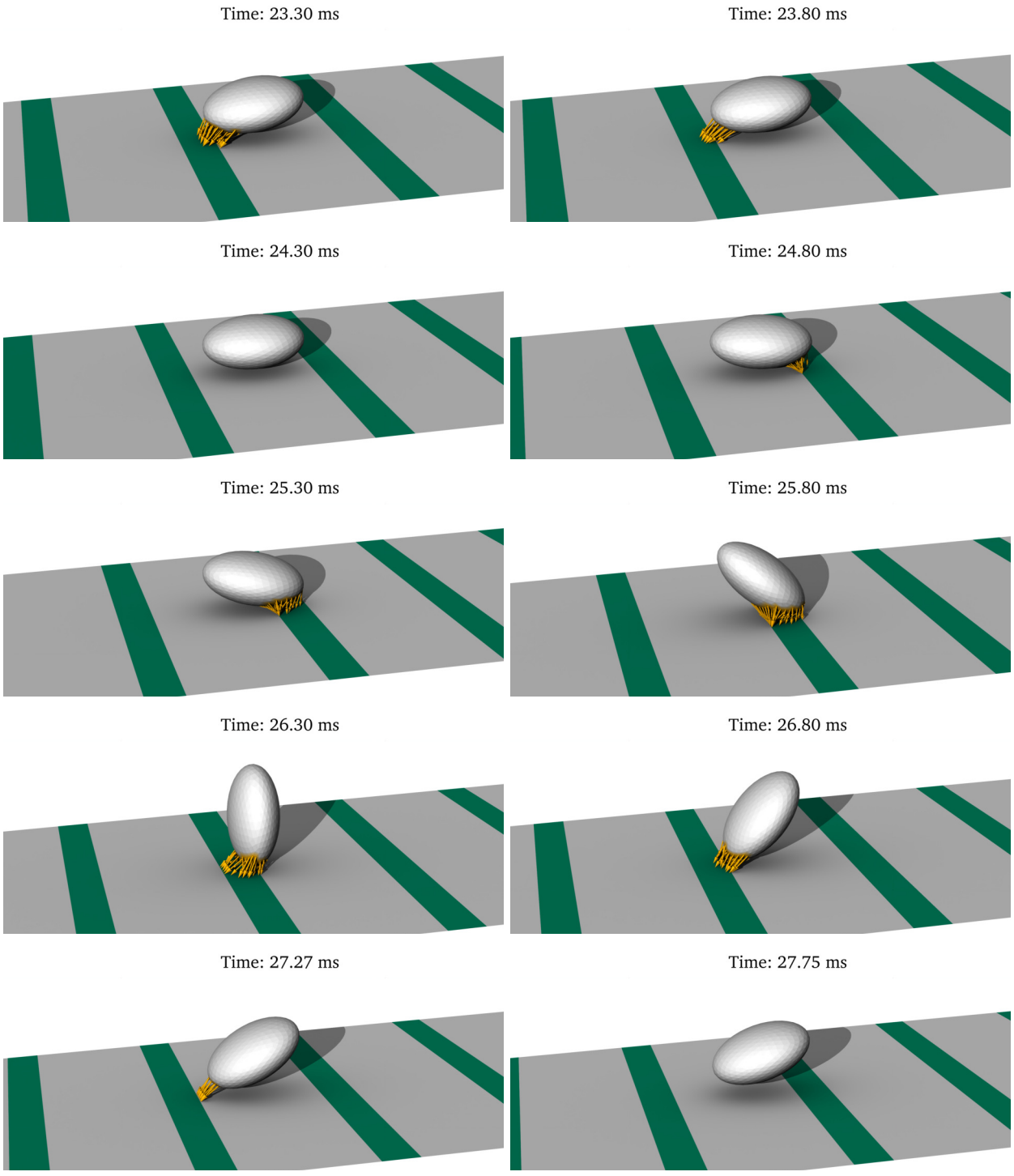

Figure 6.5: Particle adhesion over a flat surface with reduced adhesive surface. ( ) Adhesive surface. (→) Instantaneous soft bond. (→) Strong bond, resulting from the activation of a soft bond formed for over 3 ms. The movie of the simulation can be viewed at the following link:

https://youtu.be/EQpyA8CTWAA

The evolution of the particle position in the plane $(\mathbf{e}_1, \mathbf{e}_3)$ is shown on figure 6.6 for the particle adhesion on a flat surface, a sawtooth structure and a flat surface with reduced adhesive area referred to as $\mathcal{S}_{flat}$, $\mathcal{S}_{saw}$ and $\mathcal{S}_{reduced}$.

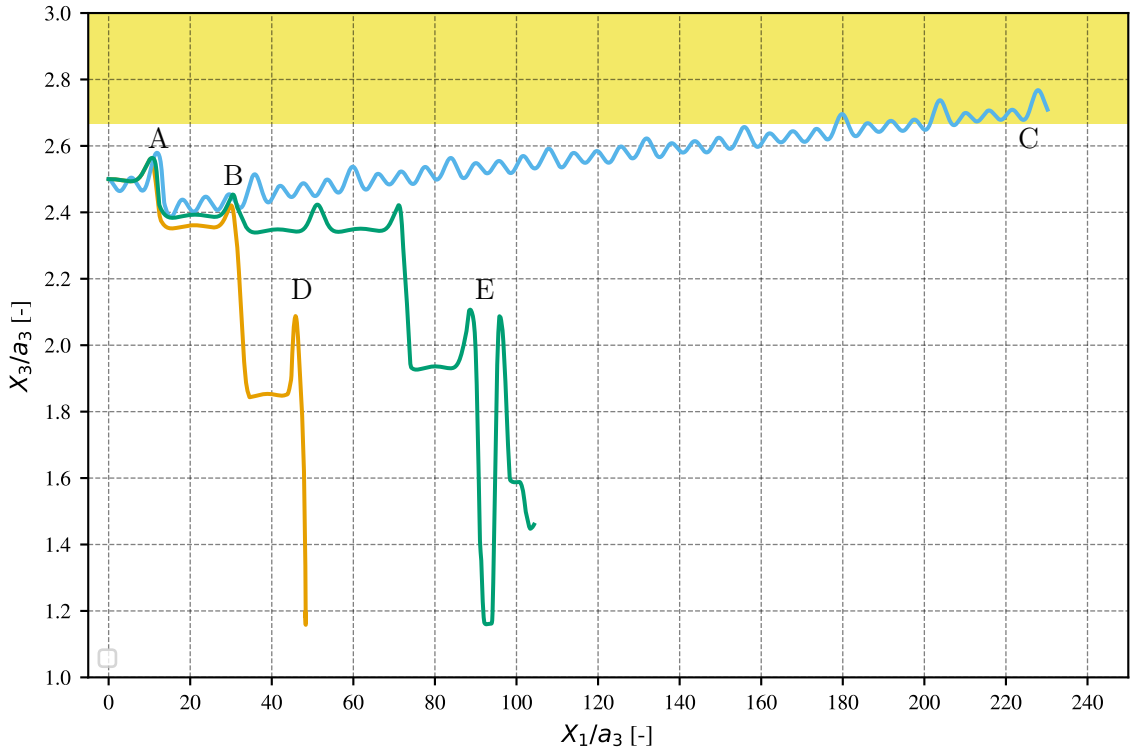

Figure 6.6: Evolution of the particle altitude over its trajectory. (——) Flat surface, (——) Sawtooth structure and (——) flat surface with reduced adhesive area. The yellow region (▬) indicates the altitudes for which the particle is out of reach for the adhesive bonds, whatever its orientation and longitudinal position relative to the pattern structure.

Jumps in particle altitude towards the wall can be observed corresponding to binding with the surface. A first binding happens for all three surfaces around $X_1 = 10a_3$ (labeled A in figure 6.6), which brings the particle down towards the wall by a small amount. The particle transported over $\mathcal{S}_{saw}$ and $\mathcal{S}_{reduced}$ are less attracted than the particle over $\mathcal{S}_{flat}$, because fewer bonds were formed for these two surfaces. When the particle performs its second flipping motion (label B), the particle forms a lot of bonds with $\mathcal{S}_{flat}$, as shown by the sharp decrease in particle altitude. The particle forms only few bonds with $\mathcal{S}_{reduced}$ as seen on figure 6.5, and no bonds are formed by the particle transported over $\mathcal{S}_{saw}$. In fact, the trajectory of this particle indicates it never forms bond outside the first ones. The drift of the particle caused by the structures is clearly seen here, with the particle finally escaping from the potential bond formation range (label C). Over $\mathcal{S}_{flat}$, the particle is brought to rest during its second flipping motion (label D). Over $\mathcal{S}_{reduced}$, the particle can be seen forming bonds which brings the particle in contact with the wall, but escaping these bonds to flip back upward in the flow in a pole-vaulting like motion (label E).

6.5 Multiple platelets aggregation

In its current state, the model is implemented to allow adhesion between multiple particles in addition to the particle to wall adhesion. Because only one bond is allowed for each surface node, particular care is taken during the bond formation process, if multiple bonds are possible.

As an example, consider nodes 1_A and 2_A of surface A, and nodes 1_B and 2_B on surface B. The surfaces are in a position for which both nodes 1_A and 2_A can bind to both 1_B and 2_B. The naive way to form bonds is to form the bonds only based on the distance between the nodes, but this could result in the formation of bond $1_A - 1_B$ and $2_A - 1_B$ if both nodes of surface A are closest from node 1_B than 2_B. To prevent bond multiplicity, the distance between all the nodes from all the particle surfaces are first computed and in the case where a distance is shorter than the bond formation threshold, the potential bond information are stored (node to node distance, nodes id, etc...). The potential bonds are the sorted from the shortest to the longest and the sorted array is then run through. Starting from the shortest possible bond, if the two nodes of both surfaces are still available (*i.e.* no other bond involving these two nodes have been formed) a bond is formed between the two nodes. This way, no node can be involved in more than one bond. In the previous example, if $1_A - 1_B$ is longer than $2_A - 1_B$, then $2_A - 1_B$ will be formed first, and nodes 2_A and 1_B will not be available anymore, resulting in the formation of bond $1_A - 2_B$ if possible.

This algorithm is not very efficient as it scales as $N \times n^2$, with N the number of particles in the simulation, and n the number of node per particle surface. However, because aggregation is not the main focus of this work, a proof of concept with a few particles is still possible.

Four particles are placed close to a flat surface, with their orientation and position chosen to allow adhesion at the start of the simulation as can be seen on figure 6.7. As this simulation is only a proof of concept, the activation of the bond was set to $0.3\,ms$ to ensure activation of the bonds is observed with a short simulation. The mesh resolution ($\Delta x = a/6$) is also smaller than the one prescribed in section 3.4.2 ($\Delta x = a/8$) and the simulation box is smaller (square base with side $20a$ and height $40a$).

Bonds can be seen forming between particles and the wall as well as between multiple particles. The bonds are also activating once they reach the threshold time. Because the simulation domain is quite small, particles can be seen leaving the domain on the right-hand side, and reentering the domain on the left-hand side after crossing the periodic boundary. The particles that are the closest to the wall are brought to rest as the bonds have been activated quickly, and the other two particles can be seen periodically rolling on top of them but not being able to adhere as they are further up in the flow, and the bonds are not balancing the hydrodynamic forces acting on them.

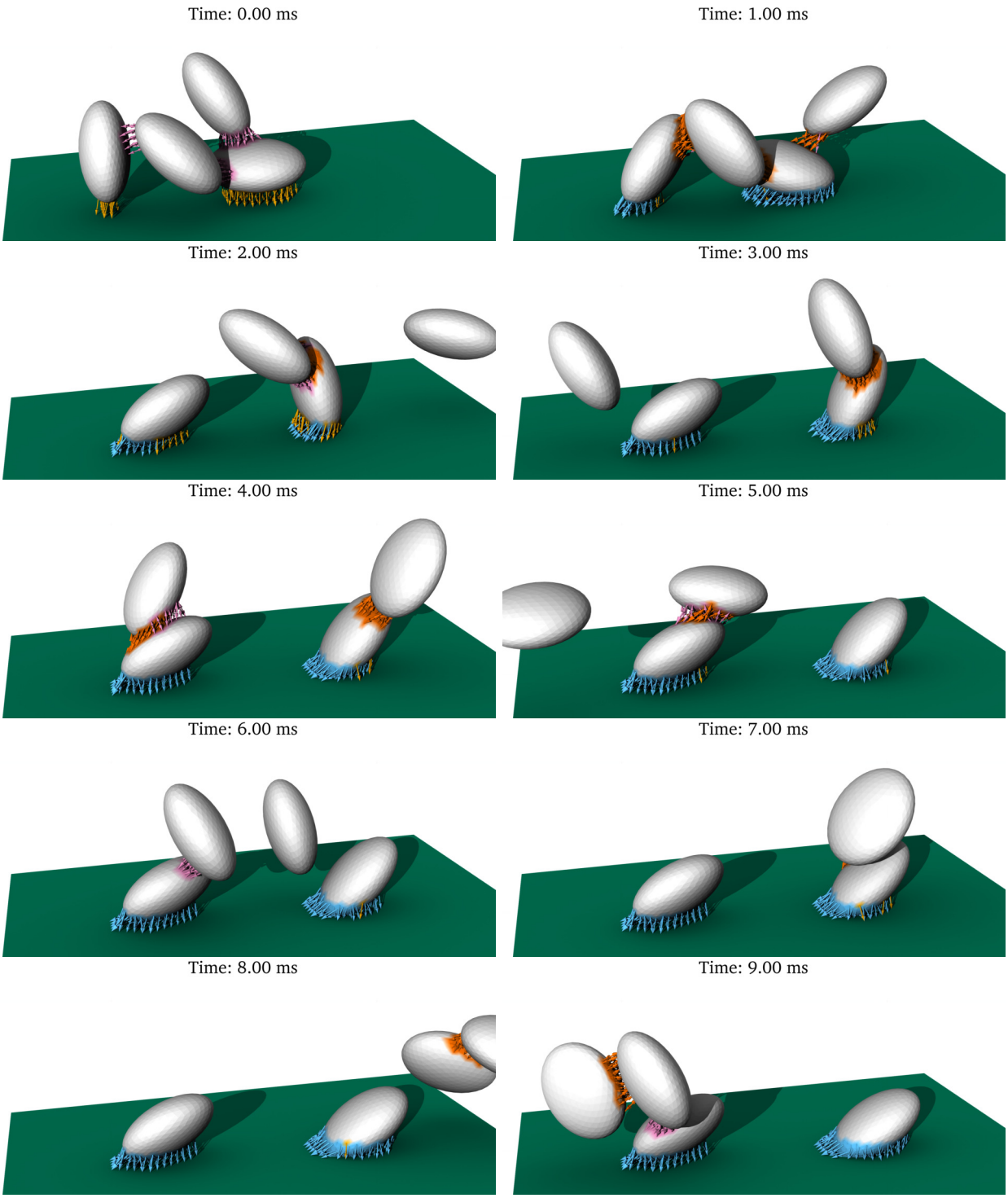

Figure 6.7: Aggregation between 4 particles. (→) Soft bond between two particles, (→) Activated strong bond between two particles, (→) Soft bond between a particle and the wall (→) Activated strong bond between a particle and the wall. The movie of the simulation can be viewed at the following link:

https://youtu.be/1bj3mtG3l3E

Chapter 7

Discussion

7.1 Conclusion

As cardiovascular diseases remain the main cause of death worldwide [WHO 2024], the need for medical devices is still very high. These devices are directly exposed to blood due to the nature of the pathologies they aim at treating and if nothing is done to prevent it, they are prone to initiating thrombus formation. In the blood circulation, thrombus formation is the natural response of the body to stop a blood leakage out of an injured vessel and allow healing of the wound. This process is initiated by the adhesion of blood platelets, followed by their activation alongside the coagulation cascade, resulting in the formation of a blood clot [Fogelson & Neeves 2015]. If this process is crucial to ensure blood vessels integrity, it is also triggered by the presence of artificial surfaces like blood contacting medical devices. Development of a thrombus at the surface of a device could lead to failure of the device or thromboembolism threatening the life of the patient. Patient receiving these devices are therefore also subjected to anticoagulant or antiplatelet therapies, even though they are associated with increased risk of bleeding [Jaffer & Weitz 2019].

Various technologies are currently investigated to improve the compatibility of such artificial surface with blood which are presented in the first chapter of this thesis. The focus of this work was the use of surface structuring in the micrometer range which have been shown experimentally to alter platelet adhesion and activation, but for which no clear conclusion have been drawn regarding its use to improve the hemocompatibility of artificial surfaces. This is addressed with a brief review of experimental results on this matter (see table 1.2), highlighting the broad range of investigated structures, materials and flow conditions which sometimes lead to contradictory results between studies. To provide further information on the interaction between blood platelet adhesion, the initial event in thrombus formation, and structuration of the artificial surface, a numerical model of platelet adhesion has been developed during this work. This numerical model was then used to study these interactions, in a reproducible environment and with more control over the parameters of the experiment. Even though the model is only an approximated representation of blood platelets, it allowed to highlight a novel drift mechanism induced by the surface structuration which could be used to repel platelets away from the surface, preventing their adhesion.

The model is based on the resolution of the surrounding plasma flow as a homogeneous incompressible Newtonian fluid, governed by the Navier-Stokes equations. This resolution is performed with the in house YALES2BIO library to which the Force Coupling Method (FCM) was added, allowing the simulation of particulate flow at small Reynolds number, for both spherical and ellipsoidal rigid particles. The theoretical background of the Navier-Stokes solver as well as the FCM are presented in chapter 3, alongside an extensive validation of the implementation. This validation allowed concluding on the working range of the simulation parameter (mesh size, particle distance to the wall and particle aspect ratio in particular).

In parallel, an analytical solution of the force acting on a spherical particle transported over structures of negligible amplitude compared to the particle radius is presented in chapter 2. The development of this analytical solution initially obtained by [Assoudi *et al.* 2018] is detailed and have been extended

to ellipsoidal particles. From this analytical solution, it appears that no net lift force can be acting on a spherical particle transported over structures of negligible amplitude, whatever the shape of the structure. Confrontation between the analytical model and simulations with the FCM was also able to show good agreement between the two models for structures of small amplitude, further validating the FCM model.

From this, numerical simulation with the FCM have been performed on structures of finite amplitude and with ellipsoidal particles. A symmetric structure, square corrugations, was first investigated and lead to local drift of the particle but no net average effect of the particle as a consequence of the reversibility of the flow. Introduction of a for-aft asymmetry in the pattern by using sawtooth structures leads to a net drift of the particle. This drift, quantified by the angle between the position of the particle before and after it performed one rotation of 180°, was observed to be positive when the sawtooth is oriented upward, and negative when oriented downward, in agreement with the reversibility of Stokes flows. The effect of various simulation parameters on this drift angle (structure pattern period, pattern height and Reynolds number) has also been investigated.

The following chapter was dedicated to providing an explanation to this drift. First, the problem is reduced to the study of the dynamics of a spherical particle instead of an ellipsoidal one, for which the drift is still observed. Then the structure have been decomposed into elementary geometrical features to investigate if a ramp up or a vertical step affected the particle differently. This investigation was not successful even though it allowed further comparison between the analytical and the FCM model. Finally, the mobility matrix of a spherical particle positioned at different locations in the sawtooth pattern allowed to highlight the contributions of the external forces on the particle drift angle. This showed that the drift of the particle is due to a slight imbalance between the positive contribution of the horizontal force and the negative contributions of the vertical force and the torque acting on the particle due to the background flow, in the generation of a vertical particle velocity. This study is also applied to a case with varied particle to wall distance, as well as for different structure height. The effect of inertia was also discussed for each of these cases.

In the end, the model which was so far only exploited to study hydrodynamic interactions between the particle and the wall, is enriched with some adhesion mechanisms. This adhesive model, even though it is phenomenological, is based on physiological values of platelets adhesive bonds properties, which are detailed in chapter 6 and translated into model parameters. This allowed reproducing qualitatively the mechanism of platelet translocation over a flat surface. The model also allowed to investigate the effect of reduced adhesive area which is often an argument employed in experimental study to justify a reduction in platelet adhesion over a structured surface. It was showed that even though the particle is not able to firmly adhere to the flat surface with reduced adhesive area, it was still in close interaction with the surface and regularly forming transient bonds. On the other hand, the sawtooth structure, which also reduces the available adhesive surface by its geometrical features, was having a reduced number of interaction with the particle as it additionnaly generates a particle drift, repulsing the particle away from the surface. Finally, the possibility to model platelet aggregation with the model in its current state is presented.

7.2 Perspectives

The numerical model of platelet adhesion which was developed allowed to highlight a novel lift mechanism for rigid spherical and ellipsoidal particles in low Reynolds number flows. The effect of various parameters on this drift have been investigated during this work, but further work is required to fully characterize this mechanism. For example, determining scaling laws for the drift angle as functions of the Reynolds number or the particle-structure distance could allow easier use of this effect for practical

applications. A deeper understanding of this mechanism could ease the determination of such laws. The decomposition of the movement using mobility matrices as presented in chapter 5 seems like an appropriate tool for that, in the context of small Reynolds number. A Stokes solver could probably perform this analysis with more accuracy, even though decreasing the Reynolds number down to 10^{-6} provided great results already. A BEM solver is currently being developed by Barthélémy Thibaud (IMAG, Université de Montpellier, post-doctoral researcher) and Giulia Malaguzzi (Politecnico di Milano, Master Student) in our team so it is expected to have results with this method in the near future. This analysis could also be extended to ellipsoidal particles easily. This could help to identify why the ellipsoidal particle are drifting more than the spherical ones. This deeper understanding of the mechanism is also the first step towards the discovery of structure generating and even greater drift.

To ensure this drift is not a numerical artifact, experimental observation of particle being repulsed by structured surfaces are also required. A preliminary experiment has been conducted by Manouk Abkarian (CBS, CNRS, Directeur de Recherche) and Rémy Fulcrand (CBS, CNRS, Ingénieur de Recherche) at the Centre de Biologie Structurale in Montpellier. Using a microfluidic setup, they injected a suspension of non-buoyant polystyrene beads in a square channel, at a flow rate of $100\,\mu L/h$ ensuring a non-inertial flow. One of the channel side was covered with sawtooth structured PDMS, obtained by molding into a cast created by photolithography. An example of the resulting structures can be observed on figure 7.1.

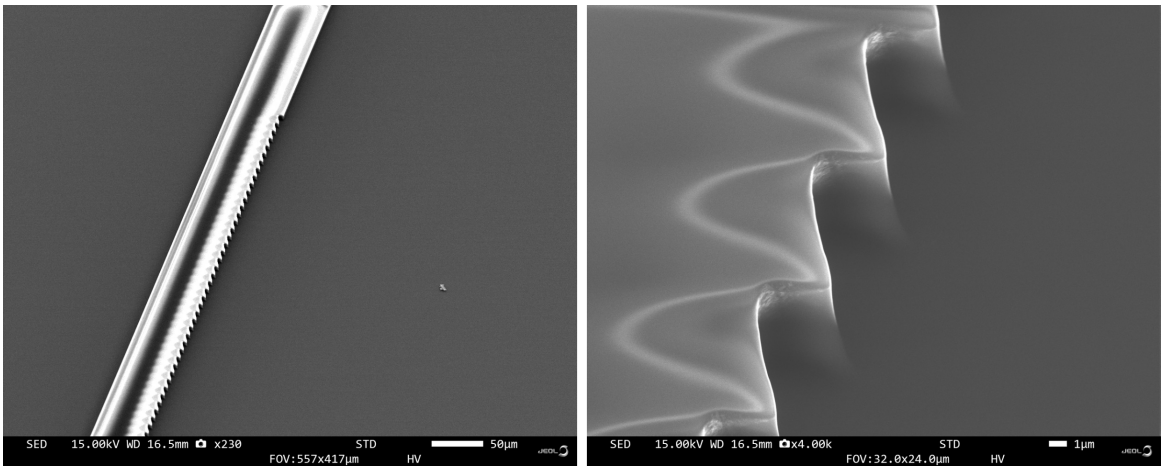

Figure 7.1: Sweeping electron microscope images of the generated sawtooth structures.

To measure the drift of the particles, the fluorescence of the beads under a laser is measured. A higher fluorescence therefore indicates a greater particle density. Figure 7.2 presents the result for both the upward and the downward sawtooth structure, where a low fluorescence signal can be observed close to the upward sawtooth structure, at the end of the channel, indicating particle have migrated away from this region. On the other hand, the downward sawtooth did not show this particle depleted region which suggests that the observed effect is the same as observed numerically.

This preliminary experiment is the first step towards further experimental validation and characterization of this drift.

In particular, the application of a similar experiment to real platelets would be very interesting. Indeed, the assumptions of the numerical model (rigidity, ellipsoidal shape and simplified adhesive mechanisms for example) make it difficult to predict whether the sawtooth structure would prevent the adhesion of blood platelets. Use of real platelets is a future objective at the CBS.

Also, this research project was initiated as a collaboration between IMAG and the Cardiovascular Engineering lab in Aachen, Germany. While the focus was on the establishment of a numerical model

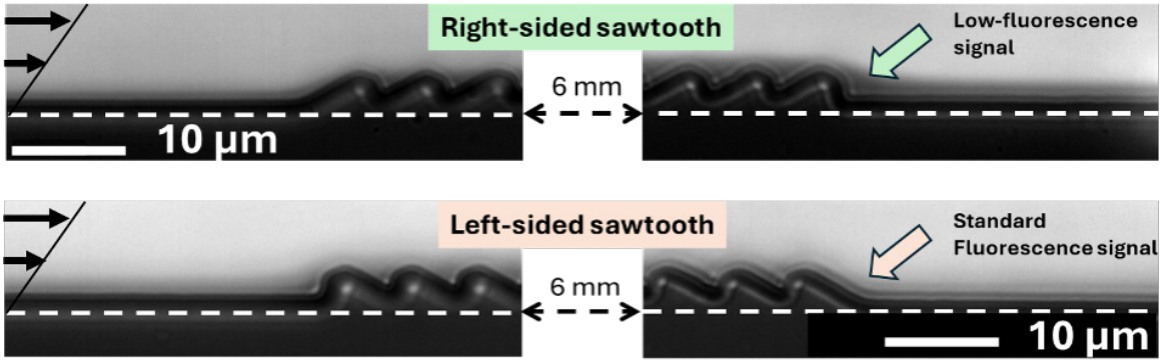

Figure 7.2: Near wall visualization of the microfluidic flow with fluorescent spherical beads in a channel with a 6 mm long structured section. Left and right column show the upstream and downstream extremities of the structured pattern respectively. A brighter field indicate a greater particle density.

at IMAG, the team at the CVE was focusing on the development of an experimental setup including generation of the microstructures, flow chamber and real-time visualization of blood platelets dynamic on the structures. Even though the interaction between the two teams did not yield significant results during the development of both the numerical and experimental setup, future collaboration could provide interesting results.

If experimental confirmations that the structures indeed reduce platelets adhesion, scaling up at the scale of a blood contacting medical device can be done by using a macroscale model. The development of such model have been initiated by the author during an internship preceeding the begining of the PhD project. The model relied on the use of spherical point particle to represent blood platelets and a Morse potential of interaction to model the adhesive mechanism of the platelets following [Yazdani *et al.* 2017]. Activation and subsequent increase in adhesion where triggered by the transport of a chemical species released by an injury site. An example of a particle aggregate formed over an injury site using this model is shown on figure 7.3.

Once the effect of the structured surface on particle repulsion is well characterized, a wall law could be derived and applied to this macroscopic model with flat walls, allowing resolution of a large domain size and large number of particles, moving towards the simulation of a real medical device.

Improvement of the biological features of the model could help predict with more accuracy the behavior of real platelets over such patterned structures. For example, it was discussed in chapter 6 that the von Willebrand Factor (vWF) had a very particular dynamic, and the two-step adhesion mechanism implemented in the current platelet adhesion model was a simplification of the adhesion of platelet on vWF. Pierre-Louis Martin (IMAG, Université de Montpellier, PhD student) is currently working on a numerical model of the dynamic of the vWF. The aim of his PhD project is to observe the effect of microstructures on the unfolding of the vWF and ultimately coupling his model with the model of blood platelets developed in this work. The alteration of the unfolding of vWF could be another way to prevent platelet adhesion, alongside the lift generated by the structure.

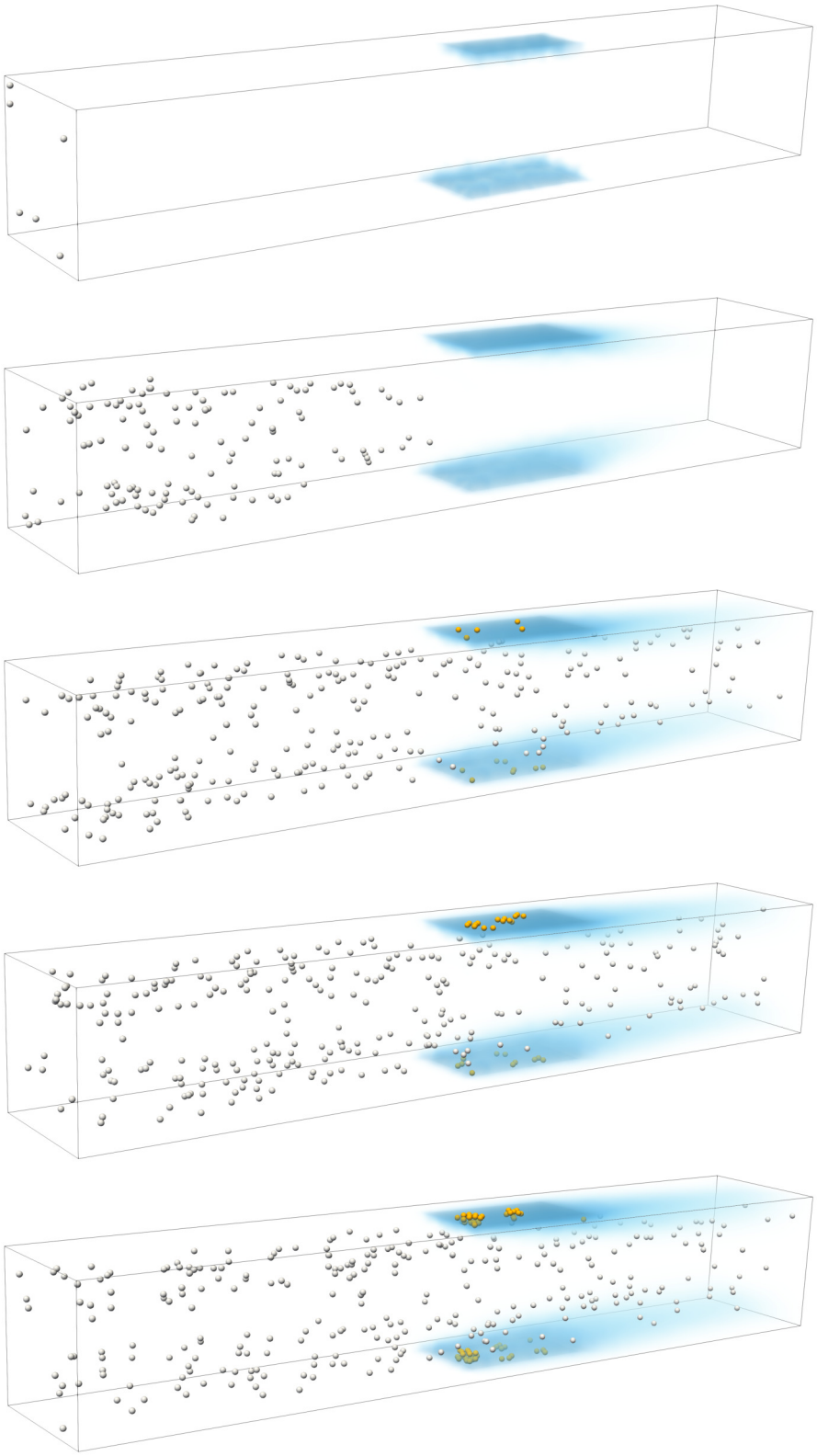

Figure 7.3: Macroscale model of platelet adhesion and aggregation. Point particles are represented by a sphere and initially injected in a resting state. ( ) An injury site is releasing a chemical species. Resting particles entering a region where the volume fraction of the activating species is greater than 0.5 are activating ( ). Adhesion and aggregation are modelled using a Morse potential following [Yazdani *et al.* 2017]. The resting particles have a reduced interaction with the wall and active particles compared to activated ones. The movie of the simulation can be viewed at the following link:

https://youtu.be/OxRkjB9cc7s

Appendices

Appendix A

Numerical resolution of the Basset-Bousinesq-Oseen equation

A.1 Translational equation

The Basset-Bousinesq-Oseen describing the evolution of the velocity of a freely falling particle in quiescent fluid due to gravity is given by [Parmar *et al.* 2011] as:

$$m_p \frac{dU_p}{dt} = \underbrace{-6\pi\mu a U_p}_{\text{Stokes drag}} - \underbrace{\frac{2}{3}\rho\pi a^3 \frac{dU_p}{dt}}_{\text{Added mass}} + \underbrace{6\rho a^2\sqrt{\pi\nu}\int_0^t \frac{dU_p(\tau)/d\tau}{\sqrt{t-\tau}}d\tau}_{\text{Basset history force}} + F^{ext} \tag{A.1}$$

To obtain a numerical solution of this equation, a 1-st order explicit scheme is used so that discretized version of equation A.1 after grouping the particle mass and added fluid mass into a single inertia term writes:

$$(m_p + m_a)\frac{U_p^n - U_p^{n-1}}{\Delta t} = -6\pi\mu a U_p^{n-1} + 6\rho a^2\sqrt{\pi\nu}\int_0^{t^{n-1}} \frac{dU_p(\tau)/d\tau}{\sqrt{t^{n-1}-\tau}}d\tau + F^{ext} \tag{A.2}$$

To compute the term related to history forces, the global integral is split into a sum of local integrals over the time steps during which the acceleration of the particle is considered constant so that:

$$\int_0^{t^{n-1}} \frac{dU_p(\tau)/d\tau}{\sqrt{t^{n-1}-\tau}}d\tau = \sum_{i=1}^{n-1} \frac{U_p^i - U_p^{i-1}}{\Delta t}\int_{t^{i-1}}^{t^i} \frac{1}{\sqrt{t^{n-1}-\tau}}d\tau \tag{A.3}$$

This allows to calculate the local integrals analytically and their expression is:

$$\int_{t^{i-1}}^{t^i} \frac{1}{\sqrt{t^{n-1}-\tau}}d\tau = \left[-2(t^{n-1}-\tau)^{1/2}\right]_{t^{i-1}}^{t^i} \tag{A.4}$$

$$= 2\left(\sqrt{t^{n-1}-t^{i-1}} - \sqrt{t^{n-1}-t^i}\right) \tag{A.5}$$

using the fact that $t^n = n\Delta t$ it results that:

$$\int_{t^{i-1}}^{t^i} \frac{1}{\sqrt{t^{n-1}-\tau}}d\tau = 2\sqrt{\Delta t}(\sqrt{n-i} - \sqrt{n-i-1}) \tag{A.6}$$

Iin the end the velocity at time t^n is obtained as:

$$U_p^n = U_p^{n-1} + \frac{F_{Drag} + F_{Basset} + F_{ext}}{m_p + m_a}\Delta t \tag{A.7}$$

with

$$F_{Drag} = -6\pi\mu a U_p^{n-1} \tag{A.8}$$

$$F_{Basset} = 12\rho a^2\sqrt{\pi\nu\Delta t}\sum_{i=1}^{n-1}\frac{U_p^i - U_p^{i-1}}{\Delta t}(\sqrt{n-i} - \sqrt{n-i-1}) \tag{A.9}$$

$$F_{ext} = -\frac{4}{3}\pi a^3(\rho_p - \rho_f) \tag{A.10}$$

This scheme was implemented in a python script and solved using constant time steps of $\Delta t = \tau/10$ with $\tau = \frac{m_p}{6\pi\mu a}$.

A.2 Rotational equation

The equation describing the evolution of the angular velocity of a freely rotating particle in quiescent fluid due to an external torque is given by:

$$I\frac{d\Omega}{dt} = T_h + T^{ext} \tag{A.11}$$

where the hydrodynamic torque is given by [Feuillebois & Lasek 1978] as:

$$\begin{aligned} T_h(t) = -8\pi\mu a^3\Big(\Omega(t) + \frac{a}{3\sqrt{\nu\pi}}\int_0^t \frac{d\Omega/d\tau}{\sqrt{(t-\tau)}}d\tau \\ - \frac{1}{3}\int_0^t \frac{d\Omega}{d\tau}\exp(\nu(t-\tau)/a^2)\mathrm{erfc}(\sqrt{\nu(t-\tau)/a^2})d\tau\Big) \end{aligned} \tag{A.12}$$

To obtain a numerical solution of this equation, a 1-st order explicit scheme is used so that discretized version of equation A.11 writes:

$$\begin{aligned} I\frac{\Omega^n - \Omega^{n-1}}{\Delta t} = -8\pi\mu a^3\Big(\Omega(t) + \frac{a}{3\sqrt{\nu\pi}}\int_0^{t^{n-1}} \frac{d\Omega/d\tau}{\sqrt{(t^{n-1}-\tau)}}d\tau \\ - \frac{1}{3}\int_0^{t^{n-1}} \frac{d\Omega}{d\tau}\exp(\nu(t^{n-1}-\tau)/a^2)\mathrm{erfc}(\sqrt{\nu(t^{n-1}-\tau)/a^2})d\tau\Big) \\ + T^{ext} \end{aligned} \tag{A.13}$$

The first term in the history forces has the same shape as for the translational case, so following equations (A.3) and (A.6) we have:

$$\int_0^{t^{n-1}} \frac{d\Omega(\tau)/d\tau}{\sqrt{t^{n-1}-\tau}}d\tau = 2\sqrt{\Delta t}\sum_{i=1}^{n-1}\frac{\Omega^i - \Omega^{i-1}}{\Delta t}(\sqrt{n-i} - \sqrt{n-i-1}) \tag{A.14}$$

For the second history term, the integral is computed by considering all the terms to be constant over a time step using a simple rectangle rule and the complementary error function from Python math package has been used.

$$\begin{aligned} &\int_0^{t^{n-1}} \frac{d\Omega}{d\tau}\exp(\nu(t^{n-1}-\tau)/a^2)\mathrm{erfc}(\sqrt{\nu(t^{n-1}-\tau)/a^2})d\tau \\ &= \sum_{i=1}^{n-1}\frac{\Omega^i - \Omega^{i-1}}{\Delta t}\exp(\nu(t^{n-1}-t^{i-1})/a^2)\mathrm{erfc}(\sqrt{(}\nu(t^{n-1}-t^{i-1})/a^2))\Delta t \end{aligned} \tag{A.15}$$

This method is not very accurate, but by using sufficiently small time steps we can limit the error.

In the end the angular velocity at time t^n is obtained as:

$$\Omega^n = \Omega^{n-1} + \frac{T_{Drag} + T_{Basset} + T_{ext}}{I}\Delta t \tag{A.16}$$

with

$$T_{Drag} = -8\pi\mu a^3 \Omega^{n-1} \tag{A.17}$$

$$T_{Basset} = -8\pi\mu a^3 \sum_{i=1}^{n-1} \frac{\Omega^i - \Omega^{i-1}}{\Delta t} \left[\frac{2a\sqrt{\Delta t}}{3\sqrt{\nu\pi}} \left(\sqrt{n-i} - \sqrt{n-i-1}\right) \right. \tag{A.18}$$

$$\left. - \frac{1}{3}\exp(\nu(t^{n-1} - t^{i-1})/a^2)\mathrm{erfc}(\sqrt{(}\nu(t^{n-1} - t^{i-1})/a^2))\Delta t \right] \tag{A.19}$$

$$T_{ext} = 10\, pN.m \tag{A.20}$$

The division by I in equation (A.16) was causing numerical issues as its value is very small for small particle radius, therefore for this rotational case, a bigger particle and a bigger domain were used as detailed in section 3.4.2.

This scheme was implemented in a python script and solved using constant time steps of $\Delta t = \tau/100$ with $\tau = \frac{I}{8\pi\mu a^3}$.

Appendix B

Estimation of the research project carbon footprint

According to the United Nations organization: *Climate change is the defining issue of our time and we are at a defining moment*[1]. Following industrial revolution, human activities driven by uncontrolled burning of fossil fuels lead to an increase in the mean temperature, increase in frequency and intensity of extreme weather events, global sea level rise and habitat destruction for many animal species, to only name few issues.

While the aim of this research project is to improve the health of a large part of the population, its negative impacts should nevertheless be mentioned. Even though numerical simulation is a powerful tool, one of its major drawback is the enormous amount of energy it requires. Indeed, electrical alimentation of the computational processors, cooling systems, data storage and initial manufacturing are all very consuming in energy.

The impact of this research project on climate change is presented by estimating the equivalent carbon dioxyde (CO2e) emissions associated with the computing ressources used during the project as well as travel to conferences. A precise estimation of the equivalent carbon dioxyde emissions is very difficult to obtain as taking into account the whole lifecycle of a laptop or a train seat is impossible, but the aim of this appendix is only to be informative so extreme precision is not required.

B.1 Computing ressources

The computing ressources used during this project can be splitted into two contributions: Office equipment and computing ressources on regional and national calculation centers.

For the office equipment, estimation of the CO2 equivalent emissions during the product manufacturing, transport, use and recycling can be found online:

- Macbook pro 14 inch M1 pro 2021 : 271 kg CO2e [2]
- 2TB HDD: 40 kg CO2e [3]
- Dell hub station: 40 kg C02e [4]
- Office chair : 23 kg CO2e [5]
- Office desk : 82 kg C02e [6]

[1] https://www.un.org/en/global-issues/climate-change

[2] hyperhttps://www.apple.com/environment/pdf/products/notebooks/14-inch_MacBook_Pro_PER_Oct2021.pdf

[3] https://arxiv.org/pdf/2207.10793

[4] https://www.dell.com/fr-fr/dt/corporate/social-impact/advancing-sustainability/climate-action/product-carbon-footprints.html

[5] https://www.arbor.eco/fr/carbon-footprint/office-chair

[6] https://www.arbor.eco/fr/carbon-footprint/office-chair

Cluster	CO2 emission [gCO2e/(h.CPU)]	Total computational time [h.CPU]	Total CO2 emission [gCO2e]
Meso@LR	1.8	228,126	410,626
Adastra	1.3	6,854,170	8,910,421
Irene	1.1	2,482,170	2,730,387
Total			12,051,434

The total equivalent CO2 emissions for the office equipment is 456 kg CO2e.

For the computational resources on regional and national clusters, the estimated emission for one CPU hour is provided by the clusters' administration. 3 different clusters were used with the CO2 equivalent emission for one CPU hour given by:

The total emissions related to the computational and office resources yield a total of about 12.5 tCO2e.

B.2 Travel expanses

Trips to conferences, workshops and project meetings were all done by train. The details are listed below:

- Research project meetings (x2): Montpellier, France - Aachen, Germany : 52 kgCO2e
- ECFD workshops (x2): Montpellier, France - Caen, France : 44 kgCO2e
- Summer school: Montpellier, France - Grenoble, France : 6 kgCO2e
- Conference ESAO2024: Montpellier, France - Aachen, Germany : 26 kgCO2e
- Conference ESAO2025: Montpellier, France - Enschede, Netherland : 28 kgCO2e
- Conference ICMF2025: Montpellier, France - Toulouse, France : 6 kgCO2e

This sums up to a total of 162 kgCO2e for the different travels.

B.3 Total

In the end, the total carbon dioxyde equivalent emissions for this research project sums up to about 12.6 tCO2e over the 3 years of the project. As a reference, current estimations for the yearly emissions by a single person in France is around 9 tCO2e, and the target emissions to limit global warming at a 1.5°C increase is 2 tCO2e yearly.

Bibliography

[Allen *et al.* 1979] R D Allen, L R Zacharski, S T Widirstky, R Rosenstein, L M Zaitlin and D R Burgess. *Transformation and Motility of Human Platelets: Details of the Shape Change and Release Reaction Observed by Optical and Electron Microscopy.* Journal of Cell Biology, vol. 83, no. 1, pages 126–142, October 1979. (Cited on pages vii and 5.)

[Apte *et al.* 2025] Gurunath Apte, Marcus Soter, Dikshita Madkatte, Doris Heinrich and Thi-Huong Nguyen. *Agarose Micro/Nanostructured Surfaces: A Step Toward an Innovative Solution for Platelet Storage Bags.* Advanced Functional Materials, vol. 35, no. 4, January 2025. (Cited on page 11.)

[Ardekani *et al.* 2007] A. M. Ardekani, R. H. Rangel and D. D. Joseph. *Motion of a Sphere Normal to a Wall in a Second-Order Fluid.* Journal of Fluid Mechanics, vol. 587, pages 163–172, September 2007. (Cited on page 43.)

[Assoudi *et al.* 2018] Redouane Assoudi, Mohamed Chaoui, François Feuillebois and Hassane Allouche. *Motion of a Spherical Particle along a Rough Wall in a Shear Flow.* Zeitschrift für angewandte Mathematik und Physik, vol. 69, no. 5, page 112, October 2018. (Cited on pages iv, ix, 22, 25, 31, 43, 45, 46, 47, 49, 50, 51, 105 and 151.)

[Belyaev 2019] Aleksey V. Belyaev. *Computer Modelling of Initial Platelet Adhesion during Microvascular Thrombosis.* Russian Journal of Numerical Analysis and Mathematical Modelling, vol. 34, no. 5, pages 241–251, October 2019. (Cited on page 4.)

[Brenner 1961] Howard Brenner. *The Slow Motion of a Sphere through a Viscous Fluid towards a Plane Surface.* Chemical Engineering Science, vol. 16, no. 3-4, pages 242–251, December 1961. (Cited on pages xvi, 34, 36, 38, 40, 42, 43, 49, 111 and 132.)

[Bureau *et al.* 2023] Lionel Bureau, Gwennou Coupier and Thomas Salez. *Lift at Low Reynolds Number.* The European Physical Journal E, vol. 46, no. 11, page 111, November 2023. (Cited on page 28.)

[Castillo-García *et al.* 2024] Adrián Castillo-García, Pedro L. Valenzuela, Gonzalo Saco-Ledo, Pedro Carrera-Bastos, Luis M. Ruilope, Alejandro Santos-Lozano and Alejandro Lucia. *Lifestyle and Cardiovascular Risk in Working Young Adults: Insights from a Nationwide Spanish Cohort.* Revista Española de Cardiología (English Edition), vol. 77, no. 10, pages 821–831, October 2024. (Cited on page 1.)

[Chaoui & Feuillebois 2002] M Chaoui and F Feuillebois. *CREEPING FLOW AROUND A SPHERE IN A SHEAR FLOW CLOSE TO A WALL.* 2002. (Cited on page 39.)

[Chaoui 1995] Mohamed Chaoui. *Migration d'une Particule Proche d'une Paroi En Écoulement de Cisaillement.* PhD thesis, 1995. (Cited on pages xix, 39 and 47.)

[Chase *et al.* 2022] Danielle L. Chase, Christina Kurzthaler and Howard A. Stone. *Hydrodynamically Induced Helical Particle Drift Due to Patterned Surfaces.* Proceedings of the National Academy of Sciences, vol. 119, no. 31, page e2202082119, August 2022. (Cited on pages 15 and 31.)

[Chen *et al.* 2011] Li Chen, Dong Han and Lei Jiang. *On Improving Blood Compatibility: From Bioinspired to Synthetic Design and Fabrication of Biointerfacial Topography at Micro/Nano Scales.* Colloids and Surfaces B: Biointerfaces, vol. 85, no. 1, pages 2–7, June 2011. (Cited on page 11.)

[Choi 2020] Sungyoung Choi. *Hydrophoresis — A Microfluidic Principle for Directed Particle Migration in Flow.* BioChip Journal, vol. 14, no. 1, pages 72–83, March 2020. (Cited on pages 15 and 31.)

[Chorin 1968] Alexandre Joel Chorin. *Numerical Solution of the Navier-Stokes Equations.* Mathematics of Computation, vol. 22, pages 745–762, 1968. (Cited on page 58.)

[Clauser *et al.* 2014] Johanna Clauser, Kathrin Gester, Jan Roggenkamp, Ilona Mager, Judith Maas, Sebastian V. Jansen and Ulrich Steinseifer. *Micro-Structuring of Polycarbonate-Urethane Surfaces in Order to Reduce Platelet Activation and Adhesion.* Journal of Biomaterials Science, Polymer Edition, vol. 25, no. 5, pages 504–518, March 2014. (Cited on pages 11 and 14.)

[Dance & Maxey 2003] S.L. Dance and M.R. Maxey. *Incorporation of Lubrication Effects into the Force-Coupling Method for Particulate Two-Phase Flow.* Journal of Computational Physics, vol. 189, no. 1, pages 212–238, July 2003. (Cited on page 77.)

[Dean & O'Neill 1963] W. R. Dean and M. E. O'Neill. *A Slow Motion of Viscous Liquid Caused by the Rotation of a Solid Sphere.* Mathematika, vol. 10, no. 1, pages 13–24, June 1963. (Cited on pages 36, 37, 39 and 41.)

[Ding *et al.* 2013] Yonghui Ding, Yang Leng, Nan Huang, Ping Yang, Xiong Lu, Xiang Ge, Fuzeng Ren, Kefeng Wang, Lijuan Lei and Xiang Guo. *Effects of Microtopographic Patterns on Platelet Adhesion and Activation on Titanium Oxide Surfaces.* Journal of Biomedical Materials Research Part A, vol. 101A, no. 3, pages 622–632, March 2013. (Cited on pages 10, 11 and 13.)

[Du *et al.* 2021] Jian Du, Elise Aspray and Aaron Fogelson. *Computational Investigation of Platelet Thrombus Mechanics and Stability in Stenotic Channels.* Journal of Biomechanics, vol. 122, page 110398, June 2021. (Cited on page 19.)

[Estevez & Du 2017] Brian Estevez and Xiaoping Du. *New Concepts and Mechanisms of Platelet Activation Signaling.* Physiology, vol. 32, no. 2, pages 162–177, March 2017. (Cited on pages 5 and 6.)

[Fan *et al.* 2024] Duanqi Fan, Xiaoli Liu and Hong Chen. *Endothelium-Mimicking Materials: A "Rising Star" for Antithrombosis.* ACS Applied Materials & Interfaces, September 2024. (Cited on page 15.)

[Feuillebois & Lasek 1978] F. Feuillebois and A. Lasek. *ON THE ROTATIONAL HISTORIC TERM IN NON-STATIONARY STOKES FLOW.* The Quarterly Journal of Mechanics and Applied Mathematics, vol. 31, no. 4, pages 435–443, 1978. (Cited on pages 71 and 160.)

[Fitzgibbon *et al.* 2015] Sean Fitzgibbon, Jonathan Cowman, Antonio J. Ricco, Dermot Kenny and Eric S. G. Shaqfeh. *Examining Platelet Adhesion via Stokes Flow Simulations and Microfluidic Experiments.* Soft Matter, vol. 11, no. 2, pages 355–367, 2015. (Cited on pages 16 and 142.)

[Fogelson & Guy 2008] Aaron L. Fogelson and Robert D. Guy. *Immersed-Boundary-Type Models of Intravascular Platelet Aggregation.* Computer Methods in Applied Mechanics and Engineering, vol. 197, no. 25-28, pages 2087–2104, April 2008. (Cited on page 17.)

[Fogelson & Neeves 2015] Aaron L. Fogelson and Keith B. Neeves. *Fluid Mechanics of Blood Clot Formation.* Annual Review of Fluid Mechanics, vol. 47, no. 1, pages 377–403, January 2015. (Cited on pages 3, 6, 7, 16, 135, 136 and 151.)

[Fogelson 1984] Aaron L Fogelson. *A Mathematical Model and Numerical Method for Studying Platelet Adhesion and Aggregation during Blood Clotting.* Journal of Computational Physics, vol. 56, no. 1, pages 111–134, October 1984. (Cited on page 16.)

[Fogelson 1992] Aaron L. Fogelson. *Continuum Models of Platelet Aggregation: Formulation and Mechanical Properties.* SIAM Journal on Applied Mathematics, vol. 52, no. 4, pages 1089–1110, August 1992. (Cited on page 16.)

[Fu *et al.* 2017] Hongxia Fu, Yan Jiang, Darren Yang, Friedrich Scheiflinger, Wesley P. Wong and Timothy A. Springer. *Flow-Induced Elongation of von Willebrand Factor Precedes Tension-Dependent Activation.* Nature Communications, vol. 8, no. 1, page 324, August 2017. (Cited on pages 135 and 137.)

[Garipcan *et al.* 2011] Bora Garipcan, Stefan Maenz, Tam Pham, Utz Settmacher, Klaus D. Jandt, Jürgen Zanow and Jörg Bossert. *Image Analysis of Endothelial Microstructure and Endothelial Cell Dimensions of Human Arteries – A Preliminary Study.* Advanced Engineering Materials, vol. 13, no. 1-2, February 2011. (Cited on page 9.)

[Geuzaine & Remacle 2009] Christophe Geuzaine and Jean-François Remacle. *Gmsh: A Three-Dimensional Finite Element Mesh Generator with Built-in Pre- and Post-Processing Facilities.* International Journal for Numerical Methods in Engineering, 2009. (Cited on page 60.)

[Glenn & Armstrong 2019] Amy Glenn and Catherine E. Armstrong. *Physiology of Red and White Blood Cells.* Anaesthesia & Intensive Care Medicine, vol. 20, no. 3, pages 170–174, March 2019. (Cited on page 3.)

[Glowinski 1999] R Glowinski. *A Distributed Lagrange Multiplier/®ctitious Domain Method for Par-ticulate ¯ows.* International Journal of Multiphase Flow, 1999. (Cited on page 62.)

[Goldmans *et al.* 1966] A J Goldmans, R G Cox and H Brenner. *Slow Viscous Motion of a Sphere Parallel to a Plane Wall-1 Motion through a Quiescent Fluid+.* 1966. (Cited on page 111.)

[Gremmel *et al.* 2016] Thomas Gremmel, Andrew Frelinger and Alan Michelson. *Platelet Physiology.* Seminars in Thrombosis and Hemostasis, vol. 42, no. 03, pages 191–204, February 2016. (Cited on pages viii, 5, 6 and 137.)

[Guermond *et al.* 2006] J.L. Guermond, P. Minev and Jie Shen. *An Overview of Projection Methods for Incompressible Flows.* Computer Methods in Applied Mechanics and Engineering, vol. 195, no. 44-47, pages 6011–6045, September 2006. (Cited on page 59.)

[Hicks 1881] W.M. Hicks. *On Toroidal Functions.* 1881. (Cited on page 37.)

[Hsu & Ganatos 1994] Richard Hsu and Peter Ganatos. *Gravitational and Zero-Drag Motion of a Spheroid Adjacent to an Inclined Plane at Low Reynolds Number.* Journal of Fluid Mechanics, vol. 268, pages 267–292, June 1994. (Cited on pages x, xi, 70, 77, 78, 79, 80, 81, 83 and 84.)

[Jaffer & Weitz 2019] Iqbal H. Jaffer and Jeffrey I. Weitz. *The Blood Compatibility Challenge. Part 1: Blood-contacting Medical Devices: The Scope of the Problem.* Acta Biomaterialia, vol. 94, pages 2–10, August 2019. (Cited on pages 7 and 151.)

[Jaffer *et al.* 2015] I. H. Jaffer, J. C. Fredenburgh, J. Hirsh and J. I. Weitz. *Medical Device-Induced Thrombosis: What Causes It and How Can We Prevent It?* Journal of Thrombosis and Haemostasis, vol. 13, pages S72–S81, June 2015. (Cited on pages 7 and 135.)

[Jeffery 1912] G.B. Jeffery. *On a Form of the Solution of Laplace's Equation Suitable for Problems Relating to Two Spheres.* 1912. (Cited on page 38.)

[Jeffery 1922] GB Jeffery. *The Motion of Ellipsoidal Particles Immersed in a Viscous Fluid.* https://royalsocietypublishing.org/doi/pdf/10.1098/rspa.1922.0078, 1922. (Cited on pages 28, 30, 70, 80 and 81.)

[Kantam *et al.* 2024] Prem Kantam, Vignesh K. Manivasagam, Tarun Kumar Jammu, Roberta Maia Sabino, Sravanthi Vallabhuneni, Young Jae Kim, Arun K. Kota and Ketul C. Popat. *Interaction of Blood and Bacteria with Slippery Hydrophilic Surfaces.* Advanced Materials Interfaces, vol. 11, no. 1, January 2024. (Cited on page 11.)

[Kim & Karrila 1991] Sangtae Kim and Seppo J. Karrila. Microhydrodynamics: Principles and selected applications. Butterworth-Heinemann Series in Chemical Engineering. Butterworth-Heinemann, Boston, 1991. (Cited on pages 62, 63, 66, 67 and 80.)

[Koh *et al.* 2010] Li Buay Koh, Isabel Rodriguez and Subbu S. Venkatraman. *The Effect of Topography of Polymer Surfaces on Platelet Adhesion.* Biomaterials, vol. 31, no. 7, pages 1533–1545, March 2010. (Cited on page 11.)

[Kurzthaler *et al.* 2024] Christina Kurzthaler, Danielle L. Chase and Howard A. Stone. *Surface Corrugations Induce Helical Near-Surface Flows and Transport in Microfluidic Channels.* Journal of Fluid Mechanics, vol. 982, page A31, March 2024. (Cited on page 31.)

[Kuwahara *et al.* 2002] Mitsuhiro Kuwahara, Mitsuhiko Sugimoto, Shizuko Tsuji, Hideto Matsui, Tomohiro Mizuno, Shigeki Miyata and Akira Yoshioka. *Platelet Shape Changes and Adhesion Under High Shear Flow.* Arteriosclerosis, Thrombosis, and Vascular Biology, vol. 22, no. 2, pages 329–334, February 2002. (Cited on page 5.)

[Lamichhane *et al.* 2016] Sujan Lamichhane, Jordan A. Anderson, Tyler Remund, Hongli Sun, Mark K. Larson, Patrick Kelly and Gopinath Mani. *Responses of Endothelial Cells, Smooth Muscle Cells, and Platelets Dependent on the Surface Topography of Polytetrafluoroethylene: Cell Responses Dependent on PTFE Surface Topography.* Journal of Biomedical Materials Research Part A, vol. 104, no. 9, pages 2291–2304, September 2016. (Cited on pages 10 and 14.)

[Lanotte *et al.* 2016] Luca Lanotte, Johannes Mauer, Simon Mendez, Dmitry A. Fedosov, Jean-Marc Fromental, Viviana Claveria, Franck Nicoud, Gerhard Gompper and Manouk Abkarian. *Red Cells' Dynamic Morphologies Govern Blood Shear Thinning under Microcirculatory Flow Conditions.* Proceedings of the National Academy of Sciences, vol. 113, no. 47, pages 13289–13294, November 2016. (Cited on page 22.)

[Liu *et al.* 2009] D. Liu, E.E. Keaveny, M.R. Maxey and G.E. Karniadakis. *Force-Coupling Method for Flows with Ellipsoidal Particles.* Journal of Computational Physics, vol. 228, no. 10, pages 3559–3581, June 2009. (Cited on pages xix, 17, 68, 70, 71, 73, 76, 77, 82 and 83.)

[Liu *et al.* 2014a] Tao Liu, Shihui Liu, Kun Zhang, Junying Chen and Nan Huang. *Endothelialization of Implanted Cardiovascular Biomaterial Surfaces: The Development from in Vitro to in Vivo.*

Journal of Biomedical Materials Research Part A, vol. 102, no. 10, pages 3754–3772, October 2014. (Cited on page 9.)

[Liu *et al.* 2014b] Xiaoli Liu, Lin Yuan, Dan Li, Zengchao Tang, Yanwei Wang, Gaojian Chen, Hong Chen and John L Brash. *Blood Compatible Materials: State of the Art.* Journal of Materials Chemistry B, 2014. (Cited on pages 8 and 9.)

[Lomholt & Maxey 2003] Sune Lomholt and Martin R. Maxey. *Force-Coupling Method for Particulate Two-Phase Flow: Stokes Flow.* Journal of Computational Physics, vol. 184, no. 2, pages 381–405, January 2003. (Cited on pages x, 62, 67, 74, 76 and 77.)

[Lomholt *et al.* 2002] S. Lomholt, B. Stenum and M.R. Maxey. *Experimental Verification of the Force Coupling Method for Particulate Flows.* International Journal of Multiphase Flow, vol. 28, no. 2, pages 225–246, February 2002. (Cited on pages 67 and 74.)

[Lomholt 2001] Sune Lomholt. *Numerical Investigations of Macroscopic Particle Dynamics in Microflows.* 2001. (Cited on pages 64 and 65.)

[Luu *et al.* 2024] Cuong Hung Luu, Nam-Trung Nguyen and Hang Thu Ta. *Unravelling Surface Modification Strategies for Preventing Medical Device-Induced Thrombosis.* Advanced Healthcare Materials, vol. 13, no. 1, page 2301039, January 2024. (Cited on page 8.)

[Martin *et al.* 2008] John Martin, Tim Shaw, J. Heggie and David Penington. *Measurement of the Density of Human Platelets and Its Relationship to Volume.* British Journal of Haematology, vol. 54, pages 337–352, July 2008. (Cited on page 96.)

[Masoud & Stone 2019] Hassan Masoud and Howard A. Stone. *The Reciprocal Theorem in Fluid Dynamics and Transport Phenomena.* Journal of Fluid Mechanics, vol. 879, page P1, November 2019. (Cited on pages 31 and 52.)

[Mathew *et al.* 2025] J Mathew, P Sankar and MA Varacallo. *Physiology, Blood Plasma.* StatPearls, 2025. (Cited on page 3.)

[Maxey & Patel 2001] M R Maxey and B K Patel. *Localized Force Representations for Particles Sedimenting in Stokes ¯ow.* International Journal of Multiphase Flow, 2001. (Cited on pages 17, 63 and 65.)

[Maxey 2017] Martin Maxey. *Simulation Methods for Particulate Flows and Concentrated Suspensions.* Annual Review of Fluid Mechanics, vol. 49, no. 1, pages 171–193, January 2017. (Cited on pages 16, 22, 61 and 62.)

[McGill *et al.* 2008] Henry C. McGill, C. Alex McMahan and Samuel S. Gidding. *Preventing Heart Disease in the 21st Century: Implications of the Pathobiological Determinants of Atherosclerosis in Youth (PDAY) Study.* Circulation, vol. 117, no. 9, pages 1216–1227, March 2008. (Cited on page 1.)

[Méndez Rojano *et al.* 2021] Rodrigo Méndez Rojano, Mansur Zhussupbekov, Wei-Tao Wu, Mehrdad Massoudi and James F. Antaki. *A Continuum Model for the Unfolding of von Willebrand Factor.* Annals of Biomedical Engineering, vol. 49, no. 9, pages 2646–2658, September 2021. (Cited on page 19.)

[Méndez Rojano *et al.* 2022] Rodrigo Méndez Rojano, Mansur Zhussupbekov, James F. Antaki and Didier Lucor. *Uncertainty Quantification of a Thrombosis Model Considering the Clotting Assay PFA-100®*. International Journal for Numerical Methods in Biomedical Engineering, vol. n/a, no. n/a, page e3595, 2022. (Cited on page 19.)

[Mendez *et al.* 2022] Simon Mendez, Alain Bérod, Christophe Chnafa, Morgane Garreau, Etienne Gibaud, Anthony Larroque, Stephanie Lindsey, Marco MARTINS Afonso, Rodrigo MENDEZ Rojano, Dorian Midou, Thomas Puiseux, Julien Sigüenza, Pierre Taraconat, Vladeta Zmijanovic and Franck Nicoud. *YALES2BIO: A General Purpose Solver Dedicated to Blood Flows*. page 25, 2022. (Cited on pages 22 and 56.)

[Michelson *et al.* 2019] Alan D. Michelson, M. Cattaneo, Andrew L. Frelinger and Peter J. Newman, editors. Platelets. Academic Press, an imprint of Elsevier, London, United Kingdom ; San Diego, CA, fourth edition édition, 2019. (Cited on pages vii, 3, 4, 5 and 9.)

[Mignon & Mendez 2021] Thierry Mignon and Simon Mendez. *A Theoretical Investigation of the Frisbee Motion of Red Blood Cells in Shear Flow*. Mathematical Modelling of Natural Phenomena, vol. 16, page 23, 2021. (Cited on page 69.)

[Milner *et al.* 2005] Keith R Milner, Alan J Snyder and Christopher A Siedlecki. *Sub-Micron Texturing for Reducing Platelet Adhesion to Polyurethane Biomaterials*. page 10, 2005. (Cited on pages 11 and 12.)

[Minelli *et al.* 2008] Caterina Minelli, Akemi Kikuta, Nataliya Tsud, Michael D Ball and Akiko Yamamoto. *A Micro-Fluidic Study of Whole Blood Behaviour on PMMA Topographical Nanostructures*. Journal of Nanobiotechnology, vol. 6, no. 1, page 3, 2008. (Cited on page 12.)

[Mitchell & Spagnolie 2015] William H. Mitchell and Saverio E. Spagnolie. *Sedimentation of Spheroidal Bodies near Walls in Viscous Fluids: Glancing, Reversing, Tumbling, and Sliding*. Journal of Fluid Mechanics, vol. 772, pages 600–629, June 2015. (Cited on pages viii, 28 and 29.)

[Mody & King 2005] Nipa A. Mody and Michael R. King. *Three-Dimensional Simulations of a Platelet-Shaped Spheroid near a Wall in Shear Flow*. Physics of Fluids, vol. 17, no. 11, page 113302, November 2005. (Cited on pages viii, xi, 20, 21, 22, 29, 30, 70, 80, 81, 82, 83, 84, 85, 91 and 120.)

[Mody & King 2008] Nipa A. Mody and Michael R. King. *Platelet Adhesive Dynamics. Part I: Characterization of Platelet Hydrodynamic Collisions and Wall Effects*. Biophysical Journal, vol. 95, no. 5, pages 2539–2555, September 2008. (Cited on page 21.)

[Müller *et al.* 2008] Bert Müller, Sabrina Lang, Marco Dominietto, Markus Rudin, Georg Schulz, Hans Deyhle, Marco Germann, Franz Pfeiffer, Christian David and Timm Weitkamp. *High-Resolution Tomographic Imaging of Microvessels*. In Stuart R. Stock, editor, SPIE Proceedings, San Diego, California, USA, August 2008. SPIE. (Cited on page 3.)

[Nicolaides 1987] R. A. Nicolaides. *Deflation of Conjugate Gradients with Applications to Boundary Value Problems*. SIAM Journal on Numerical Analysis, vol. 24, no. 2, pages 355–365, April 1987. (Cited on page 59.)

[O'Neill 1964] M. E. O'Neill. *A Slow Motion of Viscous Liquid Caused by a Slowly Moving Solid Sphere*. Mathematika, vol. 11, no. 1, pages 67–74, June 1964. (Cited on pages 36, 37 and 39.)

[Parmar *et al.* 2011] M. Parmar, A. Haselbacher and S. Balachandar. *Generalized Basset-Boussinesq-Oseen Equation for Unsteady Forces on a Sphere in a Compressible Flow.* Physical Review Letters, vol. 106, no. 8, page 084501, February 2011. (Cited on pages 70 and 159.)

[Pasol *et al.* 2005] L. Pasol, M. Chaoui, S. Yahiaoui and F. Feuillebois. *Analytical Solutions for a Spherical Particle near a Wall in Axisymmetrical Polynomial Creeping Flows.* Physics of Fluids, vol. 17, no. 7, page 073602, July 2005. (Cited on pages 36, 40, 41 and 42.)

[Peskin 2002] Charles S. Peskin. *The Immersed Boundary Method.* Acta Numerica, vol. 11, pages 479–517, January 2002. (Cited on page 17.)

[Pham *et al.* 2016] Tam Thanh Pham, Stefan Wiedemeier, Stefan Maenz, Gunter Gastrock, Utz Settmacher, Klaus D. Jandt, Jürgen Zanow, Claudia Lüdecke and Jörg Bossert. *Hemodynamic Aspects of Reduced Platelet Adhesion on Bioinspired Microstructured Surfaces.* Colloids and Surfaces B: Biointerfaces, vol. 145, pages 502–509, September 2016. (Cited on pages 10 and 14.)

[Pozrikidis 2002] C. Pozrikidis. A Practical Guide to Boundary Element Methods with the Software Library BEMLIB. CRC Press, Boca Raton, May 2002. (Cited on page 61.)

[Pozrikidis 2006] C. Pozrikidis. *Flipping of an Adherent Blood Platelet over a Substrate.* Journal of Fluid Mechanics, vol. 568, page 161, December 2006. (Cited on pages 20, 22, 82, 83 and 120.)

[Purcell 1976] E. M. Purcell. Life at Low Reynolds Number, pages 47–67. WORLD SCIENTIFIC, 1976. (Cited on pages 27 and 89.)

[Rabe *et al.* 2011] Michael Rabe, Dorinel Verdes and Stefan Seeger. *Understanding Protein Adsorption Phenomena at Solid Surfaces.* Advances in Colloid and Interface Science, vol. 162, no. 1-2, pages 87–106, February 2011. (Cited on pages 7 and 8.)

[Reasor *et al.* 2013] Daniel A. Reasor, Marmar Mehrabadi, David N. Ku and Cyrus K. Aidun. *Determination of Critical Parameters in Platelet Margination.* Annals of Biomedical Engineering, vol. 41, no. 2, pages 238–249, February 2013. (Cited on pages 4, 16 and 21.)

[Roth *et al.* 2020] Gregory A. Roth, George A. Mensah, Catherine O. Johnson, Giovanni Addolorato, Enrico Ammirati, Larry M. Baddour, Noël C. Barengo, Andrea Z. Beaton, Emelia J. Benjamin, Catherine P. Benziger, Aimé Bonny, Michael Brauer, Marianne Brodmann, Thomas J. Cahill, Jonathan Carapetis, Alberico L. Catapano, Sumeet S. Chugh, Leslie T. Cooper, Josef Coresh, Michael Criqui, Nicole DeCleene, Kim A. Eagle, Sophia Emmons-Bell, Valery L. Feigin, Joaquim Fernández-Solà, Gerry Fowkes, Emmanuela Gakidou, Scott M. Grundy, Feng J. He, George Howard, Frank Hu, Lesley Inker, Ganesan Karthikeyan, Nicholas Kassebaum, Walter Koroshetz, Carl Lavie, Donald Lloyd-Jones, Hong S. Lu, Antonio Mirijello, Awoke Misganaw Temesgen, Ali Mokdad, Andrew E. Moran, Paul Muntner, Jagat Narula, Bruce Neal, Mpiko Ntsekhe, Glaucia Moraes De Oliveira, Catherine Otto, Mayowa Owolabi, Michael Pratt, Sanjay Rajagopalan, Marissa Reitsma, Antonio Luiz P. Ribeiro, Nancy Rigotti, Anthony Rodgers, Craig Sable, Saate Shakil, Karen Sliwa-Hahnle, Benjamin Stark, Johan Sundström, Patrick Timpel, Imad M. Tleyjeh, Marco Valgimigli, Theo Vos, Paul K. Whelton, Magdi Yacoub, Liesl Zuhlke, Christopher Murray, Valentin Fuster, Gregory A. Roth, George A. Mensah, Catherine O. Johnson, Giovanni Addolorato, Enrico Ammirati, Larry M. Baddour, Noel C. Barengo, Andrea Beaton, Emelia J. Benjamin, Catherine P. Benziger, Aime Bonny, Michael Brauer, Marianne Brodmann, Thomas J. Cahill, Jonathan R. Carapetis, Alberico L. Catapano, Sumeet Chugh, Leslie T.

Cooper, Josef Coresh, Michael H. Criqui, Nicole K. DeCleene, Kim A. Eagle, Sophia Emmons-Bell, Valery L. Feigin, Joaquim Fernández-Sola, F. Gerry R. Fowkes, Emmanuela Gakidou, Scott M. Grundy, Feng J. He, George Howard, Frank Hu, Lesley Inker, Ganesan Karthikeyan, Nicholas J. Kassebaum, Walter J. Koroshetz, Carl Lavie, Donald Lloyd-Jones, Hong S. Lu, Antonio Mirijello, Awoke T. Misganaw, Ali H. Mokdad, Andrew E. Moran, Paul Muntner, Jagat Narula, Bruce Neal, Mpiko Ntsekhe, Gláucia M.M. Oliveira, Catherine M. Otto, Mayowa O. Owolabi, Michael Pratt, Sanjay Rajagopalan, Marissa B. Reitsma, Antonio Luiz P. Ribeiro, Nancy A. Rigotti, Anthony Rodgers, Craig A. Sable, Saate S. Shakil, Karen Sliwa, Benjamin A. Stark, Johan Sundström, Patrick Timpel, Imad I. Tleyjeh, Marco Valgimigli, Theo Vos, Paul K. Whelton, Magdi Yacoub, Liesl J. Zuhlke, Mohsen Abbasi-Kangevari, Alireza Abdi, Aidin Abedi, Victor Aboyans, Woldu A. Abrha, Eman Abu-Gharbieh, Abdelrahman I. Abushouk, Dilaram Acharya, Tim Adair, Oladimeji M. Adebayo, Zanfina Ademi, Shailesh M. Advani, Khashayar Afshari, Ashkan Afshin, Gina Agarwal, Pradyumna Agasthi, Sohail Ahmad, Sepideh Ahmadi, Muktar B. Ahmed, Budi Aji, Yonas Akalu, Wuraola Akande-Sholabi, Addis Aklilu, Chisom J. Akunna, Fares Alahdab, Ayman Al-Eyadhy, Khalid F. Alhabib, Sheikh M. Alif, Vahid Alipour, Syed M. Aljunid, François Alla, Amir Almasi-Hashiani, Sami Almustanyir, Rajaa M. Al-Raddadi, Adeladza K. Amegah, Saeed Amini, Arya Aminorroaya, Hubert Amu, Dickson A. Amugsi, Robert Ancuceanu, Deanna Anderlini, Tudorel Andrei, Catalina Liliana Andrei, Alireza Ansari-Moghaddam, Zelalem A. Anteneh, Ippazio Cosimo Antonazzo, Benny Antony, Razique Anwer, Lambert T. Appiah, Jalal Arabloo, Johan Ärnlöv, Kurnia D. Artanti, Zerihun Ataro, Marcel Ausloos, Leticia Avila-Burgos, Asma T. Awan, Mamaru A. Awoke, Henok T. Ayele, Muluken A. Ayza, Samad Azari, Darshan B. B, Nafiseh Baheiraei, Atif A. Baig, Ahad Bakhtiari, Maciej Banach, Palash C. Banik, Emerson A. Baptista, Miguel A. Barboza, Lingkan Barua, Sanjay Basu, Neeraj Bedi, Yannick Béjot, Derrick A. Bennett, Isabela M. Bensenor, Adam E. Berman, Yihienew M. Bezabih, Akshaya S. Bhagavathula, Sonu Bhaskar, Krittika Bhattacharyya, Ali Bijani, Boris Bikbov, Mulugeta M. Birhanu, Archith Boloor, Luisa C. Brant, Hermann Brenner, Nikolay I. Briko, Zahid A. Butt, Florentino Luciano Caetano Dos Santos, Leah E. Cahill, Lucero Cahuana-Hurtado, Luis A. Cámera, Ismael R. Campos-Nonato, Carlos Cantu-Brito, Josip Car, Juan J. Carrero, Felix Carvalho, Carlos A. Castañeda-Orjuela, Ferrán Catalá-López, Ester Cerin, Jaykaran Charan, Vijay Kumar Chattu, Simiao Chen, Ken L. Chin, Jee-Young J. Choi, Dinh-Toi Chu, Sheng-Chia Chung, Massimo Cirillo, Sean Coffey, Sara Conti, Vera M. Costa, David K. Cundiff, Omid Dadras, Baye Dagnew, Xiaochen Dai, Albertino A.M. Damasceno, Lalit Dandona, Rakhi Dandona, Kairat Davletov, Vanessa De La Cruz-Góngora, Fernando P. De La Hoz, Jan-Walter De Neve, Edgar Denova-Gutiérrez, Meseret Derbew Molla, Behailu T. Derseh, Rupak Desai, Günther Deuschl, Samath D. Dharmaratne, Meghnath Dhimal, Raja Ram Dhungana, Mostafa Dianatinasab, Daniel Diaz, Shirin Djalalinia, Klara Dokova, Abdel Douiri, Bruce B. Duncan, Andre R. Duraes, Arielle W. Eagan, Sanam Ebtehaj, Aziz Eftekhari, Sahar Eftekharzadeh, Michael Ekholuenetale, Nevine El Nahas, Islam Y. Elgendy, Muhammed Elhadi, Shaimaa I. El-Jaafary, Sadaf Esteghamati, Atkilt E. Etisso, Oghenowede Eyawo, Ibtihal Fadhil, Emerito Jose A. Faraon, Pawan S. Faris, Medhat Farwati, Farshad Farzadfar, Eduarda Fernandes, Carlota Fernandez Prendes, Pietro Ferrara, Irina Filip, Florian Fischer, David Flood, Takeshi Fukumoto, Mohamed M. Gad, Shilpa Gaidhane, Morsaleh Ganji, Jalaj Garg, Abadi K. Gebre, Birhan G. Gebregiorgis, Kidane Z. Gebregzabiher, Gebreamlak G. Gebremeskel, Lemma Getacher, Abera Getachew Obsa, Alireza Ghajar, Ahmad Ghashghaee, Nermin Ghith, Simona Giampaoli, Syed Amir Gilani, Paramjit S. Gill, Richard F. Gillum, Ekaterina V. Glushkova, Elena V. Gnedovskaya, Mahaveer Golechha, Kebebe B. Gonfa, Amir Hossein Goudarzian, Alessandra C. Goulart, Jenny S. Guadamuz,

Avirup Guha, Yuming Guo, Rajeev Gupta, Vladimir Hachinski, Nima Hafezi-Nejad, Teklehaimanot G. Haile, Randah R. Hamadeh, Samer Hamidi, Graeme J. Hankey, Arief Hargono, Risky K. Hartono, Maryam Hashemian, Abdiwahab Hashi, Shoaib Hassan, Hamid Y. Hassen, Rasmus J. Havmoeller, Simon I. Hay, Khezar Hayat, Golnaz Heidari, Claudiu Herteliu, Ramesh Holla, Mostafa Hosseini, Mehdi Hosseinzadeh, Mihaela Hostiuc, Sorin Hostiuc, Mowafa Househ, Junjie Huang, Ayesha Humayun, Ivo Iavicoli, Charles U. Ibeneme, Segun E. Ibitoye, Olayinka S. Ilesanmi, Irena M. Ilic, Milena D. Ilic, Usman Iqbal, Seyed Sina N. Irvani, Sheikh Mohammed Shariful Islam, Rakibul M. Islam, Hiroyasu Iso, Masao Iwagami, Vardhmaan Jain, Tahereh Javaheri, Sathish Kumar Jayapal, Shubha Jayaram, Ranil Jayawardena, Panniyammakal Jeemon, Ravi P. Jha, Jost B. Jonas, Jitendra Jonnagaddala, Farahnaz Joukar, Jacek J. Jozwiak, Mikk Jürisson, Ali Kabir, Tanvir Kahlon, Rizwan Kalani, Rohollah Kalhor, Ashwin Kamath, Ibrahim Kamel, Himal Kandel, Amit Kandel, André Karch, Ayele Semachew Kasa, Patrick D.M.C. Katoto, Gbenga A. Kayode, Yousef S. Khader, Mohammad Khammarnia, Muhammad S. Khan, Md Nuruzzaman Khan, Maseer Khan, Ejaz A. Khan, Khaled Khatab, Gulam M.A. Kibria, Yun Jin Kim, Gyu Ri Kim, Ruth W. Kimokoti, Sezer Kisa, Adnan Kisa, Mika Kivimäki, Dhaval Kolte, Ali Koolivand, Vladimir A. Korshunov, Sindhura Lakshmi Koulmane Laxminarayana, Ai Koyanagi, Kewal Krishan, Vijay Krishnamoorthy, Barthelemy Kuate Defo, Burcu Kucuk Bicer, Vaman Kulkarni, G. Anil Kumar, Nithin Kumar, Om P. Kurmi, Dian Kusuma, Gene F. Kwan, Carlo La Vecchia, Ben Lacey, Tea Lallukka, Qing Lan, Savita Lasrado, Zohra S. Lassi, Paolo Lauriola, Wayne R. Lawrence, Avula Laxmaiah, Kate E. LeGrand, Ming-Chieh Li, Bingyu Li, Shanshan Li, Stephen S. Lim, Lee-Ling Lim, Hualiang Lin, Ziqiang Lin, Ro-Ting Lin, Xuefeng Liu, Alan D. Lopez, Stefan Lorkowski, Paulo A. Lotufo, Alessandra Lugo, Nirmal K. M, Fabiana Madotto, Morteza Mahmoudi, Azeem Majeed, Reza Malekzadeh, Ahmad A. Malik, Abdullah A. Mamun, Navid Manafi, Mohammad Ali Mansournia, Lorenzo G. Mantovani, Santi Martini, Manu R. Mathur, Giampiero Mazzaglia, Suresh Mehata, Man Mohan Mehndiratta, Toni Meier, Ritesh G. Menezes, Atte Meretoja, Tomislav Mestrovic, Bartosz Miazgowski, Tomasz Miazgowski, Irmina Maria Michalek, Ted R. Miller, Erkin M. Mirrakhimov, Hamed Mirzaei, Babak Moazen, Masoud Moghadaszadeh, Yousef Mohammad, Dara K. Mohammad, Shafiu Mohammed, Mohammed A. Mohammed, Yaser Mokhayeri, Mariam Molokhia, Ahmed A. Montasir, Ghobad Moradi, Rahmatollah Moradzadeh, Paula Moraga, Lidia Morawska, Ilais Moreno Velásquez, Jakub Morze, Sumaira Mubarik, Walter Muruet, Kamarul Imran Musa, Ahamarshan J. Nagarajan, Mahdi Nalini, Vinay Nangia, Atta Abbas Naqvi, Sreenivas Narasimha Swamy, Bruno R. Nascimento, Vinod C. Nayak, Javad Nazari, Milad Nazarzadeh, Ruxandra I. Negoi, Sandhya Neupane Kandel, Huong L.T. Nguyen, Molly R. Nixon, Bo Norrving, Jean Jacques Noubiap, Brice E. Nouthe, Christoph Nowak, Oluwakemi O. Odukoya, Felix A. Ogbo, Andrew T. Olagunju, Hans Orru, Alberto Ortiz, Samuel M. Ostroff, Jagadish Rao Padubidri, Raffaele Palladino, Adrian Pana, Songhomitra Panda-Jonas, Utsav Parekh, Eun-Cheol Park, Mojtaba Parvizi, Fatemeh Pashazadeh Kan, Urvish K. Patel, Mona Pathak, Rajan Paudel, Veincent Christian F. Pepito, Arokiasamy Perianayagam, Norberto Perico, Hai Q. Pham, Thomas Pilgrim, Michael A. Piradov, Farhad Pishgar, Vivek Podder, Roman V. Polibin, Akram Pourshams, Dimas R.A. Pribadi, Navid Rabiee, Mohammad Rabiee, Amir Radfar, Alireza Rafiei, Fakher Rahim, Vafa Rahimi-Movaghar, Mohammad Hifz Ur Rahman, Muhammad Aziz Rahman, Amir Masoud Rahmani, Ivo Rakovac, Pradhum Ram, Sudha Ramalingam, Juwel Rana, Priyanga Ranasinghe, Sowmya J. Rao, Priya Rathi, Lal Rawal, Wasiq F. Rawasia, Reza Rawassizadeh, Giuseppe Remuzzi, Andre M.N. Renzaho, Aziz Rezapour, Seyed Mohammad Riahi, Ross L. Roberts-Thomson, Leonardo Roever, Peter Rohloff, Michele Romoli, Gholamreza Roshandel, Godfrey M. Rwegerera, Seyedmoham-

mad Saadatagah, Maha M. Saber-Ayad, Siamak Sabour, Simona Sacco, Masoumeh Sadeghi, Sahar Saeedi Moghaddam, Saeed Safari, Amirhossein Sahebkar, Sana Salehi, Hamideh Salimzadeh, Mehrnoosh Samaei, Abdallah M. Samy, Itamar S. Santos, Milena M. Santric-Milicevic, Nizal Sarrafzadegan, Arash Sarveazad, Thirunavukkarasu Sathish, Monika Sawhney, Mete Saylan, Maria I. Schmidt, Aletta E. Schutte, Subramanian Senthilkumaran, Sadaf G. Sepanlou, Feng Sha, Saeed Shahabi, Izza Shahid, Masood A. Shaikh, Mahdi Shamali, Morteza Shamsizadeh, Md Shajedur Rahman Shawon, Aziz Sheikh, Mika Shigematsu, Min-Jeong Shin, Jae Il Shin, Rahman Shiri, Ivy Shiue, Kerem Shuval, Soraya Siabani, Tariq J. Siddiqi, Diego A.S. Silva, Jasvinder A. Singh, Ambrish Singh Mtech, Valentin Y. Skryabin, Anna A. Skryabina, Amin Soheili, Emma E. Spurlock, Leo Stockfelt, Stefan Stortecky, Saverio Stranges, Rizwan Suliankatchi Abdulkader, Hooman Tadbiri, Eyayou G. Tadesse, Degena B. Tadesse, Masih Tajdini, Md Tariqujjaman, Berhane F. Teklehaimanot, Mohamad-Hani Temsah, Ayenew K. Tesema, Bhaskar Thakur, Kavumpurathu R. Thankappan, Rekha Thapar, Amanda G. Thrift, Binod Timalsina, Marcello Tonelli, Mathilde Touvier, Marcos R. Tovani-Palone, Avnish Tripathi, Jaya P. Tripathy, Thomas C. Truelsen, Guesh M. Tsegay, Gebiyaw W. Tsegaye, Nikolaos Tsilimparis, Biruk S. Tusa, Stefanos Tyrovolas, Krishna Kishore Umapathi, Brigid Unim, Bhaskaran Unnikrishnan, Muhammad S. Usman, Muthiah Vaduganathan, Pascual R. Valdez, Tommi J. Vasankari, Diana Z. Velazquez, Narayanaswamy Venketasubramanian, Giang T. Vu, Isidora S. Vujcic, Yasir Waheed, Yanzhong Wang, Fang Wang, Jingkai Wei, Robert G. Weintraub, Abrha H. Weldemariam, Ronny Westerman, Andrea S. Winkler, Charles S. Wiysonge, Charles D.A. Wolfe, Befikadu Legesse Wubishet, Gelin Xu, Ali Yadollahpour, Kazumasa Yamagishi, Lijing L. Yan, Srikanth Yandrapalli, Yuichiro Yano, Hiroshi Yatsuya, Tomas Y. Yeheyis, Yigizie Yeshaw, Christopher S. Yilgwan, Naohiro Yonemoto, Chuanhua Yu, Hasan Yusefzadeh, Geevar Zachariah, Sojib Bin Zaman, Muhammed S. Zaman, Maryam Zamanian, Ramin Zand, Alireza Zandifar, Afshin Zarghi, Mikhail S. Zastrozhin, Anasthasia Zastrozhina, Zhi-Jiang Zhang, Yunquan Zhang, Wangjian Zhang, Chenwen Zhong, Zhiyong Zou, Yves Miel H. Zuniga, Christopher J.L. Murray and Valentin Fuster. *Global Burden of Cardiovascular Diseases and Risk Factors, 1990–2019.* Journal of the American College of Cardiology, vol. 76, no. 25, pages 2982–3021, December 2020. (Cited on pages vii, 1 and 2.)

[Ruggeri & Mendolicchio 2007] Zaverio M. Ruggeri and G. Loredana Mendolicchio. *Adhesion Mechanisms in Platelet Function.* Circulation Research, vol. 100, no. 12, pages 1673–1685, June 2007. (Cited on page 6.)

[Ruggeri 2009] Zaverio M. Ruggeri. *Platelet Adhesion under Flow.* Microcirculation, vol. 16, no. 1, pages 58–83, January 2009. (Cited on pages 3, 5, 7, 17, 96, 135 and 136.)

[Sachs *et al.* 2020] Laura Sachs, Christian Denker, Andreas Greinacher and Raghavendra Palankar. *Quantifying Single-Platelet Biomechanics: An Outsider's Guide to Biophysical Methods and Recent Advances.* Research and Practice in Thrombosis and Haemostasis, vol. 4, no. 3, pages 386–401, 2020. (Cited on page 4.)

[Schneider *et al.* 2007] S. W. Schneider, S. Nuschele, A. Wixforth, C. Gorzelanny, A. Alexander-Katz, R. R. Netz and M. F. Schneider. *Shear-Induced Unfolding Triggers Adhesion of von Willebrand Factor Fibers.* Proceedings of the National Academy of Sciences, vol. 104, no. 19, pages 7899–7903, May 2007. (Cited on page 135.)

[Shiozaki *et al.* 2016] Seiji Shiozaki, Shu Takagi and Shinya Goto. *Prediction of Molecular Interaction between Platelet Glycoprotein Ibα and von Willebrand Factor Using Molecular Dynamics Simu-*

lations. Journal of Atherosclerosis and Thrombosis, vol. 23, no. 4, pages 455–464, 2016. (Cited on page 19.)

[Sigüenza *et al.* 2016] J. Sigüenza, S. Mendez, D. Ambard, F. Dubois, F. Jourdan, R. Mozul and F. Nicoud. *Validation of an Immersed Thick Boundary Method for Simulating Fluid–Structure Interactions of Deformable Membranes*. Journal of Computational Physics, vol. 322, pages 723–746, October 2016. (Cited on page 100.)

[Specogna & Trevisan 2011] Ruben Specogna and Francesco Trevisan. *A Discrete Geometric Approach to Solving Time Independent Schrödinger Equation*. Journal of Computational Physics, vol. 230, no. 4, pages 1370–1381, February 2011. (Cited on page 61.)

[Springer 2014] Timothy A. Springer. *Von Willebrand Factor, Jedi Knight of the Bloodstream*. Blood, vol. 124, no. 9, pages 1412–1425, August 2014. (Cited on page 5.)

[Taylor 1967] G.I. Taylor. *Film Notes for Low-Reynolds-number Flows*. NAtional Committee for Fluid Mechanics Films, 1967. (Cited on pages viii, 27 and 28.)

[Tong *et al.* 2023] Dudu Tong, Nidhi Soley, Reza Kolasangiani, Martin A. Schwartz and Tamara C. Bidone. *Integrin $\alpha IIb\beta 3$ Intermediates: From Molecular Dynamics to Adhesion Assembly*. Biophysical Journal, vol. 122, no. 3, pages 533–543, February 2023. (Cited on pages viii, 6, 19 and 21.)

[Tosenberger *et al.* 2012] A. Tosenberger, F. Ataullakhanov, N. Bessonov, M. Panteleev, A. Tokarev and V. Volpert. *Modelling of Thrombus Growth and Growth Stop in Flow by the Method of Dissipative Particle Dynamics*. Russian Journal of Numerical Analysis and Mathematical Modelling, vol. 27, no. 5, January 2012. (Cited on page 17.)

[Tözeren & Skalak 1977] Aydin Tözeren and Richard Skalak. *Stress in a Suspension near Rigid Boundaries*. Journal of Fluid Mechanics, vol. 82, no. 2, pages 289–307, September 1977. (Cited on pages 36, 37 and 39.)

[Udriște *et al.* 2024] Alexandru Scafa Udriște, Alexandra Cristina Burdușel, Adelina-Gabriela Niculescu, Marius Rădulescu and Alexandru Mihai Grumezescu. *Coatings for Cardiovascular Stents—An Up-to-Date Review*. International Journal of Molecular Sciences, vol. 25, no. 2, page 1078, January 2024. (Cited on page 8.)

[Vahidkhah & Bagchi 2015] Koohyar Vahidkhah and Prosenjit Bagchi. *Microparticle Shape Effects on Margination, near-Wall Dynamics and Adhesion in a Three-Dimensional Simulation of Red Blood Cell Suspension*. Soft Matter, vol. 11, no. 11, pages 2097–2109, 2015. (Cited on pages 17 and 21.)

[Vahidkhah *et al.* 2014] Koohyar Vahidkhah, Scott L. Diamond and Prosenjit Bagchi. *Platelet Dynamics in Three-Dimensional Simulation of Whole Blood*. Biophysical Journal, vol. 106, no. 11, pages 2529–2540, June 2014. (Cited on pages viii, 16, 17 and 18.)

[Vantieghem 2011] Stijn Vantieghem. *Numerical Simulations of Quasi-Static Magnetohydrodynamics Using an Unstructured Finite Volume Solver: Development and Applications*. PhD thesis, 2011. (Cited on pages 58 and 61.)

[Wang *et al.* 2018] Guiquan Wang, Micheline Abbas, Zhaosheng Yu, Annaïg Pedrono and Eric Climent. *Transport of Finite-Size Particles in a Turbulent Couette Flow: The Effect of Particle*

Shape and Inertia. International Journal of Multiphase Flow, vol. 107, pages 168–181, October 2018. (Cited on pages 71 and 80.)

[Wang *et al.* 2020] Liwei Wang, Zengsheng Chen, Jiafeng Zhang, Xiwen Zhang and Zhongjun J. Wu. *Modeling Clot Formation of Shear-Injured Platelets in Flow by a Dissipative Particle Dynamics Method*. Bulletin of Mathematical Biology, vol. 82, no. 7, page 83, July 2020. (Cited on pages viii, 17, 18 and 55.)

[WHO 2024] WHO. *The Top 10 Causes of Death*. https://www.who.int/news-room/fact-sheets/detail/the-top-10-causes-of-death, 2024. (Cited on pages vii, 1, 2 and 151.)

[Wu *et al.* 2017] Wei-Tao Wu, Megan A. Jamiolkowski, William R. Wagner, Nadine Aubry, Mehrdad Massoudi and James F. Antaki. *Multi-Constituent Simulation of Thrombus Deposition*. Scientific Reports, vol. 7, no. 1, page 42720, May 2017. (Cited on pages viii, 19 and 20.)

[Yago *et al.* 2008] Tadayuki Yago, Jizhong Lou, Tao Wu, Jun Yang, Jonathan J. Miner, Leslie Coburn, José A. López, Miguel A. Cruz, Jing-Fei Dong, Larry V. McIntire, Rodger P. McEver and Cheng Zhu. *Platelet Glycoprotein Ibα Forms Catch Bonds with Human WT vWF but Not with Type 2B von Willebrand Disease vWF*. Journal of Clinical Investigation, page JCI35754, August 2008. (Cited on page 136.)

[Yang *et al.* 2010] Yun Yang, Yuekun Lai, Qiqing Zhang, Ke Wu, Lihai Zhang, Changjian Lin and Peifu Tang. *A Novel Electrochemical Strategy for Improving Blood Compatibility of Titanium-Based Biomaterials*. Colloids and Surfaces B: Biointerfaces, vol. 79, no. 1, pages 309–313, August 2010. (Cited on page 13.)

[Yazdani *et al.* 2017] Alireza Yazdani, He Li, Jay D. Humphrey and George Em Karniadakis. *A General Shear-Dependent Model for Thrombus Formation*. PLOS Computational Biology, vol. 13, no. 1, page e1005291, January 2017. (Cited on pages viii, xviii, 4, 16, 17, 18, 19, 55, 137, 154 and 155.)

[Yazdani *et al.* 2018] Alireza Yazdani, He Li, Matthew R. Bersi, Paolo Di Achille, Joseph Insley, Jay D. Humphrey and George Em Karniadakis. *Data-Driven Modeling of Hemodynamics and Its Role on Thrombus Size and Shape in Aortic Dissections*. Scientific Reports, vol. 8, no. 1, page 2515, February 2018. (Cited on page 19.)

[Ye *et al.* 2009] Xia Ye, Yun-liang Shao, Ming Zhou, Jian Li and Lan Cai. *Research on Micro-Structure and Hemo-Compatibility of the Artificial Heart Valve Surface*. Applied Surface Science, vol. 255, no. 13-14, pages 6686–6690, April 2009. (Cited on pages iii, vii, viii, 9, 10, 11 and 13.)

[Ye *et al.* 2014] Xia Ye, Bharat Bhushan, Ming Zhou and Weining Lei. *The Surface Microstructure of Cusps and Leaflets in Rabbit and Mouse Heart Valves*. Beilstein Journal of Nanotechnology, vol. 5, pages 622–629, May 2014. (Cited on pages 9 and 10.)

[Zaninetti *et al.* 2020] Carlo Zaninetti, Laura Sachs and Raghavendra Palankar. *Role of Platelet Cytoskeleton in Platelet Biomechanics: Current and Emerging Methodologies and Their Potential Relevance for the Investigation of Inherited Platelet Disorders*. Hämostaseologie, vol. 40, no. 03, pages 337–347, August 2020. (Cited on page 4.)

[Zhang *et al.* 2015] Wei Zhang, Wei Deng, Liang Zhou, Yan Xu, Wenjun Yang, Xin Liang, Yizhen Wang, John D. Kulman, X. Frank Zhang and Renhao Li. *Identification of a Juxtamembrane*

Mechanosensitive Domain in the Platelet Mechanosensor Glycoprotein Ib-IX Complex. Blood, vol. 125, no. 3, pages 562–569, January 2015. (Cited on pages 136 and 137.)

[Zhang *et al.* 2017] Peng Zhang, Li Zhang, Marvin J. Slepian, Yuefan Deng and Danny Bluestein. *A Multiscale Biomechanical Model of Platelets: Correlating with in-Vitro Results*. Journal of Biomechanics, vol. 50, pages 26–33, January 2017. (Cited on pages 19 and 21.)

[Zhang *et al.* 2021] Peng Zhang, Jawaad Sheriff, Shmuel Einav, Marvin J. Slepian, Yuefan Deng and Danny Bluestein. *A Predictive Multiscale Model for Simulating Flow-Induced Platelet Activation: Correlating in Silico Results with in Vitro Results*. Journal of Biomechanics, vol. 117, page 110275, March 2021. (Cited on pages viii, 19 and 21.)

[Zheng *et al.* 2020] Xiaoning Zheng, Alireza Yazdani, He Li, Jay D. Humphrey and George E. Karniadakis. *A Three-Dimensional Phase-Field Model for Multiscale Modeling of Thrombus Biomechanics in Blood Vessels*. PLOS Computational Biology, vol. 16, no. 4, page e1007709, April 2020. (Cited on pages viii and 20.)

[Zhou *et al.* 2008] Ming Zhou, Jia Hong Yang, Xia Ye, Ao Ran Zheng, Gang Li, Pei Fang Yang, Yi Zhu and Lan Cai. *Blood Platelet's Behavior on Nanostructured Superhydrophobic Surface*. Journal of Nano Research, vol. 2, pages 129–136, August 2008. (Cited on pages 10, 11 and 12.)

Numerical simulation of blood platelets adhesion on structured artificial surfaces

Cardiovascular diseases remain the leading cause of death worldwide, despite advances in treatment and prevention. Blood contacting medical devices like stents, mechanical valves and ventricular assist devices are crucial in the treatment of these pathologies. However, their interaction with blood leads to activation and adhesion of blood platelets that will result in thrombus formation compromising the safety and efficiency of the device as well as requireing anti-thrombotic side treatment.

Improving the hemocompatibility of these devices remains one t-of the key challenge to their development. The most studied strategies for that rely on the use of biocompatible materials, anti adhesive coatings or endothelialization of the surface. Recently, surface topographical structuring at the micro and nanoscale emerged as a promising solution, inspired by the morphology of the endothelium, to limit the adhesion of blood platelets. However, the experimental results on this matter are often incomplete or contradictory. The aim of this research project is therefore to develop a numerical model of blood platelets adhesion to get rid of some experimental constraints, with goal to study in more detail the interactions between blood platelets and structured surfaces, both from the adhesion mechanisms point of view as well as the purely hydrodynamic point of view.

Keywords: Thrombosis, CFD, Platelet, particulate flows

Simulation numérique de l'ahdésion plaquettaire sur des surfaces artificielles microstructurées

Les maladies cardiovasculaires demeurent la principale cause de mortalité à l'échelle mondiale, malgré les avancées en prévention et en traitement. Les dispositifs médicaux implantables, tels que les stents, valves mécaniques et dispositifs d'assistance ventriculaire, sont essentiels dans la prise en charge de ces pathologies. Toutefois, leur interaction avec le sang induit des phénomènes d'activation et d'adhésion plaquettaires susceptibles de générer des thrombus, compromettant la sécurité et l'efficacité clinique de ces dispositifs et nécessitant un traitement anti-thrombotique.

L'amélioration de l'hémocompatibilité de ces appareils médicaux constitue donc un enjeu majeur. Les stratégies les plus étudiées reposent sur le choix de matériaux biocompatibles, l'application de revêtements anti-adhésifs ou l'endothélialisation des surfaces. Récemment, la structuration topographique à l'échelle micro et nanométrique a émergé comme une solution prometteuse, inspirée par la morphologie de l'endothélium vasculaire, pour limiter l'adhésion des plaquettes. Cependant, les différents résultats expérimentaux à ce sujet sont parfois incomplets voire contradictoires. L'objectif de cette thèse est donc de développer un modèle numérique de l'adhésion plaquettaire permettant de s'affranchir de certaines difficultées expérimentales, dans l'objectif d'étudier en détail les interactions entre les plaquettes sanguines et des surfaces structurées, autant du point de vue des mécanismes d'adhésion que d'un point de vue purement hydrodynamique.

Mots clés : Thrombose, CFD, Plaquettes, Ecoulements particulaires